



Veröffentlichungen der DGK

Ausschuss Geodäsie der Bayerischen Akademie der Wissenschaften

Reihe C

Dissertationen

Heft Nr. 829

Julia Neelmeijer

**Observing Inter- and Intra-Annual Glacier Changes
and Lake Loading Effects
from Synthetic Aperture Radar Remote Sensing**

München 2019

Verlag der Bayerischen Akademie der Wissenschaften

ISSN 0065-5325

ISBN 978-3-7696-5240-6

Diese Arbeit ist gleichzeitig veröffentlicht in:

Wissenschaftliche Arbeiten der Fachrichtung Geodäsie und Geoinformatik der Universität Hannover

ISSN 0174-1454, Nr. 348, Hannover 2018



Veröffentlichungen der DGK

Ausschuss Geodäsie der Bayerischen Akademie der Wissenschaften

Reihe C

Dissertationen

Heft Nr. 829

Observing Inter- and Intra-Annual Glacier Changes
and Lake Loading Effects from
Synthetic Aperture Radar Remote Sensing

Von der Fakultät für Bauingenieurwesen und Geodäsie
der Gottfried Wilhelm Leibniz Universität Hannover
zur Erlangung des Grades
Doktor-Ingenieurin (Dr.-Ing.)
genehmigte Dissertation

Vorgelegt von

Dipl.-Ing. Julia Neelmeijer

München 2019

Verlag der Bayerischen Akademie der Wissenschaften

ISSN 0065-5325

ISBN 978-3-7696-5240-6

Diese Arbeit ist gleichzeitig veröffentlicht in:
Wissenschaftliche Arbeiten der Fachrichtung Geodäsie und Geoinformatik der Universität Hannover
ISSN 0174-1454, Nr. 348, Hannover 2018

Adresse der DGK:



Ausschuss Geodäsie der Bayerischen Akademie der Wissenschaften (DGK)

Alfons-Goppel-Straße 11 • D – 80 539 München
Telefon +49 – 331 – 288 1685 • Telefax +49 – 331 – 288 1759
E-Mail post@dgk.badw.de • <http://www.dgk.badw.de>

Prüfungskommission:

Vorsitzende: Prof. Dr.-Ing. habil. Monika Sester

Referent: Prof. Dr. Mahdi Motagh

Korreferenten: Prof. Dr.-Ing. habil. Jürgen Müller
Prof. Dr. Matthias Braun

Tag der mündlichen Prüfung: 08. Oktober 2018

© 2019 Bayerische Akademie der Wissenschaften, München

Alle Rechte vorbehalten. Ohne Genehmigung der Herausgeber ist es auch nicht gestattet,
die Veröffentlichung oder Teile daraus auf photomechanischem Wege (Photokopie, Mikrokopie) zu vervielfältigen

Abstract

The new generation of spaceborne Synthetic Aperture Radar (SAR) missions, such as the TerraSAR-X/TanDEM-X or the Sentinel-1 mission, acquire data with unprecedented spatial and temporal resolution. The short revisit times of the SAR satellites and the independence from solar illumination and weather conditions enable regular monitoring of topography changes and displacement variations. This is particularly useful for applications in high-mountain areas where optical spaceborne sensors provide only limited data due to cloud coverage, and where in-situ measurements are difficult to acquire on a regular basis.

This thesis focuses on the observation of inter- and intra-annual glacier changes and lake loading-induced deformations in high-mountain areas. An essential element of the work is the exploitation of various SAR processing methods to extract seasonal displacements and topography changes that occur with magnitudes of a 10th of a millimetre over several months up to a couple of metres within a few days. Focus is laid on the reduction of signal disturbance sources that are particularly related to the mountainous setting. The main sources of error in this context are atmospheric effects and radar penetration into the ground. The investigations are carried out in three exemplary case studies in Kyrgyzstan, Central Asia, as introduced below.

In the first study, seasonal variations of glacier surface velocities are analysed on the example of the Inylchek Glacier. A detailed analysis of the flow behaviour of the bending area is achieved by applying feature tracking on TerraSAR-X data acquired in 2009 and 2010. Results show that the 3 m resolution StripMap data allows for a distinction between different surface velocities of adjacent longitudinal ice-streams. The processing of SAR data acquired every eleven days also allows the extraction of the surface motion increase during the melting period. In addition, a 100% speed-up of the lower, rather stagnant ablation area of the Southern Inylchek Glacier is captured in summer time, which has been related to the glacier lake outburst flood of Lake Merzbacher.

The second analysis deals with glacier elevation changes at the Inylchek Glacier. Three 10 m spatial resolution digital elevation models (DEMs) are generated for February 2012, March 2013 and November 2013 from bistatic TanDEM-X data, and are compared with each other as well as to the C-band Shuttle Radar Topography Mission (SRTM) DEM from the year 2000. It is shown that the intra-annual comparison between the high-resolution TanDEM-X DEMs is useful to even depict seasonal changes, although uncertainties are high due to approximated radar penetration depths. A new method to assess the glacier elevation changes in void areas based on elevation binning and slope steepness is introduced. Mass balances calculated for the decadal changes agree well with results of previously published long-term studies.

The third investigation is related to water-level induced deformations occurring at the Toktogul Reservoir. Significant changes of the water level lead to load changes on the crust, which results in subsidence in the case of water level increase and uplift in case of water level lowering. The deformation analysis is accomplished by applying the Small BAseline Subset (SBAS) method on 2004 – 2009 Envisat and 2014 – 2016 Sentinel-1 data. Whereas both datasets allow to depict an overall deformation trend within the analysed time periods, only Sentinel-1 imagery shows that the observed deformations are closely correlated to seasonal water level changes. Results are verified by a very good agreement to deformation rates estimated from elastic forward modelling with a numerical Earth model. The phase of the SAR data is heavily influenced by atmospheric effects, which are mainly related to seasonally varying stratification of the atmosphere and the daily cycle in evaporation at the open water surface. To determine the best method for the reduction of atmospheric effects, numerical weather model-based approaches are compared with phase-dependent approaches. It is found that phase-based methods are currently superior to weather model-based approaches for the application in high-mountain areas, whereas the power-law methods works best.

Keywords: SAR, inter- and intra-annual displacement, topography change, Inylchek Glacier, Toktogul Reservoir, high-mountain monitoring, Central Asia

Zusammenfassung

Die neue Generation von weltraumgestützten Synthetic Aperture Radar (SAR) Missionen, wie die TerraSAR-X/TanDEM-X oder die Sentinel-1 Mission, erfassen Daten mit bisher unerreichter räumlicher und zeitlicher Auflösung. Die kurzen Wiederkehrzeiten der SAR-Satelliten und die Unabhängigkeit von Sonnenstand und Wetterverhältnissen ermöglichen eine regelmäßige Überwachung von Änderungen in der Topographie und anderen Deformationen. Dies ist besonders vorteilhaft für Anwendungen in Hochgebirgsregionen, in denen optische raumgestützte Sensoren aufgrund von Wolkenbedeckung nur unregelmäßig Daten liefern und in-situ Messungen nur in begrenztem Umfang erhoben werden können.

Diese Arbeit konzentriert sich auf die Beobachtung von zwischen- und innerjährlichen Gletscherveränderungen und durch Wasserlast in Seen bedingte Verformungen der Erdkruste in Hochgebirgsregionen. Ein wesentliches Element der Arbeit ist die Nutzung von verschiedenen SAR-Prozessierungsmethoden, um die saisonalen Verschiebungen und Topographieänderungen zu extrahieren, die von einigen zehntel Millimetern über mehrere Monate bis zu einigen Metern innerhalb weniger Tage verlässlich detektiert werden können. Besonderes Augenmerk wird auf die Reduzierung von Signalstörquellen gelegt, die insbesondere im Zusammenhang mit der Hochgebirgslage stehen. Hauptfehlerquellen sind dabei vor allem atmosphärische Effekte und das Eindringen des Radarsignals in den Untergrund. Die Untersuchungen werden am Beispiel von drei exemplarischen Fallstudien in Kirgisistan, Zentralasien, durchgeführt.

In der ersten Studie werden die saisonalen Variationen der Gletscheroberflächengeschwindigkeiten am Beispiel des Inylchek Gletschers analysiert. Eine detaillierte Untersuchung des Fließverhaltens im Kurvenbereich des Gletschers wird durch die Anwendung der Merkmalsnachfolgungstechnik auf TerraSAR-X Daten aus den Jahren 2009 und 2010 realisiert. Die Ergebnisse zeigen, dass die 3 m Auflösung der StripMap-Daten eine Unterscheidung zwischen verschiedenen Oberflächengeschwindigkeiten benachbarter Längseisströme ermöglicht. Die Aufnahme von SAR-Daten mit einer zeitlichen Auflösung von elf Tagen erlaubt zudem die Quantifizierung der Oberflächenbewegungszunahme während der Schmelzperiode. Außerdem wird eine Verdopplung der Geschwindigkeit des unteren, eher stagnierenden Ablationsgebietes des südlichen Inylchek Gletschers im Sommer nachgewiesen, welche auf den Ausbruch des Merzbacher Gletschersees zurückgeführt wird.

Die zweite Analyse befasst sich mit Gletscherhöhenänderungen am Inylchek Gletscher. Für Februar 2012, März 2013 und November 2013 werden aus bistatischen TanDEM-X Daten drei 10 m räumlich aufgelöste digitale Höhenmodelle (DHMs) generiert und miteinander sowie mit dem C-Band Shuttle Radar Topography Mission (SRTM) DHM aus dem Jahr 2000 verglichen. Es kann gezeigt werden, dass der innerjährliche Vergleich zwischen den hochauflösenden TanDEM-X DHMs sogar saisonale Verän-

derungen abbildet, obwohl die Unsicherheiten aufgrund der nur approximierten Radar-Eindringtiefen hoch sind. Mittels einer neuen Methode wird demonstriert, wie die Gletscherhöhenveränderungen für Leerstellen in den Daten auf der Basis von Klasseneinteilung der Höhen und Hangsteilheit abgeschätzt werden können. Die für die dekadischen Veränderungen berechneten Massenbilanzen stimmen gut mit den Ergebnissen bereits veröffentlichter Langzeitstudien überein.

Die dritte Untersuchung bezieht sich auf wasserstandsbedingte Deformationen am Toktogul Stausee. Signifikante Veränderungen des Wasserspiegels führen zu Belastungsänderungen der Erdkruste, die bei Wasserspiegelanstieg zu Senkungen und bei Wasserspiegelabsenkungen zu Hebungen führen. Die Deformationsanalyse wird durch Anwendung der Small Baseline Subset (SBAS) Methode mit in den Jahren 2004 – 2009 aufgenommenen Envisat und 2014 – 2016 aufgenommenen Sentinel-1 Daten durchgeführt. Während Daten beider Sensoren den langfristigen Verlauf der Deformation innerhalb der analysierten Zeiträume abbilden können, zeigen nur Sentinel-1 basierte Messungen, dass die beobachteten Verformungen eng mit saisonalen Wasserstandsänderungen korrelieren. Die Ergebnisse werden durch eine sehr gute Übereinstimmung mit geschätzten Verformungsraten auf Basis elastischer Vorwärtsmodellierung verifiziert, die mit einem numerischen Erdmodell berechnet wurden. Der Phasenanteil der SAR Daten wird stark durch atmosphärische Effekte beeinflusst, die hauptsächlich mit der saisonal variierenden Schichtung der Atmosphäre und dem täglichen Verdunstungszyklus an der offenen Wasseroberfläche zusammenhängen. Um die beste Methode zur Verringerung der atmosphärischen Effekte zu ermitteln, werden numerische wettermodellbasierte Ansätze mit rein phasenabhängigen Ansätzen verglichen. Es wird gezeigt, dass phasenbasierte Methoden den wetterbasierten Ansätzen in Hochgebirgsregionen derzeit noch überlegen sind, wobei die auf dem Potenzgesetz basierende Methode im speziellen Fall am besten geeignet ist.

Schlagwörter: SAR, inter- und intra-jährliche Verformung, Topographieänderung, Inylchek Gletscher, Toktogul Reservoir, Hochgebirgsmonitoring, Zentralasien

Contents

1	Introduction	11
1.1	Synthetic Aperture Radar from Spaceborne Remote Sensing	13
1.2	Satellite-Based Monitoring of the Terrestrial Water Cycle	14
1.3	Remote Sensing of Water Storage in Central Asia	14
1.4	GFZ Activities in Central Asia and Study Areas in Kyrgyzstan	16
1.5	Research Objectives	17
1.6	Outline and Structure of the Thesis	18
2	Fundamentals of Synthetic Aperture Radar Remote Sensing	19
2.1	SAR Satellite Data	21
2.2	SAR Satellite Missions	22
2.3	Interferometric SAR	22
2.4	DInSAR Time Series with PSI	27
2.5	DInSAR Time Series with SBAS	28
2.6	Feature Tracking	29
3	State of the Art	31
3.1	Inter- and Intra-Annual Glacier Surface Velocities from SAR Data	33
3.2	Inter- and Intra-Annual Glacier Elevation Changes from SAR Data	34
3.3	Inter- and Intra-Annual Loading-Induced Crustal Deformations at Water Reservoirs from SAR Data	35
4	Quantification of Inylchek Glacier Surface Kinematics	37
4.1	Abstract	39
4.2	Introduction	39
4.3	Inylchek Glacier	40
4.4	Data and Methodology	42
4.4.1	TerraSAR-X Data Set	42
4.4.2	Feature Tracking	42
4.4.3	Decomposition to 3D Velocities	45
4.5	Results	46
4.6	Discussion	50
4.6.1	Error Estimation	50
4.6.2	Inter-Annual Kinematics of the Upper Southern Inylchek Glacier Branch	50
4.6.3	Lake Level Extent and GLOF	52

4.7	Conclusions	53
4.8	Acknowledgements	54
4.9	Author Contribution	55
5	Quantification of Inylchek Glacier Elevation Changes	57
5.1	Abstract	59
5.2	Introduction	59
5.3	Data	60
5.3.1	TanDEM-X Data	60
5.3.2	External DEMs	62
5.3.3	Glacier Outlines of Inylchek	63
5.4	Methodology	63
5.4.1	Interferometric Processing of TanDEM-X Data	64
5.4.2	Alignment of the SRTM and TDX DEMs	65
5.4.3	Radar Penetration Correction	69
5.4.4	DEM Elevation Difference Calculation	70
5.4.5	Accuracy Assessment	72
5.5	Results and Discussion	73
5.5.1	Uncertainty of Measurements	73
5.5.2	DEM Alignment Quality	74
5.5.3	Inylchek Elevation Changes	75
5.6	Conclusions	77
5.7	Acknowledgements	80
5.8	Author Contribution	80
6	Quantification of Toktogul Water-Level-Induced Ground Deformations	81
6.1	Abstract	83
6.2	Introduction	83
6.3	Materials and Methods	86
6.3.1	Lake Altimetry	86
6.3.2	DInSAR processing of Envisat ASAR and Sentinel-1 Data	87
6.3.3	Atmospheric Correction	88
6.3.4	Deformation Decomposition of Sentinel-1 Data	91
6.3.5	Modelling of Elastic Surface Deformations	92
6.4	Results	93
6.4.1	Atmospheric Corrections	93
6.4.2	Ground Deformation	95
6.5	Discussion	100
6.5.1	Atmospheric Corrections	100
6.5.2	Ground Deformation	101
6.6	Conclusions	102
6.7	Acknowledgments	104

6.8	Author Contribution	104
7	Subsequent Work	105
7.1	Scope of the Chapter	107
7.2	GNSS-derived Inylchek Glacier Surface Kinematics	107
7.2.1	Abstract	107
7.2.2	Author Contribution	108
7.3	Monitoring of Lake Merzbacher's GLOF Event	108
7.3.1	Abstract	109
7.3.2	Author Contribution	109
7.4	Ongoing Work at GFZ Based on the Results of this Thesis	109
8	Summary and Outlook	111
8.1	Summary of Main Results	113
8.1.1	Methodological Aspects	113
8.1.2	Monitoring of Short-Time Changes	117
8.2	Outlook	119
	Bibliography	124

1 Introduction

1.1 Synthetic Aperture Radar from Spaceborne Remote Sensing

Radio detection and ranging (radar) systems are used to determine the position or velocity of an object by measuring the time between transmitting and receiving an electromagnetic signal. By using side-looking systems, features can be unambiguously resolved in 2D, which allows to compute an image of the surveyed area. As the azimuth resolution of such an image is directly dependent on sensor distance from the observed surface and inversely dependent on the antenna length, the application of real aperture antennas from air- or spaceborne platforms is rather limited. This restriction is overcome by using Synthetic Aperture Radar (SAR) systems that use the movement of the sensor platform to generate a synthetic antenna. (Hanssen, 2001).

Interferometric SAR (InSAR) is a geodetic observing technique that evaluates the phase differences between two electromagnetic signals reflected at a common spot of the Earth's surface. There are two ways to build an interferogram that represents such phase differences: Firstly, two signals are transmitted from two slightly different locations and are then received with the same sensor. Secondly, only one antenna is used, but the response signal is detected by two receivers located at different positions.

Interferometry was introduced for the first time in 1974 to obtain topographic maps from airborne SAR data (Graham, 1974). After realizing the potential of the technique for deformation analysis – by removing the time-invariant topographic phase increment (Gabriel et al., 1989) – and after launching the first civilian SAR satellites in the 1990ies, the amount of geophysical applications of InSAR increased tremendously (Massonnet and Feigl, 1998).

InSAR allows retrieving the spatial variations of displacements and topography changes ranging from several millimetres to metres for satellite swaths several tens of kilometres wide, thereby enabling new insights into deformation processes that act over large spatial scales (Bürgmann et al., 2000). The revisit time of an early SAR satellite was typically monthly, which already allowed InSAR-based studies of both rapid deformation events like earthquakes (Massonnet et al., 1993), and slow secular processes like subsidence (Amelung et al., 1999) or fault motion (Wright et al., 2004). Additionally, fast horizontal motion as occurring over glaciated areas could be measured by applying the feature tracking technique on the SAR data (Strozzi et al., 2002).

Even though annual cycles of deformation processes were already identified, the large temporal baseline between two acquisitions offered only limited insight into high frequency surface deformations. Revisit times were greatly improved with the advent of the latest generation of SAR satellites. Missions like TerraSAR-X/TanDEM-X (TSX/TDX) or Sentinel-1 have the possibility to acquire data with a temporal baseline of eleven or twelve days. Over Europe, selected plate-boundary regions, and several Antarctic glaciers, the Sentinel-1 mission is designed to acquire data even every six days (ESA - Sentinel-1, 2018).

1.2 Satellite-Based Monitoring of the Terrestrial Water Cycle

The terrestrial branch of the water cycle is understood here as the time-variations in all possible storages of water at or underneath the ground. Those storages include water intercepted by vegetation; the snow pack at the surface; water stored at the surface in rivers, lakes, reservoirs, and wetlands; ice in high-mountain glaciers and the large continental ice-sheets; and also water stored underneath the surface in various layers of soil and underlying bedrock that extends down to the deepest aquifers. Besides those storages, the water cycle is further characterised by the fluxes between those storages, as, e.g., overland flow, drainage, river discharge, or groundwater flow.

Over the past decades, many different spaceborne remote sensing methods have been developed to observe different aspects of the terrestrial water cycle. Satellite gravimetry as realised with the GRACE mission allowed for the first time the quantification of the combined mass change in all storages from a month-by-month comparison of global gravity field models (Jacob et al., 2012). The indirect measurement concept, however, requires an averaging over areas of 100.000 km² and larger in order to efficiently suppress noise at small spatial scales. Nadir-looking satellite altimetry provides information about water level changes in both rivers and lakes that are crossed by the groundtrack of the satellite (Koblinsky et al., 1993; Schöne et al., 2017). Optical imagery can be efficiently used to survey changes in the horizontal boundaries of lakes (Heine et al., 2015), but requires clear sky conditions. Soil moisture remote sensing has been recently realised by means of the L-Band radiometers SMOS and SMAP (Al-Yaari et al., 2017).

The SAR-based methods introduced above thus offer information complementary to and sometimes maybe even superior to alternative remote sensing methods. Provided that the measurement is accomplished with a suitable wavelength and an appropriate number of satellites, SAR sensors are able to retrieve information about, e.g. soil moisture (Srivastava et al., 2009), ground water level (Béjar-Pizarro et al., 2017), lake boundaries (Heine et al., 2014), lake bathymetry (Zhang et al., 2016), glacier surface velocity (Strozzi et al., 2002), glacier surface elevation (Rankl and Braun, 2016), and water-related surface deformation processes, such as subsidence due to ground-water extraction (Motagh et al., 2017) or loading-induced changes (Kaufmann and Amelung, 2000). Most beneficial in this context is that spaceborne SAR sensors provide data with a very high spatial resolution in the range of only a few metres. Furthermore, such SAR sensors are able to acquire images regardless of weather or sunlight conditions, which allows a reliable regular collection of information.

1.3 Remote Sensing of Water Storage in Central Asia

Semi-arid to arid conditions dominate the hydroclimate in Central Asia, which makes fresh water one of the most valuable resources in the region (O'Hara, 2000; Immerzeel et al., 2010; Bernauer and Siegfried, 2012). Although the supply is limited, the demand for fresh water is still increasing, which is related to an ongoing growth in population (Karthé et al., 2015), and particularly to the overuse of water for the irrigation of farmland (Lioubimtseva and Henebry, 2009). It is thus important to develop a strategic water management to sustain fresh water availability in the future (O'Hara, 2000; Maselli et al., 2010; Bolch, 2017). An essential part of such a water management system would

be a – preferably non-governmentally organized and externally verified – low-latency monitoring of the available fresh water supply that utilizes various remote sensing techniques (Sorg et al., 2012). Freshwater is usually stored in the mountainous parts of the region, either naturally in form of high-mountain glaciers (Aizen et al., 2007a; Braun and Hagg, 2010) or within artificially dammed water reservoirs (Sorg et al., 2014). Fresh water stored in reservoirs is thus not only been used for drinking and irrigation purposes, but also for hydro-power generation.

Monitoring of water resources is an important task for the following reasons: Firstly, knowledge about the present amount and the past evolution of the stored water masses is essential for well-founded water management decisions that balance available supply with various competing needs. This is especially crucial for fresh water gained from glacial melt. Today and in the near future, more melt water will be available due to the warming climate and the associated increase in glacier melting. In the long run, however, it is expected that most glaciers will shrink dramatically, which will result in significantly fewer melt water supply (Sorg et al., 2014; Huss and Hock, 2015; Duethmann et al., 2016). The prediction of future fresh water availability thus requires the development of numerical models that are able to reproduce past time-variations of glacier mass balance as accurately as possible.

Secondly, close monitoring of the storage environment is crucial in order to detect potential natural hazards for people living downstream of fresh water bodies. For high-mountain glaciers, one of those threats is the emergence and evolution of glacial lakes. These lakes may form, for example, behind moraines that emerge from retreating glaciers (Westoby et al., 2014) or behind glacier parts that act as natural dams (Tweed and Russell, 1999). Especially dangerous are lakes that form rather unexpectedly after a sudden glacier surge, where the ice body incidentally blocks a valley outlet (Kotlyakov et al., 2008; Mergili et al., 2013). Triggers like moraine failure, avalanches or increasing water pressure might then lead to a sudden release of the water in form of a glacial lake outburst flood (GLOF) (Bolch et al., 2011a). If residents living further downstream are unaware of the growing of such a glacial lake, the unexpected GLOF event may cause severe damage to livestock and infrastructure, or even fatalities (Richardson and Reynolds, 2000; Fujita et al., 2008). Routine low-latency monitoring of sudden changes in glacier surface velocity and short-term local glacier height changes potentially allows an early detection of a glacier surge, and might thus be used to alert residents.

Another aspect for monitoring is, thirdly, the deformation of the ground around large water reservoirs. Such deformations occur due to load changes on the crust, which are induced by water level variations, and may trigger seismic tremor or landslide activities (Roeloffs, 1988; Yin et al., 2013). Knowledge about the amount and spatial extent of such loading-related deformations are thus also beneficial for early warning systems. Additionally, intra-annual monitoring of the surroundings of water reservoirs is helpful to better understand the physics of the lithosphere. Water volumes in a reservoir change in the order of several cubic kilometres, which imply a substantial load that induces an elastic or even visco-elastic deformation response of the crust (Bevis et al., 2005; Rajner and Liwosz, 2011). Knowledge about both mass load changes and the induced deformation is thus an important information that allows refinements of models of the local Earth rheology (Dill et al., 2015).

1.4 GFZ Activities in Central Asia and Study Areas in Kyrgyzstan

Monitoring and understanding of geosphere dynamics embedded in the complex System Earth with its various interacting subcycles is the central mission of the German Research Centre for Geosciences (GFZ). In Central Asia, observations of various aspects of the terrestrial water cycle have been obtained by GFZ scientists for many years (Schöne et al., 2013; Unger-Shayesteh et al., 2013; Farinotti et al., 2015). One of the focus points of the institute is the country of Kyrgyzstan, where the establishment of a local research institute – the Central-Asian Institute for Applied Geosciences (CAIAG) – was supported by GFZ. Section 1.4 “Remote Sensing” of GFZ in particular established in a joint effort with CAIAG the “Gottfried Merzbacher” Global Change Observatory at the Inylchek Glacier (GFZ Potsdam, 2018).

The research presented in this thesis has been conducted at Section 1.4 “Remote Sensing” of GFZ. It is based on data from two exemplary study sites located in Kyrgyzstan (Figure 1.1). Glacier elevation change and glacier kinematics are investigated at the Inylchek Glacier. Surface deformations associated with changing water mass loads are studied around the Toktogul Reservoir.

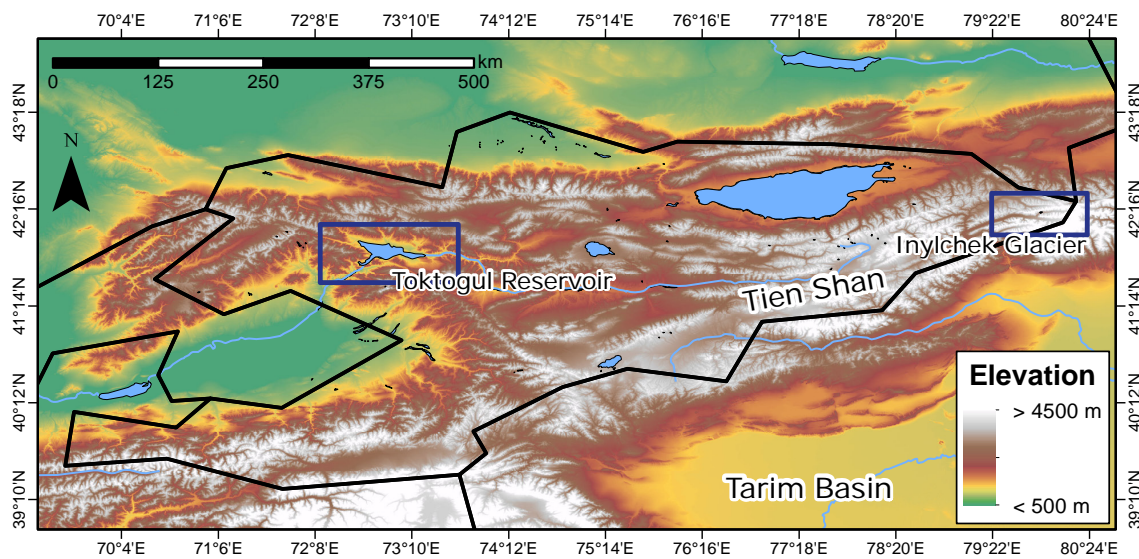


Figure 1.1: Location of the two study areas Inylchek Glacier and Toktogul Reservoir in the country of Kyrgyzstan.

The Inylchek Glacier is part of the Podeba–Khan Tengri mountain massif, located in the central Tien Shan mountain range at the eastern border of Kyrgyzstan. With a length of over 60 km and an area of about 800 km², Inylchek is one of the largest non-polar glacier systems of the world (Mayer et al., 2008). It is divided into two main parts, the Northern and the Southern Inylchek. The southern part, the larger of the two, is fed by several large tributaries, of which the highest accumulation areas are situated at about 7400 m. The glacier body itself runs down westward to a height of 2900 m (Hagg et al., 2008). The two glacier branches are separated by a glacial lake, the Lake Merzbacher. This lake drains every summer in a GLOF event, which leads to sudden flooding in urban areas located further downstream in the Tarim basin (Glazirin, 2010).

With a capacity of 19.5 km^3 , the Toktogul Reservoir is the largest artificial water reservoir in Kyrgyzstan (Tibaldi et al., 2015). Located in the north-west of Kyrgyzstan at an elevation of approximately 870 m, it is fed by melt water of the surrounding Tien Shan mountain ranges. Its largest inflow is the Naryn River. The water is mainly used for hydro-power generation during winter time and irrigation during spring-to-summer time (Keith and McKinney, 1997). This leads to large water level changes of tenths of metres within a year, but also to multi-annual periods of exaggerated water use and water replenishing phases. GFZ scientists are investigating these water level fluctuations by means of radar altimetry measurements over the period 1995 – 2017 (Schöne et al., 2017).

1.5 Research Objectives

This thesis deals with the measurement of displacements and topographic changes associated with terrestrial water storage anomalies in semi-arid, high-mountain regions of Central Asia. The focus is laid on the quantification of changes that occur in short time periods of several days to several months. This is particularly useful for a better understanding of processes that are characterised by oscillating variations and thus cannot be captured to full extent from acquisitions with long time separation. Additionally, the results can also be used to develop early warning systems that rely on regular monitoring capabilities.

The derivation of inter- and intra-annual displacements and topography changes require utilisation of new-generation SAR satellites that acquire data with short revisit cycles. In addition, the different types of applications require the use of different processing methods. Depending on the characteristics of the surface and the amount of displacement or topography change, either phase-based approaches like InSAR, or amplitude-based approaches like feature tracking are suitable – both methods are elaborated in this thesis. The developed processing strategies deal particularly with the implications of the rather challenging high-mountain setting. Furthermore, an intra-annual analysis over multiple years implies the handling of a large data volume, which makes it necessary to automate the processing as much as possible.

Based on those prerequisites, two main research questions for this thesis are formulated. The first question refers to methodological issues, the second question is related to inter- and intra-annual monitoring aspects.

- 1. Which SAR methods are useful to quantify water-related displacements and topography variations, such as glacier surface kinematics, glacier elevation change and loading-induced ground deformations around water reservoirs? What special treatment of the data is required due to the high-mountain environment?**
- 2. To what extent does the new generation of SAR satellites that provide data with a high temporal sampling allow to monitor inter- and intra-annual displacements in high-mountain regions? What are the accompanying major limitations when dealing with SAR data in that framework, and how can those be overcome?**

1.6 Outline and Structure of the Thesis

This thesis is organised as follows: Chapter 2 introduces the fundamentals of Synthetic Aperture Radar remote sensing. Here, the characteristics of a SAR signal are described and further information is given about different existing displacement retrieval methods. Following on, the importance of the research with respect to former studies is discussed in Chapter 3 – State of the Art. In the three subsequent chapters, results obtained from individual research studies are presented in form of stand-alone manuscripts: Chapter 4 deals with the extraction of Inylchek Glacier surface velocities by applying a feature tracking approach on TerraSAR-X data. Chapter 5 refers to the retrieval of the Inylchek Glacier elevation changes deduced from TanDEM-X data. Chapter 6 gives insights about loading-induced deformations around the Toktogul Reservoir as observed from Envisat and Sentinel-1 data, supported by a numerical model experiment. The presentation of the studies is followed by a short overview about related subsequent work that was published together with colleagues from GFZ (Chapter 7). Those papers are based on the findings of the previous studies and demonstrate the relevance of this work for other research activities at GFZ. Finally, the research questions are answered in detail in the synthesis (Chapter 8), which is complemented by an outlook.

This thesis is organised in a cumulative way, which means that Chapters 4 – 6 are based on individual research studies that were previously published in international peer-reviewed scientific journals. Besides formatting and referencing adjustments, the three manuscripts are presented in their original form. All references are accumulated at the end of the thesis in the bibliography. For all three papers, the main research work and writing was done by the author of this thesis.

2 Fundamentals of Synthetic Aperture Radar Remote Sensing

2.1 SAR Satellite Data

SAR sensors on board of remote sensing satellites illuminate the Earth with electromagnetic waves that are transmitted in the microwave domain. As the signal is actively sent out, the radar measurements are independent of sunlight illumination. Furthermore, the long wavelengths allow the signal to penetrate through clouds. As a consequence, the SAR sensor is able to retrieve an image of the Earth's surface from the backscattered energy 24 hours a day.

The derived SAR signal is composed of two elements, which are the amplitude and the phase of the electromagnetic wave. The amplitude information is a measurement for the amount of the collected backscattered energy, which depends on the orientation, the shape and the electrical properties of the target. The phase of the wave is a multiple of 2π plus a residual phase from the interval $-\pi$ to $+\pi$. Whereas the exact number of full waves is difficult to determine, the quantification of the phase rest is very precise (Osmanoğlu et al., 2016).

SAR energy is transmitted in a side-looking way, with the antenna usually pointing to the right in relation to the direction of flight of the satellite. This allows an unbiased solution of the SAR signal in 2D space, as the response time of the signal is an indicator of the distance at which it was reflected from the surface. Drawbacks of the side-looking system are geometry distortions in the derived image, which are called foreshortening, layover and shadowing effects (Ferretti et al., 2007a).

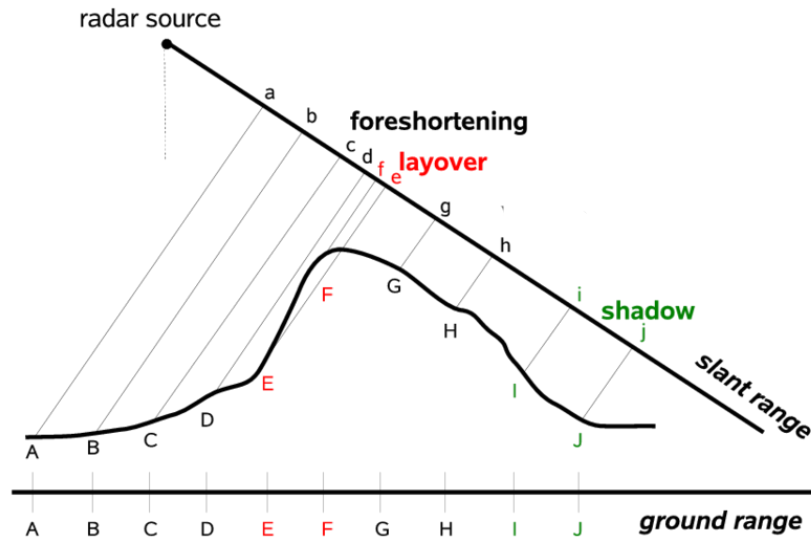


Figure 2.1: Effect of geometric distortions occurring in SAR images due to the side-looking sensing geometry (modified after Petillot et al., 2010; © 2010 IEEE, reprinted with permission).

Figure 2.1 shows the effect of geometric distortions in the high mountains due to the side-looking setting of the radar system. If the radar signal reaches the foot of a mountain before it is reflected from the top, the output appears compressed in a SAR image, which is the foreshortening effect. If the radar signal is reflected simultaneously from top and base of a mountain, foreshortening is at its maximum. If the signal is reflected from the summit prior to from the foot, layover occurs, as the response signal of the top is received earlier at the sensor than the signal from the base. This results in a placement of the backscattered energy in the SAR image towards the sensor and superimposes

the later incoming signal from the foot of the mountain. Radar shadow occurs when the signal is not able to illuminate the ground at all, as it is shielded by the high mountains.

2.2 SAR Satellite Missions

The wavelengths used for satellite-based SAR applications are X-band (~ 3 cm), C-band (~ 6 cm) and L-band (~ 24 cm). An overview about previous, current, and a number of future SAR missions is given in Figure 2.2. Major differences between the missions are not only the wavelength, but also swath width and revisit times. Further implications for science are the design as an operational or an on-demand data ordering mission, and the restricted versus open access data distribution. Restriction issues arise especially when missions are designed in a private-public-partnership (PPP), in which data are mainly commercially used. An overview about the characteristics of the most important SAR satellite missions for research purposes is given in Table 2.1. In this thesis, satellite data from Envisat, TerraSAR-X, TanDEM-X and Sentinel-1 are used.

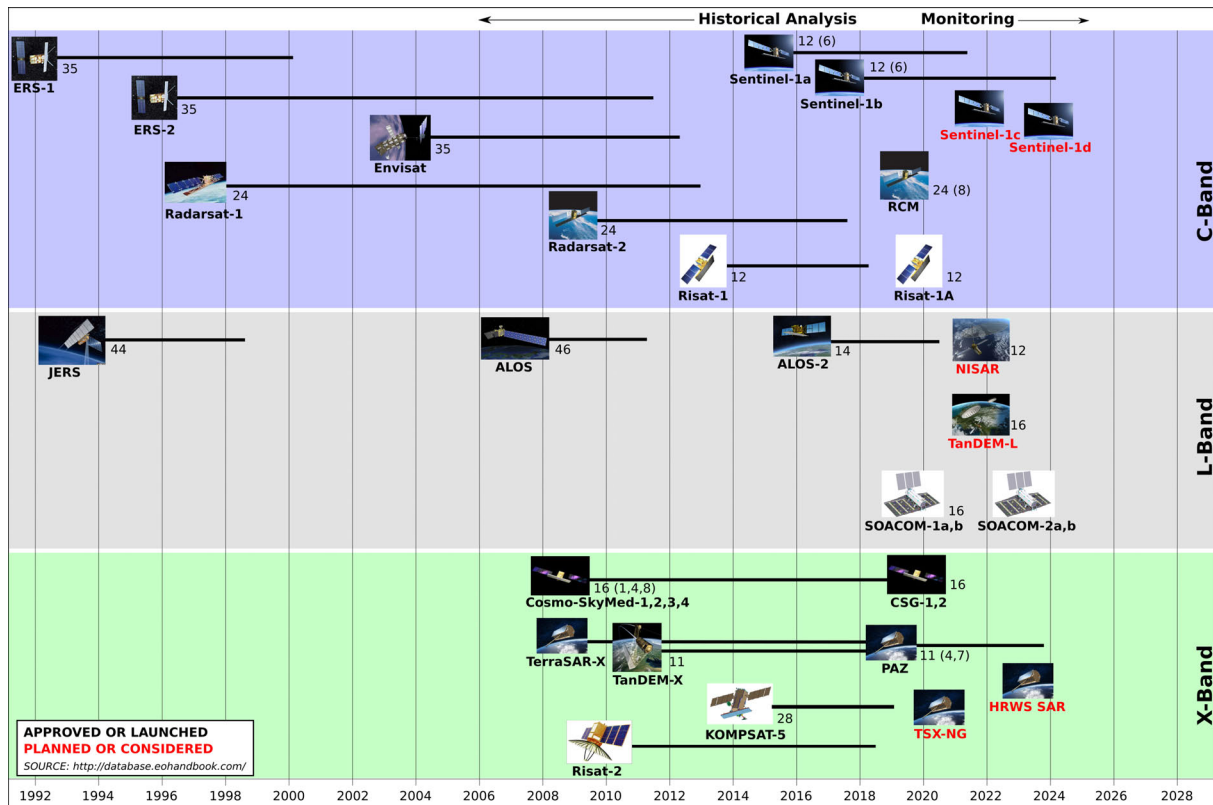


Figure 2.2: Overview about former, current and some selected future SAR satellite missions (adapted from UNAVCO, 2018; © 2018 Scott Baker/UNAVCO, reprinted with permission). Numbers indicate the temporal baseline (in days) between acquisitions. Missions that are solely used for military purposes are not shown.

2.3 Interferometric SAR

InSAR is the measurement of line-of-sight (LOS) phase differences between two SAR signals that have been transmitted or received from two slightly different locations. The method is therefore

Table 2.1: Overview about selected, most important SAR missions for research purposes so far. Operators of the SAR satellites are the European Space Agency (ESA), the Canadian Space Agency (CSA), the Japan Aerospace Exploration Agency (JAXA), the German Aerospace Center (DLR), and the Italian Space Agency (ISA).

SAR sensor/ satellite	Operator	Repeat Cycle	Spatial Resolution	Swath Width	Monitoring Mode	Data Access
ERS 1/2	ESA	35 days	30 m	100 km	operational	open access
Radarsat-1	CSA	24 days	30 m ¹	100 km	on demand	restricted
Envisat ASAR	ESA	35 days	30 m	56–100 km	operational	open access
ALOS PALSAR	JAXA	46 days	10–30 m ²	40–70 km	on demand	restricted
Cosmo-SkyMed	ISA	16 days ³	3–15 m ⁴	40 km	on demand	restricted
TerraSAR-X/TanDEM-X	DLR	11 days	9 m ⁵	30 km	on demand	restricted
Radarsat-2	CSA	24 days	25 m ⁶	100 km	on demand	restricted
Sentinel-1	ESA	6–12 days ⁷	100 m ⁸	240 km	operational	open access
ALOS-2 PALSAR-2	JAXA	14 days	10 m ⁹	70 km	on demand	restricted

¹ Standard mode. Radarsat-1 offers various modes ranging from Fine Mode (8 m spatial resolution, 45 km swath width) to ScanSAR Wide (100 m spatial resolution, 500 km swath width).

² Default mode. Spatial resolution depends on desired polarisation and ranges from 7–88 m. A ScanSAR mode further allows acquisitions with a spatial resolution of 100 m (swath width: 250–350 km).

³ Within the 16 days 4 acquisitions are taken with a temporal delay of 8, 1, 3, 4 days that is accomplished by the formation of 4 satellites.

⁴ HIMAGE mode. Cosmo-SkyMed offers more modes ranging from SpotLight (1 m spatial resolution, 10 km swath width) to HugeRegion (100 m spatial resolution, 200 km swath width).

⁵ StripMap mode (3 × 3 m spatial resolution). Further offered are acquisitions ranging from Experimental Spotlight mode (1 × 1 m spatial resolution, 10 km swath width) to ScanSAR mode (16 × 16 m spatial resolution, 100 km swath width).

⁶ Standard mode. Radarsat-2 offers various modes ranging from SpotLight (1 m spatial resolution, 18 km swath width) to ScanSAR Wide (100 m spatial resolution, 500 km swath width).

⁷ 6 days is achieved only over selected areas due to the constellation of two satellites.

⁸ Interferometric Wide Swath mode (IWS) with a resolution of 5 × 20 m (range/azimuth). Some data is also acquired in Stripmap mode (5 × 5 m spatial resolution, 80 km swath width) and Extra Wide Swath mode (25 × 100 m spatial resolution, 400 km swath width).

⁹ Stripmap Fine mode. PALSAR-2 offers various modes ranging from Spotlight (3 m spatial resolution, 25 km swath width) to ScanSAR (100 m spatial resolution, 350 km swath width).

suitable for observing changes in the topography or for the detection of displacements at the surface (Figure 2.3). InSAR is used for a variety of applications, such as seismology (Motagh et al., 2015); volcanology (Salzer et al., 2014); land subsidence/uplift detection (Motagh et al., 2017); landslide monitoring (Haghshenas Haghighi and Motagh, 2016); glaciology (Braun et al., 2011); hydrology (Gondwe et al., 2010); and forestry science (Balzter, 2001). Extensive reviews regarding the diversity of applications of InSAR are given, for example, in Gens and Van Genderen (1996); Massonnet and Feigl (1998); Hanssen (2001); Smith (2002); and Zhou et al. (2009). In this thesis, focus is laid on the applications for deriving digital elevation models (DEMs) of the surface topography to calculate elevation change and the quantification of ground displacements in horizontal and vertical direction.

To accomplish SAR interferometry, the phase differences of two SAR images are generated by calculating the conjugate complex solution, which then displays in the resulting interferogram as fringes, which are isoline bands that are showing the distance of one phase cycle to the next (Figure 2.4).

Depending on how the measurement was taken – simultaneously or repetitively – the following components are part of the phase difference signal (Osmanoğlu et al., 2016):

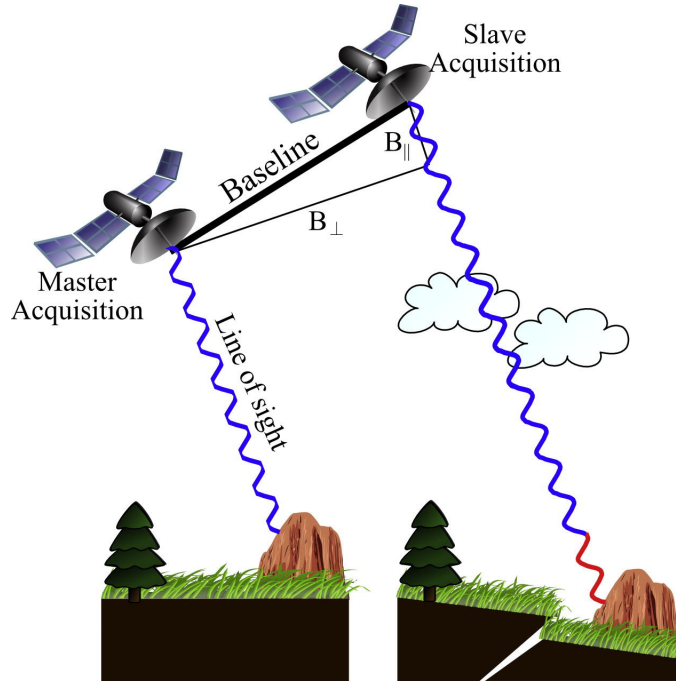


Figure 2.3: Exemplary setting of master and slave acquisitions to accomplish SAR interferometry (InSAR). A displacement between two acquisition times induces a change in the received electromagnetic phase, which is shown here in red (adapted from Osmanoglu et al., 2016; © 2016 Elsevier, reprinted with permission).

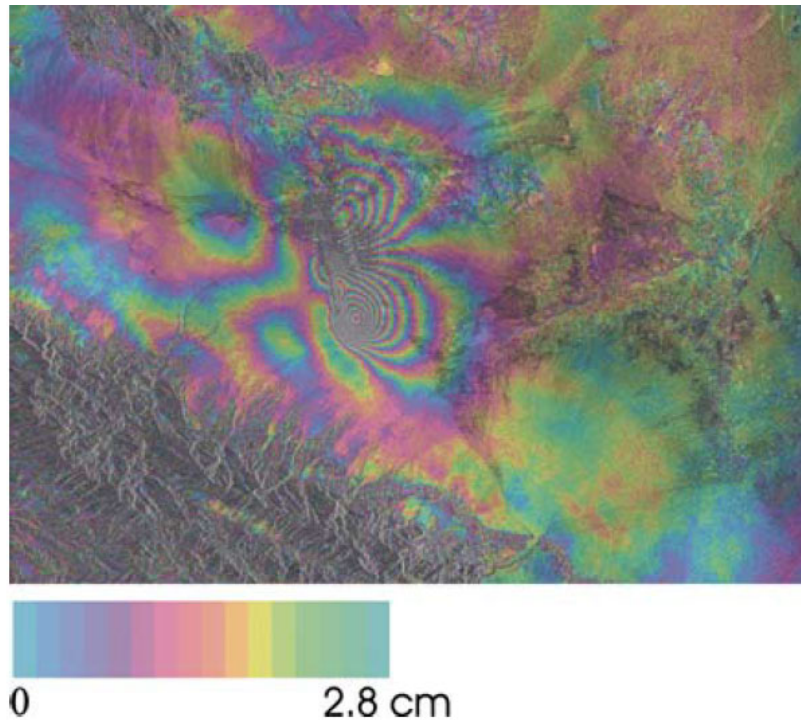


Figure 2.4: Exemplary interferogram of the coseismic displacement induced by the Bam earthquake, Iran, in 2003. One fringe denotes to half the size of the wavelength used for the measurement. In this case, Envisat C-band descending data was used for the acquisition, which results in a fringe density of 2.8 cm (modified after Motagh et al., 2006; © 2005 Springer Nature, reprinted with permission).

$$\delta\phi = \phi_{flat} + \phi_{topo} + \phi_{defo} + \phi_{atmo} + \phi_{orbit} + \phi_{scatt} + \phi_{noise}. \quad (2.1)$$

$\delta\phi$ is the measured phase difference, ϕ_{flat} the flat earth phase contribution, ϕ_{topo} the influence of the topography on the signal, ϕ_{defo} the potential deformation that occurred between two repeat-pass acquisitions, ϕ_{atmo} are atmospheric induced effects (this includes troposphere and ionosphere contributions), ϕ_{orbit} are orbital errors, ϕ_{scatt} represents phase variations due to electrical property changes of the scatterers and ϕ_{noise} is the remaining noise. Noise is attributed to the coherence of an interferogram, which depends of the following decorrelation terms (Zebker and Villasenor, 1992; Osmanoglu et al., 2016):

$$\gamma_{total} = \gamma_{spatial} + \gamma_{temporal} + \gamma_{Doppler} + \gamma_{thermal}. \quad (2.2)$$

Here, γ_{total} is the unit of measure for interferometric coherence, $\gamma_{spatial}$ is the spatial baseline decorrelation, $\gamma_{temporal}$ denotes the temporal decorrelation, $\gamma_{Doppler}$ is the dependency on the Doppler centroid, and $\gamma_{thermal}$ represents thermal effects. The spatial decorrelation refers to the horizontal distance between the locations of SAR sensors at the time of the acquisition, which cannot exceed a critical baseline. Temporal decorrelation occurs when the physical properties of a phase signal are altered too much between two repeat-pass acquisitions. Decorrelation due to the Doppler centroid happens when the satellite attitude is not equal in the master and slave acquisition. The influence of thermal effects on either sensor or target is usually negligible in SAR interferometry. Generally, if perfect correlation is achieved, γ_{total} equals 1, in a completely decorrelated interferogram γ_{total} denotes 0.

To retrieve information of a coherent interferogram, the phase differences, that are so far wrapped in fringes with values between $-\pi$ and $+\pi$, need to be extracted to relative, continuous phase values (Figure 2.5) in a process called unwrapping. A potential offset to absolute phase information can thereby only be calculated by taking into account external information such as Global Navigation Satellite System (GNSS) measurements (Osmanoglu et al., 2016). In the literature, many ways are described about how to achieve unwrapping. All of these approaches can be basically divided in either path following unwrapping algorithms (e.g. Goldstein et al., 1988; Wei Xu and Cumming, 1999; Herráez et al., 2002; Abdul-Rahman et al., 2007; Navarro et al., 2012) or path-independent unwrapping algorithms (e.g. Ghiglia and Romero, 1996; Costantini, 1998; Chen and Zebker, 2000, 2001, 2002).

Suitable image pairs for InSAR are chosen depending on the aim of the analysis. If the focus is on the derivation of the surface topography, image pairs should ideally have been taken simultaneously in order to eliminate influences such as surface deformation, changes in scattering behaviour and atmospheric effects. The setting of simultaneously acquired SAR image pairs had been used in the Shuttle Radar Topography Mission (SRTM) in 2000, which resulted in a nearly global SRTM DEM with a originally ~ 90 m (nowadays: ~ 30 m) spatial resolution (Van Zyl, 2001). Simultaneously acquired SAR data has been more recently obtained from the TerraSAR-X/TanDEM-X bistatic tandem configuration that was also especially set up to create a new global DEM – the WorldDEMTM – which is distributed with a spatial resolution of 12 m (Zink and Moreira, 2015). The usefulness and limitations of this method

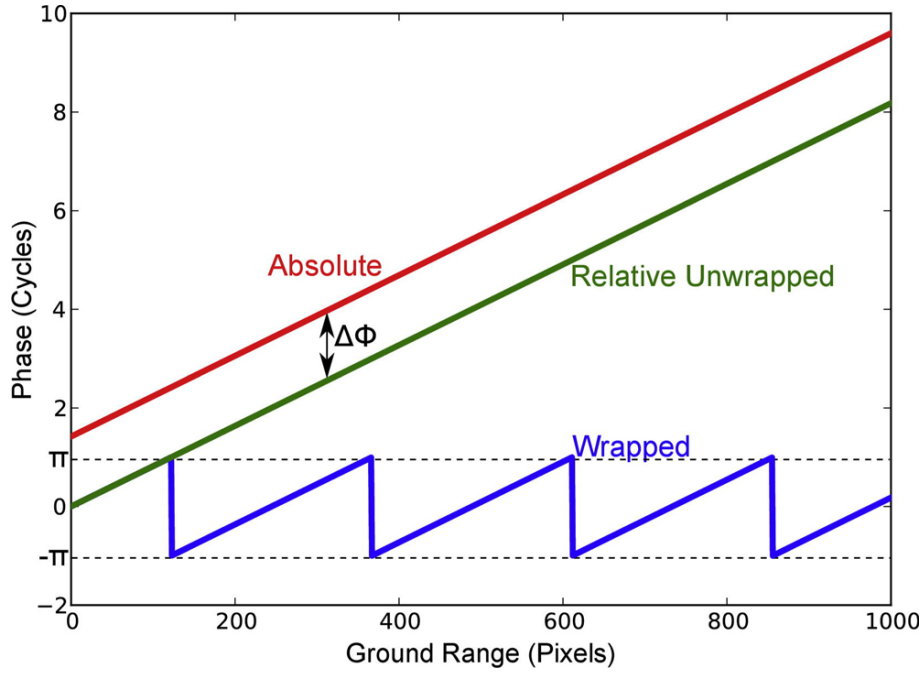


Figure 2.5: During unwrapping, the wrapped phase (blue) is resolved to relative unwrapped information (green). Additional information (as from GNSS measurements) is used to calculate the offset to absolute phase information (adapted from Osmanoglu et al., 2016; © 2016 Elsevier, reprinted with permission).

to measure glacier elevation changes are evaluated on the example of the Inylchek Glacier in Chapter 5 of this thesis.

Differential InSAR (DInSAR) is applied if the aim of the research is to measure displacements occurring between two repeat-pass acquisitions. It is accomplished by minimising influences like topography, atmosphere, scatterer behaviour, and orbital errors. Topography is efficiently removed by taking into account already existing DEMs. Orbit accuracy is in the range of a few centimetres nowadays – e.g. in each coordinate direction 5 cm for Sentinel-1 (Peter et al., 2017) – as the orbital path of a spacecraft is precisely measurable from on-board GNSS receivers. Remaining noise (including effects of scatterer behaviour change) is reduced by applying filtering techniques. The reduction of atmospheric signal disturbances is still problematic. Various ways to limit their influence exist in the literature and some of those are investigated in particularly high-mountain terrain in Chapter 6 of this thesis.

As electromagnetic phase differences between two SAR images are measured in the microwave domain, it is possible to retrieve small scale displacements that are in the order of millimetres. However, displacements may be so small that they cannot be precisely measured between two temporal closely connected SAR acquisitions. If such a deformation is part of a continuous process in time, it can be quantified by building an InSAR time series. By connecting various interferograms, the retrieval of the displacement information is achieved by simultaneously reducing the effect of atmospheric effects. The two main approaches commonly used are the Persistent Scatterers Interferometry (PSI), which aims at the retrieval of persistent scatterers and the Small Baseline Subset (SBAS) approach, which focuses rather on distributed scatterers. A more detailed explanation about both methods is given in the following two sections. It should be further noted that more recent approaches combine the

advantages of the two methods in order to increase the spatial density of the scatterer points and at the same time to increase the accuracy of the result (Rocca et al., 2013). Most prominent in this development is the SqueeSARTM method that takes into account both persistent and distributed scatterers (Ferretti et al., 2011).

2.4 DInSAR Time Series with PSI

PSI approaches aim to retrieve phase information from strongly reflecting objects that do not change over time (Figure 2.6). The size of such persistent scatterers is smaller than the SAR resolution cell, which implies that PS pixels are not affected by critical baseline decorrelation. As a consequence, a single master stack of interferograms is built that yields the overall phase change information in time with a sub-meter precision for DEMs and surface motion precision in the order of a few millimetres (Ferretti et al., 2007b). This method had been firstly described in Ferretti et al. (2000, 2001) and was further developed by Werner et al. (2003) and Kampes and Hanssen (2004). Many extensions of PSI were developed afterwards, such as the stable point network approach (Crosetto et al., 2008), or the persistent scatterer pairs approach (Costantini et al., 2012). The Stanford Method for Persistent Scatterers (StaMPS) (Hooper et al., 2004) works slightly differently: here, scatterers are chosen depending only on their phase stability in space and time without taking into consideration the amount of amplitude. This partly allows also the application of the method to natural surroundings, whereas the remaining approaches have in common that they are mainly suitable for areas with many strong, unchanging scatterers, which are typically found in urban regions only. Extensive reviews regarding these techniques are given in Osmanoglu et al. (2016) and Crosetto et al. (2016). As all of these approaches have only little potential for high-mountain applications, they are not further discussed in this thesis.

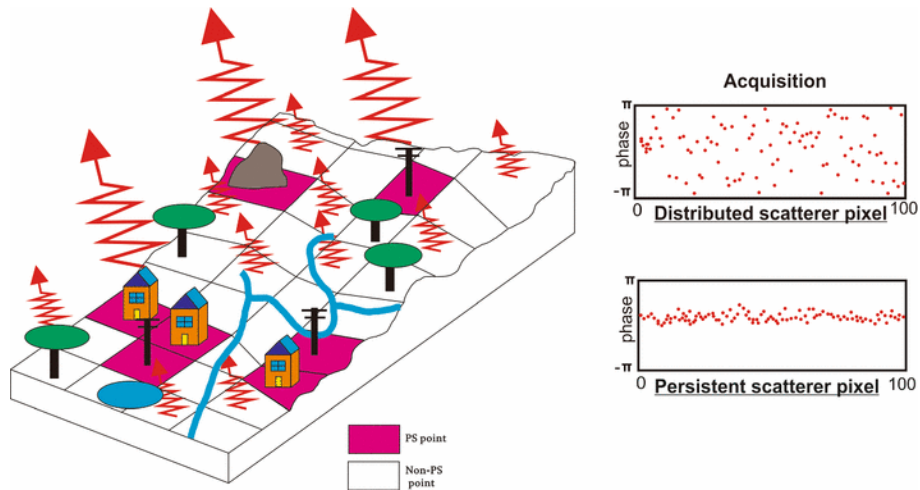


Figure 2.6: The schematic illustration shows the characteristics of persistent scatterers pixels in contrast to any other pixel containing information from distributed scatterers (adapted from Yhokha et al., 2018; © 2018 Springer Nature, reprinted with permission). The phase of distributed scatterers in various acquisitions appears random, compared to the phase of persistent scatterers, which is rather stable.

2.5 DInSAR Time Series with SBAS

The SBAS approach is based on finding coherent signals from distributed scatterers. Coherent distributed scatterers are multiple small objects in one resolution cell that lead to a response signal that is constant over the investigated time. From a stock of input acquisitions, differential interferograms are built between multiple small baseline subsets to reduce the effect of spatial decorrelation (Berardino et al., 2002; Lanari et al., 2004). Furthermore, the reduction of the temporal baseline between acquisitions allows further to mitigate the effect of temporal decorrelation (Hong et al., 2010; Hong and Wdowinski, 2014; Lanari et al., 2013).

The displacement d in a small baseline subset with the first image i and the last image j can be written as:

$$d_{ij} = d_i + d_{i+1} + \dots + d_{j-1} = \sum_{k=i}^{j-1} d_k. \quad (2.3)$$

The incremental displacement can be substituted by velocity v as follows:

$$d_{ij} = \Delta t_i v_i + \Delta t_{i+1} v_{i+1} + \dots + \Delta t_{j-1} v_{j-1} = \sum_{k=i}^{j-1} \Delta t_k v_k, \quad (2.4)$$

whereas t denotes the acquisition date and $\Delta t_i = t_{i+1} - t_i$.

The resulting system of equations can be written as (Wang et al., 2012):

$$\mathbf{G}\mathbf{m} = \mathbf{d}, \quad (2.5)$$

$$\mathbf{G}_{i,j} = \begin{bmatrix} \underbrace{\mathbf{0}}_{i-1} & \underbrace{\Delta t_i \dots \Delta t_{j-1}}_{j-i} & \underbrace{\mathbf{0}}_{n-j} \end{bmatrix}, \quad (2.6)$$

$$\mathbf{m} = [v \quad v_2 \quad \dots \quad v_{n-1}]^T. \quad (2.7)$$

n refers to the total number of the acquisitions, $\mathbf{0}$ is a zero vector that is related to acquisitions that are not covered by an interferogram $I_{i,j}$, and v_i is the velocity of the i th time-span. The acquisitions need to be ordered chronologically for all subsets.

The usage of multiple subsets help to increase the temporal sampling rate, however this has the consequence that the system given in equation 2.5 is rank-deficient and has infinite solutions. An approximate solution for this problem can be found, e.g., by applying the singular value decomposition method (Berardino et al., 2002; Lanari et al., 2004).

Appropriate phase unwrapping algorithms can be chosen independently of the SBAS technique (Berardino et al., 2002). In this thesis, unwrapping is accomplished based on a 3D unwrapping approach, implemented in the Stanford Method for Persistent Scatterers and Multi-Temporal InSAR (StaMPS/MTI) tool, developed by Hooper et al. (2012). The influence of topography is removed by

considering an external DEM, so that only deformation and atmospheric effects remain in the differential interferograms (Osmanoğlu et al., 2016). The collection of phase differences of the connected differential interferograms is then converted to an overall mean phase signal by applying a least-squares algorithm and is further treated with different approaches that reduce the impact of atmospheric signal disturbances. The result comprises a mean velocity map and a corresponding time series that contains much more coherent pixels compared to PSI techniques. As a consequence, this technique is particularly useful to measure displacements in non-urban areas. However, the limitation of temporal decorrelation that specifically appears over heavily vegetated areas is still a problem (Lanari et al., 2013). In this thesis, SBAS is successfully used to retrieve ground deformations around the Toktogul water reservoir, which is located in the Tien Shan mountain range (Chapter 6).

2.6 Feature Tracking

Large displacements occurring between the acquisition of two SAR images results in decorrelation of interferograms, which makes displacement quantification by using only the phase information impossible. There are two approaches to overcome interferogram decorrelation. The first one is simply the reduction of the temporal baseline, which might help to preserve coherence. However, if the temporal baseline is already at its minimum as defined by the satellites revisit cycle, a second way is to retrieve the displacement information by applying feature tracking, which is solely based on the amplitude information of the SAR image.

Feature tracking, also known as amplitude tracking or offset tracking, is a method in which a subpixel-wise image matching algorithm is applied on the amplitude parts of two previously coregistered SAR images. This works under the condition that the backscatter intensity of features on the surface has changed only little over time (Strozzi et al., 2002; Schubert et al., 2013). In contrast to InSAR LOS solutions, feature tracking yields results in both azimuth and range direction. While displacements in the azimuth direction contain purely horizontal information, displacements in range are a combination of both, horizontal and vertical components. The accuracy of the feature tracking method depends on the spatial resolution of the pixel cells (up to a $1/10$ th of resolution), on the amount of distinguishable features within the amplitude data and on the quality of the coregistration. It is thus less accurate than DInSAR measurements (Strozzi et al., 2002; Liu et al., 2010).

Feature tracking is most sensitive to horizontal displacements and is applied, for example, in seismology, when earthquake-induced deformations or phase changes are too large to be captured by DInSAR (Michel et al., 1999; Liu et al., 2010). It is also suitable for landslide detection in areas where the ground moves quickly or is heavily vegetated (Singleton et al., 2014; Sun and Muller, 2016) and in glaciology applications, where ice moves too fast or the surface alters too rapidly due to strong surface melting in summer time (Quincey et al., 2009b; Li et al., 2013). In this thesis, the capability to capture intra-annual glacial surface kinematics is exploited on the example of the Inylchek Glacier in Chapter 4.

3 State of the Art

3.1 Inter- and Intra-Annual Glacier Surface Velocities from SAR Data

Willis (1995) gave a comprehensive overview about potential triggers and influencing factors for short-time glacier kinematic changes. A main outcome of the study is that kinematic variations depend on whether the glacier body is rested on either hard, unyielding, and impermeable beds; or on soft, yielding, and permeable beds. In the first case, the most influencing driver for surface motion variations is basal sliding, in the latter case it is bed deformation. Willis (1995) further distinguished between hourly, daily-to-weekly, and monthly variations. According to his study, daily-to-weekly horizontal velocity changes are attributed to a correlation of surface-water inputs and glacier motion, which also includes a potential time-lag between the surface-water input into the system and the glacier motion. It was further elaborated in this study that both the occurrence of so-called glacier motion events in summer time and the varying medium-term velocity increase with respect to the upglacier distance. Potential reasons for monthly velocity changes are the relationship to melt water discharge; seasonal aspects – most glaciers move faster in spring/summer time compared to autumn/winter time; the distance to the upglacier region as the amplitude of the seasonal signal decreases towards upglacier regions; and kinematic waves of high summer velocities. The work highlighted how important it is to find exact reasons for intra-annual glacier velocity changes in order to better understand the behaviour of a particular glacial system.

Even though the need of short-time glacier monitoring was identified by Willis (1995), only few studies are available dealing with that issue. One main reason is that it is very time-consuming, costly and logistically complex to take repeated in-situ measurements on a large glacier body over a longer period as an entire season or even a year. In one exemplary study, stake measurements were used to relate intra-annual glacier surface variations to supraglacial melt water input at the John Evans Glacier in Canada (Bingham et al., 2003).

Studies that dealt with short-time glaciological process analysis from remote sensing data were published shortly afterwards, when Scambos et al. (2004) used Landsat 7 imagery to investigate inter-annual kinematic effects of the Larsen-B iceshield in Antarctica. Although optical remote sensing data is highly suitable for tracking velocity changes, the dependency on cloud-free image acquisitions always hampers the retrieval of a complete time-series over an entire season, especially when the focus is laid on high-mountain regions.

The first thorough assessment of SAR data for intra-annual glacier velocity derivation was published by Floricioiu et al. (2008). They investigated three different glacier test sites located in the Patagonia Icefield with four TSX images that were acquired within a month. This allowed an early analysis of high-frequency glacier motion changes. The study could only be accomplished as the newly launched TSX satellite had the unprecedented capability to acquire data every 11 days, which could neither be achieved with ERS-1/2 (35 days), Envisat (35 days), Radarsat-1 (24 days), or ALOS PALSAR (46 days) before. Subsequent studies based on TSX data were given by Fallourd et al. (2011) who, among other SAR scenes, used four TSX scenes covering a time-period of 11 months to investigate the glacier motion at the Chamonix Mont-Blanc test site; and by Eineder et al. (2011), who used 29 TSX acquisitions taken within one year to investigate intra-annual surface velocities of the Drygalski glacier on the Antarctic Peninsula.

In this context, an important contribution was also made by Schubert et al. (2013), who particularly investigated the capability of 11-days difference images from TSX for glacier velocity determination. In this study, the performance of traditional cross-correlation methods were compared to matching algorithms based on complex wavelet decomposition and it was concluded that the former one was more suitable to derive glacier motion values. It was furthermore argued in this study that high-resolution data, such as SpotLight data, should be even preferred over StripMap data, as in this case more distinctive features are available. The increase in the number of features significantly improved the results. The only exception are regions dominated by crevasses that also provided enough detectable features in the StripMap imagery. However, it was also mentioned that the preference of SpotLight data can be only accomplished on the expense of spatial coverage.

All these studies have in common that they underline the importance of short-time glacier surface velocity monitoring to better understand the relationship of glacier dynamics to ongoing climate change. In this thesis, the capability of detecting rapid velocity changes – such as related to GLOF events – from TSX SAR data is demonstrated for the first time in Neelmeijer et al. (2014) as presented in Chapter 4.

In the year 2014, further studies were published that also dealt with glacier surface velocity retrieval by applying feature tracking on SAR data. Exemplary named are Zhou et al. (2014), who investigated the seasonal and intra-annual velocity changes of the Polar Record Glacier by means of ERS-1/2, Envisat and ALOS PALSAR data; and Moon et al. (2014), who used five years of TSX data to investigate the glacier motion change triggers in outlet glaciers in Greenland.

3.2 Inter- and Intra-Annual Glacier Elevation Changes from SAR Data

The measurement of glacier mass balance budgets has been a topic of research for many years. Mass balances can be derived by using various methods, which are commonly named as the glaciological (e.g. Østrem and Brugman, 1991; Kaser et al., 2003), the geodetic (e.g. Mercanton, 1916; Kääb and Vollmer, 2000) and the hydrological method (e.g. Meier and Tangborn, 1965; Soruco et al., 2009). Comparisons between the agreement of the different approaches are given, for example, in Tangborn et al. (1971); Hagg et al. (2004) and Cogley (2009).

Retrieving mass balances by the application of the geodetic method is based on the assessment of the elevation change of an entire glacier area and on assumptions regarding the ice density (Huss, 2013) and the stability of the underlying bedrock (Bamber and Rivera, 2007). The retrieval of glacier elevation changes is based on either point-wise height data, such as from GNSS (e.g. Beedle et al., 2014; Shean et al., 2017), radar altimetry measurements (e.g. Ridley and Partington, 1988; Pritchard et al., 2011) and airborne laser-scanning (e.g. Favey et al., 1999; Geist et al., 2005); or on spatially comprehensive data, such as DEMs from stereo photogrammetry applied on aerial- or satellite-based optical images (e.g. Kääb, 2002; Bolch et al., 2011b) or InSAR applied on SAR imagery (e.g. Berthier et al., 2007; Gardelle et al., 2012b). Lately, also gravimetric measurements, such as those provided by the GRACE mission, were used to calculate mass balance values (e.g. Ramillien et al., 2006; Farinotti

et al., 2015; Xu et al., 2016). A review dealing particularly with geodetic methods for glacier mass balance derivation is presented in Bamber and Rivera (2007).

Deriving glacier elevation changes by means of remote sensing is highly suitable to get a spatially complete picture of the mass balance changes of a glacier or an entire catchment. However, if short-term measurements are of interest it is essential to have high accuracy remote sensing input data, as otherwise error rates quickly exceed the actually measured glacier elevation change rates. Early inter-annual glacier elevation change measurements were accomplished from aerial photogrammetry, such as in LacChapelle (1962) or Meier and Tangborn (1965). Studies dealing with intra-annual comparison appeared only in more recent times. One example is given in Geist et al. (2005), who measured intra-annual glacier changes at Engabreen, Norway, by applying airborne laser scanning. The data, retrieved between September 2001 and August 2002, were used to generate three DEMs with a vertical and horizontal accuracy in the sub-metre range.

Influences of intra- and inter-annually varying weather conditions on mass balance and the equilibrium line (ELA) were studied by Koul and Ganjoo (2010). By using stake measurements, they concluded that knowledge about the triggers of intra-annual changes is very helpful to obtain a better picture about the health of a glacier. They further reasoned that continuous monitoring refines the understanding of glacier changes occurring due to global warming effects, as e.g., the shift of the onset of the melting period to earlier months. An important indicator in that context is also the location of the ELA, which is particularly sensitive to climate change.

Berthier et al. (2014) analysed the potential to estimate intra-annual glacier elevation changes from optical imagery gained from the Pléiades mission. They concluded that these data are highly suitable for deriving DEMs, as the electromagnetic signal is reflected from the surface and does not penetrate into the ground like radar waves. However, the derivation of a gap-less and year-round set of cloud-free imagery over an entire season is hard to accomplish, especially over high-mountain areas.

Although the DEM derived from SRTM data has been used as a reference in glacier mass change studies for many years (e.g. Berthier et al., 2007; Kääb et al., 2012; Gardelle et al., 2013; Junfeng et al., 2015), a realistic possibility to derive intra-annual changes from SAR data only appeared with the launch of the TDX satellite in June 2010. This satellite was set up to fly in a tandem formation together with its twin, the TSX satellite, which enabled the generation of DEMs free from atmospheric effects. Since then, several studies appeared using TDX DEM data for multi-annual comparisons, such as Neckel et al. (2013); Rankl and Braun (2016); Neckel et al. (2017); Liu et al. (2017) or Sun et al. (2018), but only few of them truly dealt with intra-annual analysis, such as Dehecq et al. (2016). In this thesis, the potential and limitations of TDX DEM data to derive inter- and intra-annual glacier elevation changes is analysed in Neelmeijer et al. (2017), as presented in Chapter 5.

3.3 Inter- and Intra-Annual Loading-Induced Crustal Deformations at Water Reservoirs from SAR Data

Measuring ground deformations caused by lake water level changes was established only very recently. Before SAR remote sensing satellites enabled spatially distributed analyses, Kaufmann and

Amelung (2000) already used levelling data to study the ground deformations around Lake Mead, USA. Later, GNSS data such as from the Global Positioning System (GPS) offered further possibilities to retrieve point-wise, high-accuracy ground deformations. Examples are found in Bevis et al. (2004), where the elastic response around the Lago Laja in Chile was analysed; and in Wahr et al. (2013), where the focus was laid on loading effects at Lake Shasta, USA.

Only few studies exist so far that are dealing with the measurement of water loading-induced ground deformations around reservoirs and lakes from SAR data. Furuya and Wahr (2005) used ERS-1/2 and Envisat imagery to investigate deformations induced by load changes due to GLOF events in Greenland between 1993 and 2003. Cavalié et al. (2007) relied on 43 ERS-1/2 images to build a time-series between 1992 and 2002, where they measured ground deformations around Lake Mead, USA, and verified their results with a visco-elastic solid Earth model. Nof et al. (2012) also applied InSAR on in total 31 ERS-1/2 images to build a time-series between 1993 and 2001 that was used to analyse deformations at the surroundings of the Dead Sea. Zhao et al. (2016) used Envisat ASAR images to investigate deformations around the Yangzhuoyong Lake in Tibet between 2003 and 2010. Doin et al. (2015) again utilised both ERS-1/2 and Envisat imagery to measure ground deformations around the Siling Co Lake in Tibet between 1992 and 2011. Gahalaut et al. (2017) on the contrary, used six ALOS PALSAR acquisitions, obtained between 2007 and 2008, to study the loading around the Tehri reservoir, located in the Himalaya region.

Although in all those studies multiple SAR images were used to interferometrically analyse the deformation patterns, none of the studies focused on intra-annual changes, as the gathered SAR acquisitions were simply not sampled sufficiently dense in time. The study presented in Neelmeijer et al. (2018), as given in Chapter 6 of this thesis, is thus the first that aims on this topic. It is also the first study that investigates the potential of Sentinel-1 imagery for regular water reservoir monitoring purposes.

4 Quantification of Inylchek Glacier Surface Kinematics

published as:

Julia Neelmeijer, Mahdi Motagh, and Hans-Ulrich Wetzel (2014) Estimating Spatial and Temporal Variability in Surface Kinematics of the Inylchek Glacier, Central Asia, using TerraSAR-X Data. *Remote Sensing*, 6, 9239–9259, doi:10.3390/rs6109239.

This work is licensed under the Creative Commons Attribution 4.0 International License.
To view a copy of this license, visit <https://creativecommons.org/licenses/by/4.0/>.

4.1 Abstract

We use 124 scenes of TerraSAR-X data that were acquired in 2009 and 2010 to analyse the spatial and temporal variability in surface kinematics of the debris-covered Inylchek Glacier, located in the Tien Shan mountain range in Central Asia. By applying the feature tracking method to the intensity information of the radar data and combining the results from the ascending and descending orbits, we derive the surface velocity field of the glaciated area. Analysing the seasonal variations over the upper part of the Southern Inylchek branch, we find a temperature-related increase in velocity from 25 cm/d up to 50 cm/d between spring and summer, with the peak occurring in June. Another prominent velocity peak is observable one month later in the lower part of the Southern Inylchek branch. This area shows generally little motion, with values of approximately 5–10 cm/d over the year, but yields surface kinematics of up to 25 cm/d during the peak period. Comparisons of the dates of annual glacial lake outburst floods (GLOFs) of the proglacial Lake Merzbacher suggest that this lower part is directly influenced by the drainage, leading to the observed mini-surge, which has over twice the normal displacement rate. With regard to the GLOF and the related response of Inylchek Glacier, we conclude that X-band radar systems such as TerraSAR-X have a high potential for detecting and characterising small-scale glacial surface kinematic variations and should be considered for future inter-annual glacial monitoring tasks.

4.2 Introduction

The Tien Shan mountain range, located in Central Asia, contains a large number of high-mountain glacial sites. The ice has a volume of around 1000 km³ and is distributed over an area of approximately 15,000 km²; the water reservoir stored in the ice plays a major role in the supply of freshwater to the surrounding arid and semi-arid environment (Aizen et al., 2007a).

Many studies have been conducted to investigate the long-term changes of the Tien Shan glaciers with remote sensing data from e.g., Shuttle Radar Topography Mission (SRTM) and Advanced Spaceborne Thermal Emission and Reflection Radiometer (ASTER) (Aizen et al., 2007b), Landsat (Bolch, 2007), Advanced Land Observing Satellite (ALOS) (Li et al., 2013) or a combination of the former two datasets together with Corona in order to enable multi-year time series analyses (Narama et al., 2010). An extensive summary of recent investigations regarding the retreat of Tien Shan glaciers is given by Kutuzov and Shahgedanova (2009). Those studies consistently show a current decrease of the glaciated area, which has notably accelerated since 1970. Glaciers situated in the Northern Tien Shan range are more affected than those of Central Tien Shan. The observed ablation phenomena are related to an increase of the annual mean temperature, whereas a significant trend in precipitation changes has not yet been detected (Aizen et al., 2007b; Narama et al., 2010).

In contrast to these well documented long-term trends, details about seasonal to inter-annual variability of the glacier velocity or rapid responses to special events are comparatively seldom observed. Most studies only provide information about the annual mean velocity of a glacier gained from a small amount of images. Our study will investigate whether TerraSAR-X data, acquired typically on a regular 11 day basis, is sufficient to reveal details about a glacier's seasonal surface motion variability.

We chose radar data for this investigation due to its high potential for regular monitoring of critical areas like high mountains since it is not adversely affected by the solar illumination conditions or atmospheric effects like cloud cover (Erten et al., 2009; Fallourd et al., 2011).

Our study area is the Inylchek glacier, located in the Central Tien Shan mountain range. We chose this glacier as a test site for two reasons: first, it is the largest glacier in the Tien Shan mountain area, wherefore it is an important freshwater source for people living further downstream (Aizen et al., 1997), and changes in the amount of melt water are likely to have an aftermath on the velocity of the glacier. Second, the glacier site is impacted by an annual glacial lake outburst flood (GLOF), which also has consequences for the glacier's motion (Mayer et al., 2008). In this paper, we attempt to assess the seasonal glacier surface velocity variability. Significant differences in the kinematics might give clues about the expectable amount of melt water (Andersen et al., 2010) or the onset of a GLOF (Haemmig et al., 2014), which could be used as constraints in dynamic glacier modelling.

Because the application of the Interferometric Synthetic Aperture Radar (InSAR) method is not consistently possible during all seasons due to decorrelation caused by rapid movement of the glacier and surface melting particular during summer time, we apply the feature tracking method (Strozzi et al., 2002) to 116 image pairs, collected between April and October 2009 and between February and September 2010.

This paper is organised as follows: First, we provide a detailed description of the setting and special conditions of the Inylchek Glacier. In the subsequent section, we outline the feature tracking methodology used to derive surface motion information from the radar observations. Afterwards, we present in detail the spatial and temporal variability of the surface velocity gained from the displacement maps and finally, we discuss the seasonal kinematics from 2009 and 2010 with respect to the air temperature and the yearly GLOF events.

4.3 Inylchek Glacier

The Inylchek Glacier is located in the central Tien Shan mountain range between $42^{\circ}4'N$, $79^{\circ}39'E$ and $42^{\circ}15'N$, $80^{\circ}12'E$. It consists of two heavily debris-covered glacial branches, called the Northern and Southern Inylchek, which flow out of the Podeba-Khan Tengri mountain massif towards the west (Figure 4.1). The entire system stretches over 60 km and covers an area of approximately 800 km^2 (Mayer et al., 2008), at altitudes between 2900 m and 7400 m (Hagg et al., 2008). Our study focuses on the ablation region of Southern Inylchek, which is rather flat with a mean slope of 2° .

Glacial lakes are located in the valley between the two branches. The larger of them, Lake Merzbacher, covers an area of approximately 5.6 km^2 and is prevented from flowing downwards into the Inylchek valley by the Southern Inylchek, which acts as a dam across the lake. The lake drains annually with a glacial lake outburst flood (GLOF), thereby causing a sudden flooding of urban areas in Tarim basin further downstream (Wang and Gao, 1997; Jingshi and Fukushima, 1999; Glazirin, 2010).

Previous remote sensing studies based on Environmental Satellite Advanced Synthetic Aperture Radar (ENVISAT ASAR) data (Wetzel et al., 2005), ASTER imagery (Mayer et al., 2008), and

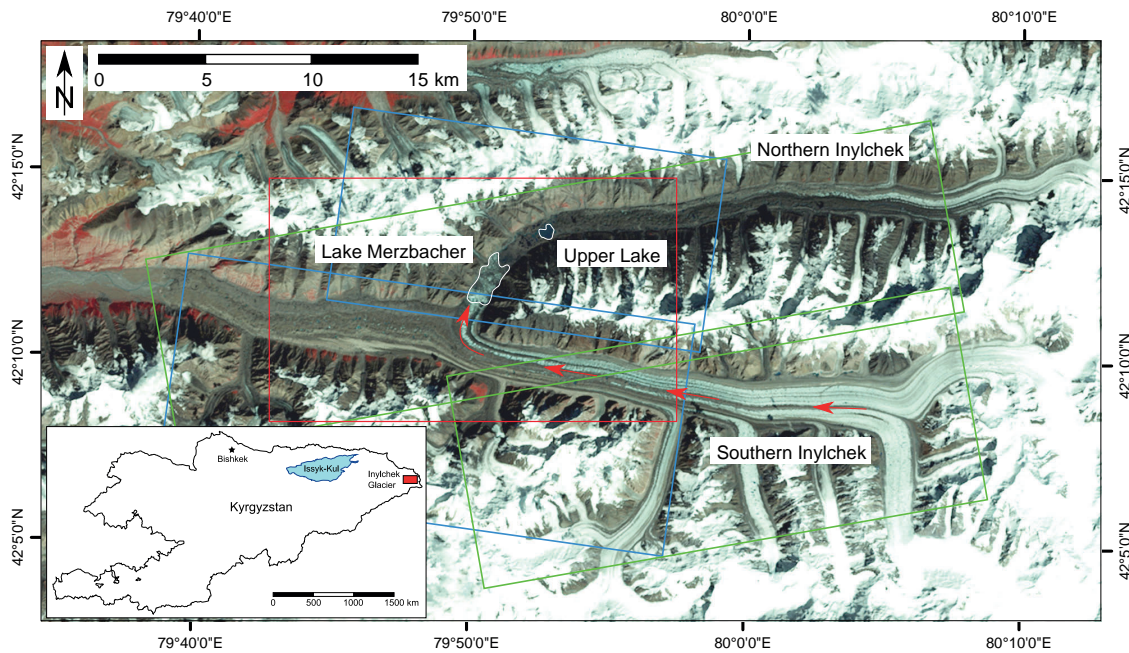


Figure 4.1: Northern and Southern Inylchek Glacier on a Landsat Thematic Mapper (Landsat TM) image from 24 August 2007. The main flow direction of the southern branch is marked by red arrows. The two lakes – Lake Merzbacher and the Upper Lake – are contoured by a white line. The location of the TerraSAR–X data frames are highlighted in green (ascending) and blue (descending) rectangles. The study area refers to the overlapping region and is outlined by a red rectangle. The inset shows the location of the Inylchek glacier within the country of Kyrgyzstan.



Figure 4.2: Bending area of Southern Inylchek showing the different parallel aligned debris layers and two bare ice ramps. In the background, the drained area of Lake Merzbacher is visible, which holds grounded icebergs. The picture was taken during a fieldwork session carried out at the Global Change Observatory “Gottfried Merzbacher” on 28 July 2012.

ASTER as well as Landsat TM scenes (Nobakht et al., 2014) indicate surface flow velocities of the upper Southern Inylchek of about 100 m/yr westwards, which corresponds to approximately 27 cm/d. At the confluence of the Northern and Southern Inylchek valleys (Figure 4.2), a part of the Southern Inylchek branch turns northwards and calves a substantial amount of ice into Lake Merzbacher. The remaining glacier mass continues to flow towards the west and is termed as lower part of Southern Inylchek within this study. This lower area and – even more pronounced – also Northern Inylchek are rather stagnant and show only slow motions of several m/yr to the west.

In addition to the remote sensing observations, discrete points marked on the glacier surface have been repeatedly surveyed with differential GPS – the Global Positioning Satellite System – during the summer months (Mayer et al., 2008), that generally confirm the annual mean flow characteristics obtained from the satellite data. Moreover, one remotely operated multi-parameter station has been installed directly on the glacier surface close to Lake Merzbacher’s ice dam in summer 2010. This station continuously provides Global Navigation Satellite System (GNSS) data, showing for example a late autumn month surface velocity of around 15 cm/d (Zech et al., 2015). Further geodetic and hydrometeorological instruments are installed at the Global Change Observatory “Gottfried Merzbacher” that is located at the confluence of the Northern and Southern Inylchek valleys.

4.4 Data and Methodology

4.4.1 TerraSAR-X Data Set

We process 116 image pairs from a total of 124 acquisitions gained in Stripmap mode and single polarisation (HH) from the TerraSAR-X satellite. The data has been taken from both ascending and descending orbits with incident angles of 22° and 35° and satellite heading angles of 350° and 188°, respectively, and covers the spring to autumn seasons of both 2009 and 2010 (Table 4.1). Pixel spacing is approximately 0.9 m in range and 2.0 m in azimuth direction, except for the descending acquisitions in 2010, where pixel spacing in range direction is only 1.4 m. At each acquisition date, two adjacent scenes have been taken that are mosaiced after performing the feature tracking procedure as outlined in the next section. The temporal baseline between two acquisitions is typically 11 days, with occasionally longer baselines of up to 33 days due to missing acquisitions. Displacements obtained from range and azimuth observations for both orbits are subsequently combined to finally arrive at 3D velocity estimates of the glacier surface (Figure 4.3).

4.4.2 Feature Tracking

The InSAR methodology has been commonly applied for investigating surface displacements from satellite radar data (Bamler and Hartl, 1998; Rosen et al., 2000). Typical application examples besides glacier kinematics (Mohr et al., 1998; Joughin et al., 2010; Mouginot et al., 2012) are earthquakes (Fialko et al., 2001; Satyabala et al., 2012; Motagh et al., 2014), landslides (Strozzi et al., 2005; Akbarimehr et al., 2013; Motagh et al., 2013) or volcanic deformation (Lu et al., 2000; Lundgren et al., 2003; Anderssohn et al., 2009). However, InSAR works only over regions that are not affected

Table 4.1: Overview of the acquisition dates for the available ascending and descending images from 2009 and 2010. On each date, two adjacent acquisitions were taken, resulting in 124 single scenes. TerraSAR-X acquires data with a repeat cycle of 11 days; data gaps are marked with a dash.

Ascending 2009	Descending 2009	Ascending 2010	Descending 2010
-	-	-	12.02.2010
-	-	20.02.2010	23.02.2010
-	-	03.03.2010	06.03.2010
-	-	-	17.03.2010
-	-	25.03.2010	28.03.2010
-	-	-	-
18.04.2009	21.04.2009	-	19.04.2010
29.04.2009	02.05.2009	27.04.2010	30.04.2010
10.05.2009	13.05.2009	08.05.2010	11.05.2010
21.05.2009	24.05.2009	19.05.2010	22.05.2010
01.06.2009	04.06.2009	30.05.2010	02.06.2010
-	-	10.06.2010	13.06.2010
23.06.2009	26.06.2009	21.06.2010	24.06.2010
04.07.2009	07.07.2009	-	-
15.07.2009	18.07.2009	13.07.2010	16.07.2010
26.07.2009	29.07.2009	24.07.2010	27.07.2010
06.08.2009	09.08.2009	04.08.2010	-
17.08.2009	-	-	-
28.08.2009	31.08.2009	26.08.2010	29.08.2010
08.09.2009	11.09.2009	-	09.09.2010
19.09.2009	22.09.2009	-	20.09.2010
30.09.2009	03.10.2009	28.09.2010	-
11.10.2009	14.10.2009	-	-

by decorrelation due to surface changes between two acquisitions. Regarding our study area, we note that coherence between image pairs is rather poor for fast flowing glaciers as Inylchek, in particular during summer months where also surface melting extensively alters the phase component of the radar signal. We therefore apply the feature tracking method (Strozzi et al., 2002), which does not rely on the phase, but only takes the backscattered intensity information of the radar image into account. The method has already been previously applied to derive glacier surface motions (Quincey et al., 2009a; Li et al., 2013; Paul et al., 2015). To process the data, we used the algorithm implemented in the SARscape software package (Sarmap, 2014).

As a first step, coregistration is performed individually on each image pair, whereas the earlier acquisition always acts as the master image. To gain sub-pixel accuracy, which is a requirement for a precise image comparison (Luckman et al., 2007), the registration is performed in a two-step procedure including coarse and fine coregistration, by which we achieve a final accuracy of 1/10 of a pixel. In the next step, horizontal shifts between intensity backscatters within the image pairs are computed based on identifying the maximum in normalised cross-correlation functions of small image patches, that are additionally oversampled by a factor of 16 for increased spatial resolution. The accuracy of the method is, however, highly dependent on distinguishable features within the intensity data (Strozzi et al., 2002).

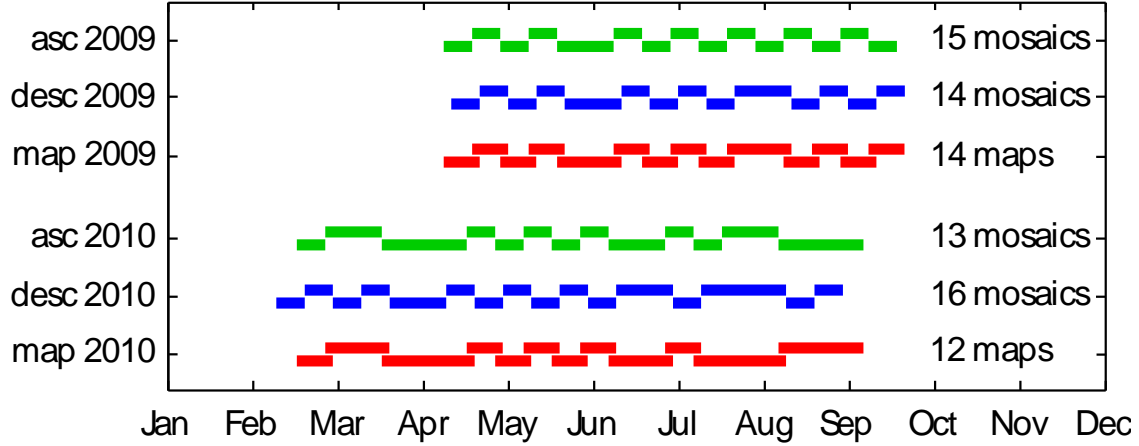


Figure 4.3: Timewise arrangement of the 116 processed image pairs for ascending (green) and descending (blue) orbits from 2009 and 2010. One bar represents one offset image derived from mosaicing two adjacent feature tracking results. During the decomposition, mosaics from both orbits are merged, resulting in a total of 26 displacement maps (red) available for the kinematic analysis.

For our application, we select window shifts of 10 and 12 pixels in range and azimuth, respectively, for all ascending and 2010 descending acquisitions. For descending acquisitions acquired in the year 2009, we use a shift of 15 pixels in range direction, thereby achieving a ground resolution of approximately 25 m in all our results. The size of the small image patch that contributes to the average cross-correlation function is chosen to be 32 pixels in both range and azimuth. To avoid noisy results in areas dominated by features rather indistinguishable in the intensity data, identified maxima with cross-correlations below 0.2 are discarded and set to no data in the offset images.

Offset values are subsequently converted into metric units by applying the associated pixel spacing values, and images are geocoded with the aid of a SRTM digital elevation model (DEM) (Jarvis et al., 2008). The DEM's original resolution of 90 m has been upsampled to an output resolution of 25×25 m which is in line with the selected window shifts applied during the feature tracking. The average amount of the SRTM geocoding error over Asia is specified as ± 8.8 m (Farr et al., 2007) which is about one third of the output resolution and hence does not affect our results. Displacement maps are mosaiced for the two adjacent scenes acquired on the same date, whereas the overlapping region is re-calculated by averaging the corresponding displacements from the upper and lower scene. Finally, averaged daily velocities are calculated by dividing displacement rates by the length of the temporal baseline for each mosaic.

Failure of the cross-correlation leads to erroneous results that contain extreme values. To prevent further processing with the corresponding pixels in the tracking results, those are set to missing values according to a threshold which is calculated from the mean (μ) of all values and the standard deviation (σ) for each individual mosaic. Every value that does not fall within the range $\mu \pm 3\sigma$ is rejected. We are aware that the tracking values are not entirely normally distributed due to a systematic difference between stable bedrock and moving glacial areas. However, the 3σ criterion is large enough to preserve all realistic displacements. Still, there remain regions that are affected by shadowing or layover in either the ascending and descending acquisitions. Based on the value of the local incidence angle of the radar beam, a mask has been created, whereas values with negative sign are assumed to

be layover areas and values greater than 90° represent shadow areas. Accordingly, regions with local incidence angles that fall either in the layover or shadow range are rejected to prevent interpretation of erroneous displacement estimates.

4.4.3 Decomposition to 3D Velocities

Since in principle four one-dimensional estimates of displacements are available from range and azimuth images of ascending and descending acquisitions for a given time interval, it is straightforward to combine them into a single estimate of 3D velocities. For a right-looking system like TerraSAR-X the displacements in azimuth d_{azi} are noted as:

$$d_e \sin \alpha + d_n \cos \alpha = d_{azi} \quad (4.1)$$

and in line-of-sight d_{ran} as:

$$-d_u \cos \theta + d_e \sin \theta \cos \alpha - d_n \sin \theta \sin \alpha = d_{ran} \quad (4.2)$$

whereas θ is the incidence angle of the radar beam, α is the heading direction of the sensor (positive clockwise from North) and $[d_u, d_e, d_n]^T$ are offsets in vertical, eastern and northern direction, respectively. Equation (4.2) regards the sign convention for offset tracking, where displacement towards the sensor yields negative values and displacement away from the sensor leads to positive values (Nagler et al., 2012; Muto and Furuya, 2013). By combining ascending (index a) and descending (index d) results, we gain the following over-determined system of equations, which is solved by applying a standard least-squares estimation technique:

$$\begin{bmatrix} -\cos \theta_a & \sin \theta_a \cos \alpha_a & -\sin \theta_a \sin \alpha_a \\ -\cos \theta_d & \sin \theta_d \cos \alpha_d & -\sin \theta_d \sin \alpha_d \\ 0 & \sin \alpha_a & \cos \alpha_a \\ 0 & \sin \alpha_d & \cos \alpha_d \end{bmatrix} \begin{bmatrix} d_u \\ d_e \\ d_n \end{bmatrix} = \begin{bmatrix} d_{ran_a} \\ d_{ran_d} \\ d_{azi_a} \\ d_{azi_d} \end{bmatrix} \quad (4.3)$$

The decomposition formula is applied to the offset mosaics that had in advance been trimmed to the same spatial extend. As a result, we gain the 3D information containing vertical and horizontal motion components of the surface glacier flow. In a final processing step, we smooth the images by applying a 5×5 boxcar filter.

Since 3D velocities are obtained from combining image pairs from both ascending and descending orbits that are acquired with a minimum delay of 3 days, we note that the 3D velocity estimates presented below must be interpreted as average displacement rates representative for a time period of 14 days under ideal circumstances. If the temporal baseline of an image pair is longer due to missing acquisitions, the averaging period increases accordingly. Within this study, no differentiating between horizontal and vertical motion components has been undertaken, instead results focus on the absolute value (i.e., the speed) of the derived 3D velocity vector.

4.5 Results

A snap-shot from July 2009 is representative for the flow regime of Inylchek glacier during the summer months (Figure 4.4). Velocities between 25 to 50 cm/d towards the west are apparent in the upper part of Southern Inylchek, whereas the lower part and Northern Inylchek show substantially smaller surface movements. The bending of the surface flow towards north in the direction of Lake Merzbacher at the confluence of the valleys is clearly visible. Besides those general features, surface velocities vary significantly both across the glacier and also in direction of the mean flow, potentially providing additional high-resolution information of the flow field.

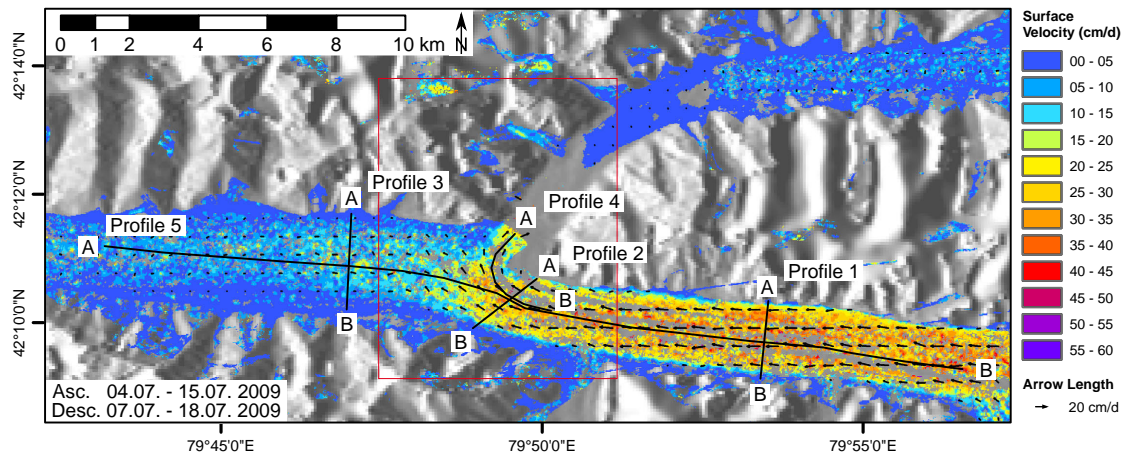


Figure 4.4: The average surface velocity resulting from the combination of the images from 4–15 June 2009 (ascending) and 7–18 June 2009 (descending). The kinematic information is projected on a hillshade image derived from SRTM DEM data. The amount of the displacement is colour-coded as well as shown by the length of the arrows. The points of the arrows indicate the flow direction of the glacier surface. The red rectangle marks the outline of the time series samples collected from 2009 and 2010 (Figure 4.5). The location of the profiles, running from A to B (Figure 4.6), are shown as black lines.

From our time series of displacement fields and hence surface motions, we present a number of snapshots for the bending region at the valley confluence, which is presumably the glaciologically most interesting area of the glacier system (Figure 4.5). Two time periods with peak velocities are recognisable: one appears in June, as we observe motion rates in the upper part of the glacier at approximately 40 cm/d for both years (Figure 4.5c,v). The second peak occurs during the summer season with velocity rates of 40 cm/d in July/August 2009 (Figure 4.5e) and 50 cm/d in July 2010 (Figure 4.5x). After the occurrence of this major peak in the summer, the glacier slows down substantially, with mean displacement rates of 25 cm/d in September 2009 (Figure 4.5g) and 2010 (Figure 4.5z).

To allow for a more quantitative comparison, we present five profiles, that are well distributed over the Southern Inylchek branch (Figure 4.6). Their locations are marked in Figure 4.4. Three of the profiles are perpendicular to the main flow direction: profile 1 represents a cross-section of the upper area, profile 2 shows a cross-section in the bending region and profile 3 gives information about the velocity variations in the lower part of the glacier. Two additional profiles oriented parallel to the glacier show the changes of the kinematic behaviour along the flow direction. Profile 4 illustrates

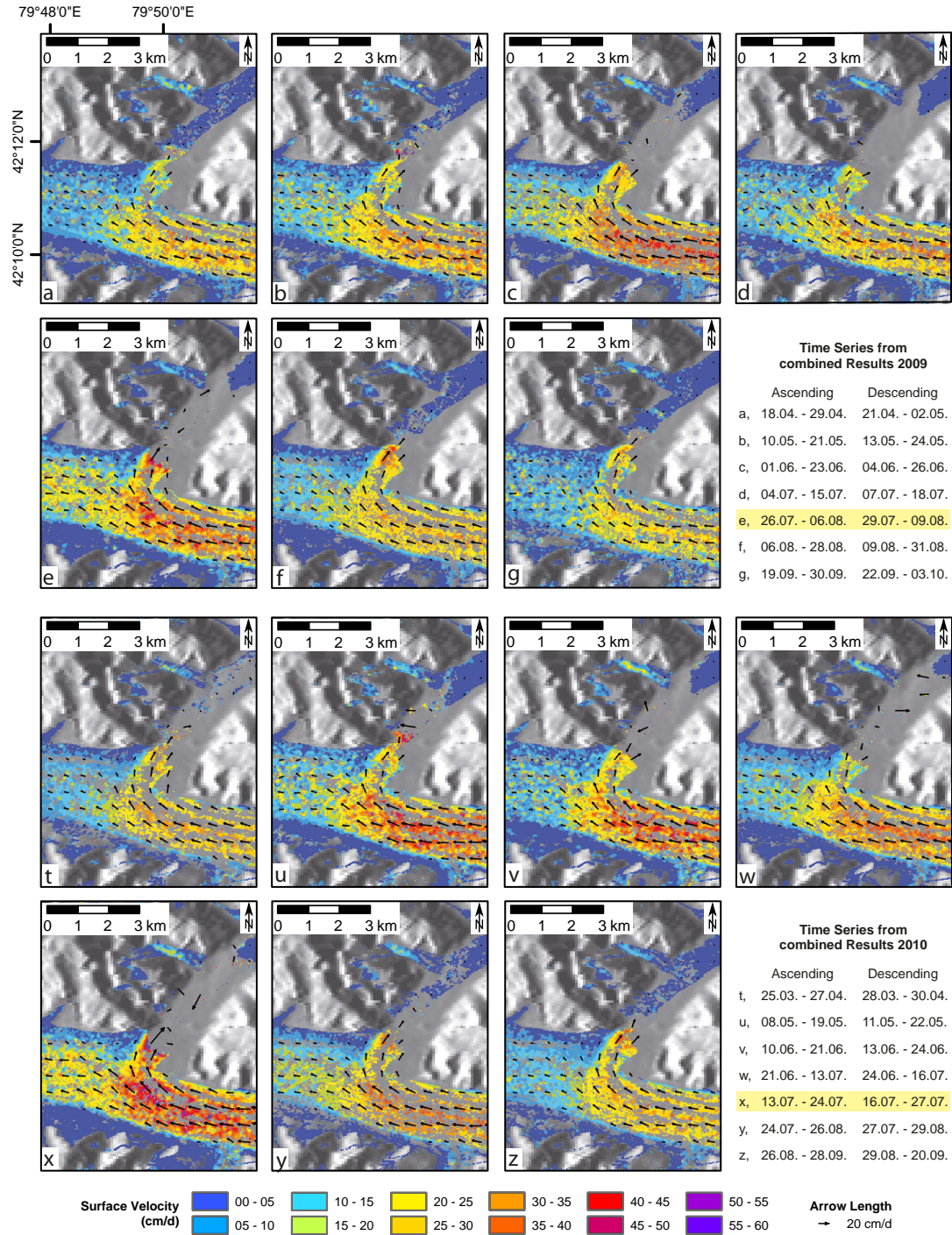


Figure 4.5: Time series examples for 2009 (top two rows) and 2010 (bottom two rows) derived from combining ascending and descending results. The yellow highlighting indicates the occurrence of the GLOF events.

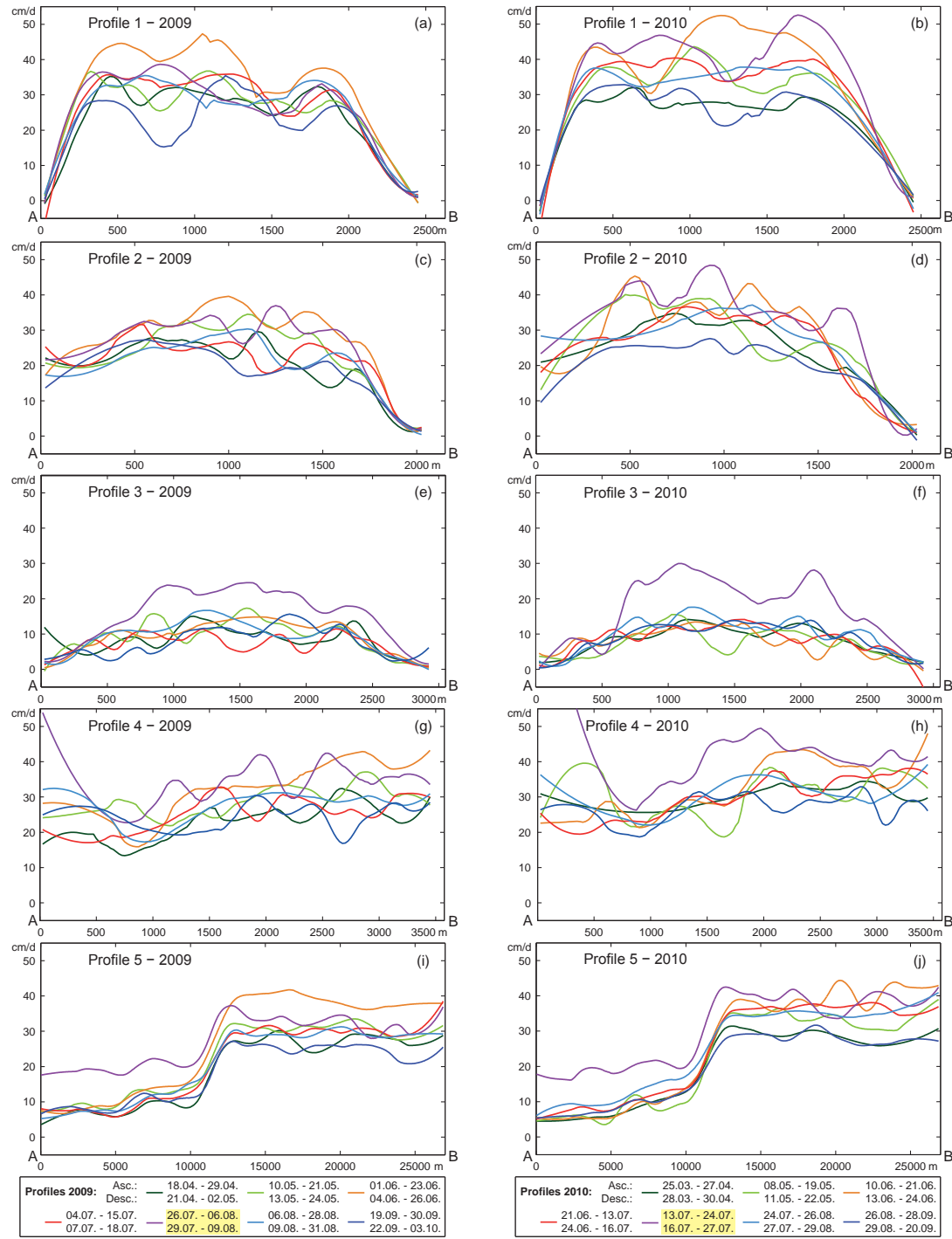


Figure 4.6: Seasonal velocity variations along three orthogonal (a–f) and two longitudinal (g–j) profile lines gained from kinematic map samples from 2009 and 2010, respectively. The alignment of the profiles 1–5 refers to the lines shown in Figure 4.4, whereas all profiles are running from A to B. Same colours represent a comparable time period; the exact time frame between the ascending and descending acquisitions can be extracted from the legend. The acquisitions covering the GLOF event are highlighted in yellow.

the ice flow turning towards the north in the bending area, and profile 5 gives an overview of nearly the entire investigation area of the Southern Inylchek branch, particularly demonstrating the motion variance between the upper and lower parts of the glacier.

In the upper area of Southern Inylchek glacier, the general alignment of the velocity rates perpendicular to the glacier flow shows roughly a typical maximum value close to the center axis of the glacier, with strongly decreased values towards the margins. However, in the broad middle area, many variations are distinguishable, reaching from a minimum of 20 cm/d up to a maximum of 50 cm/d during the seasons (profile 1 in Figure 4.6a,b). The same profile reveals that besides these variances a rising trend of the surface velocity from spring to summer is observable: spring mean values are at 25 cm/d, whereas the summer mean is found at 35–40 cm/d. Distinct peaks appear in June within both 2009 and 2010 with a maximum of 50 cm/d. Autumn values are again substantially reduced to 25–30 cm/d in both years. Particularly evident are differences at the southern margin of the glacier. In 2009, the maximum in this area is approximately 35 cm/d. In 2010, the surface of the glacier has moved much faster, yielding values of up to 50 cm/d.

At the beginning of the bending area, the incoherent motion pattern of the parallel glacial streams is still apparent, albeit with 20 % lower values (profile 2 in Figure 4.6c,d). Below the confluence area, the glacier body moves in a more uniform way, as cross-alignment variations are unincisive. The glacier velocity has slowed down and surface displacements do not vary too much during the year: the velocity rates for both 2009 and 2010 are approximately 5–10 cm/d (cp. profile 3 in Figure 4.6e,f). Nevertheless, the second peak observed in the upper area in the snap-shot images is also apparent in this region, resulting in significantly increased velocity rates of 20–25 cm/d.

The behaviour in the transitional area between the upper and the lower part of the glacier is shown in profile 4 (Figure 4.6g,h). However, some limitations have to be considered when analysing this part: the bending area is highly affected by layover effects of the nearby mountains. Thus this part of the area is masked out and cannot be interpreted. Still, the profile reveals a distinct decrease of the glacier surface flow velocity, from values of approximately 30–40 cm/d to approximately 20–30 cm/d in the middle of the bending area. On the contrary, an increasing velocity trend is observable after the ice has changed its flow direction, resulting in a faster movement of the glacier towards the lake. The strong velocity increase in summer already seen in profile 3 is also apparent directly at the calving front, where the glacier moves with a sudden rush towards Lake Merzbacher during the time of the second peak (Figure 4.5e,x, Figure 4.6g,h).

Profile 5 (Figure 4.6i,j) finally shows the overall situation, where once again the significant surface velocity drop is apparent below the bending area. It is evident that seasonal changes appear within the upper part of Southern Inylchek glacier, but barely within the lower area except for the time of the second peak. This major event occurring in August 2009 and July 2010 affects the entire region below the confluence area, whereas maximum values in the upper region appear rather earlier during June, which is especially distinctive in 2009.

4.6 Discussion

4.6.1 Error Estimation

Before discussing the variations of the surface velocity in detail, an attempt is made to estimate the magnitude of the error in our results. Based on the assumption that a non-glacier area not affected by motion should yield velocity values spanning around zero (Luckman et al., 2007; Li et al., 2013), we analysed the kinematic results of the small surface patch between the two lakes. For 2009, the average mean velocity for that region over all scenes is 2.04 cm/d with an average standard deviation of 1.19 cm/d. For 2010, the values are similar, with an average mean of 2.17 cm/d and a corresponding average standard deviation of 1.15 cm/d. Both years independently show comparable mean offset errors that are ten times lower than the calculated glacier velocity, which indicates that all signals larger than a few cm/d are well above the noise level.

Geocoding of the tracking results has been achieved with the help of the SRTM DEM that had been acquired in 2000. Assuming that similar to the neighbouring Tomur Glacier (Pieczonka et al., 2013), the Inylchek height was also lowered by approximately 15 m between 1999 and 2009 and neglecting earth curvature, the geocoding error ϵ that is introduced by a DEM height difference δH can be calculated as follows:

$$\epsilon = \delta H / \tan \theta \quad (4.4)$$

Thus, for the incident angles of $\theta_a = 22^\circ$ and $\theta_d = 35^\circ$ the geocoding error would be 37 m and 21 m, respectively. This roughly corresponds to the final resolution of our images and therefore alters the results only marginally, since it just affects the position of a line-of-sight displacement, but not the displacement vector itself.

4.6.2 Inter-Annual Kinematics of the Upper Southern Inylchek Glacier Branch

Kinematic variations found perpendicular to the glacier main flow in the upper part of the Southern Inylchek branch indicate independent moving behaviour of adjacent longitudinal streams. The strong velocity increase at the southern margin of the glacier from 2009 to 2010 has been already described in Nobakht et al. (2014) and seems to be related to a decrease in the glacial flow of the adjacent glacier tributary.

To explain the general surface motion increase from April to June over the upper Southern Inylchek branch, we include air temperature data from the European Centre for Medium-Range Weather Forecasts (ECMWF) global operational analysis (Figure 4.7). Within the data from the numerical weather prediction model, we observe in both 2009 and 2010 a constant increase of air temperatures beginning in March, reaching peak values in July/August. Together with a simultaneously occurring increase in precipitation (not shown), the air temperature increase intensifies the ablation process on the glacier's surface (Aizen et al., 1995). Through the accelerated melting of the snow situated on the surrounding mountains and on the glacier itself, additional water is introduced to the system, which penetrates

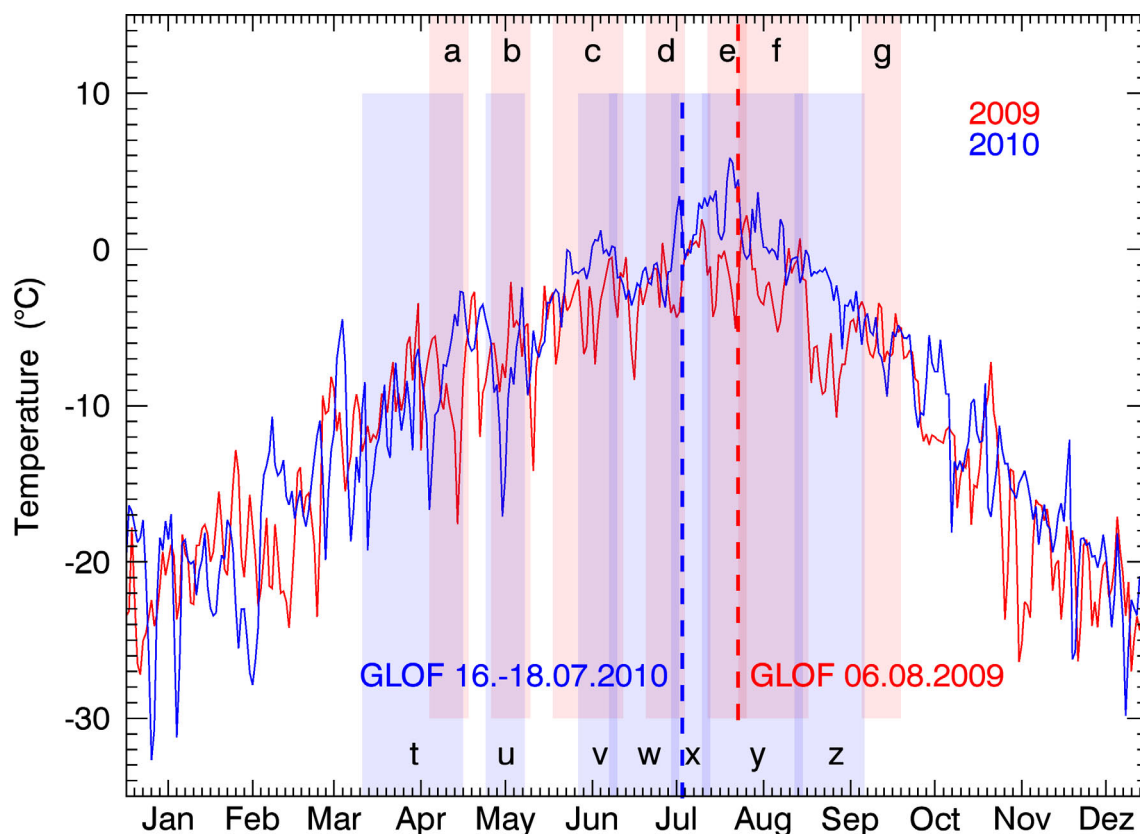


Figure 4.7: Daily 2 m-temperature values for 2009 (red) and 2010 (blue) at the Southern Inylchek area taken from the ECMWF operational model. The shaded rectangles mark the time frame that is covered by the surface velocity results shown in Figure 4.5, whereas lower-case characters refer to the according images. The dashed lines mark the GLOF in 2009 and 2010, respectively.

into the ice by means of crevasses and fractures and drains through subglacial ice tunnels. If the amount of melt water is comparatively high, these passageways are not able to adjust their size quick enough to the water flux. As a consequence, the pressure and the volume of the water at the basal base increases, leading to a reduction of the frictional strength and ultimately to an increase of the basal sliding of the glacier (Björnsson, 1998; Clarke, 2005; Cuffey and Paterson, 2010).

The comparison between averaged daily surface velocities and daily air temperature values provides an explanation for the slightly higher kinematics in 2010 than in 2009 (cp. Profile 5 in Figure 4.6i,k). At the beginning of the spring season in March/April (cp. Figure 4.5a,t) velocity values are still approximately the same in both years, although the corresponding time frame is different. In 2010 the spring result covers a time period of 36 days while in 2009 it covers a time period of 14 days, which temporally fall into the later part of the 2010 result. We thus would expect higher surface velocities in 2009 than in 2010. However, by looking at Figure 4.7, we realise that the corresponding mean air temperatures in both years are approximately the same, which may explain the similar velocities that we observe in spring 2009 and 2010.

In the middle of May, we see distinctive velocity differences in the bending area of the glacier between 2009 and 2010 (Figure 4.5b,u); in 2009 the glacier surface moves with 30–35 cm/d while in 2010 kinematics speed up to 40 cm/d. However, air temperature values for the same time span appear

rather vice versa: the mean temperature value for 2009 is $-6\text{ }^{\circ}\text{C}$ while for 2010 we observe a sharp drop in the temperature from $-4\text{ }^{\circ}\text{C}$ to $-17\text{ }^{\circ}\text{C}$ followed by a quick rise to $-3\text{ }^{\circ}\text{C}$ within two weeks. Therefore, we would expect rather lower surface velocity values in 2010. However, as seen in Figure 4.7, we observe an apparent peak in the air temperature just the week before the corresponding 2010 acquisitions, which lasts for several days and is clearly higher than temperature values for the same time period in 2009. We thus assume that the higher glacier kinematics in May 2010 should be interpreted as an aftermath of this rather warm period.

Figure 4.5c,v as well as the Profile 5 in Figure 4.6i,j show for both years surface motion values around 40 cm/d in June. Air temperatures for the corresponding time period do not substantiate this development, since mean values in 2010 are $-1\text{ }^{\circ}\text{C}$, which is clearly higher than the mean of $-4\text{ }^{\circ}\text{C}$ in 2009. A possible explanation might be the noticeable difference in the amount of precipitation values that could have a favourable effect on the glacier motion: in 2009 we have accumulated monthly values of 116 mm as compared to only 73 mm in 2010 (not shown here).

From June on, air temperatures are constantly higher in 2010 than in 2009, reaching values even above the freezing point in July and August (maximum: $6\text{ }^{\circ}\text{C}$), whereas values in 2009 are most of the time just below $0\text{ }^{\circ}\text{C}$. Air temperatures above the freezing point have a profound effect on surface melting (Sugiyama et al., 2011), in turn allowing a significant amount of melt water to be introduced into the system in summer 2010. Accordingly, mean summer 2010 velocities are mainly higher than those in 2009: 30 cm/d for July 2009 vs. 37 cm/d for July 2010 and 35 cm/d for August 2009 vs. 40 cm/d for August 2010 (Figure 4.6i,j). A convergence of the kinematics towards a mean of 25 cm/d is only observable in September again.

In summary, evidence presented above leads to the conclusion that for the upper part of the Southern Inylchek Glacier branch the amount of surface velocity correlates most of the time with air temperature. Especially air temperatures above the freezing point seem to induce an increased glacier flow. A comparable general correlation over the time with precipitation has not been found so far.

4.6.3 Lake Level Extent and GLOF

Because calm water reflects the radar beam away from the sensor, cross-correlation values over the area of Lake Merzbacher fall below the defined 0.2 threshold. As a consequence, most of the lake area is masked out during the processing. Single features that are still visible are likely to be related to ice bergs floating on the surface. By looking at the boundary of this no-data area in combination with the DEM, it is possible to extract information about the water level of the lake.

After applying the layover/shadow mask, no-data values due to the mask are overlapping those that are related to the missing backscatter information due to the outline of the lake. However, the maximum extent of Lake Merzbacher towards the Northern Inylchek branch is clearly visible. The results from the spring period show just a small no-data area in the study area (Figure 4.5b,u), which indicates that only a marginal amount of liquid water is present. With time, the outline of this gap increases, reaching its maximum extent in the summer, which correlates with the time of the appearance of the second velocity peak (Figure 4.5e,x). Along with the strong decline of the glacier

surface velocity directly after this peak, backscatter intensities are observed again for the lake area, leading to the conclusion that the water must have drained away (Figure 4.5f,y). After this point, no apparent changes in the low water level are recognisable during the autumn season.

From in-situ observations collected at the Global Change Observatory “Gottfried Merzbacher”, it is known that GLOF events of Lake Merzbacher took place on both 6 August 2009, and between 16–18 July 2010. Both events coincide well with the increased velocities of the lower part of Southern Inylchek (Figure 4.6i,j). We assume that at the beginning of the GLOF, the existing drainage tunnels of the Inylchek glacier are not large enough to allow an immediate discharge of the lake water. Thus, the significant increase of the subglacial water pressure lubricates the bed allowing for a basal sliding over large areas (Björnsson, 1998). Similar to Magnússon et al. (2007), who monitored a GLOF-induced glacier velocity increase in Iceland, we observe a strong speed-up in the bending area and particularly in the lower area, since these are the regions directly affected by the draining water. Therefore, it can be implied that the GLOF directly influences the glacier’s kinematics by triggering a so-called mini-surge. A mini-surge is characterised by at least a double speed velocity and lasts for a time period of approximately one day (Humphrey et al., 1986). As illustrated in Section 4.5, the velocity has increased by more than 100% in the lower part of the glacier, from approximately 5–10 cm/d before the GLOF to 25 cm/d during the GLOF. However, it should be noted that these values are only averaged results over an 14-day time period. Thus, we expect an even higher displacement rate during the actual draining period, since the main flooding event occurs only within a couple of days.

By comparing the dates of the GLOF events between 2009 and 2010, we note an earlier draining of the lake for about three weeks in 2010. This is easily explained by the air temperatures above the freezing point in summer 2010. The high temperatures lead to increased snow melting as well as surface melting of the glacier itself. Following on, a large amount of water is introduced to the system, which lets the water level of Lake Merzbacher rise more quickly. As a consequence, the water pressure reaches its critical threshold earlier as in 2009, which finally results in the earlier flooding.

4.7 Conclusions

In this study, radar data have been used to observe seasonal surface velocity variations of the Inylchek Glacier in Kyrgyzstan. We demonstrated that detailed monitoring of spatial and temporal kinematics variability with TerraSAR-X is feasible due to the satellites’ relatively short repetitive cycle of 11 days and the independence from solar illumination or atmosphere conditions. Another major advantage of using TerraSAR-X data is the high spatial resolution. By using Stripmap images with an original resolution of 3 m, we are able to generate final products with a resolution of 25 m that show not only the general mean velocity of the main glacier but also allows us to detect kinematic differences between individual longitudinal streams. We applied the feature tracking method to calculate the velocity field of the glacier, which yields sufficient information to derive a complete overview of the displacement of the entire glacier surface. By taking into account data from ascending and descending orbits, it is possible to derive 3D information about the kinematics.

For the observed period of 2009 and 2010, the seasonal displacement investigation for the ablation area of Southern Inylchek Glacier shows velocity rates from 25 to 50 cm/d for the active upper part,

with small changes in perpendicular flow direction. In general, lowest surface velocity values are found during April and September, whereas in May an increase of the motion rates is observed. A first velocity peak appears for both years in June with a mean of 40 cm/d. Comparison to daily air temperatures reveals a general correlation between temperature and glacier surface flow. In 2010, we observe that summer air temperatures above the freezing point lead to a significant velocity increase: mean values in 2010 are 15% higher than in 2009. In addition, the onset of the annually occurring glacial lake outburst flood (GLOF) of Lake Merzbacher is three weeks earlier in 2010 as compared to 2009.

The motion of the lower region of the Southern Inylchek branch appears homogeneously, with constant velocity rates of 5–10 cm/d over the year. This displacement rate only changes when the branch is affected by the GLOF that is associated with the second velocity peak. During the outburst, the surface kinematics increase with values reaching 25 cm/d, which is more than twice the normal rate and thus is termed as a mini-surge.

As a consequence, we conclude that the drainage of Lake Merzbacher, inducing the water to flow underneath the ice body, has a large impact on the Southern Inylchek’s movement behaviour. The source of the mini-surge is likely to be related to the rise of the water pressure at the glacier’s bottom, reducing the friction between ice and solid ground, leading to an increase of the basal slip and therefore the glacier’s velocity.

Our study gave evidence that in the future, large-scale monitoring of changes in seasonal surface kinematics of glaciers will help to improve the understanding of a glacier’s behaviour. The small and short-time, yet distinctive, velocity change characteristics could be used for example as additional input to improve or validate mass-balance estimation models by for instance applying the vertical velocity component like proposed in Strozzi et al. (2003). They could also serve as a constraint for estimating ice thickness and glacier bed topography (McNabb et al., 2012) or for modelling the spatial distribution of the surface-to-bed melt water transfer (Clason et al., 2012). Furthermore, information about the speed of glacial lake filling could be used to refine GLOF prediction models, like the one developed by Ng and Liu (2009) for the Merzbacher Lake.

For the Inylchek area, the relation between glacier alignment, tributary ice input, GLOF event, and hydrometeorological variations, and how each influences the development of the glacier’s motion is not yet fully understood. Close monitoring with high spatial and temporal resolution of the surface kinematics in connection with further hydrometeorological in-situ observations will be a basis to gain further insight into Inylchek’s glacial processes.

4.8 Acknowledgements

The authors would like to thank the anonymous reviewers for their helpful comments and suggestions to improve the quality of this paper. This study is supported by the German Federal Ministry of Research and Technology (BMBF) via the project PROGRESS (Potsdam Research Cluster for Georisk Analysis, Environmental Change and Sustainability) and by the Initiative and Networking Fund of the Helmholtz Association in the frame of Helmholtz Alliance “Remote Sensing and Earth System

Dynamics”. The TerraSAR–X data are kindly provided by the German Aerospace Center (DLR) under the proposal number HYD0289. The Landsat TM scene is made available from the U.S. Geological Survey.

4.9 Author Contribution

Julia Neelmeijer designed the research, processed the remote sensing data and wrote the main part of the manuscript. Mahdi Motagh was responsible for the scientific supervision on the development process and contributed to the manuscript writing. Hans-Ulrich Wetzel contributed to the data analyses and the manuscript writing.

5 Quantification of Inylchek Glacier Elevation Changes

published as:

Julia Neelmeijer, Mahdi Motagh, and Bodo Bookhagen (2017) High-resolution digital elevation models from single-pass TanDEM-X interferometry over mountainous regions: A case study of Inylchek Glacier, Central Asia. *ISPRS Journal of Photogrammetry and Remote Sensing*, 130, 108–121, doi:10.1016/j.isprsjprs.2017.05.011.

© 2017 Elsevier, reprinted with permission.

5.1 Abstract

This study demonstrates the potential of using single-pass TanDEM-X (TDX) radar imagery to analyse inter- and intra-annual glacier changes in mountainous terrain. Based on SAR images acquired in February 2012, March 2013 and November 2013 over the Inylchek Glacier, Kyrgyzstan, we discuss in detail the processing steps required to generate three reliable digital elevation models (DEMs) with a spatial resolution of 10 m that can be used for glacial mass balance studies. We describe the interferometric processing steps and the influence of a priori elevation information that is required to model long-wavelength topographic effects. We also focus on DEM alignment to allow optimal DEM comparisons and on the effects of radar signal penetration on ice and snow surface elevations. We finally compare glacier elevation changes between the three TDX DEMs and the C-band shuttle radar topography mission (SRTM) DEM from February 2000. We introduce a new approach for glacier elevation change calculations that depends on the elevation and slope of the terrain. We highlight the superior quality of the TDX DEMs compared to the SRTM DEM, describe remaining DEM uncertainties and discuss the limitations that arise due to the side-looking nature of the radar sensor.

5.2 Introduction

Glacial and geodetic mass balance measurements are important for quantifying glacial processes and their relationships to climate change, water availability, and sea level rise (Hagg et al., 2004; Fischer, 2011; Zemp et al., 2013). However, collecting in-situ data at remote glaciers is time-consuming, expensive and often associated with logistical difficulties (Bhambri et al., 2011; Yan et al., 2013). Digital elevation models (DEMs) that are generated from satellite remote sensing data are a powerful tool to infer glacier elevation changes in mountainous areas (Racoviteanu et al., 2007; Paul and Haeberli, 2008; Friedt et al., 2012).

In June 2010, the TanDEM-X (TDX) satellite was launched to enable, along with its twin TerraSAR-X, the generation of a new global DEM with an unprecedented spatial resolution of 12 m in the horizontal direction and a relative height accuracy of 2 m (Krieger et al., 2013). To date, the promising potential of TDX DEMs for investigations of glacier elevation changes in comparison to other remote sensing-based elevation data has been shown mainly in regions of large ice-sheets, e.g. in Antarctica (Groh et al., 2014; Rott et al., 2014; Seehaus et al., 2015; Wuite et al., 2015) and in Greenland (Bevan et al., 2015). In contrast to low-relief areas, DEM generation from interferometry is difficult in high mountainous terrain, which is one reason that few assessments based on TDX imagery are available. Example studies are from the Himalaya (Pandey and Venkataraman, 2013; Vijay and Braun, 2016), the Purogangri Ice Cap on the Tibetan Plateau (Neckel et al., 2013), the Karakoram (Rankl and Braun, 2016) and the Southern Patagonia Icefield (Jaber et al., 2013).

Most of these studies measure glacier elevation changes on the decadal timescale by subtracting a TDX DEM and a second DEM from a different data source. The C-band Shuttle Radar Topography Mission (SRTM) DEM from February 2000 is usually used as a reference DEM, but this timescale does not allow the identification of elevation changes on shorter time intervals. We aim to extend the approach by comparing multiple high-resolution (10 m) TDX DEMs to assess annual elevation changes

in a high-mountain region. We focus our efforts on detailed descriptions of the processing steps, accuracy assessment, and limitations that arise from the side-looking nature of the radar acquisitions.

The TDX DEM generation process is illustrated using the example of the Inylchek Glacier, which is a valley glacier located in the Pobeda–Khan Tengri massif in the Central Tien Shan mountain range (Fig. 5.1). It consists of two heavily debris-covered branches, the Northern and Southern Inylchek, which are separated by the Khan Tengri mountain range (6995 m a.s.l.; Glazirin, 2010) and the subglacial Lake Merzbacher. According to the glacier outline from 2000, Southern Inylchek is approximately 60 km long and covers an area of 508 km² with elevations ranging between 2860 and 7080 m a.s.l., and Northern Inylchek is approximately 33 km long and covers an area of 159 km² between elevations of 3300 and 6600 m a.s.l. Most of the accumulation on the glacier occurs during the summer months (Aizen et al., 1997, 2006a). Its equilibrium line (ELA) is located at approximately 4500 m a.s.l. (Aizen et al., 2007a). Thick debris covers the lower ablation areas and shields the ice from the sun’s radiation, which led to only a minor loss of area of 1.4% between 1990 and 2010 (Osmonov et al., 2013). Both branches of the glacier flow in an east-west direction, which is fortunate for radar sensors that follow a polar orbit. However, the main tributaries of Southern Inylchek are oriented north-south, and thus are heavily affected by layover and shadowing effects.

The Inylchek Glacier has been the subject of numerous studies. Erten et al. (2009); Li et al. (2013, 2014) and Nobakht et al. (2014) focused on the general flow dynamics, whereas Mayer et al. (2008); Neelmeijer et al. (2014) and Zech et al. (2015, 2016) investigated the glacier’s flow regime but specifically addressed the relationship to the regularly occurring glacial lake outburst floods from Lake Merzbacher. The unique setting of Lake Merzbacher has been analysed using several modelling approaches (Konovalov, 1990; Ng et al., 2007; Ng and Liu, 2009; Kingslake and Ng, 2013; Mayr et al., 2014). The glacier has also been included in regional mass balance studies (Farinotti et al., 2015; Pieczonka and Bolch, 2015; Shangguan et al., 2015).

5.3 Data

In this section, we provide an overview of the TanDEM–X Coregistered Single look Slant range Complex (CoSSC), external DEM and glacier boundary data sets that were used in this study. The abbreviations of the DEM data are listed in Table 5.1.

5.3.1 TanDEM–X Data

We used bistatic TanDEM–X StripMap Horizontal–Horizontal (HH) single polarization CoSSC data for the processing of the TanDEM–X DEMs. The large longitudinal extent of the Inylchek Glacier requires at least two adjacent acquisitions to cover the majority of the glacier body. To minimize discrepancies between the neighbouring DEMs that were used for the mosaicking, we used radar data that were acquired successively with a minimum time difference of 11 days. A total of six TDX acquisitions were computed, which resulted in three mosaicked DEMs with a spatial resolution of 10 m (Tables 5.1 and 5.2). The boundaries of all of the data acquisitions are outlined in Fig. 5.1.

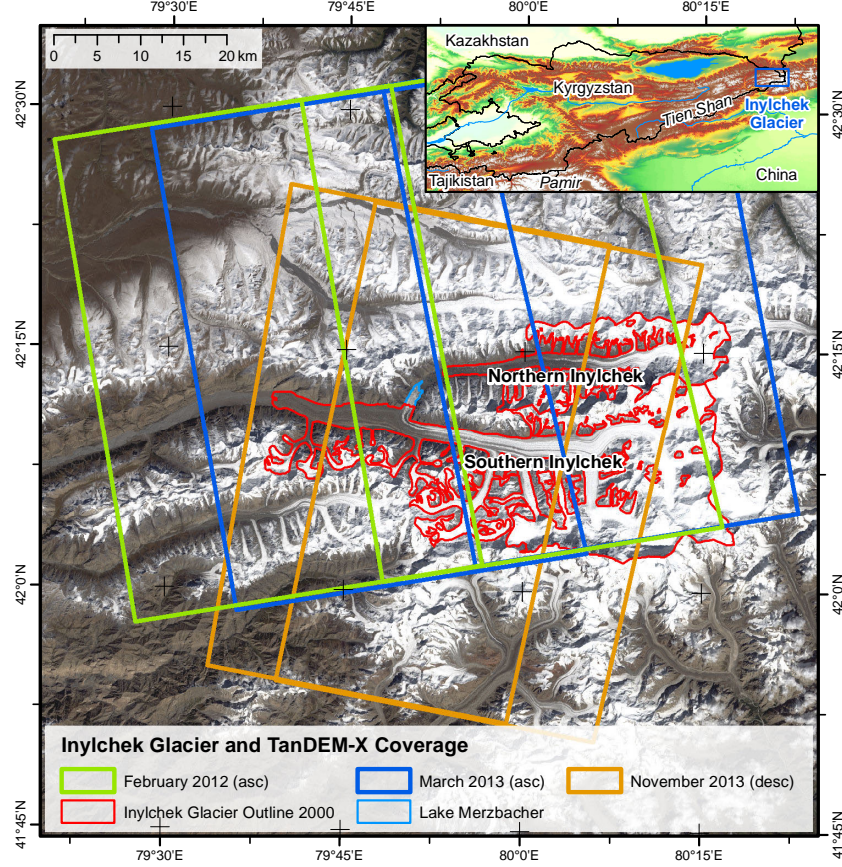


Figure 5.1: Geographic setting of the Inylchek Glacier showing the Northern and Southern Inylchek branches and Lake Merzbacher on a Landsat 8 imagery from 12 September 2014 (RGB channels: 4–3–2). The coverage and timing of the TanDEM–X radar acquisitions are highlighted with different colours (asc and desc refer to ascending and descending, respectively). Adjacent pairs are illustrated by the same colour. The small inset shows the location of Inylchek on the border between Kyrgyzstan and China.

Table 5.1: Naming conventions, origins and default resolutions of the DEMs used in this study. The SRTM DEM data were acquired between 11. and 22. February 2000. The exact acquisition dates for the mosaicked TDX DEMs are given in Table 5.2.

Abbreviation	DEM	Origin	Resolution
SDX	X-band SRTM DEM from DLR	©DLR/ASI 2010	1" x 1"
SDCv4	C-band SRTM DEM v4 from CGIAR–CSI	Jarvis et al. (2008)	3" x 3" ¹
SDCv2DLR	C-band SRTM DEM v2 from DLR	Wendleder et al. (2016)	3" x 3"
TDX1202	TanDEM–X DEM from February 2012		10 m
TDX1303	TanDEM–X DEM from March 2013		10 m
TDX1311	TanDEM–X DEM from November 2013		10 m
TDX–mosaic	mosaic of stable areas (glacier-free) from TDX1202, TDX1303 and TDX1311		10 m

¹ The 1" x 1" C-band SRTM DEM tiles that are provided by the U.S. Geological Survey were not yet available for the Inylchek Glacier area at the time that the study was conducted.

Table 5.2: Overview of the TanDEM-X acquisitions used to generate the DEMs in this study.

DEM Mosaic Name	Time	Active Satellite	Orbit	Incidence Angle (°)	Perpendicular Baseline (m)	Multilooking (Range×Azimuth)
TDX1202	30. Jan 2012	TSX	Ascending	36.2	85.6	4×5
	10. Feb 2012	TSX	Ascending	38.5	86.6	5×6
TDX1303	01. Mar 2013	TSX	Ascending	39.3	117.0	5×6
	12. Mar 2013	TDX	Ascending	37.1	112.2	4×5
TDX1311	18. Nov 2013	TDX	Descending	33.8	78.7	4×5
	29. Nov 2013	TDX	Descending	34.9	77.8	4×5

5.3.2 External DEMs

Additional DEM data are useful for TDX data-based glacier analysis in two main ways: the DEM can be used to facilitate topographic phase modelling during generation of the interferogram, and it can be used in the actual elevation change comparison. In this study, we refer to the SRTM DEM data as an external source. However, because multiple SRTM DEM versions exist, a careful consideration of an appropriate DEM data set is necessary to achieve optimal results. We initially attempted a direct alignment of our TDX DEMs to the X-band SRTM DEM (hereinafter referred to as SDX; cf. Table 5.1) provided by the German Aerospace Center (DLR) (©DLR/ASI 2010). This would have been an ideal data set for two reasons: first, Inylchek is almost completely covered by the SDX data, and second, the depth of radar penetration will only depend on the snow pack properties at the acquisition time, so complications due to different radar wavelengths could have been neglected. However, this approach is not feasible because the SDX data in our study area show a noisy surface with large elevation discrepancies compared to the C-band SRTM DEM v4 that was provided by CGIAR-CSI (Jarvis et al., 2008; hereinafter referred to as SDCv4; cf. Table 5.1), which are especially prominent in high elevation areas. After accounting for the height discrepancy between both data sets because of the different vertical datums (EGM96 geoid heights of SDCv4 vs. WGS 84 ellipsoidal heights of SDX), an elevation difference analysis that was performed on off-glacier areas yielded a standard deviation of 77 m.

These significant discrepancies are related to the single or maximum double coverage (in cross sections) of an area with the X-band sensor, whereas the C-band acquisitions were taken from multiple look directions and incident angles, which allowed for better coverage of layover/shadow areas and better smoothing of the resulting DEM (Marschalk et al., 2004). The poor quality of the SDX data in rugged terrain is related to the local incidence angle, slope, aspect and radar beam, whereas errors in the SDCv4 data occurred in areas of original voids and regions with steep slopes (Ludwig and Schneider, 2006; Kolečka and Kozak, 2014). When attempting to use the SDX data as input for topographic phase removal to create differential TanDEM-X interferograms, our results were not as satisfactory as those from the topographic phase removal using SDCv4 data. We therefore concluded that the SDX data are not sufficiently accurate for direct DEM comparisons in our study area, and we used them only for radar-penetration depth correction.

As a result, we aligned our TDX DEMs to the SDCv4. We preferred this void-filled C-band SRTM DEM version to a version that contained voids because it improves the topography removal that is

necessary to create a differential interferogram. However, areas that originally contained voids were disregarded for the final elevation change analysis.

As recommended by Nuth and Kääb (2011), we attempted to register the SDCv4 to data generated by the Geoscience Laser Altimeter System, which is mounted on the Ice, Cloud and Land Elevation Satellite (ICESat) to enable reference consistency for future glacier elevation analyses. We found three stripes of the ICESat GLA14 data that cover the Inylchek area (Zwally et al., 2014), but were challenged when trying to align the data properly. First, 60% of the 9687 original points had to be neglected, because they fall on glaciated areas, which had changed between 2003 and 2009 acquisitions. Second, the terrain surrounding the Inylchek is characterized by steep slopes, which leads to a substantial increase of the standard deviation of the ICESat elevation heights with respect to the SDCv4 heights (Carabajal and Harding, 2006). We therefore excluded points located on slopes steeper than 30° . Rejecting additional outliers that differed by more than ± 50 m from the SDCv4 data left us with a sample of 1744 (18%) valid measurements. Because these were mainly located in the northern part of our DEM section, a subsequent alignment attempt yielded unsatisfying results.

Alternatively, we used a version of a C-band SRTM DEM v2 that was computed by DLR (hereinafter referred to as SDCv2DLR; cf. Table 5.1), in which the correction towards the ICESat data was done on a global scale (Wendleder et al., 2016). This approach ensured a good absolute alignment of the SDCv4 and consequently the TDX DEMs. A drawback of this data set is that it contains many voids, which are generally located in high elevation areas where the SDCv4 data set had been interpolated or filled by additional data sets. Voids also arise from outlier removal and bilinear interpolation during resampling of the data set. As a result, we decided not to use the SDCv2DLR data set for glacier comparison but rather used it as input data to correct the alignment of the SDCv4.

5.3.3 Glacier Outlines of Inylchek

To ensure that the alignments between various data sets are performed only on stable and snow-free areas, we extracted the glacier extents provided by the Randolph Glacier Inventory v3.2 (Arendt et al., 2012; Pfeffer et al., 2014) and those stored in the Global Land Ice Measurements from Space Inventory (Khromova and Lavrentiev, 2006; Raup et al., 2007). We also used the boundary of the Inylchek Glacier from Shangguan et al. (2015). We manually adjusted this outline in the area of the two glacier tongues to meet the glacier coverage from 2000 by extracting their edges from the SDCv4 DEM. We ultimately combined all three glacier extent data sets to generate a boundary of the maximum potentially glaciated area in the study region. The outline of the Inylchek Glacier from Shangguan et al. (2015) was also used to perform elevation difference measurements.

5.4 Methodology

This section describes the generation of the TDX DEMs. We first focus on the interferometric processing chain, where we describe the parameters and discuss processing caveats. We then cover the DEM alignment procedure that must be undertaken to allow precise elevation comparison, followed

by the handling of radar signal penetration into snow and ice. Finally, we summarize the accuracy assessment.

5.4.1 Interferometric Processing of TanDEM-X Data

To derive the DEMs, we applied single-pass Interferometric Synthetic Aperture Radar (InSAR) to the TDX CoSSC data (Graham, 1974; Hanssen, 2001) using the GAMMA software (Werner et al., 2000). Multilook values were chosen to achieve a spatial resolution of 10 m (Table 5.2). Coregistering was neglected because the TDX pairs were already aligned to each other. Topography removal was done by applying the spatially resampled SDCv4 data. The differential interferograms were filtered with an adaptive filter (Goldstein and Werner, 1998) with a window size of 8 pixels, a window step size of 1 pixel and an alpha value of 0.4. Because the Inylchek area is very rugged, the coherence was estimated with respect to the slope of the terrain and adaptively alternated based on an initial coherence estimate; the window size that was used for the final calculation ranged between 7 pixels for low coherence areas and 3 pixels for high coherence areas. For the phase unwrapping, we applied the branch-cut method (Rosen et al., 1994) with a maximum branch length of 25 pixels. In contrast to minimum cost flow methods, this minimized the introduction of phase-jumps within connected areas. A caveat of this method was that remaining data gaps due to unconnected regions or low coherence values could not be resolved. These gaps were especially prominent in the high elevation mountain range between the two glacier branches. However, our main goal was to avoid introducing errors over the glaciated regions during the phase unwrapping. We thus accepted data gaps on the steep unglaciated slopes of the mountains rather than trying to resolve as many pixels as possible.

The postprocessing of the unwrapped differential interferogram consisted of several steps. First, the remaining phase jumps were removed by either manual correction (adding multiples of $\pm 2\pi$) or masking, and, missing linked areas were connected to the main interferogram where possible (Fig. 5.2). We then applied a 2D quadratic phase model to deramp our results. However, this approach was not able to entirely remove an overall ramp, and we corrected for this with a tilt-removal during the DEM alignment. After re-applying the topographic phase to the differential interferogram, we refined our DEMs by applying outlier removal, small data gap interpolation, and spatial smoothing. The outlier removal was achieved as follows. Initially, we smoothed each generated TDX DEM with a 5×5 pixel kernel. We then subtracted the result from the non-smoothed TDX DEM version and calculated the standard deviation σ of the resulting difference image without considering extrapolated values that were introduced during the smoothing procedure. Values outside the 2σ range were masked out. Next, we interpolated only very small data gaps to avoid excessive extrapolation into larger data gaps (a ‘no data’ pixel must have at least one valid neighbour). In the last refinement step, the DEM was smoothed using a 3×3 boxcar filter, again by avoiding extrapolation. Finally, the individual DEMs were geocoded to the WGS 84 system and projected to UTM coordinates with a spatial resolution of 10 m.

Each adjacent TDX DEM pair was mosaicked together. Because small tilts persisted in the generated TDX DEMs, we detrended the data pairs relative to each other before mosaicking them by calculating a linear plane fit between the overlapping area of each master and slave DEM, which was then used to

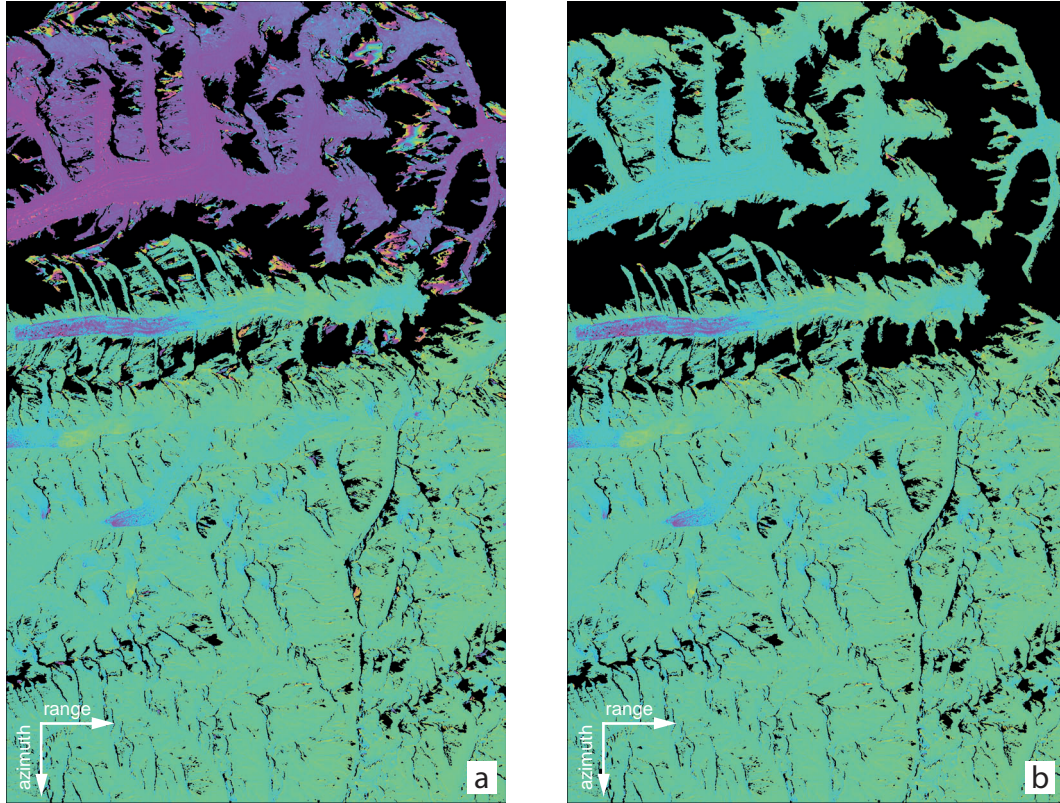


Figure 5.2: Example unwrapped differential TDX interferogram from 01. March 2013 before (a) and after (b) manual editing, in which the upper part of the differential interferogram was corrected by adding 4π to the phase. Both figures use the same colour cycle scaling.

correct the entire slave DEM. We mosaicked the two data pairs by neglecting small elevation changes that occurred between the two acquisitions (Table 5.3). If both data sets contained valid information at the same pixel location we took the mean if they did not differ by more than 10 m, otherwise the pixel was set to ‘no data’.

Table 5.3: Elevation differences of overlapping areas (including snow and ice) and those of the Inylchek Glacier only from the corresponding two TanDEM-X pairs after detrending and removal of differences greater than 10 m.

DEM Mosaic Name	Entire Overlapping Area		Inylchek Glacier Only	
	Mean (m)	Std. Dev. (m)	Mean (m)	Std. Dev. (m)
TDX1202	-0.002	2.05	-0.02	1.47
TDX1303	0.05	1.95	0.01	1.36
TDX1311	0.001	1.99	-0.11	1.48

5.4.2 Alignment of the SRTM and TDX DEMs

Before the evaluation of the glacier elevation change can be carried out, all of the available DEMs need to be carefully aligned to each other. This requires all of the data sets to be resampled to the same spatial resolution. Because our main goal is to compare glacier elevation changes between the high-

resolution TDX DEMs, we decided to fit the SDCv2DLR and SDCv4 DEMs to the TDX resolution and resampled them to 10 m. The calculation of the alignment parameters is performed on the masked versions of the DEMs, where all of the pixels on unstable terrain were removed to prevent the influence of varying glacier heights on the matching process. The determined alignment parameters are then directly applied to the complete DEMs that contain glacier areas. Additionally, one large glacier-free TDX DEM (hereinafter referred to as TDX-mosaic) was created by merging the stable areas of all three individual TDX DEMs (TDX1202, TDX1303, TDX1311). This product was used to align the TDX DEMs to the SRTM DEM data. Below, we describe the data alignment process in detail. The connections between the individual datasets are shown in Fig. 5.3.

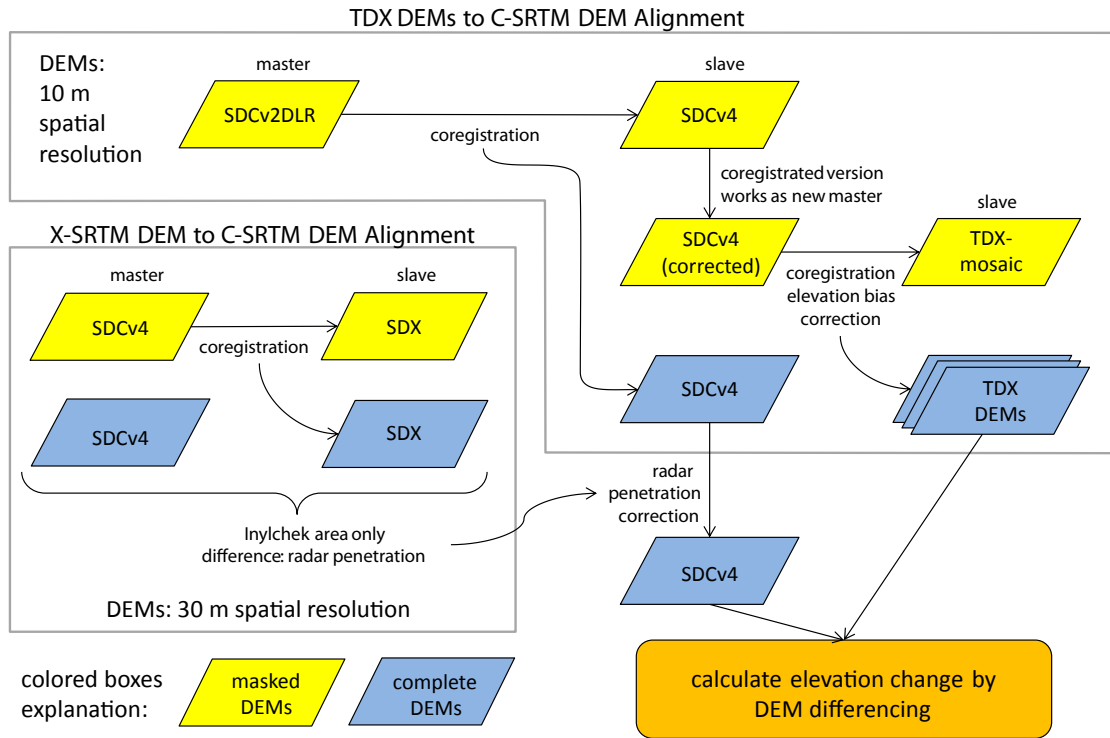


Figure 5.3: Overview of the alignment process of the DEMs and their respective links. The coregistration and elevation bias parameters are always calculated on masked DEMs that contain only the stable areas (yellow boxes). The retrieved parameters are then used to correct the complete DEMs (blue boxes). The elevation differences retrieved from the subtraction of SDCv4 from SDX are used as inputs to correct the radar penetration offset of the coregistered SDCv4. After all of the corrections were applied, the elevation change calculations were performed.

As recommended in the overview study of Paul et al. (2015), we relied on the approach described by Nuth and Kääb (2011) to properly align the DEMs. Their so-called universal coregistration is based on the dependence of the biases of the slope, aspect and elevation difference. We slightly modified the coregistration procedure; the estimations of the direction and magnitude of the shift vector were performed as described by the authors, but we did not follow their suggestion to derive the overall vertical bias by dividing the mean bias by the mean slope tangent of the terrain. Instead, we calculated the vertical offset Δz in a separate step by applying a least-squares adjustment with the following function:

$$\Delta z = a + bx + cy, \quad (5.1)$$

where x and y are the range and azimuth directions, respectively. By either estimating all three parameters (a, b and c) or setting b and c to zero, we controlled for the tilt correction between the DEMs. We refer to this step as DEM detrending.

Our approach also differs from Nuth and Kääb (2011) in that we started the iteration process with DEM detrending and thus first applied a vertical shift and then calculated the horizontal shift parameters from the universal coregistration. This change of the order of the processing steps facilitates improved horizontal matching because DEM detrending includes the removal of possibly existing tilts. If the result did not satisfy the defined threshold parameters, we repeated the detrending and registration procedures iteratively until a predefined threshold criterion was met. The final horizontal shift vector was then calculated by summing all of the individual horizontal shifts that were performed during the iteration and applying the sum to the initial slave DEM. We then applied the DEM detrending step once to this horizontally corrected slave DEM to obtain the best vertical fit as well.

During the DEM alignment, we constrained the fitting procedure as follows. DEM detrending was performed by applying weights w that depended on the corresponding slope α to each elevation difference pixel: $w = (90.0^\circ - \alpha)/90.0^\circ$. Detrending of the SDX data set benefited from a restriction of the fitting process to slopes less than 10° . For all alignment processes that involved TDX scenes, we additionally allowed for a plane tilt removal. Table 5.4 gives an overview of the applied constraints for the individual DEM pairs.

Table 5.4: Overview of the parameters applied to the DEM pairs during DEM alignment, where x and - indicate whether a constraint was applied or not. The parameters weighted slopes ($w = (90.0^\circ - \alpha)/90.0^\circ$), slope restriction ($\alpha < 10^\circ$) and plane tilt refer to the DEM detrending step (vertical offset calculation). Except for the last DEM alignment, all of the data sets were resampled to a spatial resolution of 10 m.

Aligned DEMs (Master-Slave)	Weighted Slopes	Restricted Slope	Tilting Allowed	Elevation Bias Correction
SDCv2DLR - SDCv4	x	-	-	-
SDCv4 (corrected) - TDX-mosaic	x	-	x	x
TDX1303 - TDX1202	x	-	x	-
TDX1303 - TDX1311	x	-	x	-
SDCv4 (30 m) - SDX (30 m)	x	x	-	-

The parameter calculation of the universal coregistration was based on the median values of each terrain aspect bin, which minimized the influence of outliers (boxplots of the first iteration results are given in Fig. 5.4). We also considered only slopes greater than 10° because only these elevation differences are meaningful. Pixels with elevation differences greater than 300 m were removed from the statistical analysis (Kääb, 2005). In general, the iterations continued until either the change of the magnitude of the shift vector was less than 0.2 m or the improvement of the standard deviation was less than or equal to 1%.

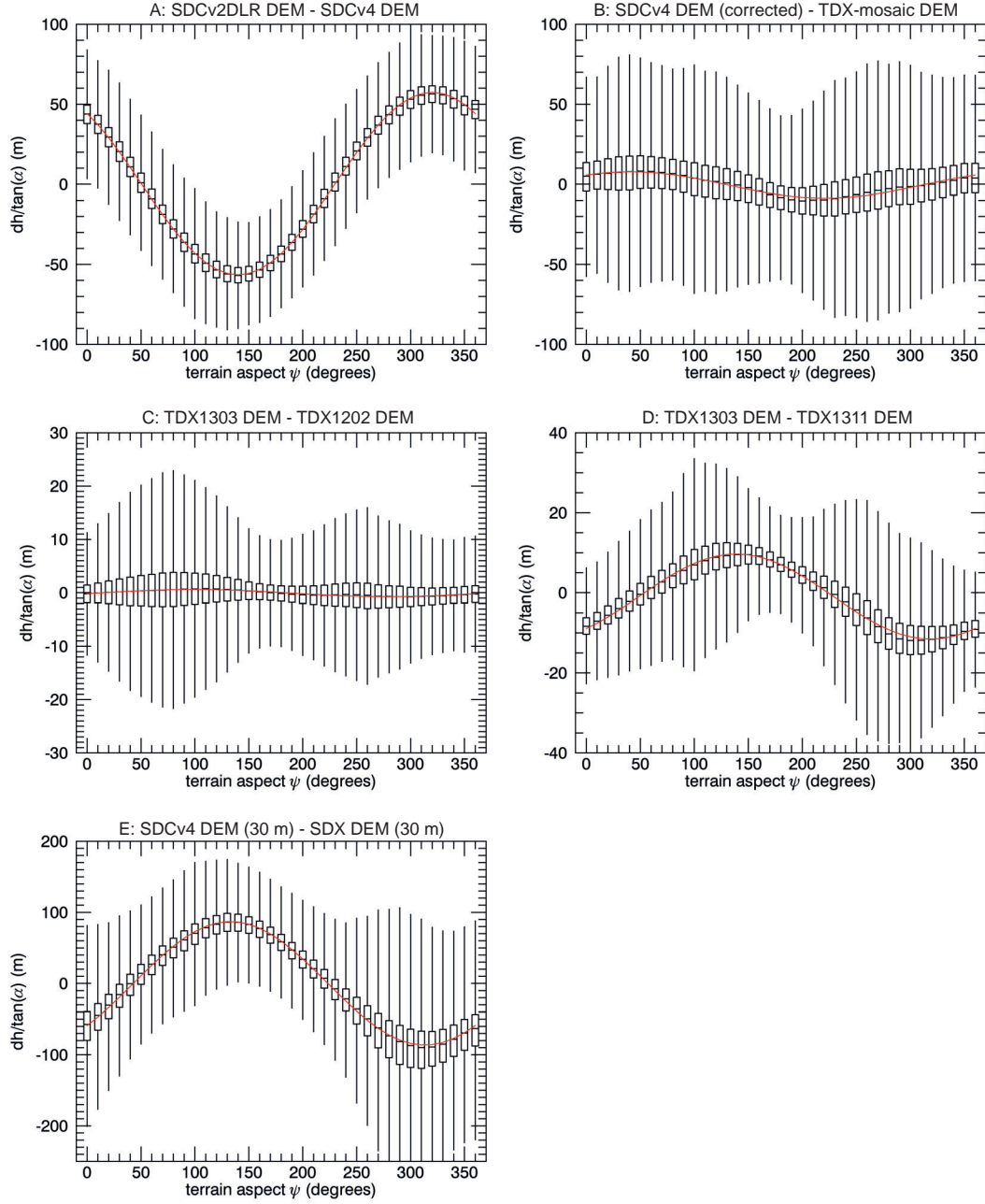


Figure 5.4: Results of the first iteration of the horizontal shift calculation after Nuth and Kääb (2011) showing the significant offsets between the available DEMs, which makes proper DEM alignment inevitable. The aligned glacier-free DEM versions are given in the titles of each plot, in which the master DEM is presented first and the slave DEM is presented second. The red line shows the corresponding fitting function. Note the different scales on the y-axis.

To account for errors that might have been introduced due to resampling of the SRTM data (Paul, 2008; Gardelle et al., 2012a), we applied an elevation bias correction after the alignment of the TDX DEMs to the SDCv4. Because the elevation differences at high elevations vary significantly, we did not apply a polynomial function as proposed in Nuth and Kääb (2011) but rather used median differences calculated from 100 m bins directly for the correction.

5.4.3 Radar Penetration Correction

Because X-band and C-band radar data are compared to each other, compensation of the signals for the different radar penetration depths is required for snow, ice and firn regions (Rignot et al., 2001; Gardelle et al., 2012a,b; Kääb et al., 2012). In our case, the radar penetration depth refers to the phase centre depth of the interferometric signal.

We estimated the difference by examining the SDX and SDCv4 (bilinearly resampled to 30 m spatial resolution) data. Because both data sets were acquired at the same time, elevation differences over the glacier area should only exist due to the different penetration characteristics of the X-band and C-band sensors. The elevation differences were thus calculated by considering only the Inylchek glacial area and evaluating the height variations of each 100 m elevation bin. The resulting elevation-dependent radar penetration variances were then applied to the SDCv4 data to enable a direct comparison with the TDX DEM glacier surface elevations. We note that this approach will only provide an approximation of the true radar penetration difference; discrepancies will persist due to different snow cover depths and characteristics between 2000, 2012 and 2013. Additionally, the incidence angle of the radar look direction and the orbit pass affect the radar penetration depth. Nevertheless, the derivation of different glacier surface heights from SDX and SDCv4 is still reasonable because most of the data sets were acquired during the winter; thus, similar conditions can be assumed.

Because the penetration difference should not exceed 10 m (Rignot et al., 2001; Gardelle et al., 2012a), we defined all of the difference values greater than ± 12 m as outliers and did not consider them for the penetration estimation. We thereby prevented erroneous X-band SRTM elevation values from affecting our results. The median values of each elevation bin were used to correct the 10 m resolution resampled SDCv4 but only for areas with elevations below 6000 m a.s.l. At higher elevations, not enough pixels per elevation bin were available to generate reliable results. Instead, we calculated the mean of the correction values applied to the elevations between 5000 and 6000 m a.s.l. and used this value to correct areas with elevations above 6000 m a.s.l.

Figure 5.5 shows the median penetration differences as a function of elevation. The values range from -1.51 m (3700 m a.s.l.) to 2.98 m (5900 m a.s.l.). As expected, the radar penetration differences between the SRTM DEMs increase with increasing elevation; in lower regions, the glacier is highly covered by debris with little snow cover. Larger snowpacks are only present at the higher elevations. Interestingly, some of the lower elevation bins show negative correction values. This is reasonable when we consider that the stable areas were also partly covered with snow, especially during the winter. During the vertical matching of the SDCv4 DEM and the SDX DEM, the radar penetration difference

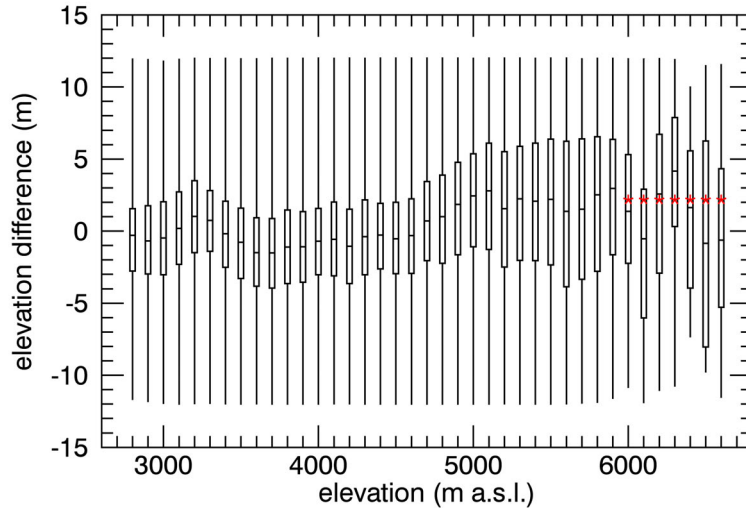


Figure 5.5: Estimation of radar penetration values for the Inylchek region in 100 m elevation bins retrieved by subtracting SDCv4 from SDX. The boxes show the median values along with the lower and upper quartiles. Whiskers refer to the sample minimum and maximum, respectively. Note that the data range is constrained to a 12 m elevation difference. Elevation differences for elevations above 6000 m were taken from the mean penetration between 5000 and 5900 m (red asterisks) because the small number of pixels does not allow reliable penetration values to be retrieved. The overall uncertainty of the radar penetration is 1.39 m, which was derived from the standard deviation of the medians for all elevation bins below 6000 m a.s.l.

due to this snow cover was removed. For debris-covered, low-elevation bins with less snow cover than the stable areas, this will result in negative radar penetration differences.

To estimate the uncertainty of the radar penetration, we calculated the standard deviation of the medians for all elevation bins below 6000 m a.s.l. and determined a value of 1.39 m, which we considered in the accuracy assessment for all direct comparisons between the SDCv4 and TDX DEM data.

5.4.4 DEM Elevation Difference Calculation

We calculated the elevation difference between each DEM pair based on the area-weighted mean difference for each 100 m elevation bin. Before retrieving the average value, we set pixels that differed by more than 3σ from the mean of each elevation bin to ‘no data’ (Gardner et al., 2012; Gardelle et al., 2013). We also neglected all interpolated pixels of the SDCv4 DEM data set (Kääb et al., 2012; Gardelle et al., 2013).

Next, all of the ‘no data’ pixels located within the glacier boundary needed to be addressed carefully before any DEM comparison was undertaken; otherwise, the final results will show under- or overestimated values. Gardelle et al. (2013) proposed using the average of the corresponding elevation bin to fill data gaps. However, we argue that the strong dependency of accumulation/ablation on the hillslope angle of the mountainous areas cannot be neglected. Figure 5.6 shows the clear dependence of the elevation change on the slopes of the terrain. Areas with lower hillslope angles are more susceptible to elevation changes, and the elevations of steeper areas are affected less. We claim that at a certain slope, the glacier elevation change can be assumed to be stable. This hypothesis is supported

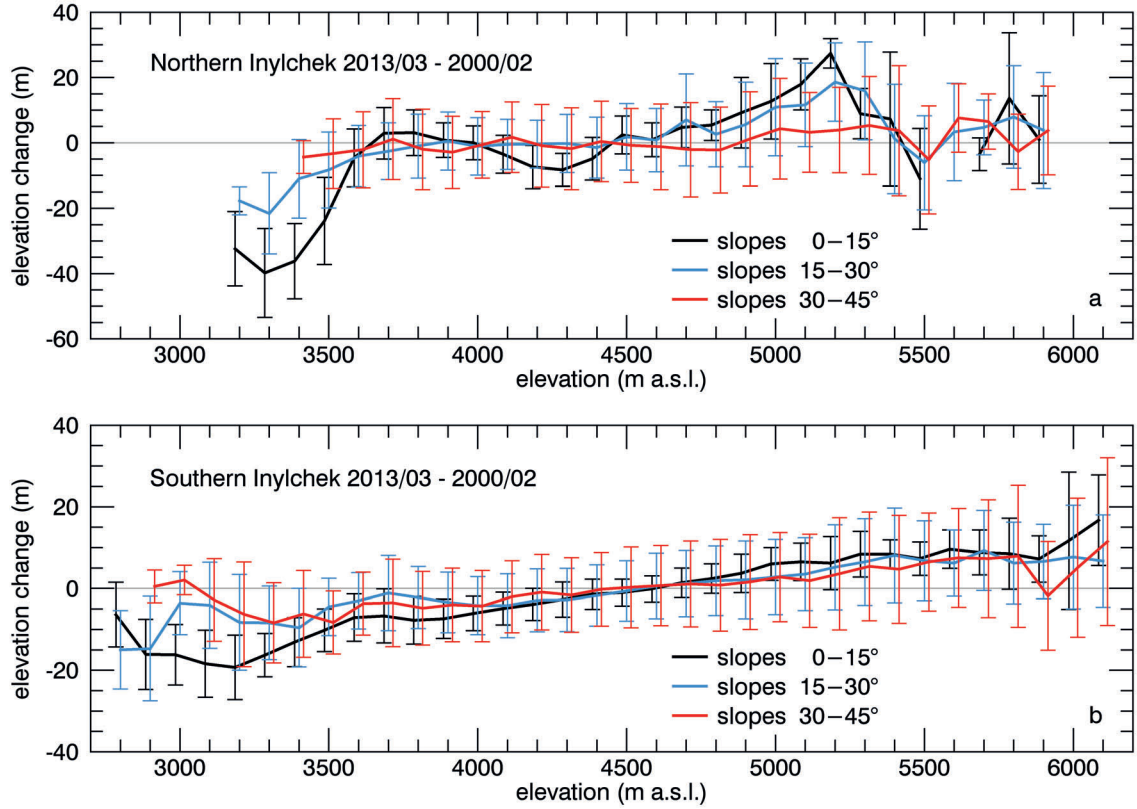


Figure 5.6: Example elevation changes from the (a) Northern Inylchek and (b) Southern Inylchek glaciers (showing mean and standard deviation values) between February 2000 (SDCv4 DEM) and March 2013 (TDX1303 DEM) as a function of elevation while separating terrain slope angles. The greatest elevation changes occur in small hillslope areas, while glacier regions with steeper slopes are affected less.

by the fact that above 50° hillslope angle, snow tends to slide off regularly (Keller and DeVecchio, 2016). Furthermore, snow nourishing glaciers on lower slopes than 50° may be transported through avalanches, which occur mainly on slopes between 35 and 40° (Keller and DeVecchio, 2016).

As a result, to fill the ‘no data’ areas, we distinguished between slopes less than and greater than 45° . For the entire glacier region, we set the elevation change of the pixels located in areas with slopes greater than 45° to zero. This had the following two effects. First, many of the data gaps were filled with zero values because most of the data gaps were in high elevation areas with steep slopes, where the TDX radar signal could not be resolved. Second, we reduced the introduction of erroneous values that might occur when a TDX DEM is subtracted from the SDCv4. These errors may be introduced due to the different resolution of the original data. Despite the applied elevation-dependent correction, the SDCv4 elevation values at high elevations can still be underestimated (Berthier et al., 2006; Paul and Haeberli, 2008; Gardelle et al., 2012a), which in turn leads to an underestimation of the calculated volume loss.

In the next step, regions with slope angles of less than 45° were treated as follows to take into account the dependency of the elevation change on the hillslope angle. Data within one elevation bin were separated into three slope classes: $0-15^\circ$, $15-30^\circ$ and $30-45^\circ$. Missing pixels were then filled with

the mean elevation change values of the corresponding elevation bin and slope class if at least 1% of the valid pixels were available to derive the mean value from. The lowest elevations where this condition did not hold were at 5300 m a.s.l. and 5600 m a.s.l. for Northern and Southern Inylchek, respectively. These elevations were well above the ELA and thus were in the accumulation region. As a result, we filled the remaining missing pixels by following the approach of Pieczonka et al. (2013), who argued that the long-term change in accumulation areas is rather small, so missing pixels in accumulation areas can be assigned to zero. Although our approach already considers several boundary conditions, we emphasize that the mean values derived for the individual classes must be evaluated carefully to avoid outlier extrapolation. A standard deviation of more than 20 m within a single class was used as a threshold to find existing unrealistic mean values, which were then eliminated from the extrapolation.

The overall elevation change ΔH was calculated as follows (Shangguan et al., 2015):

$$\Delta H = \frac{\sum_{i=1}^n \Delta h_i a_i}{A}, \quad (5.2)$$

where i is the number of elevation bins, Δh_i is the mean elevation difference for the individual elevation bin, a_i is the area of the valid pixels per elevation bin, and A is the total area of all of the elevation bins.

Special attention had to be paid to the calculation of the annual elevation change of the DEM pair for February 2000 to November 2013 because the data were not acquired during the same season. In this case, the seasonal snow height effects will bias the calculation, so we refrained from calculating an annual elevation change rate.

5.4.5 Accuracy Assessment

Several methods have been used to assess the elevation difference uncertainty $u_{\text{DEM1-DEM2}}$ between two DEMs, examples are found in studies from Gardelle et al. (2013); Pieczonka et al. (2013); Pieczonka and Bolch (2015) and Shangguan et al. (2015). Similar to the two latter studies, we used an approach that is robust to outliers in which $u_{\text{DEM1-DEM2}}$ was derived from the error of the DEM coregistration, which was estimated from the normalized median absolute deviation $\Delta\sigma$ (NMAD) of stable areas (Table 5.5). Because $\Delta\sigma$ is proportional to the median of the absolute differences between the DEM errors Δh_j ($j = 1, \dots, n$, where n is the total number of pixels in stable areas) and the median of these DEM errors $m_{\Delta h_j}$, it can be regarded as an outlier-resilient estimate of the standard deviation (Höhle and Höhle, 2009).

$$\Delta\sigma = 1.4826 \cdot \text{median}_j(|\Delta h_j - m_{\Delta h_j}|). \quad (5.3)$$

For elevation difference calculations between TDX DEMs, we assumed the same radar penetration depth; thus, $u_{\text{TDX1-TDX2}}$ denoted as:

$$u_{\text{TDX1-TDX2}} = \Delta\sigma \quad (5.4)$$

However, for the elevation differences $u_{\text{SRTM-TDX}}$ that were calculated between the SRTM and TDX DEM data, the accuracy of the radar wave penetration depth Δrw of ± 1.39 m must also be included in the uncertainty estimation:

$$u_{\text{SRTM-TDX}} = \sqrt{(\Delta\sigma)^2 + (\Delta rw)^2}. \quad (5.5)$$

Table 5.5: Statistics for stable (outside glacier) difference areas. The values between the TDX DEMs were calculated before mosaicking the three stable areas together. NMAD ($\Delta\sigma$) is the normalized median absolute deviation (see text for further explanation).

DEM Pair	Mean (m)	Median (m)	Std. Dev. (m)	NMAD (m)
SDCv4 (corrected) - TDX-mosaic	-0.19	0.03	8.07	5.04
TDX1202 - TDX1303	-0.005	-0.001	1.72	1.13
TDX1303 - TDX1311	-0.03	-0.03	2.26	1.13
TDX1202 - TDX1311	0.1	0.09	2.15	1.28

5.5 Results and Discussion

5.5.1 Uncertainty of Measurements

The largest uncertainty in our analysis arises from the significant number of missing values within the DEMs. Quantifying the impact of the filling is difficult. Because we do not take into account any reference data, we can only make assumptions about the void areas. Pieczonka and Bolch (2015) relied on ordinary kriging to fill voids. In our setting, the largest areas of missing data are at high elevations. Applying a kriging method in this case would lead to over-extrapolation, which impairs the filling, as was noted by Pieczonka and Bolch (2015). Filling all data gaps within the accumulation area with zero values may be a valid option for long-term studies because the assumption of low elevation changes for that region may be true (Pieczonka et al., 2013). However, that does not account for the inter-annual investigations in our study, where changes between consecutive years might be large. We therefore extended the approach of Gardelle et al. (2013) to fill data voids with mean elevation bin values by considering the slope-dependency of the elevation change. Due to side-looking induced geometric distortions of the radar image, most voids occur on the steeper slopes, and thus affect the edges and the higher elevations of high mountain glaciers. Because these glacier areas are affected by glacier changes differently than those on the gentler slopes (Fig. 5.6), using mean values generated from valid pixels located on these gentler slopes would lead to an overestimation of the glacier change. As a result, mean values from specific slope bins help to improve the glacier elevation change estimates. Still, the amount and width of the useful slope bins must be carefully evaluated by considering the availability of the data. Too many slope classes may result in too few valid pixels within a slope bin, and calculating mean values will become random or even impossible. For the Inylchek Glacier test site, three slope bins between 0° and 45° proved useful. As a result, we assign zero values only to pixels at high elevations with slopes greater than 45° and to areas with slopes between 0° and 45° where no valid information exists to retrieve the mean values from. We tested the impact of the latter method

by assigning values of either ± 1 m instead of zero. The elevation changes revealed maximum absolute elevation change differences of $\pm 0.04 \text{ m a}^{-1}$ (9%) and $\pm 0.07 \text{ m a}^{-1}$ (26%) for Northern and Southern Inylchek, respectively.

An additional uncertainty factor is the estimation of the different radar penetration depths of the X-band and C-band signals into snow and ice. Shangguan et al. (2015) reported greater penetration differences (1.7 m for debris free-area ablation areas and 2.1–4.3 m for elevations between 4000 and 5100 m.a.s.l.) over the Inylchek area than our investigation. However, these authors did not apply any DEM alignment between the X-band SRTM DEM and the C-band SRTM DEM in advance, and we used a strict outlier removal strategy (± 12 m), which might explain the differences.

Kääb et al. (2012) provides C-band radar wave penetration estimates for various mountainous regions of Asia that were derived by a differentiation of C-band SRTM DEM elevation to ICESat elevations. A direct comparison between their values and ours is only partially possible because we did not correct for a discrepancy that is generated by the penetration of X-band SAR into snow and ice. However, we expect that this discrepancy will play only a minor role in ice-dominated debris-free ablation regions but has a greater impact in the snow/firn-dominated areas of the accumulation region. Taking this into consideration, our penetration estimates are consistent with the values given by Kääb et al. (2012), which include 2.5 ± 0.5 m over general glacier areas, -0.8 ± 1.0 m over debris-covered ice, 0.1 ± 1.2 m over clean ice and 4.8 ± 0.7 m over the firn/snow areas of the glaciers in the East Nepal and Bhutan mountain range that, similar to Inylchek, are summer-accumulation type glaciers (Kääb et al., 2012).

It is worth noting that due to the short time period of this investigation, the uncertainties between the TDX DEMs are greater than average compared to similar studies that consider optical data such as KH-9 Hexagon and SPOT-5 data. However, we emphasize that low mass balance uncertainties of 0.10 m a^{-1} between KH-9 and SRTM data or 0.11 m a^{-1} between KH-9 and SPOT-5 data (Shangguan et al., 2015) can be only achieved when looking at long time spans (in their case, 24 years and more), whereas the same accuracy is theoretically achieved from TDX comparisons with an acquisition difference of nine years.

5.5.2 DEM Alignment Quality

The evaluation of elevation differences within stable areas between two DEMs gives insights on the quality of the DEM alignment. In our case, the comparison between the SDCv4 and TDX data yields an absolute mean elevation difference of approximately 0.2 m with a standard deviation of 8 m (Table 5.5). These discrepancies are mainly attributed to the different spatial resolutions of the DEMs. The high potential of the TDX DEM data for the analysis of glacier changes is demonstrated by the comparison of only the TDX DEMs. Here, the elevation differences are in the range of a few centimetres with corresponding standard deviation values of 2 m, which is at least two times smaller than when comparing TDX DEMs to SDCv4 data. The best agreement is achieved between the two TDX DEMs that are taken from the same orbit and incidence angle (TDX1202–TDX1303: -0.005 ± 1.72 m), but the differences with TDX1311, which had the opposite orbit, are only slightly larger (TDX1303–TDX1311:

-0.03 ± 2.26 m and TDX1202–TDX1311: 0.1 ± 2.15 m; cf. Table 5.5). However, these variations may be attributed to orbital discrepancies or processing errors as well as the different seasons of the data collection. Because snowfall over stable areas cannot be excluded, the characteristics and depth of the snow may differ on the dates of the data collection, which results in different penetration effects and ultimately in different elevation changes.

Although all TDX DEM comparisons are characterized by large absolute uncertainties compared to the corresponding elevation changes, the good quality of the DEMs is also demonstrated by the high internal consistency between the three TDX DEM pairs. The difference between the sums of the absolute glacier elevation changes of TDX1202–TDX1303 and TDX1303–TDX1311 is only 7 cm for the Northern Inylchek branch and 3 cm for the Southern Inylchek branch compared to the corresponding differences retrieved from the DEM pair that covers the time period TDX1202–TDX1311 (Table 5.6). The superior accuracy of the TDX DEMs compared to SDCv4 is also confirmed by the 4–5 times lower absolute elevation change uncertainty values of the direct TDX DEM comparisons.

Table 5.6: Elevation changes of the Southern and Northern Inylchek glacier branches.

(a) Northern Inylchek (159 km ²)		
DEM Pair	Absolute Elevation Change (m)	Elevation Change per Year (m a ⁻¹)
SDCv4 - TDX1202	-2.88 ± 5.23	-0.24 ± 0.44
SDCv4 - TDX1303	-3.68 ± 5.23	-0.28 ± 0.40
SDCv4 - TDX1311	-3.22 ± 5.23	-
TDX1202 - TDX1303	-0.34 ± 1.13	-0.32 ± 1.04
TDX1303 - TDX1311	-0.57 ± 1.13	-
TDX1202 - TDX1311	-0.84 ± 1.28	-
(b) Southern Inylchek (508 km ²)		
DEM Pair	Absolute Elevation Change (m)	Elevation Change per Year (m a ⁻¹)
SDCv4 - TDX1202	-1.69 ± 5.23	-0.14 ± 0.44
SDCv4 - TDX1303	-1.98 ± 5.23	-0.15 ± 0.40
SDCv4 - TDX1311	-1.76 ± 5.23	-
TDX1202 - TDX1303	-0.42 ± 1.13	-0.38 ± 1.04
TDX1303 - TDX1311	-0.27 ± 1.13	-
TDX1202 - TDX1311	-0.72 ± 1.28	-

5.5.3 Inylchek Elevation Changes

As shown in Table 5.6 and Fig. 5.7, both branches of the Inylchek Glacier have been affected by thinning since 2000, and the northern branch has experienced higher downwasting rates than the southern branch. Mapping the elevation changes shows the spatial distribution of areas of elevation loss and gain. The ablation area of Northern Inylchek is most severely affected by glacier loss with

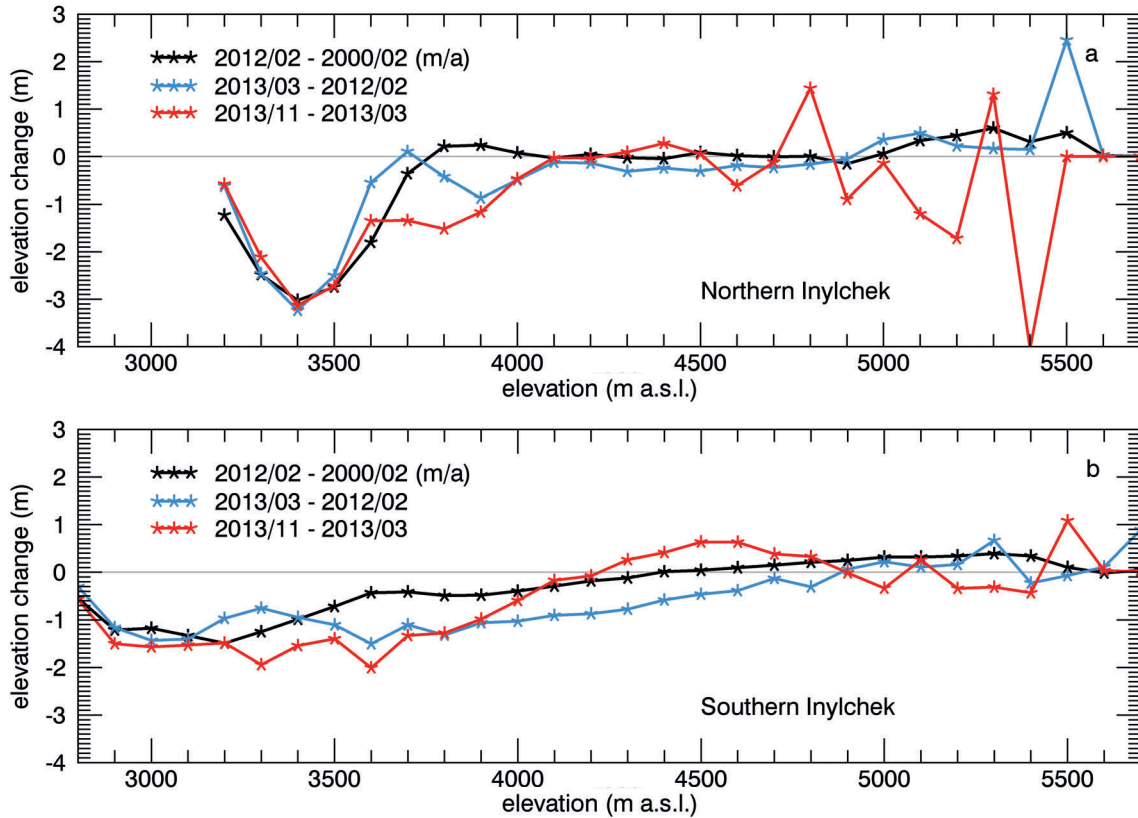


Figure 5.7: Elevation changes of a) Northern Inylchek and b) Southern Inylchek as a function of elevation. The data represent mean changes per 100 m elevation bin (marked with asterisks).

rates up to 60–70 m over 13 years, whereas the accumulation areas of both branches show slight gains of between 1 and 10 m since 2000 (Fig. 5.8). The high spatial resolution of the TDX data also allows precise mapping of the inter- and intra-annual elevation changes (Fig. 5.9), which offer a unique view on the underlying glacial processes. For example, an increase in surface elevation occurred in the middle part of the northern branch during 02/2012–03/2013 (Fig. 5.9b), and a distinct elevation loss occurred at an icefall on the main southern tributary of Southern Inylchek during 03/2013–11/2013 (Fig. 5.9c). We emphasize that changes at these short timescales cannot be observed from the annual mean elevation change shown in Fig. 5.9a. Retrieving DEMs from TDX data is therefore especially helpful for investigating inter- and intra-annual time scales.

Pieczonka and Bolch (2015) and Shangguan et al. (2015) used optical remote sensing imagery to analyse mass balance rates of the Inylchek Glacier. Both studies showed that within the time period 1975 – 1999 mass loss rates over the Southern Inylchek glacier branch were higher ($-0.27 \pm 0.45 \text{ m w.e.a}^{-1}$ in Pieczonka and Bolch (2015) and $-0.43 \pm 0.10 \text{ m w.e.a}^{-1}$ in Shangguan et al. (2015)). However, Shangguan et al. (2015) also investigated mass changes between 1999 – 2007 and reported an increase of Northern Inylchek’s downwasting values to $-0.57 \pm 0.46 \text{ m w.e.a}^{-1}$, which was higher than Southern Inylchek’s mass loss of $-0.28 \pm 0.46 \text{ m w.e.a}^{-1}$ in the same time period. For comparison purposes, we converted the 02/2000 – 03/2013 glacier elevation changes to mass balance values by applying the geodetic method. For conversion, we assumed an ice density of 850 kg m^{-3} (Huss, 2013) and used a value of $999.972 \text{ kg m}^{-3}$ for the water density. The resulting mass balance is in the order of $-0.24 \pm$

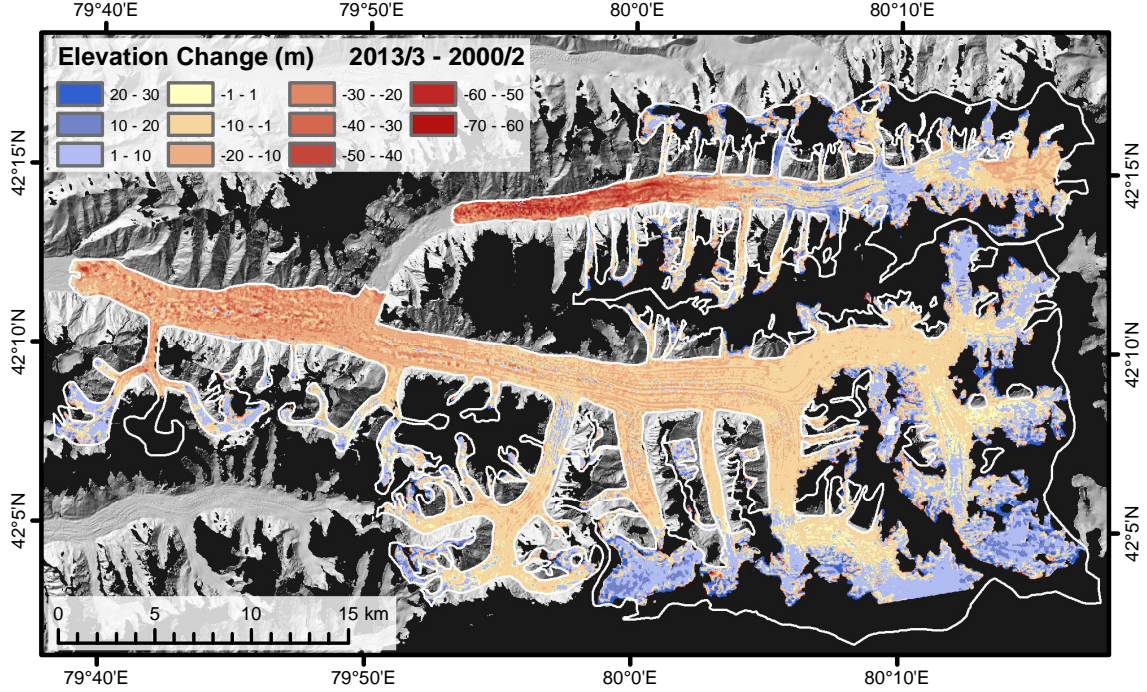


Figure 5.8: Absolute elevation changes between SDCv4 and TDX1303. The white polygons outline the Inylchek Glacier. Negative values indicate elevation losses (red), and positive values indicate elevation gains (blue).

$0.34 \text{ m w.e.a}^{-1}$ for Northern Inylchek and $-0.13 \pm 0.34 \text{ m w.e.a}^{-1}$ for Southern Inylchek. Our estimation agrees with Shangguan's findings in such a way that Northern Inylchek is losing more mass per year than Southern Inylchek. However, our results suggest that this is related rather to a deceleration of Southern Inylchek's downwasting than to a significant increase of the thinning of the Northern Inylchek branch. As the findings of Shangguan et al. (2015) resulted in significantly higher mass-loss values than our findings further research into this discrepancy is required. A potential explanation is the application of different radar penetration depth corrections in Shangguan et al. (2015). We tested the impact of the radar penetration depth on the mass balance calculation by increasing it by $\pm 1 \text{ m}$, which resulted for both glacier branches in a mass balance change of $\pm 0.06 \text{ m w.e.a}^{-1}$. This refers to a change of $\pm 25\%$ and $\pm 46\% \text{ w.e.a}^{-1}$ for Northern and Southern Inylchek, respectively. As the discrepancies to Shangguan et al. (2015) are still larger, radar penetration depth is likely not the only influencing factor. Another possible explanation might be the data voids in the accumulation regions in the study of Shangguan et al. (2015). The mass gain that we detected especially in the Southern Inylchek accumulation area was not resolved in their study (cf. to Fig. 4b in Shangguan et al. (2015)).

5.6 Conclusions

TerraSAR-X and simultaneously recorded TanDEM-X (TDX) radar data are ideal to generate digital elevation models in high-mountain areas, where weather conditions often prevent monitoring with optical remote sensing devices. Because of their spatial coverage, they are especially suitable to assess glacier elevation changes for broad areas. However, steep slopes and high relief of mountain areas make generating DEMs from single SAR image pairs a challenging task. We investigated in detail (1)

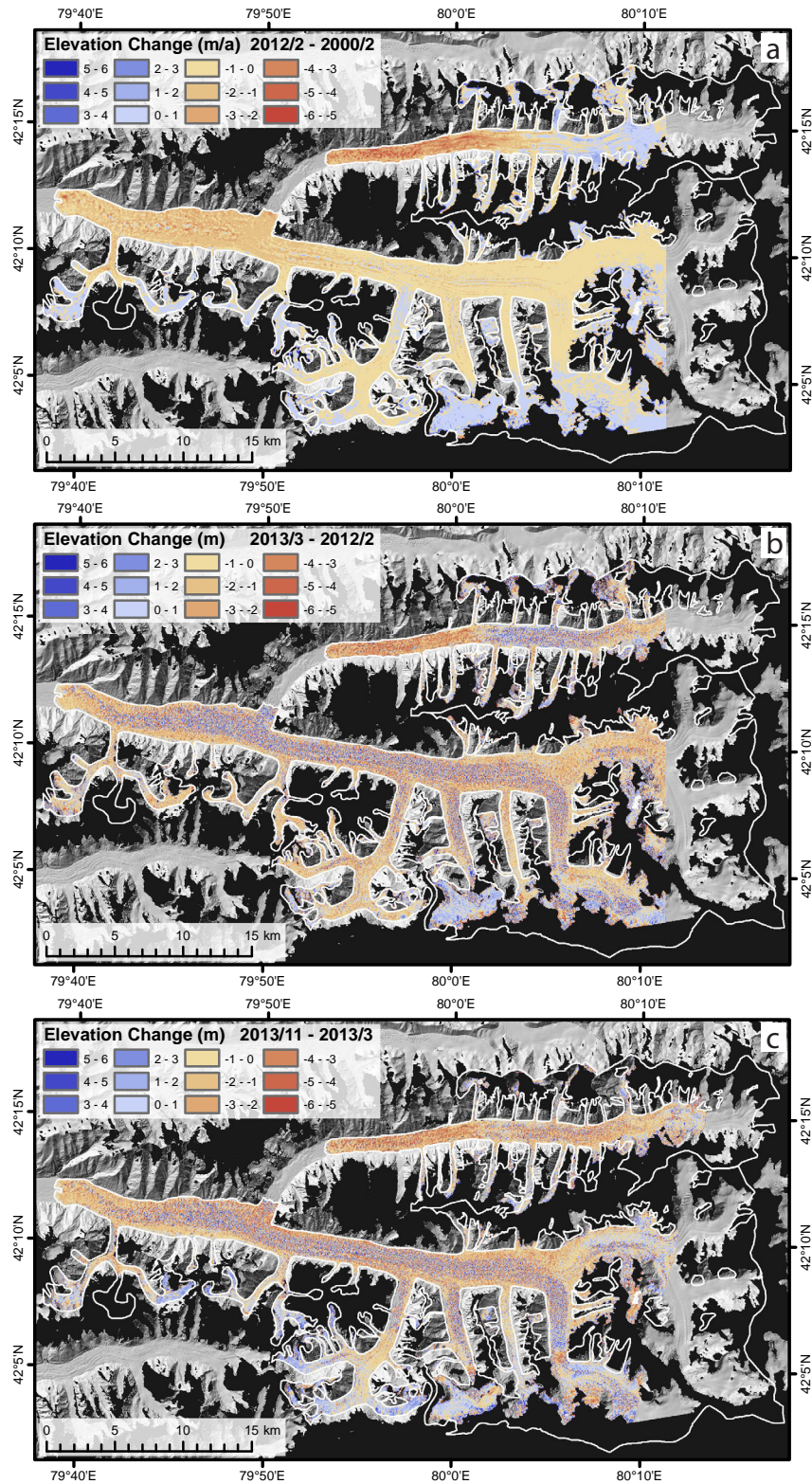


Figure 5.9: Elevation changes between the SRTM and TanDEM-X acquisitions: (a) between SDCv4 and TDX1202 (mean annual change), (b) between TDX1202 and TDX1303, and (c) between TDX1303 and TDX1311. The white line represents the boundary of the Inylchek Glacier.

the suitability of SRTM-based reference DEMs to enable long-wavelength topographic phase removal to derive differential interferograms; (2) the impact of interferometric processing parameters on DEM generation (e.g. coherence, unwrapping procedures); (3) the importance of precise DEM alignment; (4) the effect of radar penetration into snow and ice; (5) the filling of data voids in glaciated areas; and (6) the accuracy that can be achieved from using TDX based DEMs. This leads to the following conclusions:

(1) Although X-band SRTM DEM data covers our study almost completely, we use C-band SRTM DEM data for topographic phase modelling because noisy surfaces and inaccuracies at steep slopes in the X-band SRTM DEM hamper the interferogram generation.

(2) Due to the side-looking nature of the sensor, geometric distortions in the radar data resulting from foreshortening, layover and shadowing effects cannot be avoided. To prevent an erroneous glacier elevation change analysis, it is important to minimize the effects of errors due to phase jumps and low coherence over the glacier area. As a result, we prefer a branch-cut algorithm for phase unwrapping. To ensure that large glacier areas are not lost due to missing connections of separately unwrapped areas, careful evaluation and manual editing of the unwrapped interferogram is required, which makes the automation of DEM generation difficult.

(3) Precise alignment of all DEMs is inevitable for glacier elevation change calculation. We apply a modified version of the universal coregistration procedure introduced by Nuth and Kääb (2011).

(4) Glacier surface elevation differences caused by radar signal penetration into snow and ice must also be considered. This becomes even more important when data that were collected with different wavelengths are compared to each other. We analyse the impact of radar penetration due to wavelength differences by comparing height variations of C-band and X-band SRTM DEMs. The results are used to correct elevation changes estimated from comparing C-band SRTM with TDX DEMs. However, these corrections are only an approximation of the true radar penetration differences because seasonal effects, such as different snow coverage at different acquisition times, also influence the backscatter of the radar signal. These effects cannot easily be corrected for, which makes a precise estimation of the radar penetration a challenging task.

(5) The uncertainties of glacier elevation change estimates generally increase with increased data gaps of the glaciated areas. The closure of these voids should therefore preferably be done by considering additional radar data from either a different orbit or another incidence angle if the data acquisition times are not significantly different. Alternatively, elevation data from complementary optical data or other sources can be considered, but the condition of equal acquisition times is still valid. If no additional data are available, assumptions must be made regarding the glacier elevation changes in the void areas. We suggest that missing values should be derived from values of valid glacier surface areas with similar surface geometric conditions, particularly similar elevations and slope angles. If no valid data from similar areas are available, assumptions such as zero glacier elevation change in accumulation areas can be applied at the expense of significant higher uncertainties.

(6) We show that careful treatment of all of the uncertainty factors of TDX generated DEM data is required to obtain a precise, quantitative estimate of glacier elevation changes. This is especially

important when analysing intra- and inter-annual timescales. Our results show that TDX DEMs are suitable for estimating glacial elevation changes and we highlight the following key results. First, the deviations between the stable areas of all of the TDX DEMs generated here are low (max. 0.1 ± 2.15 m). Second, the TDX DEMs are internally consistent: the sums of the independently calculated glacier elevation changes from 2012/02 to 2013/03 and 2013/03 to 2013/11 differ by only 0.07 m for Northern Inylchek and 0.03 m for Southern Inylchek compared to glacier elevation changes that are calculated directly from the DEM pair from 2012/02 to 2013/11. Third, the absolute uncertainty of the glacier elevation changes is 1.13 m for the TDX DEM glacier comparisons, which is significantly lower than the 5.23 m for the comparison between the C-band SRTM and TDX DEMs. Our findings demonstrate the high potential of using single-pass TDX DEMs to monitor for glacier development in high-mountain areas. The high accuracy and spatial resolution make TDX DEMs especially suitable for investigations of highly dynamic glacier elevation changes ranging from rapid surge events to seasonal-to-decadal changes in response to global changes.

5.7 Acknowledgements

This study was supported by the Initiative and Networking Fund of the Helmholtz Association in the framework of the Helmholtz Alliance “Remote Sensing and Earth System Dynamics” (EDA). The authors thank D.H. Shangguan and T. Bolch for providing the Inylchek Glacier outline and A. Wendleder and A. Roth from the German Aerospace Center (DLR) for distributing the ICESat-corrected C-SRTM DEM. The TanDEM-X (proposal ID XTI_GLAC6883) and SRTM-X DEM data were also kindly provided by DLR. The C-SRTM DEM v4 was derived from the Consortium for Spatial Information of the Consultative Group for International Agricultural Research (CGIAR–CSI). The Landsat data were obtained from the U.S. Geological Survey.

5.8 Author Contribution

Mahdi Motagh and Julia Neelmeijer designed the study with support from Bodo Bookhagen. Julia Neelmeijer generated the TDX DEMs, adapted the DEM alignment method, determined the glacier elevation changes and prepared the manuscript. Mahdi Motagh and Bodo Bookhagen contributed to the analysis, discussion and writing.

6 Quantification of Toktogul Water-Level-Induced Ground Deformations

published as:

Julia Neelmeijer, Tilo Schöne, Robert Dill, Volker Klemann, and Mahdi Motagh (2018)
Ground Deformations around the Toktogul Reservoir, Kyrgyzstan, from Envisat ASAR and
Sentinel-1 Data – A Case Study about the Impact of Atmospheric Corrections on InSAR Time
Series. *Remote Sensing*, 10, 462, doi:10.3390/rs10030462.

This work is licensed under the Creative Commons Attribution 4.0 International License.

To view a copy of this license, visit <https://creativecommons.org/licenses/by/4.0/>.

6.1 Abstract

We present ground deformations in response to water level variations at the Toktogul Reservoir, located in Kyrgyzstan, Central Asia. Ground deformations were measured by Envisat Advanced Synthetic Aperture Radar (ASAR) and Sentinel-1 Differential Interferometric Synthetic Aperture Radar (DInSAR) imagery covering the time periods 2004 – 2009 and 2014 – 2016, respectively. The net reservoir water level, as measured by satellite radar altimetry, decreased approximately 60 m ($\sim 13.5 \text{ km}^3$) from 2004 – 2009, whereas for 2014 – 2016, the net water level increased by approximately 51 m ($\sim 11.2 \text{ km}^3$). The individual Small Baseline Subset (SBAS) interferograms were heavily influenced by atmospheric effects that needed to be minimized prior to the time series analysis. We tested several approaches including corrections based on global numerical weather model data, such as the European Centre for Medium-Range Weather Forecasts (ECMWF) operational forecast data, the ERA-5 reanalysis, and the ERA-Interim reanalysis, as well as phase-based methods, such as calculating a simple linear dependency on the elevation or the more sophisticated power-law approach. Our findings suggest that, for the high-mountain Toktogul area, the power-law correction performs the best. Envisat descending time series for the period of water recession reveal mean line-of-sight (LOS) uplift rates of 7.8 mm/yr on the northern shore of the Toktogul Reservoir close to the Toktogul city area. For the same area, Sentinel-1 ascending and descending time series consistently show a subsidence behaviour due to the replenishing of the water reservoir, which includes intra-annual LOS variations on the order of 30 mm. A decomposition of the LOS deformation rates of both Sentinel-1 orbits revealed mean vertical subsidence rates of 25 mm/yr for the common time period of March 2015 – November 2016, which is in very good agreement with the results derived from elastic modelling based on the TEA12 Earth model.

6.2 Introduction

The water levels of large artificial water reservoirs constructed for hydroelectric power generation and irrigation are prone to significant changes over the course of a year. This periodic loading of the crust causes ground deformations of the surrounding area, alters pore pressure and changes stress on underlying faults and fractures, which may ultimately induce seismicity (Simpson et al., 1988). The amount of ground deformations of a reservoir's surrounding can either be measured on individual points with levelling (Kaufmann and Amelung, 2000) or Global Navigation Satellite System (GNSS) measurements (Bevis et al., 2004; Wahr et al., 2013) or measured in a spatially continuous manner by means of Differential Synthetic Aperture Radar Interferometry (DInSAR). Thus far, in studies that are based on SAR data, either ERS-1/2 (Cavalié et al., 2007; Nof et al., 2012), Envisat Advanced Synthetic Aperture Radar (ASAR) (Zhao et al., 2016) or a combination of those sensors (Furuya and Wahr, 2005; Doin et al., 2015) were used to quantify the regional deformation around a lake. Recently, ground deformations due to the water level changes in the Tehri Reservoir in the Himalaya region was investigated with ALOS PALSAR data (Gahalaut et al., 2017).

Our aim in this study is to measure ground deformations induced by water level changes in the Toktogul Reservoir, which is located at N41.8° E72.9° in the northwest of Kyrgyzstan, Central Asia

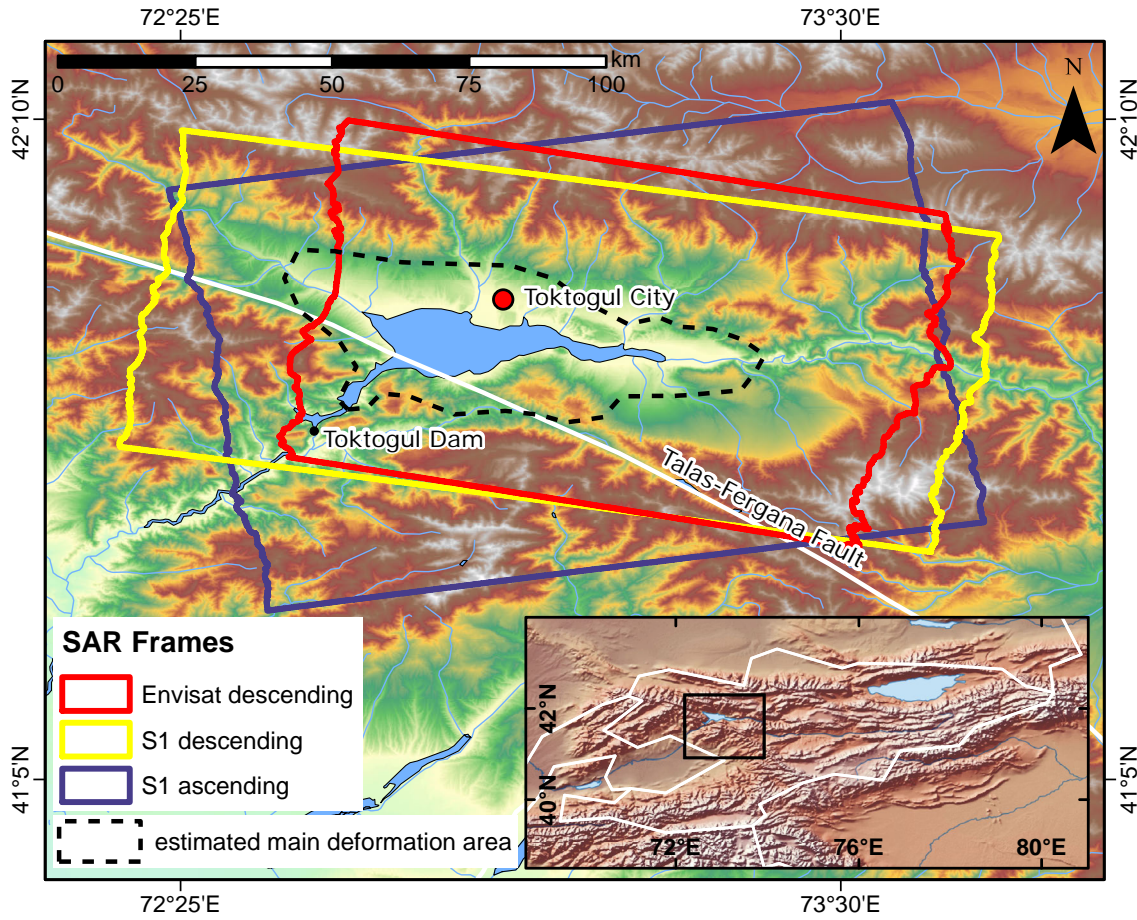


Figure 6.1: Location the Toktogul Reservoir, city and dam with the outlines of the cut SAR data frames that are used for the final analysis. The alignment of the Talas–Fergana Fault is based on vector data from the Kyrgyzstan Disaster Risk Data Platform (2017). The dashed outline denotes the estimated area of the main deformation. The inset shows the location of the area within Kyrgyzstan.

(Figure 6.1). This reservoir is fed by the Naryn River, which originates from glacial melt water of the Tien Shan mountain range. The lake is located at an elevation of approximately 870 m, and surrounding mountains reach elevations of 4300 m. It has existed since 1975, when the construction of the 214 m high and 293 m wide Toktogul Dam was completed (Simpson et al., 1981; Tibaldi et al., 2015). At high water (Figure 6.2c), the reservoir has a length of 65 km, a width of 12 km, a surface area of 284 km², and a maximum depth of 200 m (Tibaldi et al., 2015). As the water level decreases, the eastern elongated part, where the Naryn River enters the lake, goes dry (Figure 6.2b). Toktogul is the largest artificial water reservoir in the Syr Darya Basin, with a maximum capacity of 19.5 km³ (Savoskul et al., 2003). Its main purposes are power generation for the Kyrgyz population in winter time and irrigation of agricultural areas located downstream in Uzbekistan and Kazakhstan in summer time (Keith and McKinney, 1997; Savoskul et al., 2003). These activities lead to a trans-boundary water policy conflict, which resulted in an exaggerated use of water in some years that could not be compensated by the incoming amount of water until the beginning of the following winter season (Figure 6.2).

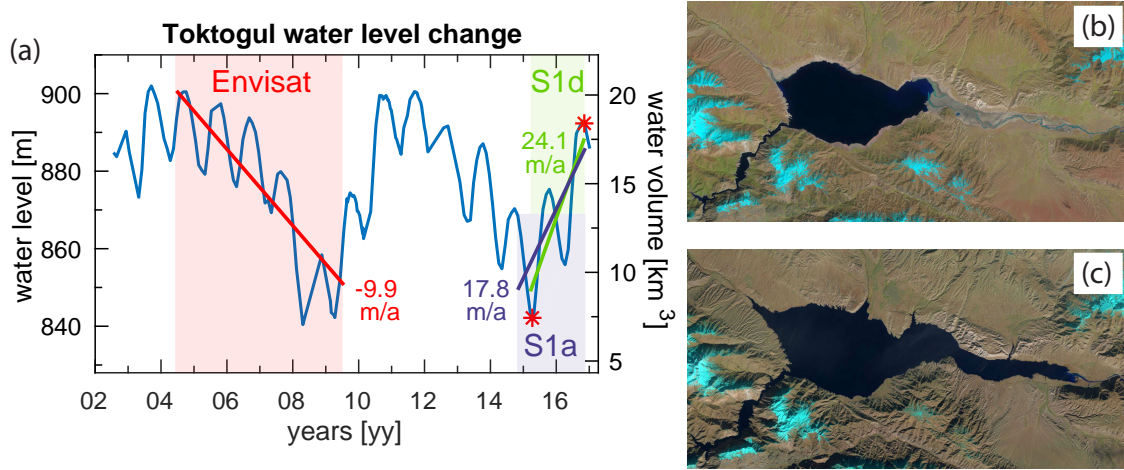


Figure 6.2: (a) Toktogul water level change between 2002 and 2016 obtained from satellite radar altimetry. Red, purple and green highlighted periods correspond to Envisat and Sentinel-1 ascending (S1a) and Sentinel-1 descending (S1d) acquisition times, respectively. The corresponding regression lines denote the average water increase per year for each of the three SAR time series (note that differences between S1a and S1d are due to different covered time periods). The red asterisks correspond to the reservoir extents at low and high water levels, which are shown by Landsat-8 images from (b) 11.04.2015 and (c) 07.11.2016, respectively.

The southwestern edge of the reservoir coincides at a length of 20 km with the Talas–Fergana Fault, an area with moderate-to-high seismicity. Larger earthquakes of magnitude M 7.6 have been reported for the Chatkal Range in 1946, 65 km west of the Toktogul Reservoir (Simpson et al., 1981), and of magnitude M_S 7.3 for the Suusamyrl Valley in 1992, 70 km northeast of the Toktogul Reservoir (Ghose et al., 1997). No major events have been recorded in the direct lake area since the construction of the dam. Seismic activity is still constantly monitored at the power station with seismometers (Dovgan, 2012), but no ground-based geodetic observations are available to assess the deformation of the surrounding area.

Consequently, we measure the ground deformations of this particular region by interferometrically analysing a time series of Envisat ASAR data for the time period 2004 – 2009, in which the net water level decreased by approximately 60 m ($\sim 13.5 \text{ km}^3$), and a time series of Sentinel-1 data for the time period 2014 – 2016, in which the net water level increased by approximately 51 m ($\sim 11.2 \text{ km}^3$) (Figure 6.2). We expect that these large load changes on the ground lead to an uplift of the surrounding area in the case of water recession and to a subsidence response in the case of water replenishing.

Sentinel-1 is the latest generation of the European Space Agency’s (ESA) SAR missions and consists of two satellites, Sentinel-1A and Sentinel-1B, that were launched in April 2014 and April 2016, respectively. Together, these C-band-based SAR satellites are able to cover most regions of the world with the interferometric wide (IW) swath mode (swath width: 250 km; spatial resolution: $5 \times 20 \text{ m}$ in range and azimuth, respectively) from the same relative orbit every twelve days, whereas Europe and some selected areas are even monitored with a temporal resolution of six days. Compared to the Envisat ASAR C-band sensor, which only acquired data every 35 days with a swath width of 56–100 km (image mode single-look complex (IMS); spatial resolution: $8 \times 4 \text{ m}$ in range and azimuth,

respectively), this mission is predestined for monitoring not only persistent linear deformations, but also intra-annual deformation changes on a large spatial scale.

Atmospheric effects in the SAR data caused by vertical stratification and turbulent water vapour variations play an important role in time series investigations (Zebker et al., 1997; Fialko, 2006; Puysségur et al., 2007; Nof et al., 2012). We therefore apply various correction approaches based on either global numerical weather models (in particular, the European Centre for Medium-Range Weather Forecasts (ECMWF) operational forecast analysis, the ERA-5 reanalysis and the ERA-Interim (ERA-I) reanalysis) or empirical models that rely on the dependency of the phase on the elevation of the terrain (in particular, the linear dependency and the power-law approach of Bekaert et al., 2015a). The time series with the best working atmospheric correction approach is then used for a comparison to the reservoir's water level variations that are extracted from satellite altimetry data. The measured ground deformation rates are further compared to the results obtained from elastic modelling of the surface deformations.

6.3 Materials and Methods

6.3.1 Lake Altimetry

At present, radar altimetry (RA) is widely used not only for monitoring global sea level changes but increasingly also for measuring the water levels of rivers and lakes for hydrology applications (Birkett, 1994; Crétaux et al., 2016; Schöne et al., 2017). Since the early 1990s, a series of RA missions have provided continuous measurements of water surface heights with 10- and 35-day repeat intervals. Novel processing technologies, such as retracking, allow the extraction of the water levels of smaller inland water bodies and reservoirs (Crétaux et al., 2016). The accuracies of the derived water levels are slightly worse compared to open ocean applications but can still reach 5 cm. For hydrological applications, the water levels can be converted into volume changes using supplementary information such as hypsometry or lake extents extracted from remote sensing data.

The water level of the Toktogul Reservoir has been measured with RA since 1995 – in particular, mostly every 35 days by the European ERS-2, Envisat and later by the Indo-French AltiKa missions. Some data are also available from the US-French Jason-1 and Jason-2 and the European CryoSat-2 missions. Using all available RA data, applying up-to-date environmental correction models and cross-checking for and applying inter-mission biases, a homogeneous time series of reservoir heights and reservoir volumes is constructed (Figure 6.2a). The internal accuracy is estimated from all high-rate measurements of one reservoir crossing (e.g., ~50 measurements for AltiKa) and is mostly within the expected 5 cm root mean square error (RMSE) range with slightly higher values for the earlier missions.

In the case of the Toktogul Reservoir, sparse historical monthly volume information of the total volume is available for the full range of water levels from CA WATER Info (2017) between 1984 and 2000, and some more recent information is made available by the reservoir operator (JSC “Electric Stations”, 2017). This allows the construction of a polynomial transfer function ($R^2=0.9998$) which can be used

for converting all water height levels into reservoir volumes. These data can then be used to verify the accuracy of the RA-derived water heights, which is approximately ± 0.3 m (Schöne et al., 2017).

6.3.2 DInSAR processing of Envisat ASAR and Sentinel-1 Data

We use Envisat ASAR IMS and Sentinel-1 IW SAR data to monitor deformations around the Toktogul Reservoir area. The Envisat data, only available in the descending orbit, were acquired between December 2003 and July 2009 and cover a time of decreasing annual water level, whereas Sentinel-1 ascending (S1a) and descending (S1d) acquisitions analysed for the time period of October 2014 until December 2016 correspond to an increasing annual water level. In the Envisat acquisition period, the highest water level measured with RA (referenced to the EIGEN-6C3 static gravity field (Förste et al., 2013)) was 900.5 m on 10 May 2004, and the lowest was 840.4 m on 22 April 2008. In the Sentinel-1 acquisition period, the lowest measured water level was 842.2 m on 24 April 2015, and the highest was 892.9 m on 29 October 2016 (Figure 6.2).

Data preprocessing is performed with the GAMMA software (Werner et al., 2000) as follows. First, for both sensors, single-look complex images are imported taking into account precise orbit ephemerides; in the case of Sentinel-1 data only, bursts covering the area of interest are concatenated. Second, images of each SAR time series are individually coregistered and cropped to the desired area of interest. Because Sentinel-1 data require a precise coregistration accuracy of a few thousands of a pixel in azimuth to prevent contamination with phase variations due to along-track differences in the Doppler centroids (Prats et al., 2010; Prats-Iraola et al., 2012), we rely on the spectral diversity method for coregistration (Scheiber and Moreira, 2000; Wegmüller et al., 2016). The outlines of the cropped SAR data frames are shown in Figure 6.1.

The single-look, coregistered SAR images are used to construct a network of interferograms by applying the Small Baseline Subset (SBAS) technique (Berardino et al., 2002) implemented in StaMPS/MTI, the Stanford Method for Persistent Scatterers and Multi-Temporal InSAR (Hooper et al., 2012). The main objective of this approach is to generate interferograms from pixels that decorrelate only slightly over short time intervals. To identify such pixels, interferograms are built from SAR acquisitions that match the criteria of having small perpendicular, temporal and Doppler baselines but with the restriction that all selected interferograms should be connected; thus, no isolated cluster is allowed in the network (Hooper, 2008). We constrain the Envisat network by a maximum spatial baseline of 500 m and a maximum temporal baseline of 2000 days, whereas at the same time, the overall coherence between two interferograms should be at least 0.4. In the Sentinel-1 case, we use constraint values of 200 m, 365 days and 0.5. In the following, the selected interferograms are treated with topography removal and geocoding, for which we rely on the 1-arc resolution Shuttle Radar Topography Mission (SRTM) digital elevation model (DEM). The results are visually inspected, and decorrelated interferograms are discarded from the network. Unwrapping of the remaining interferograms is achieved by using a 3-dimensional phase unwrapping approach (Hooper and Zebker, 2007). Displacement values in line-of-sight (LOS) are subsequently retrieved by least-squares inversion of the unwrapped interferograms with respect to a reference area selected outside of the main deformation region (N 41.6930° E 73.1660°, radius: 2 km).

By carefully investigating the residuals of the unwrapped phase of the SBAS interferograms and the inverted interferograms, we neglect scenes that introduce errors to the time series. The main error source is thus the snow coverage in winter time. After some problematic scenes are removed, we iteratively repeat the process of unwrapping, inverting and discarding until all remaining interferograms could be reliably unwrapped. A summary of the amounts of the used scenes and interferograms along with the corresponding SAR sensor specifications is presented in Table 6.1. The final network for all three SAR time series is shown in Figure 6.3.

Table 6.1: SAR data specifications and summary of the amount of images used in the final networks. The covered time period that could be reliably unwrapped is as follows for the individual time series: Envisat: 24.10.2004 – 05.07.2009, Sentinel-1, descending (desc.): 23.03.2015 – 12.11.2016, ascending (asc.): 24.10.2014 – 18.11.2016.

Satellite	Orbit	Path	Acquisition Time (UTC)	Mean Angle of Incidence	Heading Angle	Amount of Scenes	Amount of interferograms
Envisat	desc.	277	05:23	23.4°	-167.8°	22	53
Sentinel-1	desc.	5	01:13	39.7°	-170.1°	20	49
Sentinel-1	asc.	100	13:06	43.3°	9.4°	28	96

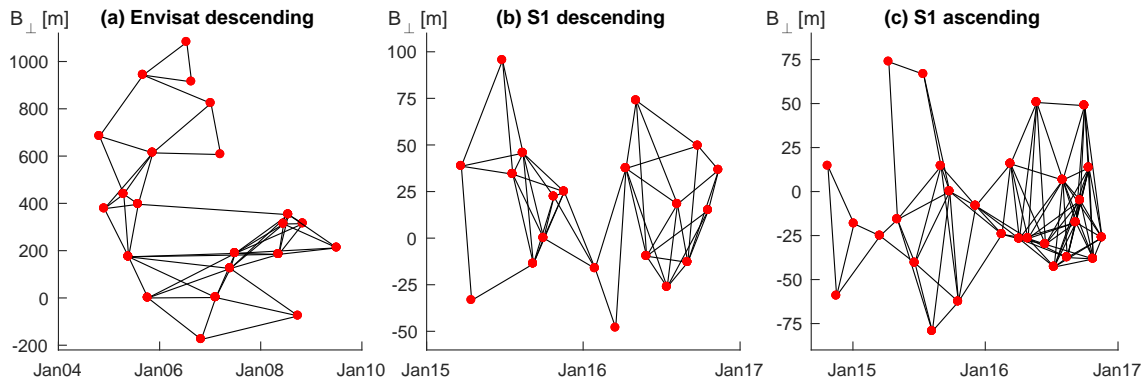


Figure 6.3: Small Baseline Subset (SBAS) networks after offending interferograms are removed for (a) Envisat descending; (b) Sentinel-1 descending and (c) Sentinel-1 ascending time series. Red dots denote the time of the image acquisitions, and black lines show the interferograms.

All interferograms remaining in the network are further treated by removing (1) individual phase ramps, (2) the overall topography error, (3) estimated atmospheric influences, and (4) the phase oscillator drift (Envisat data only) (Marinković and Larsen, 2015). From all these aspects, the most influential and simultaneously most challenging error aspect to remove is the effect of the atmosphere. Multiple approaches dealing with this issue are discussed in the following section.

6.3.3 Atmospheric Correction

Because the Toktogul Reservoir is located in a high-mountain area, atmospheric disturbances in the data are inevitable and must be corrected to avoid a misinterpretation as a loading signal. The success of atmospheric correction methods is highly dependent on the characteristics of the area of

interest in terms of topography and its dominance either in stratified tropospheric delay or dynamical local weather and turbulence (Bekaert et al., 2015b). To reduce the impact of atmospheric artifacts in the Toktogul SAR data, we apply a range of tropospheric correction methods implemented in the MATLAB-based Toolbox for Reducing Atmospheric InSAR Noise (TRAIN, version 2beta) from Bekaert et al. (2015b).

The applied techniques can be divided into two main categories: (1) global numerical weather-model-based and (2) phase-based correction methods. In theory, weather-model-based approaches should be more effective because they should be able to compensate not only for vertical stratification, but also for turbulent water vapour variations in the lower troposphere. However, previous studies have shown that the success of the exact representation of stratification and turbulence is highly dependent on the area of interest (Doin et al., 2009) and that global models, such as ERA-I, also suffer from coarse temporal and spatial resolutions (Jolivet et al., 2014). This disadvantage is now compensated for by newer available weather model data such as the ERA-5 reanalysis that are shipped with increased spatial and temporal resolutions. However, note that this type of data is not always easy to access and that it is currently only available for a limited range of time.

For comparison, we further apply phase-based corrections. These corrections have the advantage that the required external data are readily available but the disadvantage that they can only be used to treat vertical stratification, not turbulence mixtures. However, as Bekaert et al. (2015b) noted in his study, in regions where tropospheric delay is mainly correlated to topography, phase-based methods potentially outperform weather-based approaches.

We neglect spectrometer-related correction methods based on the Medium Resolution Imaging Spectrometer (MERIS) or the Moderate Resolution Imaging Spectroradiometer (MODIS) for the following reasons: MERIS data are available for Envisat data only and MODIS data are acquired between approximately 5:00 a.m. and 7:30 a.m. UTC. This differs by more than an hour from Sentinel-1 acquisition times (Table 6.1); thus, changes in atmospheric water vapour conditions may introduce more errors rather than correcting for turbulence. Furthermore, correction with spectrometer data requires daytime acquisitions under cloud-free conditions (Barnhart and Lohman, 2013), which is often not the case in high-mountain areas.

Finally, we determine the best atmospheric correction by evaluating the RMSE values of deformation in time. To avoid an influence of loading-induced deformation on the analysis, we excluded for the RMSE calculation the area of main deformation (cf. Figure 6.1) from the overall atmosphere-corrected interferograms. For comparison, we also calculate the RMSE for unwrapped results that are only corrected for the DEM error and orbital plane but not for atmosphere. The derived RMSE values are an indicator of the best-performing atmosphere removal algorithm, but note that the absolute values of different SAR frames cannot be compared because the extents of the frames differ. The Sentinel-1 ascending image, for example, covers much more high-mountain areas compared to the Sentinel-1 descending images; thus, higher error values can be expected. Furthermore, the amount and location of the SBAS-derived points within the SAR frames also vary.

Tropospheric Delays from Numerical Weather Models

Temperature, relative humidity and pressure information from numerical weather models can be used to compute the hydrostatic and wet tropospheric delay (Doin et al., 2009; Jolivet et al., 2011; Bekaert et al., 2015b). For the Toktogul case, we apply three global models based on ECMWF data: first, the ECMWF operational forecast analysis (opECMWF); second, the ERA-5 global atmospheric reanalysis; and third, the ERA-I global atmospheric reanalysis. From these models, only the ERA-I solution is currently freely accessible at a reduced spatial resolution.

The opECMWF data are expected to be the most accurate of the three models because these data are used for routine short-term predictions. These data are distributed with a temporal resolution of 6 h, a spatial resolution of 0.1° and 25 pressure levels. Since July 2017, the new ERA-5 reanalysis has been available for the time period 2010 – 2016. Similar to opECMWF, ERA-5 comes with a high spatial resolution of 0.1° but has an increased temporal resolution of 1 h. Upper-air information is delivered at 37 pressure levels. The available ERA-5 data currently do not cover the Envisat acquisition time period. We therefore also consider the former ERA-I reanalysis that is available for the time period from 1979 to present. This reanalysis is also delivered with a temporal resolution of 6 h and contains 37 pressure levels, but it has a coarse spatial resolution of 0.75° (Dee et al., 2011).

To compare the influence of the temporal resolution, we apply two versions of the ERA-5 data: the hourly reanalysis and an artificially reduced version with a 6 h temporal resolution, similar to the ERA-I data. An overview of the model specifications is presented in Table 6.2.

Table 6.2: Parameters of the applied numerical weather-model-based atmosphere corrections.

Model	Spatial Resolution	Temporal Resolution	Pressure Levels
opECMWF	0.1°	6 h	25
ERA-5 1 h	0.1°	1 h	37
ERA-5 6 h	0.1°	6 h	37
ERA-I	0.75°	6 h	37

Phase-Based Tropospheric Delays

The Toktogul Reservoir is surrounded by high-mountain ranges, which influence the moisture content of the troposphere, which consequently has an impact on the phase delay of the radar signal. It is therefore straightforward to apply correction methods such as the power-law and linear tropospheric approaches that use the correlation of the phase signal with the topography.

The linear tropospheric correction assumes a uniform troposphere that is directly correlated to the elevation of the terrain. In principle, a linear relationship between phase delay and terrain height is estimated and subtracted from the entire interferogram. To prevent real tectonic signals from being taken into account during the linear dependency analysis, we exclude the estimated deformation area around the Toktogul Reservoir from the calculation (cf. Figure 6.1).

The power-law correction technique (Bekaert et al., 2015a) is more sophisticated than the linear approach, as it considers a spatially varying troposphere within an interferogram. The method assumes a non-varying delay at the relative top of the troposphere and then applies a power-law function on the phase delay variations depending on elevation. It thus considers phase delays mainly due to hydrostatic and wet components of the refractivity. Delays due to the liquid component and the influence of the ionosphere on C-band SAR data are neglected because their influence is assumed to be small (Bekaert et al., 2015a).

First approximations of the tropospheric delays that are used as coefficients for the power-law method can be calculated from balloon sounding data as distributed by the University of Wyoming (Bekaert et al., 2015a). We extract data for the Envisat and Sentinel-1 acquisition periods from the Taraz station (station no. 38341 at N 42.85° E 71.38°), which is located approximately 170 km north-west of Toktogul. We constrain the upper troposphere height to 10 km and extract a corresponding mean power-law decay coefficient of 1.51 ± 0.01 from the sounding data, which we use for all three InSAR time series.

The estimation of the spatially varying relation between topography and tropospheric phase is based on the assumption that the tropospheric signal is present in all wavelength scales. Tropospheric effects should thus be removed from the interferogram by band-filtering the signal, choosing a band for filtering that is insensitive to other signals such as turbulent troposphere, orbital errors and deformation. Furthermore, spatial variability of the phase delay is provided by dividing the area into multiple smaller windows, in which the coefficient describing the relation between topography and tropospheric phase is calculated locally (Bekaert et al., 2015b,a).

In the Toktogul case, we have a pronounced topography around the reservoir, allowing us to set the window size to be comparatively small. Empirical tests show that, for the SAR time series, the following window sizes work best (window overlap: 50%): Sentinel-1, descending: 77×59 km; Sentinel-1, ascending: 68×78 km; and Envisat: 60×62 km. The relationship between topography and phase delay is computed for the following filtering band ranges: 2–4, 2–8, 2–16, 4–8, 4–16, 4–32, 8–16, 8–32, 8–64, 16–32, 16–64, 32–64, 32–128, and 64–128 km.

6.3.4 Deformation Decomposition of Sentinel-1 Data

Because Sentinel-1 data are available from two different orbits, it is possible to decompose the deformation into a vertical part and a horizontal part. However, because there are only two observations available, we cannot directly compute the 3D vector components. We thus neglect potential displacements in the north-south direction, for which LOS measurements are the least sensitive in any case due to the near polar orbit of the spacecraft.

The average S1d and S1a LOS displacement points are interpolated to 200×200 m grids, which are used as input for the deformation decomposition. Furthermore, we ensure that only results covering the same time period (March 2015 – November 2016) are considered for the decomposition. The mean LOS displacements of the ascending (d_a) and descending (d_d) orbits are then used to discriminate

between vertical d_v and east-west d_e displacements by solving the following equation (Fialko et al., 2001; Motagh et al., 2017):

$$\begin{pmatrix} d_a \\ d_d \end{pmatrix} = \begin{pmatrix} \cos \theta_a & -\cos \alpha_a \sin \theta_a \\ \cos \theta_d & -\cos \alpha_d \sin \theta_d \end{pmatrix} \begin{pmatrix} d_v \\ d_e \end{pmatrix}, \quad (6.1)$$

where θ_a and θ_d represent the incidence angles and α_a and α_d are the heading angles of Sentinel-1's ascending and descending orbits, respectively.

6.3.5 Modelling of Elastic Surface Deformations

Considering surface deformations induced by short periodic mass variations, such as intra-annual water level changes, the purely elastic, instantaneous response of the Earth is an adequate approximation. In a spherical harmonic representation, the coefficients of the vertical and horizontal deformations and the geoid changes can be related linearly to the surface mass load through degree-dependent load Love numbers. Farrell (1972) outlines the calculation of properly weighted sums of the load Love numbers for a given Earth model to form Green's functions that provide the distance-dependent elastic response of the Earth model due to a unit point mass. Assigning the point mass response to any extended mass distribution by means of a convolution integral over the loaded region leads to the global displacement field. Because the convolution occurs in the spatial domain, the Green's function approach is particularly useful if the spherical harmonic representation of the surface mass load is dominated by high-degree coefficients, such as in our case of the highly heterogeneous distribution of non-loaded and loaded regions around the Toktogul lake.

Rather than using one globally defined Green's function for a customary idealization of the Earth by a model composed of spherically symmetric layers, we calculated geographically dependent local Green's functions (Dill et al., 2015) that are valid especially for the crustal structure beneath the Toktogul region. For small-scale heterogeneous mass loads, the geological structure of the shallow crust becomes the most important; thus, we replaced the outermost 71 km of the 1D PREM Earth model (Dziewonski and Anderson, 1981) by the lateral variability given in the crustal model TEA12 provided by Tesauro et al. (2012). The deformation response depends mainly on the lithology of the upper and lower crystalline crustal layers (granite, mafic granite, diabase, diorite, and olivine), their thicknesses, and the varying thickness of the overlaying sediments. The changes in the crustal properties from PREM to TEA12 affect the near-field values of the local Green's functions for distances to the load lower than 100 km.

To simulate elastic Earth surface deformations, the local Green's function model was applied to the water storage variations composed from the Toktogul lake level changes as observed by satellite RA (Figure 6.2a), in combination with the changes of the lake surface area given by Landsat-8 images (Figure 6.2b,c). Finally, the trend in the modelled surface deformation was calculated for the same period as for the Sentinel-1 descending acquisition time S1d.

6.4 Results

A first general result of our study is that Sentinel-1 products are superior to Envisat results in the following aspects: (1) the wide swath of the Sentinel-1 sensor allows more freedom in cutting the scenes to the desired area of interest; hence, we capture the western region of the reservoir better with the Sentinel-1 time series than with the Envisat ones; (2) due to the higher temporal acquisition sampling, Sentinel-1 interferograms are affected less by decorrelation, which leads to a higher point density than in the Envisat time series. This again results in a better area coverage that can be taken into account for the deformation analysis; (3) since the orbital tube of Sentinel-1 is very narrow, the length of the spatial baseline between two images is a no critical rejection criterion, which ultimately leads again to a denser network of interferograms. In the following, we will provide more details regarding the improvement of the results due to different atmospheric corrections and then regarding the ground deformation correlated to water level changes. Furthermore, we provide a comparison of Sentinel-1-derived vertical ground deformation to elastic modelling results.

6.4.1 Atmospheric Corrections

First, we analyse the RMSE values of the individual power-law results, where we had applied different filter bands. It appears that, in the Toktogul case, small- to medium-scale bands generally perform better than longer ones (Table 6.3), but the results are not consistent among the three different SAR time series, which may again be explained by the different SAR frame extents. In the case of the Envisat descending time series, the lowest RMSE value of 8.0 mm is achieved with the 8–64 km filter band; in the case of S1d, the lowest RMSE value is 7.0 mm, derived by applying filter bands for a range of 4–32 km and 8–64 km; and in the case of S1a, the lowest RMSE of 10.6 mm is found for filter bands of 2–8 km and 4–8 km range. In the following sections, whenever the results of the power-law correction method are mentioned, we are referring to the results from the best-performing filter band.

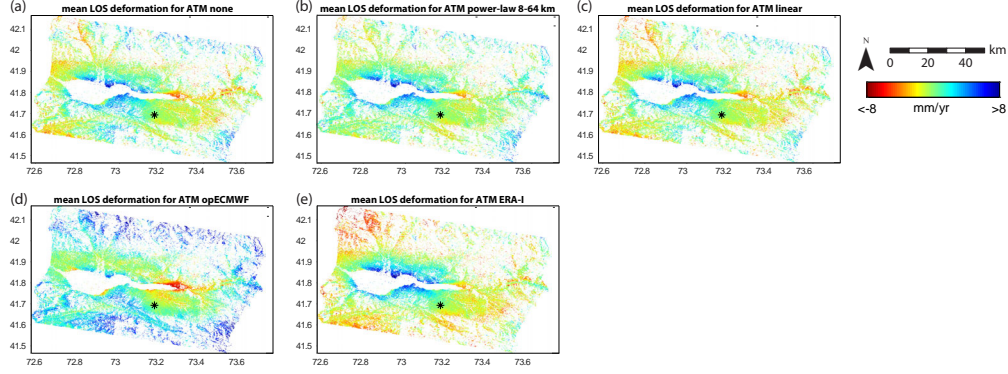
Table 6.3: Root mean square errors for different power-law filtering bands. The best results are highlighted in bold. The area of main deformation (cf. Figure 6.1) is excluded from this estimation.

Band [km]:	2–4	2–8	2–16	4–8	4–16	4–32	8–16	8–32	8–64	16–32	16–64	32–64	32–128	64–128
Envisat RMSE [mm]:	8.5	8.2	8.1	8.3	8.1	8.2	8.2	8.1	8.0	9.0	8.1	8.2	8.2	9.3
S1d RMSE [mm]:	7.1	7.3	7.3	7.2	7.2	7.0	7.5	7.1	7.0	7.5	7.3	7.6	7.2	7.6
S1a RMSE [mm]:	10.7	10.6	10.8	10.6	10.8	10.8	10.9	10.9	11.1	11.1	11.2	11.4	11.2	11.6

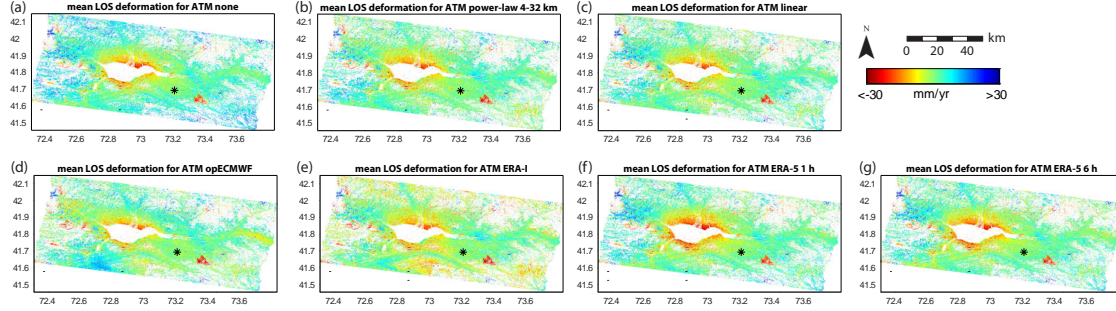
We now compare the RMSE values of the different correction techniques to determine the best atmospheric correction solution. The results show that although phase-based methods are not able to represent turbulence mixtures, their correction performs superior to the weather-model-based methods for all three SAR time series, which in all cases yield even higher RMSE values compared to the non-atmosphere-corrected time series (Table 6.4). This is also true for the ERA-5 1h solution with the highest temporal and spatial resolutions, which surprisingly does not lead to any improvement compared to the other numerical weather-based approaches.

Among the phase-based corrections, the power-law method performs better than the linear one, although differences are small or (in the case of Envisat) even non-existent (Figure 6.4). This behaviour

(1) Envisat descending



(2) Sentinel-1 descending



(3) Sentinel-1 ascending

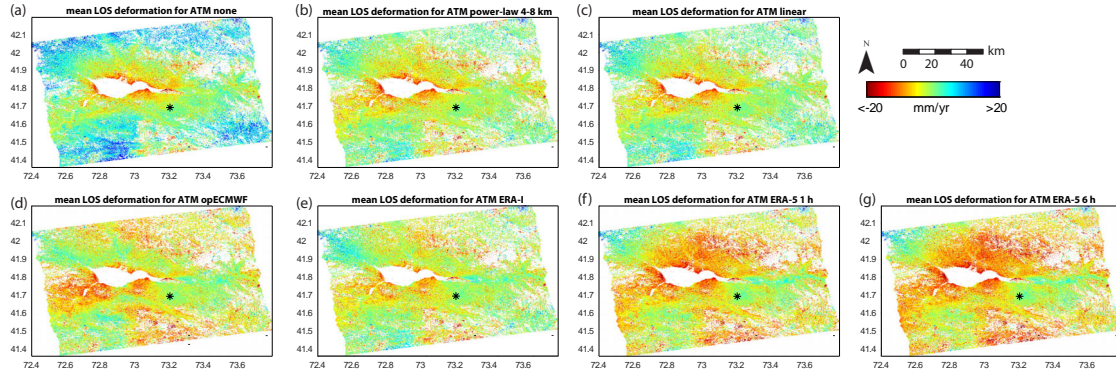


Figure 6.4: Mean line-of-sight (LOS) deformation values for various atmospheric corrections of the (1) Envisat descending; (2) Sentinel-1 descending and (3) Sentinel-1 ascending time series. (a) no atmospheric correction applied; (b) best results of the power-law technique; (c) linear dependency on the topography; (d) correction with the operational weather model (opECMWF) analysis; (e) ERA-I weather model correction; (f) the ERA-5 1 h temporal resolution solution and (g) the ERA-5 6 h temporal resolution solution. The black asterisks show the location of the reference point.

Table 6.4: Root mean square errors for different atmospheric correction techniques. ERA-5 data cover only the Sentinel-1 acquisition period and thus cannot be used for improving the Envisat time series. The best results are highlighted in bold. The area of main deformation (cf. Figure 6.1) is excluded from this estimation.

Atmospheric Correction:	None	Best Power-Law	Linear	opECMWF	ERA-I	ERA-5 1 h	ERA-5 6 h
Envisat RMSE [mm]:	8.8	8.0	8.0	13.1	11.5	-	-
S1d RMSE [mm]:	9.9	7.0	7.5	10.1	10.7	12.0	11.3
S1a RMSE [mm]:	12.6	10.6	11.0	12.9	13.4	13.8	14.0

is expected because the power-law method is able to adapt to the variation of the vertical stratification and calculates individual corrections for windows smaller than the entire interferogram, whereas linear correction works on the entire image only. At the end, the best filter bands of the power-law technique improve the RMSE of Envisat by 9% from 8.8 mm to 8.0 mm, of S1d by 29% from 9.9 mm to 7.0 mm and of S1a by 16% from 12.6 mm to 10.6 mm.

Analysing the performance of different atmospheric correction methods in time (Figure 6.5) reveals that most variances appear in summer time and that winter acquisitions are much less affected. Furthermore, in the S1a time series, ground deformation variations due to different applied atmospheric correction approaches are significantly higher than in S1d or Envisat time series.

6.4.2 Ground Deformation

The ground deformation pattern is discussed on the basis of the average Envisat, S1d and S1a power-law-corrected deformation maps (Figure 6.6 – note that the red triangle area at the southeastern corner of the S1d time series shows an unwrapping artifact that we did not correct for because it is located far from the reservoir area and thus did not hamper our analysis). We additionally show the correlation of the water level data to the corresponding deformation data for four selected points (Figure 6.7). For these examples, the water level amplitudes are fitted to the power-law-corrected SAR time series to highlight the amount of their correlation. Note that we do not correct for any potential time lag between water level change and deformation during this fit and that differences between the overall ascending and descending Sentinel-1 LOS deformations are mainly due to the different time period coverages.

From the spatial perspective, all three mean deformation maps reveal a significant LOS deformation of the bedrock areas around the entire Toktogul Reservoir, whereas the strongest deformations are found north of the lake close to the Toktogul city area (point P1). In the time of water recession (Envisat time series), we observe for P1 LOS uplift rates of 7.8 mm/yr, which converts to 0.78 mm per one metre of water level loss. The reverse behaviour of subsidence is monitored for the time of water filling (Sentinel-1 time series). Here, the mean LOS values are on the order of -19.8 mm/yr (-0.82 mm per 1 m water level increase) and -11 mm/yr (-0.62 mm per 1 m water level increase) in the case of S1d and S1a, respectively. The intra-annual time series (Figure 6.7) for point P1 shows that the correlation between LOS deformation and water fit are higher for the Envisat ($R^2=0.85$) and S1d ($R^2=0.88$) time series compared to the S1a ($R^2=0.62$) time series. From the Sentinel-1 data, it is

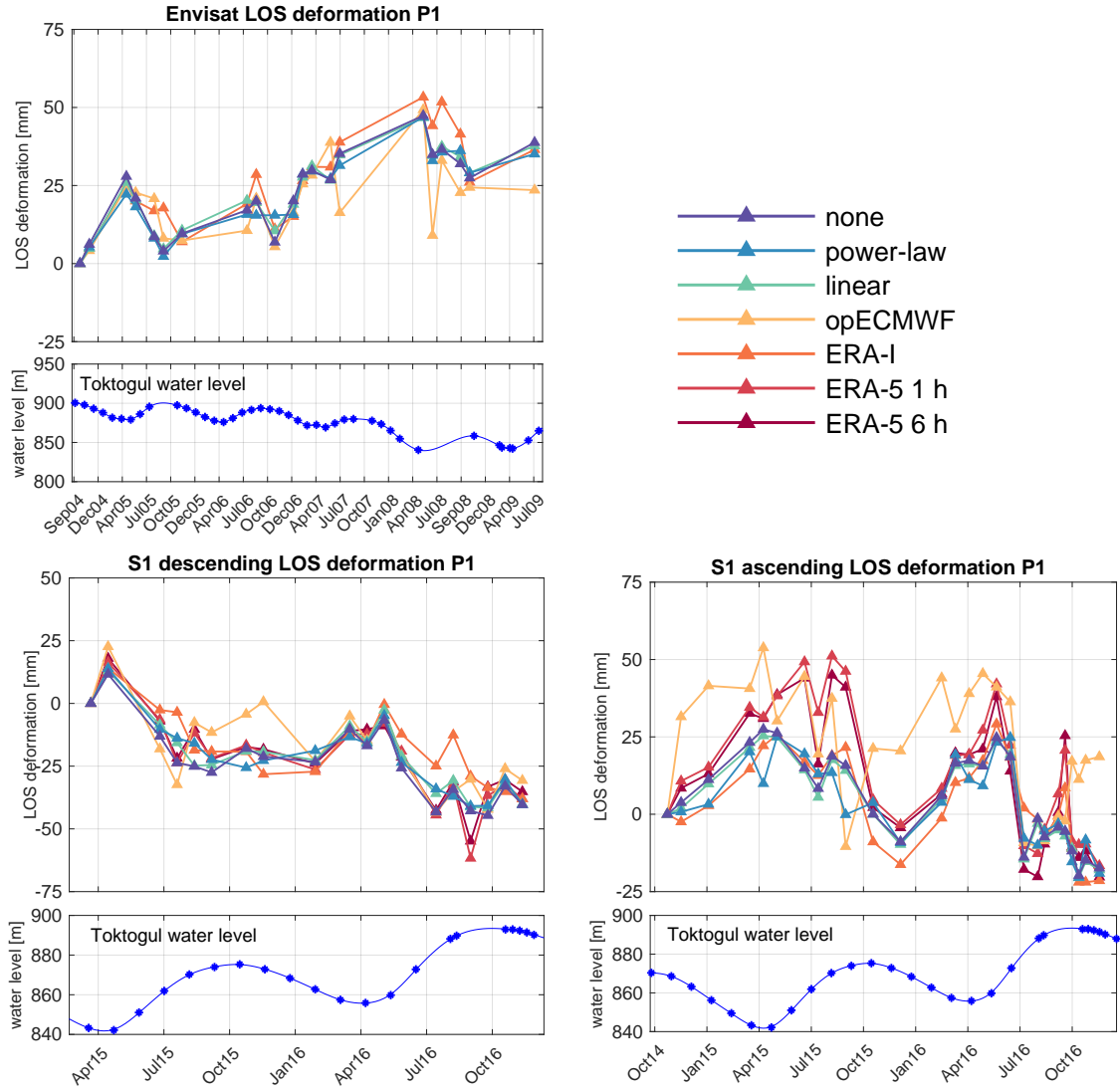


Figure 6.5: Variances of the LOS deformation in time for all applied atmospheric corrections. The location of the exemplary point P1 is shown in Figure 6.6. For better visualization, deformation markers have been connected with lines, although that does not imply that we expect linear deformation in between.

clear that intra-annual LOS deformation changes appear simultaneously with the water level changes, which indicates an elastic response of the surface. At location P1, these intra-annual LOS deformation variations are on the order of 30 mm and more.

The same deformation process but with decreased rates and lower correlation rates are found west of the Talas–Fergana Fault (point P2). LOS values (and water level fit correlation rates) are on the order of 3.8 mm/yr ($R^2=0.52$), -10.4 mm/yr ($R^2=0.51$), and -9.7 mm/yr ($R^2=0.54$) for Envisat, S1d and S1a, respectively, which convert to 0.38 mm, -0.43 mm and -0.54 mm per 1 m water level change.

Very intriguing are the results of a small area close to the reservoir (point P3) that do not show a distinct correlation to any water level changes. In all three SAR data time series, we find no significant deformation rates (LOS values are on the order of 0.1 mm/yr, -0.5 mm/yr and -0.1 mm/yr for Envisat,

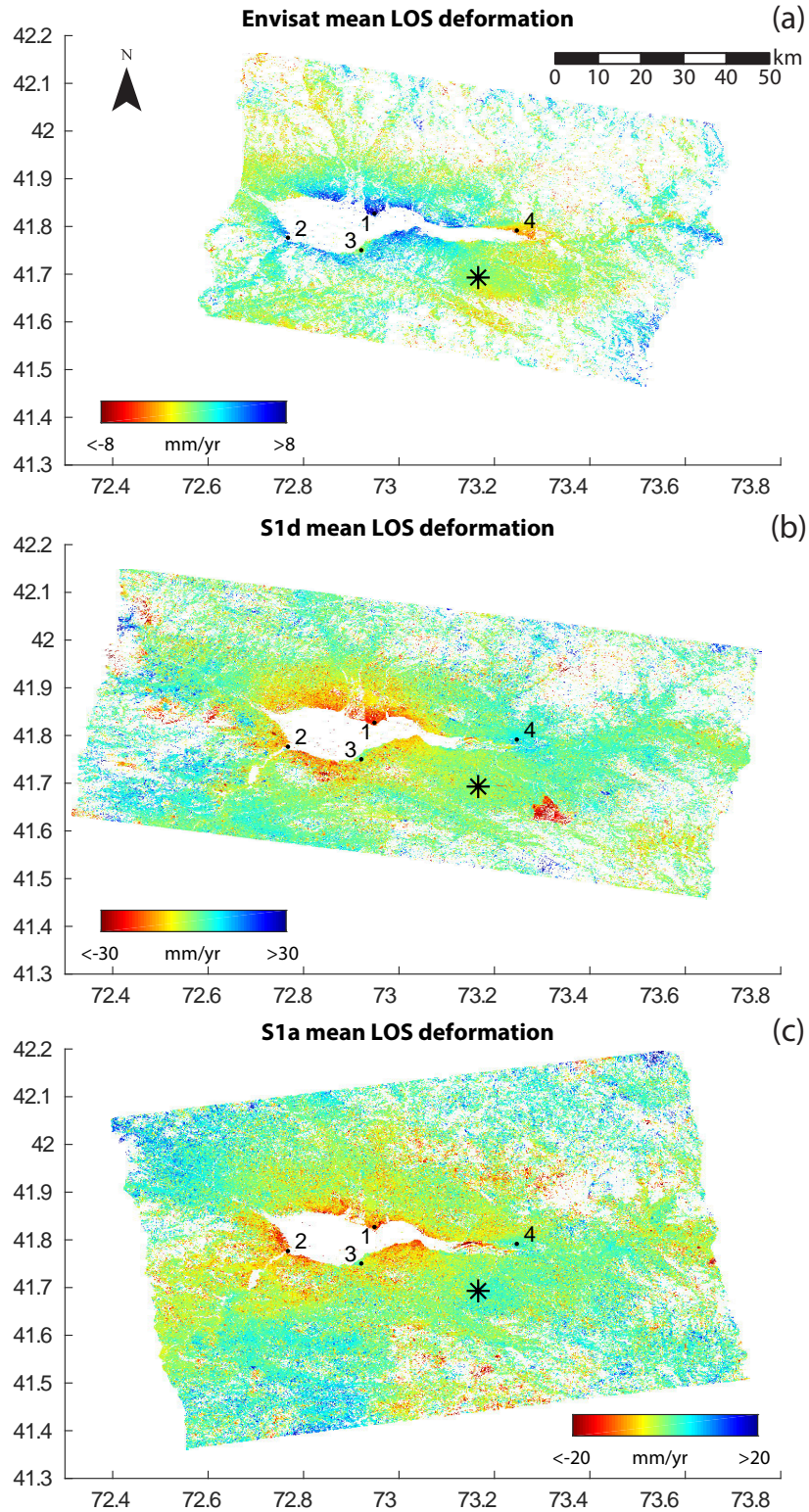


Figure 6.6: Power-law-corrected mean LOS deformation maps for (a) Envisat; (b) S1d and (c) S1a SAR time series. Points 1–4 show the locations of the deformation time series shown in Figure 6.7, and the black asterisk denotes the reference point used in the time series. The red triangle area in the southeast corner of the S1d time series shows an unwrapping artifact that we did not correct for.

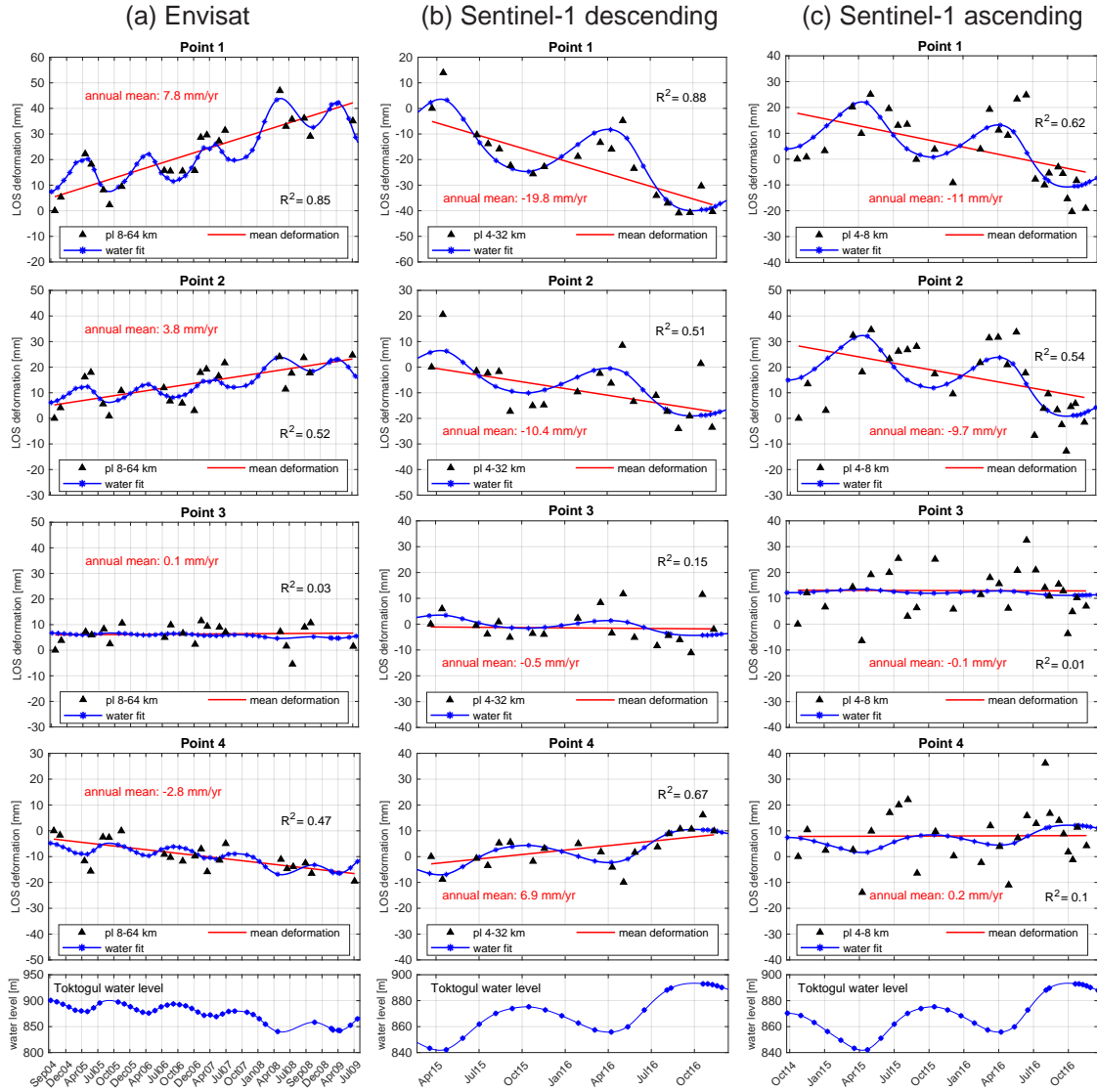


Figure 6.7: (a) Envisat; (b) S1d and (c) S1a power-law-corrected LOS deformation in time (black triangles) for points 1–4 as in Figure 6.6. The red lines indicate the annual mean LOS deformation for the investigated time period. The blue lines in the bottom diagrams show the true Toktogul water level change, whereas the blue lines in the point figures represent the best fit of this water level to the shown deformation.

S1d and S1a, respectively), and intra-annual water level fit correlation rates (R^2) are consistently below 0.2.

In the eastern region, at the entrance of the Naryn River (point P4), we observe contradictory but clearly intra-annual correlated deformation rates compared to points P1 and P2. Here, we find mean LOS subsidence rates of -2.8 mm/yr (-0.28 mm per 1 m water level change and $R^2=0.47$) during the water recession phase captured by Envisat data and mean LOS uplift rates of 6.9 mm/yr (0.29 mm per 1 m water level change and $R^2=0.67$) in the S1d time series that covers a water replenishing phase. Compared to S1d, S1a LOS deformation is less explicit and also only yields a low water level fit correlation value of $R^2=0.1$.

The availability of ascending and descending data in the Sentinel-1 case allows a decomposition of the mean deformation data in the vertical and east-west directions (Figure 6.8) that can be compared to vertical deformation rates obtained from elastic modelling. For the purpose of decomposition, we truncated the ascending SAR time series to fit the time period of the descending SAR time series. Overall, the long-wave spatial pattern of the Sentinel-1-derived vertical deformation around the reservoir correlates very well with the trend in the vertical displacement for the same time interval as calculated by the elastic response of the Earth model due to water load changes (Figure 6.8a,c,d). In the case of the horizontal deformation, S1 measurements yield only noise but no definite deformation in one direction or the other (Figure 6.8b).

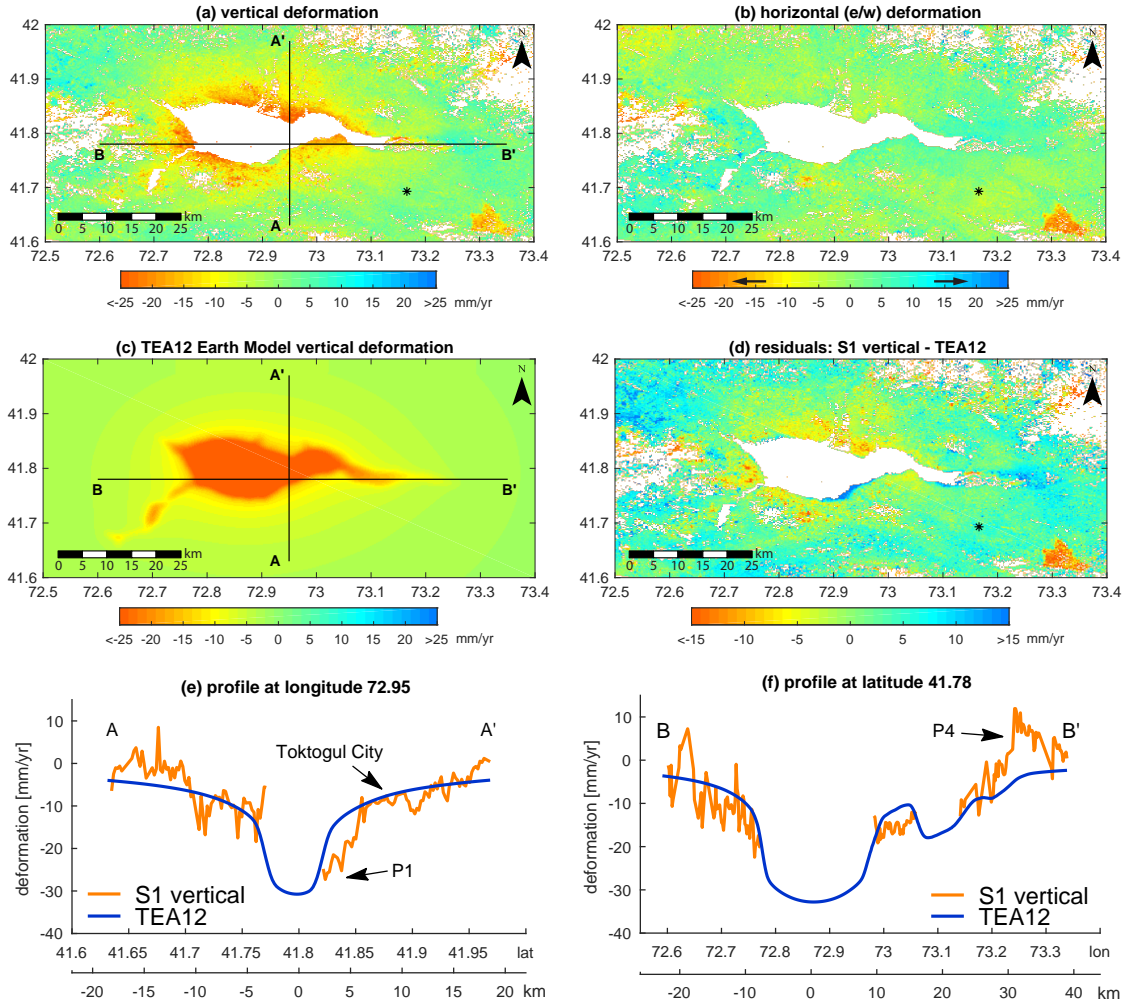


Figure 6.8: (a) vertical and (b) horizontal (east/west) components of the decomposed Sentinel-1 ascending and descending LOS deformations for the time period March 2015 – November 2016. Input data for the decomposition are the power-law-corrected mean LOS deformation maps; (c) vertical deformation from elastic modelling with the TEA12 Earth model; and (d) residuals from Sentinel-1 minus modelled vertical deformation. Negative values in the vertical case refer to subsidence, and blue values refer to uplift. In the horizontal case, positive values denote a motion towards the east, and negative values denote a motion towards the west. The black asterisk shows the location of the reference point. Measured and modelled vertical deformation rates for profiles $\overline{AA'}$ and $\overline{BB'}$ are given in (e), (f), respectively.

Two perpendicular profiles further illustrate how well the measured and modelled data fit together and up to which distance the area is deforming. The 2 km closest to the reservoir are affected the most by subsidence rates of approximately -25 mm/yr (-1.07 mm per 1 m water level increase) (Figure 6.8e). The Toktogul city area is affected less by approximately -10 mm/yr (-0.41 mm per 1 m per 1 m water level increase). Non-affected areas are only found at a distance of approximately 15 km away from the reservoir shoreline. The comparison to modelled data also clearly outlines the anomaly of the measured uplift signal at point P4 (Figure 6.8f).

6.5 Discussion

Our study shows that DInSAR remote-sensing-derived displacements that were properly corrected for atmospheric effects can explain loading-induced ground deformations at the Toktogul Reservoir. The very good agreement of Sentinel-1 decomposed results to predictions of an elastic surface deformation model based on TEA12 proves that the derived LOS deformations can be mainly attributed to vertical displacements. In the following, we will discuss the artifacts remaining after atmospheric corrections and provide reasons for the observed variances of the ground deformations.

6.5.1 Atmospheric Corrections

It is often argued that the occurrence of atmospheric turbulences is random and thus cancel each other out when calculating the average LOS deformation (Zebker et al., 1997; Fialko, 2006; Puysségur et al., 2007). However, we observe that artifacts remaining after the atmospheric correction that we mainly attribute to non-corrected turbulence do have an influence on the averaged LOS deformations in our case (Figure 6.4). Doin et al. (2009) argue that the sign and amplitude of stratified tropospheric delay in high-mountain areas do not appear randomized. It is thus likely that non-corrected vertical stratification leaks into the results, leading to the observed differences and also to significant alterations in the LOS time series (Figure 6.5). These alterations appear mainly in the summer months, which can be related to increased water vapour content in the atmosphere compared to winter time. Furthermore, in summer, high evaporation rates originating from the lake surface also contribute to SAR signal delays.

The low performance of the weather-model-driven corrections may be explained by several reasons. First, the Toktogul Reservoir is located in a valley that is surrounded by high mountains, which leads to micro-climate artefacts that are not well captured by global numerical models. Second, within the region of Central Asia, in situ weather stations used to constrain the models are sparse; thus, the accuracy of the model predictions might not be comparable to a region such as Europe, where significantly more in situ data are available (Haiden et al., 2015). Third, especially in high-mountain areas, weather conditions are prone to rapid changes; hence, even a 1-h temporal resolution of a weather model might not be sufficient to represent the atmospheric conditions at the SAR acquisition time. Fourth, an increase in RMSE values after weather-model-based corrections was also found by Bekaert et al. (2015b), who attributed this to the incorrect estimation of the location of turbulence in the weather models.

6.5.2 Ground Deformation

The area with the highest deformation rates is north of the lake at P1, which is reasonable because it is located closest to the lake centre and its shoreline is rather flat (Figure 6.9a). Here, the two short time series of Sentinel-1 show a clear intra-annual correlation to the water level changes. Although the R^2 is also high in the Envisat case, intra-annual variations are less obvious due to the much lower temporal sampling. The area in the west (P2), close to the Talas–Fergana Fault, is also prone to the same intra-annual deformation, but at lower rates. Here, the slopes of the high mountains are much steeper than at P1 and even reach the shoreline (Figure 6.9b).

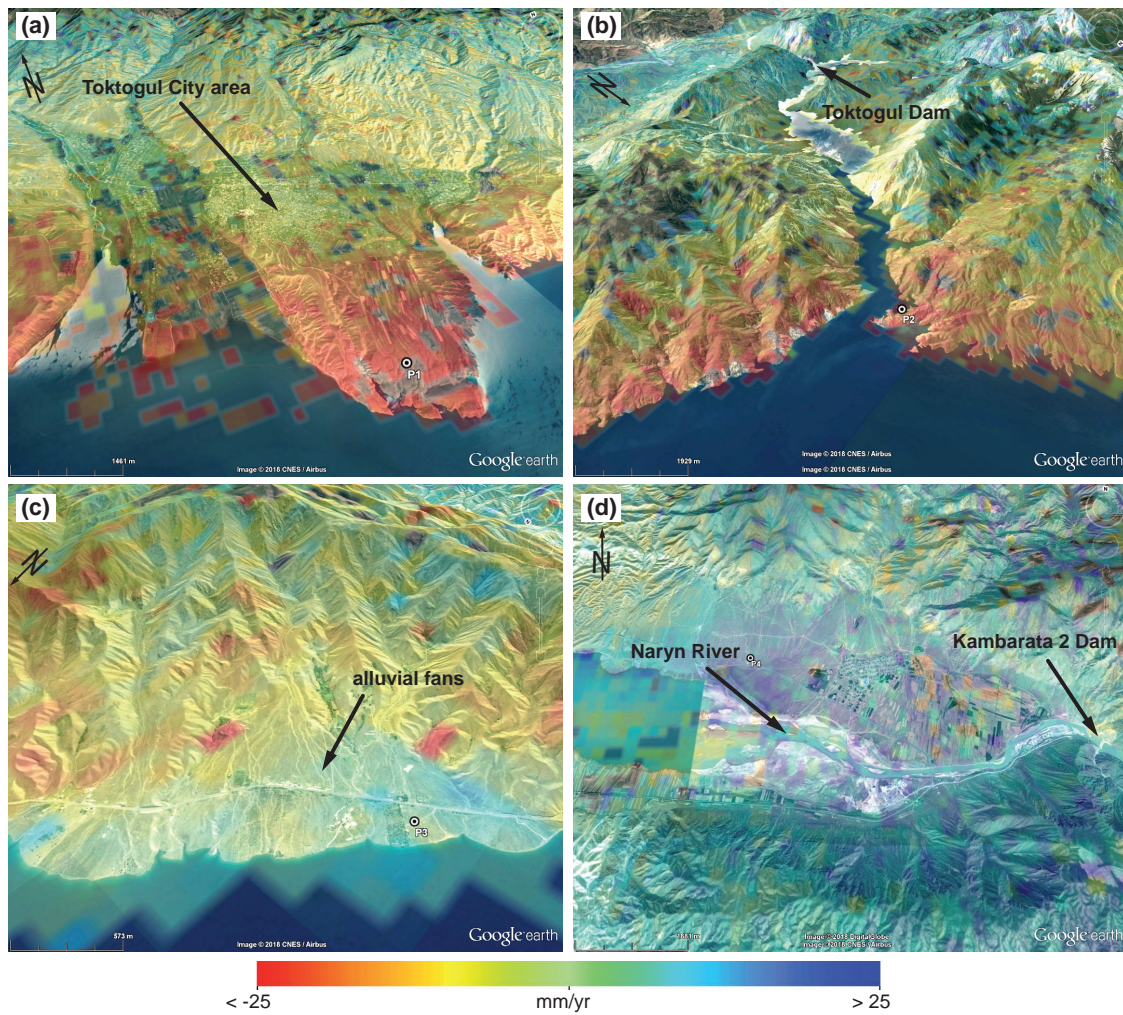


Figure 6.9: Vertical deformation extracted from Sentinel-1 decomposition around (a) point P1 and the Toktogul city area; (b) point P2; (c) alluvial fans at point P3 and (d) the Naryn River entrance area at point P4. For the locations of the points, refer to Figure 6.6. Background imagery provided by Google® Earth.

Anomalies in the overall deformation pattern are found at P3 and P4. As these are stringent in all time series, it is straightforward to assume that they are induced by local characteristics of the ground and not due to remaining atmospheric effects, artificial changes of landcover such as construction

work or the influence of the Kambarata–2 hydropower plant, which is located east of the Naryn River entrance (Figure 6.9d) and only started operating in 2010 (Havenith et al., 2015).

For P3, where no deformation could be measured, an overlay on DEM and optical remote sensing data reveals that this area is characterized by alluvial fans that are rather flat and consist of fluvial sediments (Figure 6.9c). The inverse deformation at P4 is also located in a rather flat and sedimentary area at the entrance of the Naryn River (Figure 6.9d). We believe that, in both areas, the height change in ground water level is the main source for the observed deformation pattern. At times of high reservoir water level, the ground water level in the sedimentary areas at P3 and P4 will also be higher compared to times at low reservoir water level. The increased amount of ground water and soil moisture prevents the SAR signal from penetrating as deep into the ground as in the case of dry material. This effect leads to a measured “uplift” signal at P4 in the Sentinel–1 time series, although the area is rather subsiding (cf. the model results in Figure 6.8c). However, because the area at P4 is very shallow and thus affected by only a small amount of load change, the reduced signal penetration into the ground is dominating. Conversely, we observe a “subsidence” signal in the Envisat time series because the ground water level is becoming lower here. In the case of P3, however, the area is located much more closely to the lake centre; thus, it is likely here that both effects, loading/unloading and radar penetration changes, are compensating each other, leading to the observed “non-deformation”. The hypothesis that the same process is affecting the deformation measurements at both locations is further underlined by the fact that residuals between measured and modelled deformations are on the same order at P3 and P4 (Figure 6.8d).

Another process that has the same contradictory effect is the compaction of the sediments at times of lower ground water levels and soil swelling at times of higher ground water levels. The related deformation might also contribute to the observed signals, but presumably at a much lower rate.

Compared to Envisat and S1d, a significantly lower correlation between LOS deformation and water level fit is found for the S1a time series. This result indicates that the atmospheric correction was rather poor for the S1a data. We relate this to increased lake evaporation rates that locally increase the moisture content in the low-level atmosphere since S1a data were acquired during local evening hours (UTC+6 h). In comparison, Envisat and S1d images were captured at noon and during morning hours, respectively. The relation to evaporation is further indicated by the fact that LOS deformation rates with the highest offsets from the water level fit can be found in summer time (Figure 6.7c). We view this mismatch of atmospheric correction also as the main driver for why we do not observe a clear uplift signal at P4 in the S1a time series. In principle, this can be overcome by an extension of the time series, although here it is not likely that the water level will increase much in the upcoming year because the reservoir is already at full capacity.

6.6 Conclusions

We have investigated the suitability of Sentinel–1 and Envisat SAR data for capturing surface loading effects due to water level changes in the Toktogul Reservoir. Since the study area is situated in a high-mountain terrain, the SAR acquisitions are severely affected by atmospheric noise that had to be removed prior to the deformation analysis. In our study, we have tested a global numerical

weather model and phase-based removal approaches and found that, for the Toktogul area, the power-law method of Bekaert et al. (2015a) performed the best. However, the S1a evening acquisitions in summer time were significantly influenced by remaining atmospheric effects that we relate to non-corrected lake evaporation. We thus recommend for similar studies to either focus on morning or noon acquisitions or to make an effort to reduce the impact of such remaining effects.

Although only two years of Sentinel-1 data (2014 – 2016) were used, we found a strong correlation between the increase in the water level and the subsidence of the surrounding region. Areas north of the lake and within a range of 2 km to the shore were affected the most (25 mm/yr, which corresponds to a deformation rate of -1.07 mm per 1 m water level change), but measurable deformations occurred as far as 15 km away from the shore. Due to the dense acquisition interval, we were also able to retrieve intra-annual LOS deformation variations on the order of 30 mm. The analysis of intra-annual time series and water level change further revealed that ground deformations occurred simultaneously with water level changes, which indicated an elastic deformation response. We therefore estimated ground deformation rates with an elastic forward model that was based on the TEA12 Earth model. The results showed that the modelled ground deformation rates fit very well with our Sentinel-1 measured vertical deformations.

The SAR time series from Envisat was considerably longer (2004 – 2009). This time period was characterized by an overall release of the Toktogul Reservoir water; hence, we retrieved a corresponding inter-annual uplift deformation of the area. However, clearly correlated intra-annual changes were not extracted, which was related to the less temporal density of SAR acquisitions.

In terms of the Toktogul case study, our estimations of the dimension and spatial extent of deformation can contribute to seismic hazard prediction maps as presented by Abdrakhmatov et al. (2003) or Bindi et al. (2012). The Talas–Fergana Fault to the southwest of the reservoir is a potential trigger for earthquakes. Such an event is especially dangerous if it induces a landslide as in the M_S 7.3 Suusamyr earthquake in 1992. If such a landslide collapses into the reservoir, it may induce a tsunami, which poses a severe threat to the dam (Tibaldi et al., 2015).

We see several avenues for further research in the study area that would benefit from continuous intra-annual monitoring with Sentinel-1 data: (1) for areas such as the city of Toktogul, it is important to assess the potential consequences of the identified deformations and their implications on the stability of the buildings; (2) in combination with the observed Toktogul water level changes, the effects of varying water levels at the Kambarata 2 dam should be investigated. Focus should therefore be on the connections of the corresponding ground deformations to those of the Toktogul Reservoir. (3) Continuous SAR monitoring of the mountain slopes facing towards the lake can help in the early detection of instabilities such as slope failures that may eventually collapse into the lake (Tibaldi et al., 2015); and (4) via the elastic modelling, the deformations estimated from remote sensing in combination with the directly observed water mass loads allow constraining the specific Earth structure in the Toktogul region.

6.7 Acknowledgments

The Sentinel-1 and Envisat data used for this study are provided by the European Space Agency/Copernicus. The SRTM DEM data were derived from the Consortium for Spatial Information of the Consultative Group for International Agricultural Research (CGIAR-CSI). The Landsat data were obtained from the U.S. Geological Survey. We thank Deutscher Wetterdienst, Offenbach, Germany, and European Centre for Medium Range Weather Forecast, Reading, U.K., for providing data from ECMWF's operational forecast model, the ERA-5 reanalysis and the ERA-I reanalysis. This work was funded by the Initiative and Networking Fund of the Helmholtz Association in the framework of the Helmholtz Alliance "Remote Sensing and Earth System Dynamics" (EDA) and by the CAWa project (Contract No. AA7090002), funded by the German Federal Foreign Office. The study contributes to the "Advanced Earth System Modelling Capacity" (ESM) project of the Helmholtz Association of German Research Centres. We also appreciate the valuable comments and constructive suggestions of four anonymous reviewers, which greatly helped us to improve our manuscript.

6.8 Author Contribution

Mahdi Motagh and Julia Neelmeijer designed the study together. Julia Neelmeijer accomplished the InSAR and atmosphere correction processing, analysis and wrote the manuscript. Tilo Schöne processed the lake altimetry data and wrote the corresponding section of the manuscript. Robert Dill and Volker Klemann performed the modelling and provided the content for the related section. Mahdi Motagh contributed to the analysis, discussion and writing.

7 Subsequent Work

7.1 Scope of the Chapter

This chapter intends to demonstrate how the work of this thesis contributes to further research activities at the GFZ Potsdam and the Global Change Observatory “Gottfried Merzbacher” located at the Inylchek Glacier. The remote sensing-based information about high-resolution surface velocities and the new TDX DEM of the area are complementary to research activities that involve regular fieldwork of GFZ researchers to retrieve in-situ data at the observatory. The joint analysis of the results gained from those different research approaches led to the publication of two further peer-reviewed manuscripts, to which the author of this thesis contributed as co-author.

In the following, the abstracts of these publications are presented and the particular author contributions are outlined. Furthermore, a brief overview about ongoing but not yet published work is given in order to underline the importance of the previously presented case studies for GFZ’s research activities.

7.2 GNSS-derived Inylchek Glacier Surface Kinematics

published as:

Cornelia Zech, Tilo Schöne, Julia Neelmeijer, Alexander Zubovich, Roman Galas (2015) Geodetic Monitoring Networks: GNSS-Derived Glacier Surface Velocities at the Global Change Observatory Inylchek (Kyrgyzstan). In: *Rizos C., Willis P. (eds) IAG 150 Years. International Association of Geodesy Symposia*, vol 143., Springer, Cham, pp. 557–563, doi:10.1007/1345_2015_38.

7.2.1 Abstract

The German Research Centre for Geosciences (GFZ, Potsdam, Germany) and the Central-Asian Institute for Applied Geosciences (CAIAG, Bishkek, Kyrgyzstan) jointly established the Global Change Observatory “Gottfried Merzbacher” at the Inylchek Glacier in eastern Kyrgyzstan which is one of the largest non-polar glaciers of the world and consists of two glacier streams. The flow of melt water from the northern tributary forms a lake (Lake Merzbacher) that is dammed by the calving ice front of the southern Inylchek Glacier. At least once a year a glacial lake outburst flood (GLOF) occurs and the complete water of the Lake Merzbacher drains through sub-glacial channels. To monitor the glacier dynamics including the post-drainage ice dam response, a small network of remotely operated multi-parameter stations (ROMPS) was installed at different locations at the glacier. Directly located near the ice dam, a continuously measuring kinematic GNSS station provides precise long-term data of variations in the dynamics of the ice dam for the years 2010, 2011 and 2012. While the station reflects the horizontal motion of the ice dam towards the Lake Merzbacher, the vertical component shows a clear loss of elevation as a “long-term” response after the GLOF lasting for several weeks instead of only a few days. In correspondence to the elevation decrease, the surface velocity has a higher variability due to a relaxing process of the ice dam but changes significantly to a nearly constant velocity during the winter time.

7.2.2 Author Contribution

The author of this thesis contributed to this paper by providing high-resolution surface velocities of the bending area of the Southern Inylchek Glacier gained from feature tracking on TSX SAR satellite data (Figure 7.1). These measurements were used to validate the glacier velocities derived from the continuously recording GNSS station, which is placed on top of the glacier surface close to the ice-dam at the edge of Lake Merzbacher. Although GNSS and SAR data were collected in the same season from different years, a direct comparison of the independently obtained results showed good agreement. This underlines the potential of the complementary aspect of both geodetic techniques: whereas remote sensing is able to observe the glacier motion in the spatial domain for a certain time-period, point-wise, continuously measuring GNSS data document motions with very high temporal resolution.

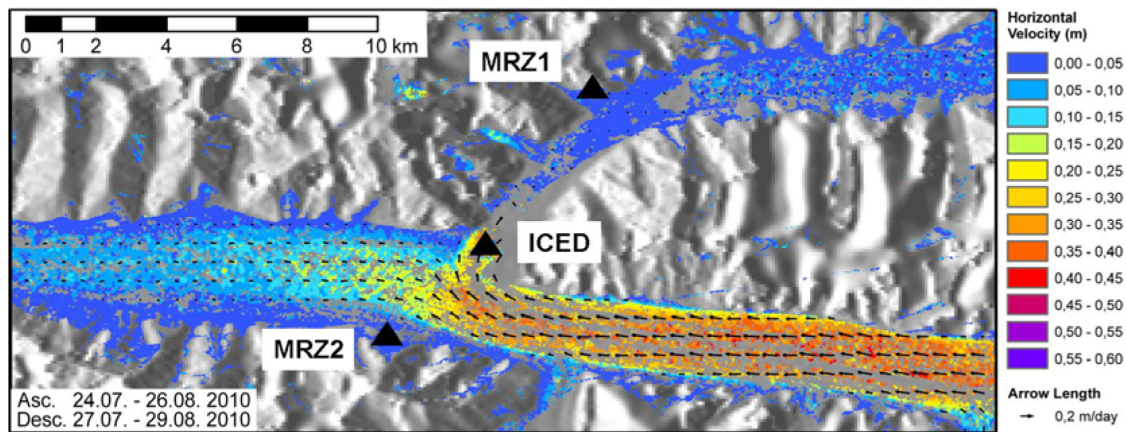


Figure 7.1: Mean surface motion of the Inylchek Glacier between July and August 2010 as from TSX data. The location of reference GNSS stations is marked with black triangles, ICED is the station located on the glacier surface (adapted from Zech et al., 2015; © 2015 Springer Nature, reprinted with permission).

In addition to the processing of the TSX data, the author wrote the accompanying section of the manuscript, and was involved in the discussion and interpretation of the results.

7.3 Monitoring of Lake Merzbacher's GLOF Event

published as:

Cornelia Zech, Tilo Schöne, Julia Neelmeijer, and Alexander Zubovich (2016) Continuous Kinematic GPS Monitoring of a Glacier Lake Outburst Flood. In: *Freymueller J.T., Sánchez L. (eds) International Symposium on Earth and Environmental Sciences for Future Generations. International Association of Geodesy Symposia*, vol 147., Springer, Cham, pp. 339–347, doi:10.1007/1345_2016_246.

7.3.1 Abstract

Natural glacier events such as ice avalanches, debris flows or glacier lake outburst floods (GLOF) may have hazardous impacts on the downstream area of the glacier and can cause severe destructions. The Inylchek Glaciers in Kyrgyzstan, are one of the largest non-polar glacier systems in the world. Each year, an ice-dammed lake is formed (Lake Merzbacher) by melt water which drains predominantly every year suddenly within a few days causing a destructive flood. To understand the mechanism of the GLOF, a network of continuously operating GPS stations at the Inylchek Glaciers provide daily horizontal and vertical positions of the ice-dam in front of the Merzbacher Lake. Irrespective of the general motion during the year, the ice-dam is strongly influenced by the formation and outburst of the lake. Especially the vertical position and surface velocities increase shortly before the GLOF supporting the assumption that the ice-dam adjacent to the lake becomes afloat. After the GLOF, e.g. in 2014, the elevation decreases rapidly by 20 m within 8 days. In 2015, the GLOF changes in timing, magnitude and available lake water volume but the motion pattern of the ice-dam is similar compared to the year before. These comparable results have the potential to develop an early warning system for the glacier-dammed lake outburst flood.

7.3.2 Author Contribution

The author of this thesis contributed to this paper by extracting lake level, extent, and volume of Lake Merzbacher shortly before the GLOF events in summer time 2005, 2013, 2014, and 2015. This was accomplished by manually analysing optical and radar remote sensing data to retrieve the latest location of the ice dam and the extent of the lake. By projecting the lake boundaries on the previously generated DEM from November 2013, water volume and water level height of Lake Merzbacher were extracted with a ± 2 m water level accuracy (Figure 7.2). The November 2013 DEM was particularly useful for that task, as the lake was empty at the time of the TDX data acquisition, which allowed a survey of the lake bathymetry. Furthermore, the location of the ice-dam was at a rather retreated position, which enabled an estimation of the lake volume for events where the dam was located further towards the lake.

Additionally to the DEM generation, water level height, lake extent, and water volume extraction of Lake Merzbacher, the author wrote the related section of the manuscript, and contributed to the analysis and discussion of the results.

7.4 Ongoing Work at GFZ Based on the Results of this Thesis

For future regionally focused glacier studies, seasonal ascending and descending TSX data have been obtained over the entire Inylchek Glacier for the years 2012 – 2014. This provides a unique opportunity to extend the previous glacier surface velocity investigation to the entire system and allows an inter- and intra-annual analysis over several years. Additionally, in-situ GNSS data have been collected by the author for various points on the glacier in a field work campaign during summer 2012, which will allow for a validation of the results.

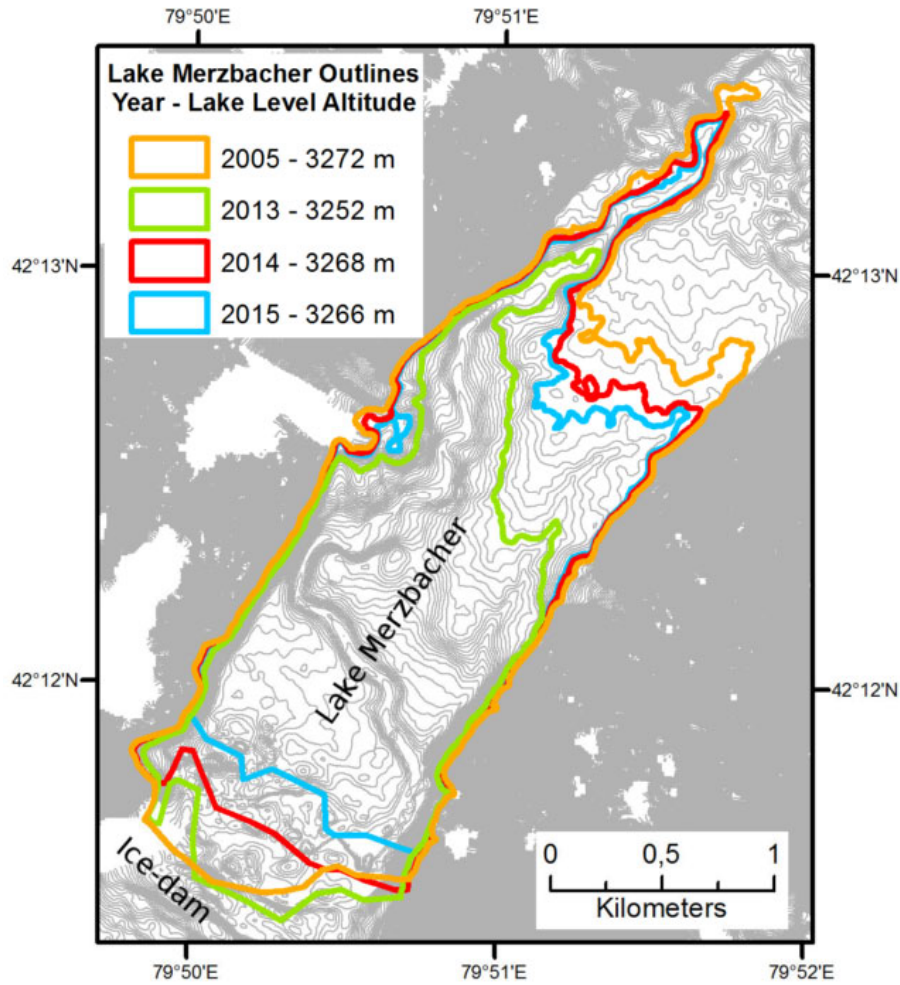


Figure 7.2: Bathymetry of Lake Merzbacher as derived from the November 2013 TDX DEM. The equidistance between contour lines is 2 m. The extracted maximum lake extents are provided for the years 2005, 2013, 2014 and 2015 (adapted from Zech et al., 2016; © 2016 Springer Nature, reprinted with permission).

To prepare a study for the regional analysis of Tien Shan glacier kinematics, seasonal TSX data were also ordered for the Akshiirak Glacier system, the Golubin Glacier, and the Abramov Glacier during the years 2013 – 2014. This is complemented by the availability of seasonal TDX data, collected in 2012 – 2014 for all four mentioned glaciers systems, which will allow a combined analysis of surface motion variation and elevation changes.

Furthermore, colleagues of Section 1.3 “Earth System Modelling” currently use the derived Sentinel-1 deformations at the Toktogul area to test different plausible local Green’s functions as discussed in Dill et al. (2015). The results of these tests are of interest for future refinements of the numerical Earth Model used to routinely generate geophysical correction models for various fields of geodesy.

8 Summary and Outlook

8.1 Summary of Main Results

This thesis focuses on the assessment of various SAR methods for monitoring water storage systems such as glaciers and reservoirs located in high-mountain terrain. Focus is laid on the potential for quantifying inter- and intra-annual changes through the use of new generation SAR satellite data. The summary of the most important results are provided with regard to the research questions stated in Section 1.5.

8.1.1 Methodological Aspects

Which SAR methods are useful to quantify water-related displacements and topography variations, such as glacier surface kinematics, glacier elevation change and loading-induced ground deformations around water reservoirs? What special treatment of the data is required due to the high-mountain environment?

Water-related displacements in high-mountain terrain are manifold and although they cannot be analysed by a single universal method, SAR data are applicable for multiple investigations. The choice of the best processing approach depends on various parameters, which are: (1) amount of displacement and (2) amount of surface characteristics change to be expected between SAR acquisitions; (3) orientation of the investigated displacement (vertical versus horizontal); and (4) the continuity of the displacement in time.

1. Depending on whether the expected amount of displacement between SAR acquisitions is in the millimetre-to-centimetre range or in the decimetre-to-metre domain, different SAR approaches must be applied to the data. Small-scale deformations can be approached with DInSAR methods, if feasible in combination with time series analysis. Large-scale displacements, however, which cannot be further divided into smaller pieces by simply using more SAR images, lead to decorrelation of the SAR phase differences. In this case, feature tracking is the best SAR-based option to quantify changes.

2. Decorrelation is also caused by the amount of change in surface characteristics between SAR acquisitions. These surface changes are often related to a certain season. Snowfall is particularly affecting high-mountain areas in winter time. Vegetation is another key parameter that affects mainly summer images, although this has not been a major issue in the semi-arid area of Kyrgyzstan, which lacks large regions with high vegetation. For glaciated areas, debris cover is rather favourable for SAR investigations as it provides characteristic surface features that are particularly useful for tracking purposes. Additionally, debris cover hampers the penetration of the radar signal into snow and ice. On the contrary, open snow and ice regions are affected by surface melting in spring and summer, which also significantly alters the glacier's surface. For studies focusing on the derivation of annual mean glacier changes and mean surface deformations, it is thus recommended to derive displacement rates from SAR images that are least effected by such effects, which is usually the case for autumn acquisitions.

3. Depending on the orientation in which the main displacement is to be expected, either InSAR or feature tracking is better suited for the analysis. InSAR delivers only displacements in a single

direction, which is line-of-sight. The results are thus most sensitive to vertical displacements, partly sensitive to changes in east/west direction, and least sensitive to north/east-occurring displacements. Feature tracking, instead, delivers displacements in azimuth and range direction, whereas azimuth displacements represent a purely horizontal motion and range results depict a combination of horizontal and vertical motion. Although that makes feature tracking looking favourable compared to phase-based methods, it must be noted that InSAR methods yield a much higher accuracy than any feature tracking approach.

4. The continuity of the displacement in time determines whether it is useful to apply time series analysis or not. The application of time series can be used with the phase-based InSAR approach, but also with feature tracking. However, if monitored changes are really small, the application of time series is not just an option, but essential to allow the discrimination of error sources from the displacement signal in the SAR data. Main error sources in this context are atmospheric effects and the penetration of the radar signal into the ground.

This thesis focuses on water-related displacements, such as glacier surface velocities and glacier elevation changes, as well as on deformations caused by changes of the water level in reservoirs. It is shown in Chapter 4 that high-mountain glacier surface velocities in the range of several centimetres per day lead to quick decorrelation of SAR interferograms. Furthermore, decorrelation occurs due to rapid surface changes during the melting period. This favours the application of the feature tracking method. Although the test case of the Inylchek Glacier is oriented mainly east/west, which is theoretically very suitable for InSAR studies, the fact that glaciers can be aligned in all directions also supports the recommendation of the feature tracking approach in general.

In the Inylchek Glacier test case, high spatial resolution images are chosen to particularly study the bending area of the glacier in which the ice turns towards Lake Merzbacher. This has the drawback that not the entire glacier area can be investigated, as the TerraSAR-X sensor can only acquire data either at high-resolution and reduced swath width, or at lower resolution with a wide swath. Still, the novelty of using high-resolution StripMap data allows for the generation of a detailed picture of the ice movement. It is thus possible to distinguish between kinematic differences of adjacent longitudinal ice-streams, which has not been described in other studies before. This could not have been accomplished with coarser resolution data, as the accuracy of the feature tracking technique is limited by the pixel size of the image. The advantages of the high-resolution dataset are further shown in a follow-up study (Section 7.2), where remote-sensing based Inylchek Glacier surface velocities are compared to motions observed from a continuous GNSS station that is located on the glacier surface close to the ice-dam facing Lake Merzbacher. Although the temporal coverage of the data is not exactly the same, the velocity rates from both geodetic techniques are in very good agreement.

Glacier elevation changes are determined in Chapter 5 by subtracting glacier heights derived at different times. On the contrary to surface motion quantification, the InSAR scenes from two different acquisitions in time are not directly compared to each other. Instead, two acquisitions taken at exactly the same time are used to build DEMs, which are then used for the comparison. The retrieval of two simultaneous acquisitions is possible due to the special bistatic tandem configuration of the TerraSAR-X and TanDEM-X satellites, which cannot be accomplished by other SAR missions. The

bistatic configuration provides the unique opportunity to study glacier elevation changes that occurred within short time intervals. However, since the TSX/TDX tandem constellation is not always in bistatic mode during the mission period, there are further restrictions regarding data availability. Furthermore, regular acquisitions of bistatic SAR data over one area were only taken for a selected number of times for the generation of the WorldDEM™. In addition to those existing data, SAR images are only acquired on-demand and thus no global homogeneous data collection is carried out. This implies that, although being a unique opportunity for glacier elevation change studies, the application of this method cannot be easily adopted for other regions and especially not for arbitrary time periods.

Besides glacier elevation change studies, the retrieval of up-to-date, high resolution mountain DEMs is also beneficial for investigating related phenomena, such as GLOF events. In the study introduced in Section 7.3 it is demonstrated how a TDX-based DEM can be used to estimate the volume of the Merzbacher Lake shortly before the GLOF. This is accomplished by combining DEM data with the surface lake extent retrieved from optical and SAR imagery collected before the occurrence of the GLOF event. Such a study is useful for better understanding trends and trigger mechanisms for sub-glacial lake evolution.

In contrast to glacier velocities, the deformation induced by water level changes is much smaller and mainly in vertical direction, which allows for the application of InSAR time series techniques. In Chapter 6, the SBAS approach is used for the first time on Sentinel-1 imagery to quantify deformations around a water reservoir. Due to the short acquisition interval and the wide swath of the Sentinel-1 data, the entire region of the Toktogul Reservoir is covered and intra-annual deformations are identified. Snowfall in winter images makes the set-up of the SBAS network difficult, but as the vegetation is low, longer time-spans to generate coherent interferograms are used to successfully stabilise the network throughout the whole year.

If the displacement is monitored with SAR sensors observing from multiple viewing positions at the same time, it is further possible to apply decomposition approaches in order to better resolve the direction of the movement. If multiple acquisitions from different sensors are not available, ascending and descending imagery from a single mission can be considered for decomposition by neglecting small time offsets between these scenes. In case of InSAR, this limits the overall result to displacement discrimination in just two dimensions. The third dimension, to which the sensor is least sensitive – usually north/south due to the polar orbits of almost all SAR satellites – is neglected in this case (Chapter 6). In case of feature tracking, ascending and descending azimuth and range results are combined in such a way that 3D motion is retrieved (Chapter 4).

The study of the three different displacement types further shows that SAR data gained over high-mountain areas are particularly affected by the following effects: (1) high amount of geometric distortions in the data; (2) radar penetration into the ground; (3) strong atmospheric effects in interferograms; and (4) difficulties in finding suitable reference areas. Furthermore, processing is significantly improved if (5) a very accurate DEM for precise topography removal is available.

1. The elevation of high mountains introduces strong distortions in radar images, which particularly hampers glacier studies (Chapter 4 and Chapter 5). Specifically layover and shadow effects induced by high-mountain ranges overlapping flat, glaciated areas lead to data voids that are most prominent

on north-south orientated valley glaciers. In contrast to layover and shadowing, foreshortening is less critical, as the investigated glacier and its tributaries are gently sloped, so that no significant foreshortening effects are identified. To minimise the influence of these distortions it is recommended to pay attention that the area of interest is neither in the near-range nor in the far range of the scene. It is furthermore beneficial if the look angle is chosen in such a way that the glacier surface is minimally affected by layover and shadowing effects. In most cases a rather large look angle should be preferred, as in this case the influence of layover is limited. However, it must be carefully evaluated if the choice of a large look angle leads to undesired shadow effects in the far range.

Remaining voids due to geometric effects can be reduced if data from multiple orbits are available for a similar period, which allows for a combination of the results. However, if high-mountain DEMs are generated only from one single TDX pair, voids in the area of interest often cannot be ruled out. In the Inylchek Glacier elevation change study (Chapter 5), the absolute height of the topography at a given date is not critically important, but rather the amount of topography changes between two certain dates. In this case, assumptions based on the behaviour of the surrounding region with the same characteristics help to approximate the unknown changes in the voids. In this thesis, a new method for such estimations is introduced that depends on the elevation as well as on the steepness of the slopes.

2. Correction for radar penetration is especially crucial when glaciated areas are investigated with InSAR techniques. The depth of the SAR signal penetration depends on the wavelength and the characteristics of the ground, such as wetness and dielectric properties. An increase in wavelength leads to an increase in penetration depth, and dry snow areas are more affected than wet snow or icy areas (Chapter 5). Another aspect is a near-surface ground water level in sedimentary areas that affects deformation measurements (Chapter 6). The effect of penetration is not easily overcome: In terms of DEM comparison, ideally DEMs are created from data acquired with the same wavelength, which allows to neglect penetration-induced changes if the conditions of snowfall and wetness can be assumed to be similar at both acquisition times. Furthermore, a relative effect of radar penetration can be investigated by comparing results gained from simultaneous acquisitions of two different sensors with different wavelengths. This is demonstrated in Chapter 5 with the X-band-based SRTM DEM and the C-band-based SRTM DEM. If absolute measurements are desired, such as the absolute heights of the topography, alternative data like GNSS measurements, radar or laser altimetry measurements – like from the ICESat satellite – or external non-SAR-based DEMs are very beneficial for correction purposes.

3. If InSAR methods are applied on two consecutive images, atmospheric effects cannot be neglected. Particularly in high-mountain regions, vertical stratification is dominating and is not cancelled out by simple image stacking. Chapter 6 compares several atmosphere removal approaches with a particular focus on implications due to high elevations. Here, for the first time the operational ECMWF analysis data as well as the global reanalyses ERA-Interim and ERA-5 are evaluated against the linear dependency and the power-law approach with regard to their usefulness for atmosphere delay estimation. It is shown that for the particular region in Kyrgyzstan characterised by a dominant micro-climate in a basin-shaped area of interest, numerical model-based approaches do not improve the results. Instead,

phase-based methods should be preferred, of which the power-law method works best. In the particular case of water reservoirs, the influence of evaporation further impacts interferograms significantly. It is found that morning acquisitions are less affected than evening acquisitions, as less water vapour is present in the atmosphere due to generally lower temperatures during the night.

4. Displacements measured with SAR data can only be given relative to a presumably stable area. In high-mountain terrain, such reference areas are not always easy to locate. If glacier systems are of interest, a separation between on-glacier and off-glacier is usually made, of which the latter is considered to be stable. The glacier body is clearly discriminated from the surroundings and changes are only analysed within the glacier outline. On the contrary, deformations in reservoir surroundings do not have such a clear boundary. In this case, a reference location should be selected in a low and comparatively flat region away from the lake where no deformation is to be expected and only minimal atmospheric effects are assumed. As this is not always easy to find, it is worth to consider one or more potential reference locations already during the cropping of the images.

5. For all applications, it is further beneficial to have an accurate and preferably high-resolution DEM available. This is important, firstly, as a DEM is used as a reference during the coregistration of the images. Secondly, in all DInSAR-based approaches, a DEM is used for topography removal. So far, open access DEMs with global coverage are provided with a spatial resolution of maximum 30 m. Exemplary named here are the SRTM DEM, ASTER GDEM2 or ALOS World 3D data sets. Such DEMs are often provided with limited accuracy in the high-mountain areas due to voids, distinct spikes and wells, stripes or noise artefacts. In addition, all of the data sets mentioned are now several years old. More favourable is thus the use of an up-to-date, high-spatial resolution reference DEM as available from TanDEM-X data. However, as these data are commercially distributed, access is often limited. In some selected regions, even finer DEMs gained from airborne laser scanning might exist, but these are even more difficult to acquire than commercial TDX data.

8.1.2 Monitoring of Short-Time Changes

To what extent does the new generation of SAR satellites that provide data with a high temporal sampling allow to monitor inter- and intra-annual displacements in high-mountain regions? What are the accompanying major limitations when dealing with SAR data in that framework, and how can those be overcome?

All three studies show that the high temporal sampling of the new generation satellites is highly favourable for monitoring inter- and intra-annual displacements. In Chapter 4 it is successfully analysed, how the glacier flow velocities vary within a year and that even short-time changes due to single events like the GLOF can be measured with SAR data. In Chapter 5, the potential of TDX data for DEM generation is evaluated. In this case, intra-annual comparisons reveal locations with pronounced ice loss or gain, such as a local thickening in the central part of the Northern Inylchek Glacier, or the distinct thinning of an icefall in the tributary of the Southern Inylchek. The short revisit time of the satellites is thus highly suitable for continuous monitoring and could also be used for early-warning purposes.

It is further shown in Chapter 6 that intra-annual deformations around the Toktogul Reservoir are well correlated with seasonal water level changes. This indicates a purely elastic response of the crust, which is verified by a very good agreement to deformation rates predicted from an elastic numerical Earth model. Precise measurements of deformations around large reservoirs with significant water level changes are thus highly suitable for the refinement of the parametrisation of the local rheology of the crust.

In addition to the decrease of the revisit cycle, processing SAR data from new generation satellites further benefits from very precise orbital positions compared to older missions. The very small orbit tubes, e.g. a radius of 50 m root mean square width for Sentinel-1 (EOPORTAL - Sentinel-1, 2018), ensure that coherence in interferograms is never lost by an exceedance of the critical perpendicular baseline.

Regarding coherence loss, the main limitation usually arises from seasonal effects, which lead to decorrelation of the data. In high-mountain areas, the most problematic issues are snowfall and large surface alterations during the melting period. In intra-annual studies, these issues cannot simply be neglected. Therefore, the following approaches are recommended: If snow cover leads to decorrelation, manual selection of single interferograms can still provide the opportunity to build connected networks. Furthermore, relaxing the temporal baseline threshold in such a way that autumn images are connected with spring images can also help to build a robust SBAS network. To retrieve displacement rates for the winter time, it is further an option to consider SAR data acquired with a longer wavelength, as for example in the L-band. Although not tested in this thesis, the effect of decorrelation should be reduced, which offers the opportunity to retrieve data from time periods in which X-band or C-band data might fail (Malinverni et al., 2014).

The effect of surface melting on glaciated areas is also difficult to overcome. During the melting period, the surface of the glacier is rather wet, which leads to a reduced backscatter signal. If some signal can still be collected, the phase is often altered so that coherence in interferograms is lost. Feature tracking can be applied in areas with large phase-differences, but this method also fails in areas without backscatter. In that case, it might be worth to evaluate SAR imagery acquired with a smaller look angle, which leads to an increase in the collected backscatter signal. Another limitation for feature tracking is the absence of distinct features on the ground. This occurs especially in accumulation areas characterised by a rather homogeneous snow cover. Acquisitions from SAR sensors transmitting in C-band or L-band could be advantageous there, as those wavelengths are able to penetrate deeper into the snow. The signal is thus reflected from compressed ice with potentially more structure. In addition, feature tracking methods also work on optical imagery, which could be used as a supplement to the SAR data, as long as the lack of features does not prevent displacement retrievals at all.

Compared to studies focusing on deformations over periods of many years, intra- and inter-annual studies are mostly affected by the increase of uncertainties. This is due to the effect that with smaller temporal baselines and thus with smaller investigated displacement rates, noise has a relatively larger impact on the measurements (Chapter 5 and Chapter 6). The Signal-to-noise ratios must therefore always be considered when interpreting such results.

In this context, it should be noted that in Chapter 5 a rather conservative approach was applied to estimate the uncertainty values of the glacier elevation changes. Here the uncertainty calculation was based on the differences of the stable areas of the DEMs and, if applicable, on the overall uncertainty of the radar penetration depth. The result is therefore to be interpreted as mean uncertainty for a single pixel, but is directly compared to the mean glacier elevation changes, which leads to relatively high uncertainty rates. It should be emphasized, however, that although these uncertainties are larger than the derived mean glacier elevation changes, the result is still meaningful, since the elevation changes of the individual pixels are usually greater than those of the given uncertainties. The correctness of the results is also confirmed by the very good agreement of the independently derived glacier elevation changes from the three DEMs. In order to ensure a better comparison between mean glacier elevation changes and the uncertainty rates, it is therefore suggested for future work to rely on a different approach for estimating uncertainties which takes into account the distance of the spatial autocorrelation of elevation differences off glaciers. This method described in Gardelle et al. (2013) considers the standard deviation of the mean glacier elevation change for each individual elevation bin and is therefore better suited to describe the uncertainty rate of the total mean glacier elevation change.

Of all previously identified problems in SAR data processing, most influencing noise sources for short-term investigations are the effects of atmosphere and radar penetration. This is because the absolute change in results due to the noise source remains within a certain range, but the displacement rates analysed between short-term acquisitions are usually smaller than in long-term studies. Noise has thus a much larger influence on the results. Efforts to reduce the influence of such effects as described in Section 8.1.1 are therefore particularly important for studies focusing on short-term variations.

Another issue associated to monitoring short-time variations with a high temporal sampling is the significant increase in data managing. The set-up of time series analysis results in the handling of a large amount of data, which makes automated processing chains essential. To save disk space, data processing should be limited to the particular area of interest. Furthermore, the selection of this study area should be accomplished as early as possible in the processing chain. In this thesis, the regional selection is always done directly after the coregistration of the SAR images. This has the advantage that the data stack used for subsequent processing contains only images which have exactly the same size and have been resampled only once. The image stack is then processed depending on the selected method: in the feature tracking case, it is straightforward to measure displacements between chronologically successive images so that feature changes at the surface are minimal (Chapter 4). In the SBAS case, multiple small baseline subset interferograms are connected to each other in such a way that the inversion of the unwrapped results yields minimal residual errors (Chapter 6).

8.2 Outlook

This thesis focused on measuring intra- and inter-annual displacements and topography changes in high-mountain areas. It was shown that in particular growing uncertainties are problematic for the investigation of short-time changes. It is thus recommended for future studies to prioritise efforts to

decrease the influence of the largest uncertainty factors, which are radar penetration and atmospheric effects.

The effect of radar penetration into the ground can be reduced if stereo-imagery from simultaneously acquired high resolution optical data, such as Pléiades data, is used for comparison (Berthier et al., 2014; Dehecq et al., 2016). As the set-up of an optical data-based, consistent time series over high-mountain areas is unlikely due to cloud coverage limitations, a suitable method would be to process only selected, cloud-free optical images that serve as a height reference. The time series itself is again built from radar imagery, and only later corrected by the additional stereo DEMs.

Regarding atmosphere correction, it must be noted that the feasibility of the power-law method is most likely limited to certain high-mountain settings, but might fail in other regions. An effort should thus be made to make better use of weather model information and combine dataset from GNSS and weather models. Most promising in this context is the Generic Atmospheric Correction Online Service for InSAR (GACOS), which currently delivers the tropospheric delay based on high resolution ECMWF weather model and DEM data, but aims to integrate also GPS-estimated tropospheric delay products (Yu et al., 2017a,b).

All three investigations presented in this thesis are generally designed as capability studies, and processing and analysis is thus limited to a rather small area. In order to better understand the overall behaviour of an entire catchment and its response to weather and climate changes and its contribution to sea-level rise, the local focus should be broadened to regional scale studies such as in Rankl and Braun (2016) or Malz et al. (2018) and later on even to continental studies that comprise multiple mountain ranges. For the Tien Shan mountain range, Farinotti et al. (2015) already estimated glacier mass balance rates from GRACE-based gravimetry, laser altimetry, and glaciological modelling. This could be complemented by a joint analysis of the regional glacier elevation changes and inter- and intra-annual glacier surface kinematics as accomplished in Neckel et al. (2017) for some selected glaciers in Tibet. If SAR data from one satellite is not sufficient for the analysis or encounters too many processing problems, the combination of multi-source satellite data is promising (Round et al., 2017). Combined with high-resolution meteorological data, such a holistic glacier displacement analysis would help to better identify areas that are more influenced by present-day climate change than others. Ultimately, short-time changes should be monitored in all semi-arid regions of the world, which would be an important supplement to studies such as from Gardelle et al. (2013) and Brun et al. (2017), where mean glacier mass balance estimates were calculated for the entire Central Asia region from SRTM DEM and optical stereo imagery.

In potential follow-on studies, results should be generated in a largely non-interactive fashion and fed into global glacier inventory databases such as the GLIMS, RGI or the GAMDAM glacier inventories, where products are disseminated to a wide range of users. Due to the big amount of data that would need to be regularly analysed, processing would be quite demanding in terms of computing resources, which means that suitable processing strategies need to be assessed before starting the calculations. One option could be that products are generated on large cloud computing systems and change detection would be automatised by the setting of certain thresholds. If the monitoring is set-up as early warning system for significant variations as induced, e.g. by glacier surges, a regular threat

detection process could be run on some coarse resolution imagery by primarily multilooking the SAR data. Processing load could be further reduced by considering only imagery with a temporal resolution of, for example, one month, which could be potentially increased for the critical time of the melting period. For areas in which potential changes are identified, SAR images would be reprocessed with a higher spatial and temporal resolution. A joint analysis with meteorological data may then allow the identification of potential triggers. Another conceivable approach that should be explored further is the use of artificial intelligence for the detection of significant displacement and topography changes. Modern machine learning techniques, such as neural networks or support vector machines, are able to classify remote sensing data with only a limited amount of training effort (Nijhawan et al., 2016), and are thus promising tools for real-time data analysis over large areas. Such tools for fast change detection are most advantageous if they are integrated into early warning networks. In terms of glacier monitoring in Central Asia, such a system would focus, e.g., on the detection of glacier surges as well as on the identification of glacial lake emergence to warn residents downstream about the potential threat.

Additionally to the application of an early-warning system, annual calculations of regional glacier elevation changes can be used for updates on the glacier mass balance state. This would be particularly useful for the investigation of long term trends, which need to be assessed to derive estimations about the fresh water availability in the future. In this case, SAR data would be most useful for local variability and anomaly investigations, while the development of the overall mass balance could be further advanced by accompanying satellite gravity missions, such as GRACE-FO that was just successfully launched on May 22nd, 2018 (NASA Spaceflight, 2018).

In terms of water reservoir monitoring, Sentinel-1 based analysis should also be extended to global monitoring of large water reservoirs. Despite being able to detect episodic deformations that might hint to landslide or seismic activities, knowledge about deformation rates, gradients and spatial coverage can help in improving rheological models of the Earth. In this context, processing time can also be significantly reduced for highly coherent new generation satellite data if not an elaborate amplitude dispersion method is needed for the identification of distributed scatterers as in StaMPS/MTI, but rather simple coherence-based thresholds are considered (Motagh et al., 2017).

Furthermore, deformations due to loading effects are not confined to artificial reservoirs, but also occur on much broader spatial and temporal scales. Most prominent in this context is the glacial isostatic adjustment (GIA) that describes the ongoing relaxation process of the mantle after the latest ice age 16,000 years ago. Stockamp et al. (2015) already demonstrated that multi-sensor SAR-based investigations allow GIA extraction over Scotland. SAR data from new-generation satellites that operate particularly with a wide swath footprint can thus potentially be used to quantify these changes at much larger scales that are especially prominent over Northern America, Northern Eurasia, Patagonia, and Antarctica. A detailed spatial variation analysis would pose a novel contribution to already existing GIA models, such as described in Peltier (2004), which are then again used for signal separation purposes. An exemplary case is the correction of GIA in sea level observations, which are derived from tide gauge data, altimetry data or gravimetric data (Tamisiea and Mitrovica, 2011).

Furthermore, GIA models are also important to decide whether GIA effects need to be considered in permafrost thawing studies from geodetic data (Vey et al., 2013).

Improvements in all studies could further be made when high-resolution DEMs, such as the WorldDEMTM, become open access. This would not only be very beneficial for topography removal attempts, which would then result in smaller residual fringe density compared to calculations with a void-filled SRTM DEM version, but would also help to improve geocoding of the final products. This would further ease the comparison of following-up studies, which are consequently referenced to the same high-resolution DEM product.

TSX/TDX as well as Sentinel-1 have already provided data for several years. Near future satellite missions promise to add even more benefits to a potential monitoring system. The newest mission in this context is PAZ, a Spanish sibling of the TSX satellite, which was launched on February 22nd, 2018. Its orbit constellation is designed in such a way that it shares the same orbit as the TSX/TDX satellites, providing thus SAR data with even shorter revisit times when it is operated in combination with those two (EOPORTAL - PAZ, 2018). DLR in a PPP conjunction with Airbus plans to succeed the TerraSAR-X mission with the follow-on TerrSAR-NG mission that will ensure the continuation of TSX measurements, but will also allow a very high resolution data retrieval down to 0.25 m at a 5 km swath. It is also designed to be set up as a so-called "WorldSAR" constellation, in which other partners can join with further investments and own satellites, which can then be operated in a coordinated manner with TerraSAR-NG (EOPORTAL - TerraSAR-NG, 2018). Furthermore, the PPP is designing a mission concept called High Resolution Wide Swath SAR (HRWS-SAR) that aims for the combination of high-resolution data acquisition over an exceptionally wide swath (WMOSAT, 2018). A potential launch date is envisaged for 2022. Such a mission could be most useful for glacier velocity estimation, as higher resolution provides more visible features and could thus close gaps where feature tracking on coarser spatial resolution imagery would fail (Schubert et al., 2013).

Besides the continuation of X-band satellite SAR missions, DLR and Airbus are further planning to launch the TanDEM-L mission operating in L-band. This would be an important contribution to water-related studies as it provides an unique opportunity to globally measure changes in soil moisture. Additionally, this tandem mission can provide insights into ice-flow and melting processes within glaciers, as the signal would penetrate into snow and ice for some tenth of metres (AWI, 2018).

New insights into deformation processes are also expected from the SAR data of the future Canadian Radarsat Constellation mission, which is planned for launch in 2018. The successor of the current Radarsat-2 mission will consist of three satellites equipped with C-band SAR sensors, which will allow a monitoring with a revisit cycle of four days. The mission is designed in such a way that the number of satellites could be even increased to six (EOPORTAL - Radarsat Constellation, 2018). This would further improve coherence preservation and could thus be most useful for glacier investigations, particularly during the glaciologically interesting melting period.

Of interest will be also the planned NISAR mission, which is a collaboration between the U.S. National Aeronautics and Space Administration (NASA) and the Indian Space Research Organization. It is scheduled for launch in 2020 – 2021 and will provide for the first time a combination of S-band and L-band sensors on a single satellite, which will be an important tool for radar penetration studies.

As this mission is partly run by NASA, it is likely that all data will be freely available. This is not the case for future missions from PPP consortia, where data will be commercially distributed and free access for science purposes is limited. Most beneficial for regular monitoring studies will therefore continue to be the European Sentinel-1 mission with its open-access data policy. The continuation of the current Sentinel-1 A/B satellites has been already announced. In 2015, a contract was signed for the the construction of succeeding C/D satellites (ESA, 2018).

For future SAR missions aiming for intra-annual monitoring, it is always beneficial to have multiple satellites operating together to keep revisit times as short as possible. The simultaneous operation of several sensors with different bands could further help to better understand the effects of radar penetration. Spatial resolution should be as high as possible without loss of significant ground coverage, which can be achieved by recently developed multi-channel architectures (Krieger et al., 2010). In addition, a well-distributed network of receiving antennas would make it possible to increase downlink capacities, which in turn would lead to more available data. It is furthermore important that access to the data is granted to everybody for free as developing countries that are located in the critical arid and semi-arid regions of the world would otherwise not be able to get access. A constantly running background acquisition plan ensures continuous availability of global SAR data, which is most critical for intra-annually monitoring purposes.

Bibliography

- Abdrakhmatov, K., Havenith, H.-B., Delvaux, D., Jongmans, D., and Trefois, P. (2003) Probabilistic PGA and Arias Intensity maps of Kyrgyzstan (Central Asia). *Journal of Seismology*, 7, 203–220, doi:10.1023/A:1023559932255.
- Abdul-Rahman, H. S., Gdeisat, M. A., Burton, D. R., Lalor, M. J., Lilley, F., and Moore, C. J. (2007) Fast and robust three-dimensional best path phase unwrapping algorithm. *Applied Optics*, 46, 6623, doi:10.1364/AO.46.006623.
- Aizen, V. B., Aizen, E. M., and Melack, J. M. (1995) Climate, snow cover, glaciers, and runoff in the Tien Shan, Central Asia. *Journal of the American Water Resources Association*, 31, 1113–1129, doi:10.1111/j.1752-1688.1995.tb03426.x.
- Aizen, V. B., Aizen, E. M., Dozier, J., Melack, J. M., Sexton, D. D., and Nesterov, V. N. (1997) Glacial regime of the highest Tien Shan mountain, Pobeda-Khan Tengry massif. *Journal Of Glaciology*, 43, 503–512, doi:10.3189/S0022143000035115.
- Aizen, V. B., Aizen, E. M., Joswiak, D. R., Fujita, K., Takeuchi, N., and Nikitin, S. A. (2006a) Climatic and atmospheric circulation pattern variability from ice-core isotope/geochemistry records (Altai, Tien Shan and Tibet). *Annals of Glaciology*, 43, 49–60, doi:10.3189/172756406781812078.
- Aizen, V. B., Kuzmichenok, V. A., Surazakov, A. B., and Aizen, E. M. (2006b) Glacier changes in the central and northern Tien Shan during the last 140 years based on surface and remote-sensing data. *Annals of Glaciology*, 43, 202–213, doi:10.3189/172756406781812465.
- Aizen, V. B., Aizen, E. M., and Kuzmichonok, V. A. (2007a) Glaciers and hydrological changes in the Tien Shan: simulation and prediction. *Environmental Research Letters*, 2, 045019, doi:10.1088/1748-9326/2/4/045019.
- Aizen, V. B., Kuzmichenok, V. A., Surazakov, A. B., and Aizen, E. M. (2007b) Glacier changes in the Tien Shan as determined from topographic and remotely sensed data. *Global and Planetary Change*, 56, 328–340, doi:10.1016/j.gloplacha.2006.07.016.
- Akbarimehr, M., Motagh, M., and Haghshenas, M. (2013) Slope Stability Assessment of the Sarcheshmeh Landslide, Northeast Iran, Investigated Using InSAR and GPS Observations. *Remote Sensing*, 5, 3681–3700, doi:10.3390/rs5083681.
- Al-Yaari, A., Wigneron, J.-P., Kerr, Y., Rodriguez-Fernandez, N., O'Neill, P. E., Jackson, T. J., De Lannoy, G. J. M., Al Bitar, A., Mialon, A., Richaume, P., Walker, J. P., Mahmoodi, A., and Yueh, S. (2017) Evaluating soil moisture retrievals from ESA's SMOS and NASA's SMAP brightness temperature datasets. *Remote Sensing of Environment*, 193, 257–273, doi:10.1016/j.rse.2017.03.010.
- Amelung, F., Galloway, D. L., Bell, J. W., Zebker, H. A. and Lacznaiak, R. J. (1999) Sensing the ups and downs of Las Vegas: InSAR reveals structural control of land subsidence and aquifer-system deformation. *Geology*, 27, 483–486, doi:10.1130/0091-7613(1999)027<0483:STUADO>2.3.CO;2.
- Andersen, M. L., Larsen, T. B., Nettles, M., Elosegui, P., van As, D., Hamilton, G. S., Stearns, L. A., Davis, J. L., Ahlstrøm, A. P., de Juan, J., Ekström, G., Stenseng, L., Khan, S. A., Forsberg, R., and Dahl-Jensen, D. (2010) Spatial and temporal melt variability at Helheim Glacier, East Greenland, and its effect on ice dynamics. *Journal of Geophysical Research*, 115, F04041, doi:10.1029/2010JF001760.
- Anderssohn, J., Motagh, M., Walter, T. R., Rosenau, M., Kaufmann, H., and Oncken, O. (2009) Surface deformation time series and source modeling for a volcanic complex system based on satellite wide swath and image mode interferometry: The Lazufre system, central Andes. *Remote Sensing of Environment*, 113, 2062–2075, doi:10.1016/j.rse.2009.05.004.
- Arendt, A., Bolch, T., Cogley, J. G., Gardner, A. S., Hagen, J.-O., Hock, R., Kaser, G., Pfeffer, W. T., Moholdt, G., Paul, F., Radić, V., Andreassen, L., Bajracharya, S., Barrand, N., Beedle, M., Berthier, E., Bhambri, R., Bliss, A., Brown, I., Burgess, D., Burgess, E., Cawkwell, F., Chinn, T., Copland, L., Davies, B., De Angelis,

- H., Dolgova, E., Filbert, K., Forester, R., Fountain, A., Frey, H., Giffen, B., Glasser, N., Gurney, S., Hagg, W. J., Hall, D., Haritashya, U., Hartmann, G., Helm, C., Herreid, S., Howat, I., Kapustin, G., Khromova, T., Kienholz, C., König, M., Kohler, J., Kriegel, D., Kutuzov, S., Lavrentiev, I., Le Bris, R., Lund, J., Manley, W., Mayer, C., Miles, E., Li, X., Menounos, B., Mercer, A., Mölg, N., Mool, P., Nosenko, G., Negrete, A., Nuth, C., Pettersson, R., Racoviteanu, A. E., Ranzi, R., Rastner, P., Rau, F., Raup, B., Rich, J., Rott, H., Schneider, C., Seliverstov, Y., Sharp, M., Sigurðsson, O., Stokes, C., Wheate, R., Winsvold, S., Wolken, G., Wyatt, F., and Zheltyhina, N. (2012) Randolph Glacier Inventory - A Dataset of Global Glacier Outlines: Version 3.2. *Global Land Ice Measurements from Space*, Boulder Colorado, USA. Digital Media.
- AWI (2018). Available online: <https://www.awi.de/nc/en/about-us/service/press/press-release/new-satellite-technology-promises-great-progress-for-glacier-research.html> (accessed on April 24, 2018).
- Balzter, H. (2001) Forest mapping and monitoring with interferometric synthetic aperture radar (InSAR). *Progress in Physical Geography*, 25, 159–177, doi:10.1177/030913330102500201.
- Bamber, J. L. and Rivera, A. (2007) A review of remote sensing methods for glacier mass balance determination. *Global and Planetary Change*, 59, 138–148, doi:10.1016/j.gloplacha.2006.11.031.
- Bamler, R. and Hartl, P. (1998) Synthetic aperture radar interferometry. *Inverse Problems*, 14, 1–54, doi:10.1088/0266-5611/14/4/001.
- Barnhart, W. D. and Lohman, R. B. (2013) Characterizing and estimating noise in InSAR and InSAR time series with MODIS. *Geochemistry, Geophysics, Geosystems*, 14, 4121–4132, doi:10.1002/ggge.20258.
- Beedle, M. J., Menounos, B., and Wheate, R. (2014) An evaluation of mass-balance methods applied to Castle Creek Glacier, British Columbia, Canada. *Journal of Glaciology*, 60, 262–276, doi:10.3189/2014JoG13J091.
- Bekaert, D. P. S., Hooper, A. J., and Wright, T. J. (2015a) A spatially variable power law tropospheric correction technique for InSAR data. *Journal of Geophysical Research: Solid Earth*, 120, 1345–1356, doi:10.1002/2014JB011558.
- Bekaert, D. P. S., Walters, R., Wright, T., Hooper, A. J., and Parker, D. (2015b) Statistical comparison of InSAR tropospheric correction techniques. *Remote Sensing of Environment*, 170, 40–47, doi:10.1016/j.rse.2015.08.035.
- Béjar-Pizarro, M., Ezquerro, P., Herrera, G., Tomás, R., Guardiola-Albert, C., Ruiz Hernández, R. M., Fernández Merodo, J. A., Marchamalo, M., and Martínez, R. (2017) Mapping groundwater level and aquifer storage variations from InSAR measurements in the Madrid aquifer, Central Spain. *Journal of Hydrology*, 547, 678–689, doi:10.1016/j.jhydrol.2017.02.011.
- Berardino, P., Fornaro, G., Lanari, R., and Sansosti, E. (2002) A new algorithm for surface deformation monitoring based on small baseline differential SAR interferograms. *IEEE Transactions on Geoscience and Remote Sensing*, 40, 2375–2383, doi:10.1109/TGRS.2002.803792.
- Bernauer, T. and Siegfried, T. (2012) Climate change and international water conflict in Central Asia. *Journal of Peace Research*, 49, 227–239, doi:10.1177/0022343311425843.
- Berthier, E., Arnaud, Y., Vincent, C., and Rémy, F. (2006) Biases of SRTM in high-mountain areas: Implications for the monitoring of glacier volume changes. *Geophysical Research Letters*, 33, L08502, doi:10.1029/2006GL025862.
- Berthier, E., Arnaud, Y., Kumar, R., Ahmad, S., Wagnon, P., and Chevallier, P. (2007) Remote sensing estimates of glacier mass balances in the Himachal Pradesh (Western Himalaya, India). *Remote Sensing of Environment*, 108, 327–338, doi:10.1016/j.rse.2006.11.017.
- Berthier, E., Vincent, C., Magnússon, E., Gunnlaugsson, Á., Pitte, P., Le Meur, E., Masiokas, M., Ruiz, L., Pálsson, F., Belart, J. M. C., and Wagnon, P. (2014) Glacier topography and elevation changes derived from Pléiades sub-meter stereo images. *The Cryosphere*, 8, 2275–2291, doi:10.5194/tc-8-2275-2014.
- Bevan, S. L., Luckman, A., Khan, S. A., and Murray, T. (2015) Seasonal dynamic thinning at Helheim Glacier. *Earth and Planetary Science Letters*, 415, 47–53, doi:10.1016/j.epsl.2015.01.031.
- Bevis, M., Kendrick, E., Cser, A., and Smalley, R. (2004) Geodetic measurement of the local elastic response to the changing mass of water in Lago Laja, Chile. *Physics of the Earth and Planetary Interiors*, 141, 71–78, doi:10.1016/j.pepi.2003.05.001.

- Bevis, M., Alsdorf, D., Kendrick, E., Fortes, L. P., Forsberg, B., Smalley Jr., R., and Becker, J. (2005) Seasonal fluctuations in the mass of the Amazon River system and Earth's elastic response. *Geophysical Research Letters*, 32, L16308, doi:10.1029/2005GL023491.
- Bhambri, R., Bolch, T., and Chaujar, R. K. (2011) Mapping of debris-covered glaciers in the Garhwal Himalayas using ASTER DEMs and thermal data. *International Journal of Remote Sensing*, 32, 8095–8119, doi:10.1080/01431161.2010.532821.
- Bindi, D., Abdrakhmatov, K., Parolai, S., Mucciarelli, M., Grünthal, G., Ischuk, A., Mikhailova, N., and Zschau, J. (2012) Seismic hazard assessment in Central Asia: Outcomes from a site approach. *Soil Dynamics and Earthquake Engineering*, 37, 84–91, doi:10.1016/j.soildyn.2012.01.016.
- Bingham, R. G., Nienow, P. W., and Sharp, M. J. (2003) Intra-annual and intra-seasonal flow dynamics of a High Arctic polythermal valley glacier. *Annals of Glaciology*, 37, 181–188, doi:10.3189/172756403781815762.
- Birkett, C. M. (1994) Radar altimetry: A new concept in monitoring lake level changes. *Eos, Transactions American Geophysical Union*, 75, 273, doi:10.1029/94EO00944.
- Björnsson, H. (1998) Hydrological characteristics of the drainage system beneath a surging glacier. *Nature*, 395, 771–774, doi:10.1038/27384.
- Bolch, T. (2007) Climate change and glacier retreat in northern Tien Shan (Kazakhstan/Kyrgyzstan) using remote sensing data. *Global and Planetary Change*, 56, 1–12, doi:10.1016/j.gloplacha.2006.07.009.
- Bolch, T. (2017) Hydrology: Asian glaciers are a reliable water source. *Nature*, 545, 161–162, doi:10.1038/545161a.
- Bolch, T., Peters, J., Yegorov, A., Pradhan, B., Buchroithner, M. F., and Blagoveshchensky, V. (2011a) Identification of potentially dangerous glacial lakes in the northern Tien Shan. *Natural Hazards*, 59, 1691–1714, doi:10.1007/s11069-011-9860-2.
- Bolch, T., Pieczonka, T., and Benn, D. I. (2011b) Multi-decadal mass loss of glaciers in the Everest area (Nepal Himalaya) derived from stereo imagery, *The Cryosphere*, 5, 349–358, doi:10.5194/tc-5-349-2011.
- Braun, L. and Hagg, W. J. (2010) Present and future impact of snow cover and glaciers on runoff from mountain regions – comparison between Alps and Tien Shan. In: *IHP-HWRP-Berichte*, 8, 36–43.
- Braun, M., Pohjola, V. A., Pettersson, R., Möller, M., Finkelnburg, R., Falk, U., Scherer, D., and Schneider, C. (2011) Changes of glacier frontal positions of vestfonna (nordautlandet, svalbard). *Geografiska Annaler: Series A, Physical Geography*, 93, 301–310, doi:10.1111/j.1468-0459.2011.00437.x.
- Brun, F., Berthier, E., Wagnon, P., Kääb, A., and Treichler, D. (2017) A spatially resolved estimate of High Mountain Asia glacier mass balances from 2000 to 2016. *Nature Geoscience*, 10, 668–673, doi:10.1038/ngeo2999.
- Bürgmann, R., Rosen, P. A., and Fielding, E. J. (2000) Synthetic Aperture Radar Interferometry to Measure Earth's Surface Topography and Its Deformation. *Annual Review of Earth and Planetary Sciences*, 28, 169–209, doi:10.1146/annurev.earth.28.1.169.
- CA WATER Info (2017). Available online: www.cawater-info.net (accessed on January 31, 2017, authorisation required for data retrieval).
- Carabajal, C. C. and Harding, D. J. (2006) SRTM C-Band and ICESat Laser Altimetry Elevation Comparisons as a Function of Tree Cover and Relief. *Photogrammetric Engineering & Remote Sensing*, 72, 287–298, doi:10.14358/PERS.72.3.287.
- Cavalié, O., Doin, M.-P., Lasserre, C., and Briole, P. (2007) Ground motion measurement in the Lake Mead area, Nevada, by differential synthetic aperture radar interferometry time series analysis: Probing the lithosphere rheological structure. *Journal of Geophysical Research*, 112, B03403, doi:10.1029/2006JB004344.
- Chen, C. W. and Zebker, H. A. (2000) Network approaches to two-dimensional phase unwrapping: intractability and two new algorithms. *Journal of the Optical Society of America A*, 17, 401, doi:10.1364/JOSAA.17.000401.
- Chen, C. W. and Zebker, H. A. (2001) Two-dimensional phase unwrapping with statistical models for nonlinear optimization. In: *IGARSS 2000. IEEE 2000 International Geoscience and Remote Sensing Symposium. Taking the Pulse of the Planet: The Role of Remote Sensing in Managing the Environment. Proceedings (Cat. No.00CH37120)*, vol. 7, pp. 3213–3215, IEEE, doi:10.1109/IGARSS.2000.860386.

- Chen, C. W. and Zebker, H. A. (2002) Phase unwrapping for large SAR interferograms: statistical segmentation and generalized network models. *IEEE Transactions on Geoscience and Remote Sensing*, 40, 1709–1719, doi:10.1109/TGRS.2002.802453
- Clarke, G. K. C. (2005) Subglacial processes. *Annual Review of Earth and Planetary Sciences*, 33, 247–276, doi:10.1146/annurev.earth.33.092203.122621.
- Clason, C., Mair, D. W. F., Burgess, D. O., and Nienow, P. W. (2012) Modelling the delivery of supraglacial meltwater to the ice/bed interface: application to southwest Devon Ice Cap, Nunavut, Canada. *Journal of Glaciology*, 58, 361–374, doi:10.3189/2012JoG11J129.
- Cogley, J. G. (2009) Geodetic and direct mass-balance measurements: comparison and joint analysis. *Annals of Glaciology*, 50, 96–100, doi:10.3189/172756409787769744. doi:10.3189/S026030550000762X.
- Costantini, M. (1998) A novel phase unwrapping method based on network programming. *IEEE Transactions on Geoscience and Remote Sensing*, 36, 813–821, doi:10.1109/36.673674.
- Costantini, M., Malvarosa, F., and Minati, F. (2012) A General Formulation for Redundant Integration of Finite Differences and Phase Unwrapping on Sparse Multidimensional Domain. *IEEE Transactions on Geoscience and Remote Sensing*, 50, 758–768, doi:10.1109/TGRS.2011.2162630.
- Crétaux, J.-F., Abarca-del Río, R., Bergé-Nguyen, M., Arsen, A., Drolon, V., Clos, G., and Maisongrande, P. (2016) Lake Volume Monitoring from Space. *Surveys in Geophysics*, 37, 269–305, doi:10.1007/s10712-016-9362-6.
- Crosetto, M., Biescas, E., Duro, J., Closa, J., and Arnaud, A. (2008) Generation of advanced ERS and Envisat Interferometric SAR products using the Stable Point Network technique. *Photogrammetric Engineering & Remote Sensing*, 74, 443–450, doi:10.14358/PERS.74.4.443.
- Crosetto, M., Monserrat, O., Cuevas-González, M., Devanthéry, N., and Crippa, B. (2016) Persistent Scatterer Interferometry: A review. *ISPRS Journal of Photogrammetry and Remote Sensing*, 115, 78–89, doi:10.1016/j.isprsjprs.2015.10.011.
- Cuffey, K. M. and Paterson, W. S. B. (2010) The Physics of Glaciers, 4th ed. *Butterworth-Heinemann/Elsevier*, Burlington, MA, USA, pp. 223–283.
- Dee, D. P., Uppala, S. M., Simmons, A. J., Berrisford, P., Poli, P., Kobayashi, S., Andrae, U., Balmaseda, M. A., Balsamo, G., Bauer, P., Bechtold, P., Beljaars, A. C. M., van de Berg, L., Bidlot, J., Bormann, N., Delsol, C., Dragani, R., Fuentes, M., Geer, A. J., Haimberger, L., Healy, S. B., Hersbach, H., Hólm, E. V., Isaksen, I., Kållberg, P., Köhler, M., Matricardi, M., McNally, A. P., Monge-Sanz, B. M., Morcrette, J.-J., Park, B.-K., Peubey, C., de Rosnay, P., Tavolato, C., Thépaut, J.-N., and Vitart, F. (2011) The ERA-Interim reanalysis: configuration and performance of the data assimilation system. *Quarterly Journal of the Royal Meteorological Society*, 137, 553–597, doi:10.1002/qj.828.
- Dehecq, A., Millan, R., Berthier, E., Gourmelen, N., Trouvé, E., and Vionnet, V. (2016) Elevation Changes Inferred From TanDEM-X Data Over the Mont-Blanc Area: Impact of the X-Band Interferometric Bias. *IEEE Journal of Selected Topics in Applied Earth Observations and Remote Sensing*, 9, 3870–3882, doi:10.1109/JSTARS.2016.2581482.
- Dill, R., Klemann, V., Martinec, Z., and Tesauero, M. (2015) Applying local Green's functions to study the influence of the crustal structure on hydrological loading displacements. *Journal of Geodynamics*, 88, 14–22, doi:10.1016/j.jog.2015.04.005.
- Doin, M.-P., Lasserre, C., Peltzer, G., Cavalié, O., and Doubre, C. (2009) Corrections of stratified tropospheric delays in SAR interferometry: Validation with global atmospheric models. *Journal of Applied Geophysics*, 69, 35–50, doi:10.1016/j.jappgeo.2009.03.010.
- Doin, M.-P., Twardzik, C., Ducret, G., Lasserre, C., Guillaso, S., and Jianbao, S. (2015) InSAR measurement of the deformation around Siling Co Lake: Inferences on the lower crust viscosity in central Tibet. *Journal of Geophysical Research: Solid Earth*, 120, 5290–5310, doi:10.1002/2014JB011768.
- Dovgan, V. (2012) Seismometric Monitoring of Toktogul Hydroelectric Power Station. In: *IV International Conference "Problems of Cybernetics and Informatics" (PCI'2012)*, Baku, Azerbaijan, 12.-14. September 2012; pp. 81–84.

- Duethmann, D., Menz, C., Jiang, T., and Vorogushyn, S. (2016) Projections for headwater catchments of the Tarim River reveal glacier retreat and decreasing surface water availability but uncertainties are large. *Environmental Research Letters*, 11, 054024, doi:10.1088/1748-9326/11/5/054024.
- Dziewonski, A.M., Anderson, D.L. (1981) Preliminary reference Earth model. *Physics of the Earth and Planetary Interiors*, 25, 297–356, doi:10.1016/0031-9201(81)90046-7.
- Eineder, M., Abdel Jaber, W., Floricioiu, D., Rott, H., and Yague-Martinez, N. (2011) Glacier flow and topography measurements with TerraSar-X and TanDEM-X. *2011 IEEE International Geoscience and Remote Sensing Symposium (IGARSS)*, pp. 3835–3838, doi:10.1109/IGARSS.2011.6050067.
- EOPORTAL - PAZ (2018). Available online: <https://directory.eoportal.org/web/eoportal/satellite-missions/p/paz> (accessed on April 24, 2018).
- EOPORTAL - Radarsat Constellation (2018). Available online: <https://directory.eoportal.org/web/eoportal/satellite-missions/r/rcm> (accessed on April 24, 2018).
- EOPORTAL - Sentinel-1 (2018). Available online: <https://directory.eoportal.org/web/eoportal/satellite-missions/c-missions/copernicus-sentinel-1> (accessed on May 23, 2018).
- EOPORTAL - TerraSAR-NG (2018). Available online: <https://directory.eoportal.org/web/eoportal/satellite-missions/t/tsx-ng> (accessed on April 24, 2018).
- Erten, E., Reigber, A., Hellwich, O., and Prats, P. (2009) Glacier Velocity Monitoring by Maximum Likelihood Texture Tracking. *IEEE Transactions on Geoscience and Remote Sensing*, 47, 394–405, doi:10.1109/TGRS.2008.2009932.
- ESA - Sentinel-1 (2018). Available online: <https://sentinel.esa.int/web/sentinel/missions/sentinel-1/observation-scenario> (accessed on May 14, 2018).
- ESA (2018). Available online: http://www.esa.int/Our_Activities/Observing_the_Earth/Copernicus/Sentinel-1/Deal_sealed_for_new_Sentinel-1_satellites (accessed on 24.04.2018).
- Fallourd, R., Harant, O., Trouvé, E., Nicolas, J.-M., Gay, M., Walpersdorf, A., Mugnier, J.-L., Serafini, J., Rosu, D., Bombrun, L., Vasile, G., Cotte, N., Vernier, F., Tupin, F., Moreau, L., and Bolon, P. (2011) Monitoring Temperate Glacier Displacement by Multi-Temporal TerraSAR-X Images and Continuous GPS Measurements. *IEEE Journal of Selected Topics in Applied Earth Observations and Remote Sensing*, 4, 372–386, doi:10.1109/JSTARS.2010.2096200.
- Farinotti, D., Longuevergne, L., Moholdt, G., Duethmann, D., Mölg, T., Bolch, T., Vorogushyn, S., and Güntner, A. (2015) Substantial glacier mass loss in the Tien Shan over the past 50 years. *Nature Geoscience*, 8, 716–722, doi:10.1038/ngeo2513.
- Farr, T. G., Rosen, P. A., Caro, E., Crippen, R., Duren, R., Hensley, S., Kobrick, M., Paller, M., Rodriguez, E., Roth, L., Seal, D., Shaffer, S., Shimada, J., Umland, J., Werner, M., Oskin, M., Burbank, D., and Alsdorf, D. (2007) The shuttle radar topography mission. *Reviews of Geophysics*, 45, RG2004, doi:10.1029/2005RG000183.
- Farrell, W.E. (1972) Deformation of the Earth by surface loads. *Reviews of Geophysics*, 10, 761–797, doi:10.1029/RG010i003p00761.
- Favey, E., Geiger, A., Gudmundsson, G. H., and Wehr3, A. (1999) Evaluating the Potential of an Airborne Laser-scanning System for Measuring Volume Changes of Glaciers. *Geografiska Annaler, Series A: Physical Geography*, 81, 555–561, doi:10.1111/1468-0459.00083.
- Ferretti, A., Prati, C., and Rocca, F. (2000) Nonlinear subsidence rate estimation using permanent scatterers in differential SAR interferometry. *IEEE Transactions on Geoscience and Remote Sensing*, 38, 2202–2212, doi:10.1109/36.868878.
- Ferretti, A., Prati, C., and Rocca, F. (2001) Permanent scatters in SAR interferometry. *IEEE Transactions on Geoscience and Remote Sensing*, 39, 8–20, doi:10.1109/36.898661.
- Ferretti, A., Monti-Guarnieri, A., Prati, C., Rocca, F., and Massonnet, D. (2007a) InSAR Principles: Guidelines for SAR Interferometry Processing and Interpretation. In: *ESA Publications*, vol. 19, ESTEC, Noordwijk.

- Ferretti, A., Savio, G., Barzaghi, R., Borghi, A., Musazzi, S., Novali, F., Prati, C., and Rocca, F. (2007b) Submillimeter accuracy of InSAR time series: Experimental validation. *IEEE Transactions on Geoscience and Remote Sensing*, 45, 1142–1153, doi:10.1109/TGRS.2007.894440.
- Ferretti, A., Fumagalli, A., Novali, F., Prati, C., Rocca, F., and Rucci, A. (2011) A new algorithm for processing interferometric data-stacks: SqueeSAR. *IEEE Transactions on Geoscience and Remote Sensing*, 49, 3460–3470, doi:10.1109/TGRS.2011.2124465.
- Fialko, Y. (2006) Interseismic strain accumulation and the earthquake potential on the southern San Andreas fault system. *Nature*, 441, 968–971, doi:10.1038/nature04797.
- Fialko, Y., Simons, M., and Agnew, D. (2001) The complete (3-D) surface displacement field in the epicentral area of the 1999 M_W 7.1 Hector Mine Earthquake, California, from space geodetic observations. *Geophysical Research Letters*, 28, 3063–3066, doi:10.1029/2001GL013174.
- Fischer, A. (2011) Comparison of direct and geodetic mass balances on a multi-annual time scale. *The Cryosphere*, 5, 107–124, doi:10.5194/tc-5-107-2011.
- Floricioiu, D., Eineder, M., Rott, H., and Nagler, T. (2008) Velocities of Major Outlet Glaciers of the Patagonia Icefield Observed by TerraSAR-X. In: *IGARSS 2008 - 2008 IEEE International Geoscience and Remote Sensing Symposium*, vol. 4, pp. IV-347–IV-350, IEEE, Boston, Massachusetts, U.S.A., doi:10.1109/IGARSS.2008.4779729.
- Förste, C., Bruinsma, S., Abrykosov, O., Flechtner, F., Dahle, C., Neumayer, K.-H., Barthelmes, F., König, R., Marty, J.-C., Lemoine, J.-M., and Biancale, R. (2013) EIGEN-6C3 – The newest high resolution global combined gravity field model based on the 4th release of the GOCE Direct Approach. In: *Proceedings of the 2013 IAG Scientific Assembly, 150th Anniversary of the IAG*, Potsdam, Germany, September 2013.
- Friedt, J.-M., Tolle, F., Bernard, É., Griselin, M., Laffly, D., and Marlin, C. (2012) Assessing the relevance of digital elevation models to evaluate glacier mass balance: application to Austre Lovénbreen (Spitsbergen, 79°N), *Polar Record*, 48, 2–10, doi:10.1017/S0032247411000465.
- Fujita, K., Suzuki, R., Nuimura, T., and Sakai, A. (2008) Performance of ASTER and SRTM DEMs, and their potential for assessing glacial lakes in the Lunana region, Bhutan Himalaya. *Journal of Glaciology*, 54, 220–228, doi:10.3189/002214308784886162.
- Furuya, M. and Wahr, J. M. (2005) Water level changes at an ice-dammed lake in west Greenland inferred from InSAR data. *Geophysical Research Letters*, 32, L14501, doi:10.1029/2005GL023458.
- Gabriel, A. K., Goldstein, R. M. and Zebker, H. A. (1989) Mapping small elevation changes over large areas: Differential radar interferometry. *Journal of Geophysical Research: Solid Earth*, 94, 9183–9191, doi:10.1029/JB094iB07p09183.
- Gahalaut, V., Yadav, R. K., Sreejith, K. M., Gahalaut, K., Bürgmann, R., Agrawal, R., Sati, S., and Kumar, A. (2017) InSAR and GPS measurements of crustal deformation due to seasonal loading of Tehri reservoir in Garhwal Himalaya, India. *Geophysical Journal International*, 209, 425–433, doi:10.1093/gji/ggx015.
- Gardelle, J., Berthier, E., and Arnaud, Y. (2012a) Impact of resolution and radar penetration on glacier elevation changes computed from DEM differencing. *Journal of Glaciology*, 58, 419–422, doi:10.3189/2012JoG11J175.
- Gardelle, J., Berthier, E., and Arnaud, Y. (2012b) Slight mass gain of Karakoram glaciers in the early twenty-first century. *Nature Geoscience*, 5, 322–325, doi:10.1038/ngeo1450.
- Gardelle, J., Berthier, E., Arnaud, Y., and Kääb, A. (2013) Region-wide glacier mass balances over the Pamir-Karakoram-Himalaya during 1999–2011. *The Cryosphere*, 7, 1263–1286, doi:10.5194/tc-7-1263-2013.
- Gardner, A., Moholdt, G., Arendt, A., and Wouters, B. (2012) Accelerated contributions of Canada’s Baffin and Bylot Island glaciers to sea level rise over the past half century. *The Cryosphere*, 6, 1103–1125, doi:10.5194/tc-6-1103-2012.
- Geist, T., Elvehøy, H., Jackson, M., and Stötter, J. (2005) Investigations on intra-annual elevation changes using multi-temporal airborne laser scanning data: case study Engabreen, Norway. *Annals of Glaciology* 42, 195–201, doi:10.3189/172756405781812592.
- Gens, R. and Van Genderen, J. L. (1996) Review Article SAR interferometry—issues, techniques, applications. *International Journal of Remote Sensing*, 17, 1803–1835, doi:10.1080/01431169608948741.

- GFZ Potsdam - Global Change Observatory Central Asia - Glacier Observatory Inylchek (2018). Available online: <https://www.gfz-potsdam.de/en/section/global-geomonitoring-and-gravity-field/topics/geodetic-hazard-monitoring/glacier-observatory-inylchek/> (accessed on May 01, 2018).
- Ghiglia, D. C. and Romero, L. A. (1996) Minimum Lp-norm two-dimensional phase unwrapping. *Journal of the Optical Society of America A*, 13, 1999, doi:10.1364/JOSAA.13.001999.
- Ghose, S., Mellors, R. J., Korjenkov, A. M., Hamburger, M. W., Pavlis, T. L., Pavlis, G. L., Omuraliev, M., Mamurov, E., and Muraliev, A. R. (1997) The $M_S = 7.3$ 1992 Suusamyr, Kyrgyzstan, Earthquake in the Tien Shan: 2. Aftershock Focal Mechanisms and Surface Deformation. *Bulletin of the Seismological Society of America*, 87, 23–38, 1997.
- Glazirin, G. E. (2010) A century of investigations on outbursts of the ice-dammed lake Merzbacher (central Tien Shan). *Austrian Journal of Earth Sciences*, 103, 171–179.
- Goldstein, R. M. and Werner, C. L. (1998) Radar interferogram filtering for geophysical applications. *Geophysical Research Letters*, 25, 4035–4038, doi:10.1029/1998GL900033.
- Goldstein, R. M., Zebker, H. A., and Werner, C. L. (1988) Satellite radar interferometry: Two-dimensional phase unwrapping. *Radio Science*, 23, 713–720, doi:10.1029/RS023i004p00713.
- Gondwe, B. R. N., Hong, S. H., Wdowinski, S., and Bauer-Gottwein, P. (2010) Hydrologic dynamics of the ground-water-dependent Sian Ka'an wetlands, Mexico, derived from InSAR and SAR data. *Wetlands*, 30, 1–13, doi:10.1007/s13157-009-0016-z.
- Graham, L. (1974) Synthetic interferometer radar for topographic mapping. *Proceedings of the IEEE*, 62, 763–768, doi:10.1109/PROC.1974.9516.
- Groh, A., Ewert, H., Rosenau, R., Fagioli, E., Gruber, C., Floricioiu, D., Abdel Jaber, W., Linow, S., Flechtner, F., Eineder, M., Dierking, W., and Dietrich, R. (2014) Mass, Volume and Velocity of the Antarctic Ice Sheet: Present-Day Changes and Error Effects. *Surveys in Geophysics*, 35, 1481–1505, doi:10.1007/s10712-014-9286-y.
- Haemmig, C., Huss, M., Keusen, H., Hess, J., Wegmüller, U., Ao, Z., and Kulubayi, W. (2014) Hazard assessment of glacial lake outburst floods from Kyagar glacier, Karakoram mountains, China. *Annals of Glaciology*, 55, 34–44, doi:10.3189/2014AoG66A001.
- Hagg, W. J., Braun, L. N., Uvarov, V. N., and Makarevich, K. G. (2004) A comparison of three methods of mass-balance determination in the Tuyuksu glacier region, Tien Shan, Central Asia. *Journal of Glaciology*, 50, 505–510, doi:10.3189/172756504781829783.
- Hagg, W. J., Mayer, C., Lambrecht, A., and Helm, A. (2008) Sub-debris melt rates on southern Inylchek Glacier, central Tian Shan. *Geografiska Annaler, Series A: Physical Geography*, 90, 55–63, doi:10.1111/j.1468-0459.2008.00333.x.
- Haghshenas Haghighi, M. and Motagh, M. (2016) Assessment of ground surface displacement in Taihape landslide, New Zealand, with C- and X-band SAR interferometry. *New Zealand Journal of Geology and Geophysics*, 59, 136–146, doi:10.1080/00288306.2015.1127824.
- Haiden, T., Janousek, M., Bauer, P., Bidlot, J., Dahoui, M., Ferranti, L., Prates, F., Richardson, D., and Vitart, F. (2015) Evaluation of ECMWF forecasts, including 2014–2015 upgrades. In: *ECMWF Technical Memoranda*, 765, pp. 1–51.
- Hanssen, R. F. (2001) Radar Interferometry. *Remote Sensing and Digital Image Processing*, vol. 2, Kluwer Academic Publishers, Dordrecht, doi:10.1007/0-306-47633-9.
- Havenith, H.-B., Torgoev, I., Torgoev, A., Strom, A., Xu, Y., and Fernandez-Steege, T. (2015) The Kambarata 2 blast-fill dam, Kyrgyz Republic: blast event, geophysical monitoring and dam structure modelling. *Geoenvironmental Disasters*, 2, 11, doi:10.1186/s40677-015-0021-x.
- Heine, I., Francke, T., Rogaß, C., Medeiros, P., Bronstert, A., Förster, S. (2014) Monitoring Seasonal Changes in the Water Surface Areas of Reservoirs Using TerraSAR-X Time Series Data in Semiarid Northeastern Brazil. *IEEE Journal of Selected Topics in Applied Earth Observations and Remote Sensing*, 7, 2323819, doi:10.1109/JSTARS.2014.2323819.

- Heine, I., Stüve, P., Kleinschmit, B., and Itzerott, S. (2015) Reconstruction of Lake Level Changes of Groundwater-Fed Lakes in Northeastern Germany Using RapidEye Time Series. *Water*, 7, 4175–4199, doi: 10.3390/w7084175.
- Herráez, M. A., Burton, D. R., Lalor, M. J., and Gdeisat, M. A. (2002) Fast two-dimensional phase-unwrapping algorithm based on sorting by reliability following a noncontinuous path. *Applied Optics*, 41, 7437, doi: 10.1364/AO.41.007437.
- Höhle, J. and Höhle, M. (2009) Accuracy assessment of digital elevation models by means of robust statistical methods. *ISPRS Journal of Photogrammetry and Remote Sensing*, 64, 398–406, doi:10.1016/j.isprsjprs.2009.02.003.
- Hong, S. H. and Wdowinski, S. (2014) Multitemporal Multitrack Monitoring of Wetland Water Levels in the Florida Everglades Using ALOS PALSAR Data With Interferometric Processing. *IEEE Geoscience and Remote Sensing Letters*, 11, 1355–1359, doi:10.1109/LGRS.2013.2293492.
- Hong, S. H., Wdowinski, S., Kim, S. W., and Won, J. S. (2010) Multi-temporal monitoring of wetland water levels in the Florida Everglades using interferometric synthetic aperture radar (InSAR). *Remote Sensing of Environment*, 114, 2436–2447, doi:10.1016/j.rse.2010.05.019.
- Hooper, A., Zebker, H., Segall, P., and Kampes, B. (2004) A new method for measuring deformation on volcanoes and other natural terrains using InSAR persistent scatterers. *Geophysical Research Letters*, 31, 1–5, doi:10.1029/2004GL021737.
- Hooper, A. J. (2008) A multi-temporal InSAR method incorporating both persistent scatterer and small baseline approaches. *Geophysical Research Letters*, 35, L16302, doi:10.1029/2008GL034654.
- Hooper, A. J. and Zebker, H. A. (2007) Phase unwrapping in three dimensions with application to InSAR time series. *Journal of the Optical Society of America A*, 24, 2737–2747, doi:10.1364/JOSAA.24.002737.
- Hooper, A. J., Bekaert, D. P. S., Spaans, K., and Arıkan, M. (2012) Recent advances in SAR interferometry time series analysis for measuring crustal deformation. *Tectonophysics*, 514–517, 1–13, doi:10.1016/j.tecto.2011.10.013.
- Humphrey, N., Raymond, C., and Harrison, W. (1986) Discharges of Turbid Water during Mini-Surges of Variegated Glacier, Alaska, U.S.A. *Journal of Glaciology*, 32, 195–207.
- Huss, M. (2013) Density assumptions for converting geodetic glacier volume change to mass change. *The Cryosphere*, 7, 877–887, doi:10.5194/tc-7-877-2013.
- Huss, M. and Hock, R. (2015) A new model for global glacier change and sea-level rise. *Frontiers in Earth Science*, 3, 1–22, doi:10.3389/feart.2015.00054.
- Immerzeel, W. W., van Beek, L. P. H., and Bierkens, M. F. P. (2010) Climate Change Will Affect the Asian Water Towers. *Science*, 328, 1382–1385, doi:10.1126/science.1183188.
- Jaber, W. A., Floricioiu, D., Rott, H., and Eineder, M. (2013) Surface elevation changes of glaciers derived from SRTM and TanDEM-X DEM differences. In: *2013 IEEE International Geoscience and Remote Sensing Symposium - IGARSS*, pp. 1893–1896, IEEE, doi:10.1109/IGARSS.2013.6723173.
- Jacob, T., Wahr, J., Pfeffer, W. T., and Swenson, S. (2012) Recent contributions of glaciers and ice caps to sea level rise. *Nature*, 482, 514–518, doi:10.1038/nature10847.
- Jarvis, A., Reuter, H. I., Nelson, A., and Guevara, E. (2008) Hole-filled seamless SRTM data V4. *International Center for Tropical Agriculture (CIAT)*. Available online: <http://srtm.csi.cgiar.org> (accessed on May 23, 2014).
- Jingshi, L. and Fukushima, Y. (1999) Recent change and prediction of glacier-dammed lake outburst floods from Kunmalik River in southern Tien Shan, China. In: *Hydrological Extremes: Understanding, Predicting, Mitigating, Proc. of IUGG 99 Symposium HIS*, Gottschalk, L., Olivry, J.-C., Reed, D., Rosbjerg, D., Eds., IAHS Publisher: Birmingham, UK, pp. 99–107.
- Jolivet, R., Grandin, R., Lasserre, C., Doin, M.-P., and Peltzer, G. (2011) Systematic InSAR tropospheric phase delay corrections from global meteorological reanalysis data. *Geophysical Research Letters*, 38, L17311, doi: 10.1029/2011GL048757.

- Jolivet, R., Agram, P. S., Lin, N. Y., Simons, M., Doin, M.-P., Peltzer, G., and Li, Z. (2014) Improving InSAR geodesy using Global Atmospheric Models. *Journal of Geophysical Research: Solid Earth*, 119, 2324–2341, doi:10.1002/2013JB010588.
- Joughin, I., Smith, B. E., and Abdalati, W. (2010) Glaciological advances made with interferometric synthetic aperture radar. *Journal of Glaciology*, 56, 1026–1042, doi:10.3189/002214311796406158.
- JSC “Electric Stations” (2017). Available online: www.energo-es.kg (accessed on January 31, 2017).
- Junfeng, W., Shiyin, L., Wanqin, G., Junli, X., Weijia, B., and Donghui, S. (2015) Changes in Glacier Volume in the North Bank of the Bangong Co Basin from 1968 to 2007 Based on Historical Topographic Maps, SRTM, and ASTER Stereo Images. *Arctic, Antarctic, and Alpine Research*, 47, 301–311, doi:10.1657/AAAR00C-13-129.
- Kääb, A. (2002) Monitoring high-mountain terrain deformation from repeated air- and spaceborne optical data: Examples using digital aerial imagery and ASTER data. *ISPRS Journal of Photogrammetry and Remote Sensing*, 57, 39–52, doi:10.1016/S0924-2716(02)00114-4.
- Kääb, A. (2005) Remote Sensing of Mountain Glaciers and Permafrost Creep. *Schriftenreihe Physische Geographie*, vol. 48, Geographisches Institut der Universität Zürich, Zürich.
- Kääb, A. and Vollmer, M. (2000) Surface geometry, thickness changes and flow fields on creeping mountain permafrost: automatic extraction by digital image analysis. *Permafrost and Periglacial Processes*, 11, 315–326, doi:10.1002/1099-1530(200012)11:4<315::AID-PPP365>3.0.CO;2-J.
- Kääb, A., Berthier, E., Nuth, C., Gardelle, J., and Arnaud, Y. (2012) Contrasting patterns of early twenty-first-century glacier mass change in the Himalayas. *Nature*, 488, 495–498, doi:10.1038/nature11324.
- Kampes, B. M. and Hanssen, R. F. (2004) Ambiguity resolution for permanent scatterer interferometry. *IEEE Transactions on Geoscience and Remote Sensing*, 42, 2446–2453, doi:10.1109/TGRS.2004.835222.
- Karthe, D., Chalov, S., and Borchardt, D. (2015) Water resources and their management in central Asia in the early twenty first century: status, challenges and future prospects. *Environmental Earth Sciences*, 73, 487–499, doi:10.1007/s12665-014-3789-1.
- Kaser, G., Fountain, A., and Jansson, P. (2003) A manual for monitoring the mass balance of mountain glaciers. *IHP-VI Technical Documents in Hydrology*, no. 59., UNESCO, Paris, 2003.
- Kaufmann, G. and Amelung, F. (2000) Reservoir-induced deformation and continental rheology in vicinity of Lake Mead, Nevada. *Journal of Geophysical Research: Solid Earth*, 105, 16341–16358, doi:10.1029/2000JB900079.
- Keith, J. E. and McKinney, D. C. (1997) Options Analysis of the Operation of the Toktogul Reservoir. In: *New Independent States Issue Paper No.7, Central Asia Mission, U.S. Agency for International Development*, 1997.
- Keller, E. A. and DeVecchio, D. E. (2016) Natural Hazards: Earth’s Processes as Hazards, Disasters, and Catastrophes, Fourth Edition. Routledge, New York.
- Khromova, T. (submitter) and Lavrentiev, I. (analyst) (2006) GLIMS Glacier Database. *National Snow and Ice Data Center*, Boulder Colorado, USA, doi:10.7265/N5V98602.
- Kingslake, J. and Ng, F. (2013) Quantifying the predictability of the timing of jökulhlaups from Merzbacher Lake, Kyrgyzstan. *Journal of Glaciology*, 59, 805–818, doi:10.3189/2013JoG12J156.
- Koblinsky, C. J., Clarke, R. T., Brenner, A. C., and Frey, H. (1993) Measurement of river level variations with satellite altimetry. *Water Resources Research*, 29, 1839–1848, doi:10.1029/93WR00542.
- Kolecka, N. and Kozak, J. (2014) Assessment of the Accuracy of SRTM C- and X-Band High Mountain Elevation Data: a Case Study of the Polish Tatra Mountains. *Pure and Applied Geophysics*, 171, 897–912, doi:10.1007/s00024-013-0695-5.
- Konovalov, V. G. (1990) Methods for the computations of onset date and daily hydrograph of the outburst from the Mertzbacher Lake, Tien-shan. In: *Hydrology in Mountainous Regions. I - Hydrological Measurements; the Water Cycle, Proceedings of two Lausanne Symposia*, August 1990, 193, pp. 181–188.

- Kotlyakov, V. M., Osipova, G. B., and Tsvetkov, D. G. (2008) Monitoring surging glaciers of the Pamirs, central Asia, from space. *Annals of Glaciology*, 48, 125–134, doi:10.3189/172756408784700608.
- Koul, M. N. and Ganjoo, R. K. (2010) Impact of inter- and intra-annual variation in weather parameters on mass balance and equilibrium line altitude of Naradu Glacier (Himachal Pradesh), NW Himalaya, India. *Climatic Change*, 99, 119–139, doi:10.1007/s10584-009-9660-9.
- Krieger, G., Younis, M., Gebert, N., Huber, S., Bordoni, F., Patyuchenko, A., and Moreira, A. (2010) Advanced Concepts for High-Resolution Wide-Swath SAR Imaging. In: *Proceedings of the 8th European Conference on Synthetic Aperture Radar - EUSAR*, pp. 1–4, Aachen, Germany, 2010.
- Krieger, G., Zink, M., Bachmann, M., Bräutigam, B., Schulze, D., Martone, M., Rizzoli, P., Steinbrecher, U., Walter Antony, J., De Zan, F., Hajnsek, I., Papathanassiou, K., Kugler, F., Rodriguez Cassola, M., Younis, M., Baumgartner, S., López-Dekker, P., Prats, P., and Moreira, A. (2013) TanDEM-X: A radar interferometer with two formation-flying satellites, *Acta Astronautica*, 89, 83–98, doi:10.1016/j.actaastro.2013.03.008.
- Kutuzov, S. and Shahgedanova, M. (2009) Glacier retreat and climatic variability in the eastern Terskey-Alatoo, inner Tien Shan between the middle of the 19th century and beginning of the 21st century. *Global and Planetary Change*, 69, 59–70, doi:10.1016/j.gloplacha.2009.07.001.
- Kyrgyzstan Disaster Risk Data Platform (2017). Available online: <http://geonode.mes.kg> (accessed on March 10, 2017).
- LacChapelle, E. (1962) Assessing Glacier mass Budgets by Reconnaissance Aerial Photography. *Journal of Glaciology*, 4, 290–297, doi:10.3198/1962JoG4-33-290-297.
- Lanari, R., Mora, O., Manunta, M., Mallorquí, J. J., Berardino, P., and Sansosti, E. (2004) A small-baseline approach for investigating deformations on full-resolution differential SAR interferograms. *IEEE Transactions on Geoscience and Remote Sensing*, 42, 1377–1386, doi:10.1109/TGRS.2004.828196.
- Lanari, R., Casu, F., Manzo, M., Zeni, G., Berardino, P., Manunta, M., and Pepe, A. (2013) An Overview of the Small BAseline Subset Algorithm: A DInSAR Technique for Surface Deformation Analysis. In: *Deformation and Gravity Change: Indicators of Isostasy, Tectonics, Volcanism, and Climate Change*, vol. 1, pp. 637–661, Birkhäuser Basel, Basel, doi:10.1007/978-3-7643-8417-3_2.
- Li, J., Li, Z., Zhu, J., Ding, X., Wang, C., and Chen, J. (2013) Deriving surface motion of mountain glaciers in the Tuomuer-Khan Tengri Mountain Ranges from PALSAR images. *Global and Planetary Change*, 101, 61–71, doi:10.1016/j.gloplacha.2012.12.004.
- Li, J., Li, Z., Ding, X., Wang, Q., Zhu, J., and Wang, C. (2014) Investigating mountain glacier motion with the method of SAR intensity-tracking: Removal of topographic effects and analysis of the dynamic patterns. *Earth-Science Reviews*, 138, 179–195, doi:10.1016/j.earscirev.2014.08.016.
- Lioubimtseva, E. and Henebry, G. (2009) Climate and environmental change in arid Central Asia: Impacts, vulnerability, and adaptations. *Journal of Arid Environments*, 73, 963–977, doi:10.1016/j.jaridenv.2009.04.022.
- Liu, B., Jiang, W., Zhang, J., Luo, Y., and Gong, L. (2010) Wenchuan earthquake ruptures located by offset-tracking procedure of ENVISAT ASAR amplitude images. *Earthquake Science*, 23, 283–287, doi:10.1007/s11589-010-0724-8.
- Liu, G., Fan, J.-H., Zhao, F., Mao, K.-B., and Dou, C.-Y. (2017) Monitoring elevation change of glaciers on Geladandong Mountain using TanDEM-X SAR interferometry. *Journal of Mountain Science*, 14, 859–869, doi:10.1007/s11629-016-3992-5.
- Lu, Z., Wicks, C., Dzurisin, D., Thatcher, W., Freymueller, J. T., McNutt, S. R., and Mann, D. (2000) Aseismic inflation of Westdahl Volcano, Alaska, revealed by satellite radar interferometry. *Geophysical Research Letters*, 27, 1567–1570, doi:10.1029/1999GL011283.
- Luckman, A., Quincey, D. D., and Bevan, S. L. (2007) The potential of satellite radar interferometry and feature tracking for monitoring flow rates of Himalayan glaciers. *Remote Sensing of Environment*, 111, 172–181, doi:10.1016/j.rse.2007.05.019.
- Ludwig, R. and Schneider, P. (2006) Validation of digital elevation models from SRTM X-SAR for applications in hydrologic modeling. *ISPRS Journal of Photogrammetry and Remote Sensing*, 60, 339–358, doi:10.1016/j.isprsjprs.2006.05.003.

- Lundgren, P., Berardino, P., Coltelli, M., Fornaro, G., Lanari, R., Puglisi, G., Sansosti, E., and Tesauro, M. (2003) Coupled magma chamber inflation and sector collapse slip observed with synthetic aperture radar interferometry on Mt. Etna volcano. *Journal of Geophysical Research*, 108, 2247, doi:10.1029/2001JB000657.
- Magnússon, E., Rott, H., Björnsson, H., and Pálsson, F. (2007) The impact of jökulhlaups on basal sliding observed by SAR interferometry on Vatnajökull, Iceland. *Journal of Glaciology*, 53, 232–240, doi:10.3189/172756507782202810.
- Malinvernì, E. S., Sandwell, D. T., Tassetti, A. N., and Cappelletti, L. (2014) InSAR decorrelation to assess and prevent volcanic risk. *European Journal of Remote Sensing*, 47, 537–556, doi:10.5721/EuJRS20144730.
- Malz, P., Meier, W., Casassa, G., Jaña, R., Skvarca, P., and Braun, M. (2018) Elevation and Mass Changes of the Southern Patagonia Icefield Derived from TanDEM-X and SRTM Data. *Remote Sensing*, 10, 188, doi:10.3390/rs10020188.
- Marinković, P. and Larsen, Y. (2015) On Resolving the Local Oscillator Drift Induced Phase Ramps in ASAR and ERS1/2 Interferometric Data — The Final Solution. In: *Fringe 2015 workshop (ESA SP-731)*, Frascati, Italy, 23.-27. March, 2015.
- Marschall, U., Roth, A., Eineder, M., and Suchandt, S. (2004) Comparison of DEMs derived from SRTM / X- and C-band. In: *IEEE International Geoscience and Remote Sensing Symposium 2004 - IGARSS '04. Proceedings*, vol. 7, pp. 4531–4534, doi:10.1109/IGARSS.2004.1370162.
- Maselli, D., Arynova, N., Ershova, N., Ivanova, N., Bilenko, V., and Liniger, H. (2010) Managing water in a dynamic Setting: The challenges of change in Central Asia. In: *Global Change and Sustainable Development: A Synthesis of Regional Experiences from Research Partnerships. Perspectives / NCCR North-South*, vol. 5, Hans, H., Wiesmann, U. (eds.), pp. 223–239, Bern: Geographica Bernensia.
- Massonnet, D. and Feigl, K. L. (1998) Radar interferometry and its application to changes in the Earth's surface. *Reviews of Geophysics*, 36, 441–500, doi:10.1029/97RG03139.
- Massonnet, D., Rossi, M., Carmona, C., Adragna, F., Peltzer, G., Feigl, K., and Rabaute, T. (1993) The displacement field of the Landers earthquake mapped by radar interferometry. *Nature*, 364, 138–142, doi:10.1038/364138a0.
- Mayer, C., Lambrecht, A., Hagg, W. J., Helm, A., and Scharrer, K. (2008) Post-drainage ice dam response at Lake Merzbacher, Inylchek glacier, Kyrgyzstan. *Geografiska Annaler, Series A: Physical Geography*, 90, 87–96, doi:10.1111/j.1468-0459.2008.00336.x.
- Mayr, E., Juen, M., Mayer, C., Usabaliev, R., and Hagg, W. J. (2014) Modeling Runoff from the Inylchek glaciers and Filling of Ice-Dammed Lake Merzbacher, Central Tian Shan. *Geografiska Annaler: Series A, Physical Geography*, 96, 609–625, doi:10.1111/geoa.12061.
- McNabb, R., Hock, R., O'Neel, S., Rasmussen, L., Ahn, Y., Braun, M., Conway, H., Herreid, S., Joughin, I., Pfeffer, W. T., Smith, B., and Truffer, M. (2012) Using surface velocities to calculate ice thickness and bed topography: a case study at Columbia Glacier, Alaska, USA. *Journal of Glaciology*, 58, 1151–1164, doi:10.3189/2012JoG11J249.
- Meier, M. F. and Tangborn, W. V. (1965) Net Budget and Flow of South Cascade Glacier, Washington. *Journal of Glaciology*, 5, 547–566, doi:10.3189/S0022143000018608.
- Mercanton, P. (1916) Vermessungen am Rhonegletscher/ Mensuration au glacier du Rhône: 1874–1915. *Neue Denkschriften der Schweizerischen Naturforschenden Gesellschaft*, 52.
- Mergili, M., Müller, J. P., and Schneider, J. F. (2013) Spatio-temporal development of high-mountain lakes in the headwaters of the Amu Darya River (Central Asia). *Global and Planetary Change*, 107, 13–24, doi:10.1016/j.gloplacha.2013.04.001.
- Michel, R., Avouac, J.-P., and Taboury, J. (1999) Measuring ground displacements from SAR amplitude images: Application to the Landers Earthquake. *Geophysical Research Letters*, 26, 875–878, doi:10.1029/1999GL900138.
- Mohr, J. J., Reeh, N., and Madsen, S. N. (1998) Three-dimensional glacial flow and surface elevation measured with radar interferometry. *Nature*, 391, 273–276, doi:10.1038/34635.

- Moon, T., Joughin, I., Smith, B., van den Broeke, M. R., van de Berg, W., Noel, B., and Usher, M. (2014) Distinct patterns of seasonal Greenland velocity. *Geophysical Research Letters*, 41, 7209–7216, doi:10.1002/2014GL061836.
- Motagh, M., Klotz, J., Tavakoli, F., Djamour, Y., Arabi, S., Wetzel, H. U., and Zschau, J. (2006) Combination of Precise Leveling and InSAR Data to Constrain Source Parameters of the $M_W = 6.5$, 26 December 2003 Bam Earthquake. *Pure and Applied Geophysics*, 163, 1–18, doi:10.1007/s00024-005-0005-y.
- Motagh, M., Wetzel, H.-U., Roessner, S., and Kaufmann, H. (2013) A TerraSAR-X InSAR study of landslides in southern Kyrgyzstan, Central Asia. *Remote Sensing Letters*, 4, 657–666, doi:10.1080/2150704X.2013.782111.
- Motagh, M., Beavan, J., Fielding, E. J., and Haghsheenas, M. (2014) Postseismic Ground Deformation Following the September 2010 Darfield, New Zealand, Earthquake From TerraSAR-X, COSMO-SkyMed, and ALOS InSAR. *IEEE Geoscience and Remote Sensing Letters*, 11, 186–190, doi:10.1109/LGRS.2013.2251858.
- Motagh, M., Bahroudi, A., Haghighi, M. H., Samsonov, S., Fielding, E., and Wetzel, H.-U. (2015) The 18 August 2014 $M_W 6.2$ Mormori, Iran, Earthquake: A Thin-Skinned Faulting in the Zagros Mountain Inferred from InSAR Measurements. *Seismological Research Letters*, 86, 775–782, doi:10.1785/0220140222.
- Motagh, M., Shamshiri, R., Haghsheenas Haghighi, M., Wetzel, H.-U., Akbari, B., Nahavandchi, H., Roessner, S., and Arabi, S. (2017) Quantifying groundwater exploitation induced subsidence in the Rafsanjan plain, southeastern Iran, using InSAR time-series and in situ measurements. *Engineering Geology*, 218, 134–151, doi:10.1016/j.enggeo.2017.01.011.
- Mouginot, J., Scheuchl, B., and Rignot, E. (2012) Mapping of Ice Motion in Antarctica Using Synthetic-Aperture Radar Data. *Remote Sensing*, 4, 2753–2767, doi:10.3390/rs4092753.
- Muto, M. and Furuya, M. (2013) Surface velocities and ice-front positions of eight major glaciers in the Southern Patagonian Ice Field, South America, from 2002 to 2011. *Remote Sensing of Environment*, 139, 50–59, doi:10.1016/j.rse.2013.07.034.
- Nagler, T., Rott, H., Hetzenecker, M., Scharrer, K., Magnússon, E., Floricioiu, D., and Notarnicola, C. (2012) Retrieval of 3D-glacier movement by high resolution X-band SAR data. In: *Proceedings of the 2012 IEEE International Geoscience and Remote Sensing Symposium (IGARSS)*, Munich, Germany, 22.–27. July 2012, pp. 3233–3236.
- Narama, C., Kääb, A., Duishonakunov, M., and Abdrakhmatov, K. (2010) Spatial variability of recent glacier area changes in the Tien Shan Mountains, Central Asia, using Corona (~1970), Landsat (~2000), and ALOS (~2007) satellite data. *Global and Planetary Change*, 71, 42–54, doi:10.1016/j.gloplacha.2009.08.002.
- NASA Spaceflight (2018). Available online: <https://www.nasaspaceflight.com/2018/05/falcon-9-iridium-next-6-grace-fo-launch/> (accessed on May 23, 2018).
- Navarro, M. A., Estrada, J. C., Servin, M., Quiroga, J. A., and Vargas, J. (2012) Fast two-dimensional simultaneous phase unwrapping and low-pass filtering. *Optics Express*, 20, 2556, doi:10.1364/OE.20.002556.
- Neckel, N., Braun, A., Kropáček, J., and Hochschild, V. (2013) Recent mass balance of the Purogangri Ice Cap, central Tibetan Plateau, by means of differential X-band SAR interferometry. *The Cryosphere*, 7, 1623–1633, doi:10.5194/tc-7-1623-2013.
- Neckel, N., Loibl, D., and Rankl, M. (2017) Recent slowdown and thinning of debris-covered glaciers in southeastern Tibet. *Earth and Planetary Science Letters*, 464, 95–102, doi:10.1016/j.epsl.2017.02.008.
- Neelmeijer, J., Motagh, M., and Wetzel, H.-U. (2014) Estimating Spatial and Temporal Variability in Surface Kinematics of the Inylchek Glacier, Central Asia, using TerraSAR-X Data. *Remote Sensing*, 6, 9239–9259, doi:10.3390/rs6109239.
- Neelmeijer, J., Motagh, M., and Bookhagen, B.: High-resolution digital elevation models from single-pass TanDEM-X interferometry over mountainous regions: A case study of Inylchek Glacier, Central Asia. *ISPRS Journal of Photogrammetry and Remote Sensing*, 130, 108–121, doi:10.1016/j.isprsjprs.2017.05.011.
- Neelmeijer, J., Schöne, T., Dill, R., Klemann, V., and Motagh, M. (2018) Ground Deformations around the Toktogul Reservoir, Kyrgyzstan, from Envisat ASAR and Sentinel-1 Data - A Case Study about the Impact of Atmospheric Corrections on InSAR Time Series. *Remote Sensing*, 10, 462, doi:10.3390/rs10030462.
- Ng, F. and Liu, S. (2009) Temporal dynamics of a jökulhlaup system. *Journal of Glaciology*, 55, 651–665, doi:10.3189/002214309789470897.

- Ng, F., Liu, S., Mavlyudov, B., and Wang, Y. (2007) Climatic control on the peak discharge of glacier outburst floods. *Geophysical Research Letters*, 34, 1–5, doi:10.1029/2007GL031426.
- Nijhawan R., Das, J., and Balasubramanian, R. (2016) Comparison of Support Vector Machine and Artificial Neural Network for Delineating Debris Covered Glacier. In: *SmartCom 2016: Smart Trends in Information Technology and Computer Communications*, Unal, A., Nayak, M., Mishra, D., Singh, D., and Joshi A. (eds), Communications in Computer and Information Science, vol 628. Springer, Singapore, doi:10.1007/978-981-10-3433-6_66.
- Nobakht, M., Motagh, M., Wetzel, H.-U., Roessner, S., and Kaufmann, H. (2014) The Inylchek Glacier in Kyrgyzstan, Central Asia: Insight on Surface Kinematics from Optical Remote Sensing Imagery. *Remote Sensing*, 6, 841–856, doi:10.3390/rs6010841.
- Nof, R. N., Ziv, A., Doin, M.-P., Baer, G., Fialko, Y., Wdowinski, S., Eyal, Y., and Bock, Y. (2012) Rising of the lowest place on Earth due to Dead Sea water-level drop: Evidence from SAR interferometry and GPS. *Journal of Geophysical Research: Solid Earth*, 117, B05412, doi:10.1029/2011JB008961.
- Nuth, C. and Kääb, A. (2011) Co-registration and bias corrections of satellite elevation data sets for quantifying glacier thickness change. *The Cryosphere*, 5, 271–290, doi:10.5194/tc-5-271-2011.
- O'Hara, S. L. (2000) Central Asia's water resources: Contemporary and future management issues. *International Journal of Water Resources Development*, 16, 423–441, doi:10.1080/713672501.
doi:10.1126/science.258.5079.115.
- Osmanoğlu, B., Sunar, F., Wdowinski, S., and Cabral-Cano, E. (2016) Time series analysis of InSAR data: Methods and trends. *ISPRS Journal of Photogrammetry and Remote Sensing*, 115, 90–102, doi:10.1016/j.isprsjprs.2015.10.003.
- Osmonov, A., Bolch, T., Xi, C., Kurban, A., and Guo, W. (2013) Glacier characteristics and changes in the Sary-Jaz River Basin (Central Tien Shan, Kyrgyzstan) – 1990–2010. *Remote Sensing Letters*, 4, 725–734, doi:10.1080/2150704X.2013.789146.
- Östrem, G. and Brugman, M. (1991) Glacier Mass-Balance Measurements: A Manual for Field and Office Work. In: *NHRI Science Report*, no. 4, Geographisches Institut Universität Zürich.
- Pandey, P. and Venkataraman, G. (2013) Comparison of DEMs derived from TanDEM-X and SRTM-C for Himalayan terrain. In: *2013 IEEE International Geoscience and Remote Sensing Symposium - IGARSS*, pp. 322–325, IEEE.
- Paul, F. (2008) Calculation of glacier elevation changes with SRTM: Is there an elevation-dependent bias? *Journal of Glaciology*, 54, 945–946, doi:10.3189/002214308787779960.
- Paul, F. and Haeberli, W. (2008) Spatial variability of glacier elevation changes in the Swiss Alps obtained from two digital elevation models. *Geophysical Research Letters*, 35, L21502, doi:10.1029/2008GL034718.
- Paul, F., Bolch, T., Kääb, A., Nagler, T., Nuth, C., Scharrer, K., Shepherd, A., Strozzi, T., Ticconi, F., Bhambri, R., Berthier, E., Bevan, S., Gourmelen, N., Heid, T., Jeong, S., Kunz, M., Lauknes, T. R., Luckman, A., Merryman Boncori, J. P., Moholdt, G., Muir, A., **Neelmeijer, J.**, Rankl, M., VanLooy, J., and Van Niel, T. (2015) The glaciers climate change initiative: Methods for creating glacier area, elevation change and velocity products. *Remote Sensing of Environment*, 162, 408–426, doi:10.1016/j.rse.2013.07.043.
- Peltier, W. (2004) Global glacial isostasy and the surface of the ice-age Earth: The ICE-5G (VM2) Model and GRACE, *Annual Review of Earth and Planetary Sciences*, 32, 111–149, doi:10.1146/annurev.earth.32.082503.144359.
- Peter, H., Jäggi, A., Fernández, J., Escobar, D., Ayuga, F., Arnold, D., Wermuth, M., Hackel, S., Otten, M., Simons, W., Visser, P., Hugentobler, U. and Féménias, P. (2017) Sentinel-1A – First precise orbit determination results, *Advances in Space Research*, 60, 879–892, doi:10.1016/j.asr.2017.05.034.
- Petillot, I. Trouvé, E., Bolon, P., Julea, A., Yan, Y., Gay, M., and Vanpe, J. M. (2010) Radar-Coding and Geocoding Lookup Tables for the Fusion of GIS and SAR Data in Mountain Areas, *IEEE Geoscience and Remote Sensing Letters*, 7, 309–313, doi:10.1109/LGRS.2009.2034118.
- Pfeffer, W. T., Arendt, A. A., Bliss, A., Bolch, T., Cogley, J. G., Gardner, A. S., Hagen, J.-O., Hock, R., Kaser, G., Kienholz, C., Miles, E. S., Moholdt, G., Mölg, N., Paul, F., Radić, V., Rastner, P., Raup, B. H., Rich, J., and Sharp, M. J. (2014) The Randolph Glacier Inventory: a globally complete inventory of glaciers. *Journal of Glaciology*, 60, 537–552, doi:10.3189/2014JoG13J176.

- Pieczonka, T. and Bolch, T. (2015) Region-wide glacier mass budgets and area changes for the Central Tien Shan between ~1975 and 1999 using Hexagon KH-9 imagery. *Global and Planetary Change*, 128, 1–13, doi:10.1016/j.gloplacha.2014.11.014.
- Pieczonka, T., Bolch, T., Junfeng, W., and Shiyin, L. (2013) Heterogeneous mass loss of glaciers in the Aksu-Tarim Catchment (Central Tien Shan) revealed by 1976 KH-9 Hexagon and 2009 SPOT-5 stereo imagery. *Remote Sensing of Environment*, 130, 233–244, doi:10.1016/j.rse.2012.11.020.
- Prats, P., Marotti, L., Wollstadt, S., and Scheiber, R. (2010) Investigations on TOPS interferometry with TerraSAR-X. In: *2010 IEEE International Geoscience and Remote Sensing Symposium (IGARSS)*, Honolulu, Hawaii, 25.–30. July 2010, pp. 2629–2632, doi:10.1109/IGARSS.2010.5650037.
- Prats-Iraola, P., Scheiber, R., Marotti, L., Wollstadt, S., and Reigber, A. (2012) TOPS Interferometry With TerraSAR-X. *IEEE Transactions on Geoscience and Remote Sensing*, 50, 3179–3188, doi:10.1109/TGRS.2011.2178247.
- Pritchard, H. D., Luthcke, S. B., and Fleming, A. H. (2011) Understanding ice-sheet mass balance: Progress in satellite altimetry and gravimetry. *Journal of Glaciology*, 56, 1151–1161, doi:10.3189/002214311796406194.
- Puysségur, B., Michel, R., and Avouac, J.-P. (2007) Tropospheric phase delay in interferometric synthetic aperture radar estimated from meteorological model and multispectral imagery. *Journal of Geophysical Research*, 112, B05419, doi:10.1029/2006JB004352.
- Quincey, D. J., Copland, L., Mayer, C., Bishop, M., Luckman, A., and Belò, M. (2009a) Ice velocity and climate variations for Baltoro Glacier, Pakistan. *Journal of Glaciology*, 55, 1061–1071.
- Quincey, D. J., Luckman, A., and Benn, D. (2009b) Quantification of Everest region glacier velocities between 1992 and 2002, using satellite radar interferometry and feature tracking. *Journal of Glaciology*, 55, 596–606, doi:10.3189/002214309789470987.
- Racoviteanu, A. E., Manley, W. F., Arnaud, Y., and Williams, M. W. (2007) Evaluating digital elevation models for glaciologic applications: An example from Nevado Coropuna, Peruvian Andes. *Global and Planetary Change*, 59, 110–125, doi:10.1016/j.gloplacha.2006.11.036.
- Rajner, M. and Liwosz, T. (2011) Studies of crustal deformation due to hydrological loading on GPS height estimates. *Geodesy and Cartography*, 60, 135–144, doi:10.2478/v10277-012-0012-y.
- Ramillien, G., Lombard, A., Cazenave, A., Ivins, E. R., Llubes, M., Remy, F., and Biancale, R. (2006) Inter-annual variations of the mass balance of the Antarctica and Greenland ice sheets from GRACE. *Global and Planetary Change*, 53, 198–208, doi:10.1016/j.gloplacha.2006.06.003.
- Rankl, M. and Braun, M. (2016) Glacier elevation and mass changes over the central Karakoram region estimated from TanDEM-X and SRTM/X-SAR digital elevation models. *Annals of Glaciology*, 57, 273–281, doi:10.3189/2016AoG71A024.
- Raup, B., Racoviteanu, A. E., Khalsa, S. J. S., Helm, C., Armstrong, R., and Arnaud, Y. (2007) The GLIMS geospatial glacier database: A new tool for studying glacier change. *Global and Planetary Change*, 56, 101–110, doi:10.1016/j.gloplacha.2006.07.018.
- Richardson, S. D. and Reynolds, J. M. (2000) An overview of glacial hazards in the Himalayas. *Quaternary International*, 65–66, 31–47, doi:10.1016/S1040-6182(99)00035-X.
- Ridley, J. K. and Partington, K. C. (1988) A model of satellite radar altimeter return from ice sheets. *International Journal of Remote Sensing*, 9, 601–624, doi:10.1080/01431168808954881.
- Rignot, E., Echelmeyer, K., and Krabill, W. (2001) Penetration depth of interferometric synthetic-aperture radar signals in snow and ice. *Geophysical Research Letters*, 28, 3501–3504, doi:10.1029/2000GL012484.
- Rocca, F., Rucci, A., Ferretti, A., and Bohane, A.: Advanced InSAR interferometry for reservoir monitoring, *First Break*, 31, 77–85.
- Roeloffs, E. A. (1988) Fault stability changes induced beneath a reservoir with cyclic variations in water level. *Journal of Geophysical Research: Solid Earth*, 93, 2107–2124, doi:10.1029/JB093iB03p02107.
- Rosen, P. A., Werner, C. W., and Hiramatsu, A. (1994) Two-dimensional phase unwrapping of SAR interferograms by charge connection through neutral trees. *Proceedings IGARSS'94*, Pasadena, 8.–12. August, 1994.

- Rosen, P. A., Hensley, S., Joughin, I. I., Li, F., Madsen, S. N., Rodriguez, E., and Goldstein, R. M. (2010) Synthetic aperture radar interferometry. *Proceedings of the IEEE*, 88, 333–382, doi:10.1109/5.838084.
- Rott, H., Floricioiu, D., Wuite, J., Scheiblauer, S., Nagler, T., and Kern, M. (2014) Mass changes of outlet glaciers along the Nordenskjöld Coast, northern Antarctic Peninsula, based on TanDEM-X satellite measurements. *Geophysical Research Letters*, 41, 8123–8129, doi:10.1002/2014GL061613.
- Round, V., Leinss, S., Huss, M., Haemmig, C., and Hajsek, I. (2017) Surge dynamics and lake outbursts of Kyagar Glacier, Karakoram, *The Cryosphere*, 11, 723–739, doi:10.5194/tc-11-723-2017.
- Salzer, J. T., Nikkhoo, M., Walter, T. R., Sudhaus, H., Reyes-Dávila, G., Bretón, M., and Arámbula, R. (2014) Satellite radar data reveal short-term pre-explosive displacements and a complex conduit system at Volcán de Colima, Mexico. *Frontiers in Earth Science*, 2, 1–11, doi:10.3389/feart.2014.00012.
- Sarmap (2014). Available online: <http://www.sarmap.ch> (accessed on February 17, 2014).
- Satyabala, S. P., Yang, Z., and Bilham, R. (2012) Stick-slip advance of the Kohat Plateau in Pakistan. *Nature Geoscience*, 5, 147–150, doi:10.1038/ngeo1373, 2012.
- Savoskul, O., Chevnina, E., Perziger, F., Vasilina, L., Baburin, V., Danshin, A. I., Matyakubov, B., and Murakaev, R. (2003) Water, climate, food, and environment in the Syr Darya Basin. In: *Contribution to the project ADAPT*, July 2003.
- Scambos, T. A., Bohlander, J. A., Shuman, C. A., and Skvarca, P. (2004) Glacier acceleration and thinning after ice shelf collapse in the Larsen B embayment, Antarctica. *Geophysical Research Letters*, 31, L18402, doi:10.1029/2004GL020670.
- Scheiber, R. and Moreira, A. (2000) Coregistration of interferometric SAR images using spectral diversity. *IEEE Transactions on Geoscience and Remote Sensing*, 38, 2179–2191, doi:10.1109/36.868876.
- Schöne, T., Zech, C., Unger-Shayesteh, K., Rudenko, V., Thoss, H., Wetzel, H.-U., Gafurov, A., Illigner, J., and Zubovich, A. (2013) A new permanent multi-parameter monitoring network in Central Asian high mountains - from measurements to data bases. *Geoscientific Instrumentation, Methods and Data Systems*, 2, 97–111, doi:10.5194/gi-2-97-2013.
- Schöne, T., Dusik, E., Illigner, J., and Klein, I. (2017) Water in Central Asia: Reservoir Monitoring with Radar Altimetry Along the Naryn and Syr Darya Rivers- In: *International Association of Geodesy Symposia*, pp. 349–357, doi:10.1007/1345_2017_265.
- Schubert, A., Faes, A., Kääb, A., and Meier, E. (2013) Glacier surface velocity estimation using repeat TerraSAR-X images: Wavelet- vs. correlation-based image matching. *ISPRS Journal of Photogrammetry and Remote Sensing*, 82, 49–62, doi:10.1016/j.isprsjprs.2013.04.010.
- Seehaus, T., Marinsek, S., Helm, V., Skvarca, P., and Braun, M. (2015) Changes in ice dynamics, elevation and mass discharge of Dinsmoor–Bombardier–Edgeworth glacier system, Antarctic Peninsula. *Earth and Planetary Science Letters*, 427, 125–135, doi:10.1016/j.epsl.2015.06.047.
- Shangguan, D. H., Bolch, T., Ding, Y. J., Kröhnert, M., Pieczonka, T., Wetzel, H. U., and Liu, S. Y. (2015) Mass changes of Southern and Northern Inylchek Glacier, Central Tian Shan, Kyrgyzstan, during ~1975 and 2007 derived from remote sensing data. *The Cryosphere*, 9, 703–717, doi:10.5194/tc-9-703-2015.
- Shean, D. E., Christianson, K., Larson, K. M., Ligtenberg, S. R., Joughin, I. R., Smith, B. E., Max Stevens, C., Bushuk, M., and Holland, D. M. (2017) GPS-derived estimates of surface mass balance and ocean-induced basal melt for Pine Island Glacier ice shelf, Antarctica. *The Cryosphere*, 11, 2655–2674, doi:10.5194/tc-11-2655-2017.
- Simpson, D. W., Hamburger, M. W., Pavlov, V. D., and Nersesov, I. L. (1981) Tectonics and seismicity of the Toktogul Reservoir Region, Kirgizia, USSR. *Journal of Geophysical Research*, 86, 345, doi:10.1029/JB086iB01p00345.
- Simpson, D. W., Leith, W., and Scholz, C. (1988) Two types of reservoir-induced seismicity. *Bulletin of the Seismological Society of America*, 78, 2025–2040.
- Singleton, A., Li, Z., Hoey, T., and Muller, J. P. (2014) Evaluating sub-pixel offset techniques as an alternative to D-InSAR for monitoring episodic landslide movements in vegetated terrain. *Remote Sensing of Environment*, 147, 133–144, doi:10.1016/j.rse.2014.03.003.

- Smith, L. C. (2002) Emerging Applications of Interferometric Synthetic Aperture Radar (InSAR) in Geomorphology and Hydrology. *Annals of the Association of American Geographers*, 92, 385–398, doi:10.1111/1467-8306.00295.
- Sorg, A., Bolch, T., Stoffel, M., Solomina, O., and Beniston, M. (2012) Climate change impacts on glaciers and runoff in Tien Shan (Central Asia). *Nature Climate Change*, 2, 725–731, doi:10.1038/nclimate1592.
- Sorg, A., Mosello, B., Shalpykova, G., Allan, A., Hill Clarvis, M., and Stoffel, M. (2014) Coping with changing water resources: The case of the Syr Darya river basin in Central Asia. *Environmental Science & Policy*, 43, 68–77, doi:10.1016/j.envsci.2013.11.003.
- Soruco, A., Vincent, C., Francou, B., Ribstein, P., Berger, T., Sicart, J. E., Wagnon, P., Arnaud, Y., Favier, V., and Lejeune, Y. (2009) Mass balance of Glacier Zongo, Bolivia, between 1956 and 2006, using glaciological, hydrological and geodetic methods. *Annals of Glaciology*, 50, 1–8, doi:10.3189/172756409787769799.
- Srivastava, H. S., Patel, P., Sharma, Y., and Navalgund, R. R. (2009) Large-Area Soil Moisture Estimation Using Multi-Incidence-Angle RADARSAT-1 SAR Data. *IEEE Transactions on Geoscience and Remote Sensing*, 47, 2528–2535, doi:10.1109/TGRS.2009.2018448.
- Stockamp, J., Li, Z., Bishop, P., Hansom, J., Rennie, A., Petrie, E., Tanaka, A., Bingley, R., and Hansen, D. (2015) Investigating glacial isostatic adjustment in Scotland with InSAR and GPS observations. In: *Proceedings of Fringe 2015: Advances in the Science and Applications of SAR Interferometry and Sentinel-1 InSAR Workshop*, SP-731, doi:10.5270/Fringe2015.pp171.
- Strozzi, T., Luckman, A., Murray, T., Wegmüller, U., and Werner, C. L. (2002) Glacier motion estimation using SAR offset-tracking procedures. *IEEE Transactions on Geoscience and Remote Sensing*, 40, 2384–2391, doi:10.1109/TGRS.2002.805079.
- Strozzi, T., Gudmundsson, G. H., and Wegmüller, U. (2003) Estimation of the surface displacement of Swiss alpine glaciers using satellite radar interferometry. *EARSeL eProceedings*, 2, 3–7.
- Strozzi, T., Farina, P., Corsini, A., Ambrosi, C., Thüring, M., Zilger, J., Wiesmann, A., Wegmüller, U., and Werner, C. L. (2005) Survey and monitoring of landslide displacements by means of L-band satellite SAR interferometry. *Landslides*, 2, 193–201, doi:10.1007/s10346-005-0003-2.
- Sugiyama, S., Skvarca, P., Naito, N., Enomoto, H., Tsutaki, S., Tone, K., Marinsek, S., and Aniya, M. (2011) Ice speed of a calving glacier modulated by small fluctuations in basal water pressure. *Nature Geoscience*, 4, 597–600, doi:10.1038/ngeo1218.
- Sun, L. and Muller, J. P. (2016) Evaluation of the use of sub-pixel offset tracking techniques to monitor landslides in densely vegetated steeply sloped areas. *Remote Sensing*, 8, 659, doi:10.3390/rs8080659.
- Sun, Y., Jiang, L., Liu, L., Sun, Q., Wang, H., and Hsu, H. (2018) Mapping glacier elevations and their changes in the Western Qilian Mountains, Northern Tibetan Plateau, by bistatic InSAR. *IEEE Journal of Selected Topics in Applied Earth Observations and Remote Sensing*, 11, 68–78, doi:10.1109/JSTARS.2017.2764751.
- Tamisiea, M. E. and Mitrovica, J. X. (2011) The Moving boundaries of Sea Level Change: Understanding the Origins of Geographic Variability. *Oceanography*, 24, 24–39, doi:10.5670/oceanog.2011.25.
- Tangborn, W. V., Krimmel, R. M., and Meier, M. F. (1971) A comparison of glacier mass balance by glaciological, hydrological and mapping methods, South Cascade Glacier, Washington Wendell. In: *Snow and Ice-Symposium-Neiges et Glaces (Proceedings of the Moscow Symposium)*, August 1971, pp. 185–196.
- Tesauro, M., Audet, P., Kaban, M. K., Bürgmann, R., and Cloetingh, S. (2012) The effective elastic thickness of the continental lithosphere: Comparison between rheological and inverse approaches. *Geochemistry, Geophysics, Geosystems*, 13, Q09001, doi:10.1029/2012GC004162.
- Tibaldi, A., Corazzato, C., Rust, D., Bonali, F., Pasquarè Mariotto, F., Korzhnikov, A., Oppizzi, P., and Bonzanigo, L. (2015) Tectonic and gravity-induced deformation along the active Talas–Fergana Fault, Tien Shan, Kyrgyzstan. *Tectonophysics*, 657, 38–62, doi:10.1016/j.tecto.2015.06.020.
- Tweed, F. S. and Russell, A. J. (1999) Controls on the formation and sudden drainage of glacier-impounded lakes: Implications for jökulhlaup characteristics. *Progress in Physical Geography*, 23, 79–110, doi:10.1191/030913399666727306.
- UNAVCO, Baker, S. (2018) Personal communication, November 11, 2018.

- Unger-Shayesteh, K., Vorogushyn, S., Farinotti, D., Gafurov, A., Duethmann, D., Mandychev, A., and Merz, B. (2013) What do we know about past changes in the water cycle of Central Asian headwaters? A review. *Global and Planetary Change*, 110, 4–25, doi:10.1016/j.gloplacha.2013.02.004.
- Van Zyl, J. J. (2001) The shuttle radar topography mission (SRTM): A breakthrough in remote sensing of topography. *Acta Astronautica*, 48, 559–565, doi:10.1016/S0094-5765(01)00020-0.
- Vey, S., Steffen, H., Müller, J., and Boike, J. (2013) Inter-annual water mass variations from GRACE in central Siberia. *Journal of Geodesy*, 87, 287–299, doi:10.1007/s00190-012-0597-9.
- Vijay, S. and Braun, M. (2016) Elevation Change Rates of Glaciers in the Lahaul-Spiti (Western Himalaya, India) during 2000–2012 and 2012–2013. *Remote Sensing*, 8, 1038, doi:10.3390/rs8121038.
- Wahr, J., Khan, S. A., van Dam, T., Liu, L., van Angelen, J. H., van den Broeke, M. R., and Meertens, C. M. (2013) The use of GPS horizontals for loading studies, with applications to northern California and southeast Greenland. *Journal of Geophysical Research: Solid Earth*, 118, 1795–1806, doi:10.1002/jgrb.50104.
- Wang, R. and Gao, Q. (1997) Preliminary study on flash floods in Tarim River basin. *Chinese Geographical Science*, 7, 53–58, doi:10.1007/s11769-997-0072-3.
- Wang, H., Wright, T. J., Yu, Y., Lin, H., Jiang, L., Li, C. and Qui, G. (2012) InSAR reveals coastal subsidence in the Pearl River Delta, China. *Geophysical Journal International*, 19, 1119–1128, doi:10.1111/j.1365-246X.2012.05687.x.
- Wegmüller, U., Werner, C., Strozzi, T., Wiesmann, A., Frey, O., and Santoro, M. (2016) Sentinel-1 IWS mode support in the GAMMA software. *Procedia Computer Science*, 100, 431–436, doi:10.1109/APSAR.2015.7306242.
- Wei Xu and Cumming, I. (1999) A region-growing algorithm for InSAR phase unwrapping. *IEEE Transactions on Geoscience and Remote Sensing*, 37, 124–134, doi:10.1109/36.739143.
- Wendleder, A., Felber, A., Wessel, B., Huber, M., and Roth, A. (2016) A Method to Estimate Long-Wave Height Errors of SRTM C-Band DEM. *IEEE Geoscience and Remote Sensing Letters*, 13, 5, 696–700, doi:10.1109/LGRS.2016.2538822.
- Werner, C. L., Wegmüller, U., Strozzi, T., and Wiesmann, A. (2001) GAMMA SAR and Interferometric Processing Software. In: *Proceedings of ERS-ENVISAT Symposium*, edited by Sawaya-Lacoste, H., European Space Agency Publications Division, Noordwijk, Gothenburg, Sweden, October 2000.
- Werner, C. L., Wegmüller, U., Strozzi, T., and Wiesmann, A. (2003) Interferometric point target analysis for deformation mapping. In: *IGARSS 2003. 2003 IEEE International Geoscience and Remote Sensing Symposium. Proceedings (IEEE Cat. No.03CH37477)*, vol. 7, pp. 4362–4364, IEEE, doi:10.1109/IGARSS.2003.1295516.
- Westoby, M. J., Glasser, N. F., Hambrey, M. J., Brasington, J., Reynolds, J. M., and Hassan, M. A. (2014) Reconstructing historic glacial lake outburst floods through numerical modelling and geomorphological assessment: Extreme events in the himalaya. *Earth Surface Processes and Landforms*, 39, 1675–1692, doi:10.1002/esp.3617.
- Wetzel, H.-U., Reigber, A., Richter, A., and Michajljow, W. (2005) Gletschermonitoring und Gletscherseebrüche am Inyltschik (Zentraler Tienshan) - Interpretation mit optischen und Radarsatelliten. In: *GEO-GOVERNMENT - Wirtschaftliche Innovation durch Geodaten: Vorträge; 25. wissenschaftlich-technische Jahrestagung der DGPF*, Seyfert, E., Eds, Publikationen der Deutschen Gesellschaft für Photogrammetrie, Fernerkundung und Geoinformation e.V.: Potsdam, Germany, pp. 341–350.
- Willis, I. C. (1995) Intra-annual variations in glacier motion: a review. *Progress in Physical Geography*, 19, 61–106, doi:10.1177/030913339501900104.
- WMOSAT (2018). Available online: <https://www.wmo-sat.info/oscar/instruments/view/1097> (accessed on April 27, 2018).
- Wright, T. J., Parsons, B., England, P. C., and Fielding, E. J. (2004) InSAR Observations of Low Slip Rates on the Major Faults of Western Tibet. *Science*, 305, 236–239, doi:10.1126/science.1096388.
- Wuite, J., Rott, H., Hetzenecker, M., Floricioiu, D., De Rydt, J., Gudmundsson, G. H., Nagler, T., and Kern, M. (2015) Evolution of surface velocities and ice discharge of Larsen B outlet glaciers from 1995 to 2013. *The Cryosphere*, 9, 957–969, doi:10.5194/tc-9-957-2015.

- Xu, Z., Schrama, E. J., Van Der Wal, W., Van Den Broeke, M., and Enderlin, E. M. (2016) Improved GRACE regional mass balance estimates of the Greenland ice sheet cross-validated with the input-output method. *The Cryosphere*, 10, 895–912, doi:10.5194/tc-10-895-2016.
- Yan, S., Guo, H., Liu, G., and Ruan, Z. (2013) Mountain glacier displacement estimation using a DEM-assisted offset tracking method with ALOS/PALSAR data. *Remote Sensing Letters*, 4, 494–503, doi:10.1080/2150704X.2012.754561.
- Yhokha, A., Goswami, P. K., Chang, C.-P., Yen, J.-Y., Ching, K.-E. and Manini Aruche, K. (2018) Application of Persistent Scatterer Interferometry (PSI) in monitoring slope movements in Nainital, Uttarakhand Lesser Himalaya, India. *Journal of Earth System Science*, 127, 6, doi:10.1007/s12040-017-0907-y.
- Yin, Y., Huang, B., Wang, W., Wei, Y., Ma, X., Ma, F., and Zhao, C. (2016) Reservoir-induced landslides and risk control in Three Gorges Project on Yangtze River, China. *Journal of Rock Mechanics and Geotechnical Engineering*, 8, 577–595, doi:10.1016/j.jrmge.2016.08.001.
- Yu, C., Li, Z., and Penna, N. T. (2017a) Interferometric synthetic aperture radar atmospheric correction using a GPS-based iterative tropospheric decomposition model. *Remote Sensing of Environment*, 204, 109–121, doi:10.1016/j.rse.2017.10.038.
- Yu, C., Penna, N. T., and Li, Z. (2017b) Generation of real-time mode high-resolution water vapor fields from GPS observations. *Journal of Geophysical Research*, 122, 2008–2025, doi:10.1002/2016JD025753.
- Zebker, H. A. and Villasenor, J. (1992) Decorrelation in interferometric radar echoes. *IEEE Transactions on Geoscience and Remote Sensing*, 30, 950–959, doi:10.1109/36.175330.
- Zebker, H. A., Rosen, P. A., and Hensley, S. (1997) Atmospheric effects in interferometric synthetic aperture radar surface deformation and topographic maps. *Journal of Geophysical Research: Solid Earth*, 102, 7547–7563, doi:10.1029/96JB03804.
- Zech, C., Schöne, T., **Neelmeijer, J.**, Zubovich, A., and Galas, R. (2015) Geodetic Monitoring Networks: GNSS-Derived Glacier Surface Velocities at the Global Change Observatory Inylchek (Kyrgyzstan). In: *IAG 150 Years. International Association of Geodesy Symposia*, Rizos C., Willis P. (eds), vol 143. Springer, Cham, pp. 557–563, doi:10.1007/1345_2015_38.
- Zech C., Schöne T., **Neelmeijer J.**, and Zubovich A. (2016) Continuous Kinematic GPS Monitoring of a Glacier Lake Outburst Flood. In: *International Symposium on Earth and Environmental Sciences for Future Generations. International Association of Geodesy Symposia*, Freymueller J.T., Sánchez L. (eds), vol 147. Springer, Cham, pp. 339–347, doi:10.1007/1345_2016_246.
- Zemp, M., Thibert, E., Huss, M., Stumm, D., Rolstad Denby, C., Nuth, C., Nussbaumer, S. U., Moholdt, G., Mercer, A., Mayer, C., Joerg, P. C., Jansson, P., Hynek, B., Fischer, A., Escher-Vetter, H., Elvehøy, H., and Andreassen, L. M. (2013) Reanalysing glacier mass balance measurement series. *The Cryosphere*, 7, 1227–1245, doi:10.5194/tc-7-1227-2013.
- Zhang, S., Förster, S., Medeiros, P., de Araújo, J. C., Motagh, M., and Waske, B. (2016) Bathymetric survey of water reservoirs in north-eastern Brazil based on TanDEM-X satellite data. *Science of the Total Environment*, 571, 575–593, doi:10.1016/j.scitotenv.2016.07.024.
- Zhao, W., Amelung, F., Doin, M.-P., Dixon, T. H., Wdowinski, S., and Lin, G. (2016) InSAR observations of lake loading at Yangzhuoyong Lake, Tibet: Constraints on crustal elasticity. *Earth and Planetary Science Letters*, 449, 240–245, doi:10.1016/j.epsl.2016.05.044.
- Zhou, C., Zhou, Y., Deng, F., Ai, S., Wang, Z., and Dongchen, E. (2014) Seasonal and interannual ice velocity changes of Polar Record Glacier, East Antarctica. *Annals of Glaciology*, 55, 45–51, doi:10.3189/2014AoG66A185.
- Zhou, X., Chang, N.-B., and Li, S. (2009) Applications of SAR Interferometry in Earth and Environmental Science Research. *Sensors*, 9, 1876–1912, doi:10.3390/s90301876.
- Zink, M. and Moreira, A. (2015) TanDEM-X: A Challenging Radar Mission for Generating a New Earth's Topography. In: *Geomorphometry for Geosciences*, pp. 1–4.
- Zwally, H. J., Schutz, R., Bentley, C., Bufton, J., Herring, T., Minster, J., Spinhirne, J., and Thomas, R. (2014) GLAS/ICESat L2 Global Land Surface Altimetry Data, Version 34. *Tech. rep., NASA National Snow and Ice Data Center Distributed Active Archive Center*, Boulder Colorado, USA, doi:10.5067/ICESAT/GLAS/DATA227.

Acknowledgements

This thesis could not have been accomplished without the support of many people to whom I would like to express my deepest gratitude.

First of all, I would like to thank my supervisor Prof. Dr. Mahdi Motagh for trusting in me for many years, for giving me the freedom to follow my research interests, for sharing his immense knowledge of SAR processing tips and tricks, for supporting my desire to attend many conferences, and for giving me the time to fail and learn.

I am grateful to Prof. Dr. Hermann Kaufmann and Prof. Dr. Luis Guanter, the heads of Section 1.4 Remote Sensing of GFZ, for developing and maintaining a super-friendly working environment that enables young researchers to engage quickly and make contact with many colleagues. Thank you for letting us focus on our work!

My sincere thanks goes to Dr. Hans-Ulrich Wetzol, the expert for all Kyrgyzstan related problems. Thank you Uli for always being available for questions, for immediately providing data whenever you have it available, and most especially for organising an exciting field trip to the Inylchek Glacier.

I would like to acknowledge all my co-authors who have supplied me with additional data and analysis on my work, who have provided constructive feedback, who have contributed a lot to improving the manuscripts, and who have always made me feel that we are doing great research together.

One person I would like to thank in particular is Sylvia Magnussen, the administrator of our section. Sylvia, it was a great pleasure to develop the GAMMA forum together with you. Thank you so much for being open to many new ideas and for always supporting me in case of technical problems.

Special gratitude goes to my proofreaders Katrin, Udo and Henryk, who dedicated their free time to reading the thesis carefully and helped me a lot in finding errors and flaws.

Furthermore, I would like to give a big thanks to all my office mates during the years. Randolph, Christin, Nina, Fredi, and Claudia, thank you for all the fun in the office, for joyful discussions far from research, and for always being a cheer-up during difficult times.

A big thank you goes also to all colleagues of Section 1.4 who created a fantastic working atmosphere and who always had an open ear for questions. Many thanks to the running group for the regular motivation to free the head from work with just another training round. And also thank you PhD's for all the fun during our crafting sessions!

Finally, I would like to embrace my family and friends, who never lost trust and always provided me with moral and emotional support. Thank you Henryk for never ceasing to believe in me and also thank you kids for reminding me every day that there is so much more to life than a doctoral thesis.

Curriculum Vitae

Personal Information

Julia Neelmeijer

born on April 7th, 1986 in Dresden

Work Experience

since 02/2012	Research Assistant at the Helmholtz-Centre Potsdam, German Research Centre for Geosciences (GFZ), Section 1.4 Remote Sensing
12/2015 – 09/2016	Maternity and Parental Leave
05/2014 – 08/2014	Parental Leave
07/2013 – 01/2014	Maternity and Parental Leave

Stay Abroad

10/2008 – 02/2009	Internship at the Universidad de Concepción, Chile
08/2004 – 08/2005	Work and Travel, New Zealand

Education

08/2005 – 02/2012	Studies of Cartography at the Technical University Dresden, Graduation: Diploma
09/1996 – 06/2004	Hans-Erlwein Gymnasium Dresden, Graduation: Abitur

Wissenschaftliche Arbeiten der Fachrichtung Geodäsie und Geoinformatik der Leibniz Universität Hannover

(Eine vollständige Liste der Wiss. Arb. ist beim Geodätischen Institut, Nienburger Str. 1, 30167 Hannover erhältlich.)

Nr. 321	ZADDACH, Sebastian:	Zum Beitrag Bayesscher Schätzverfahren in der Vergleichswertermittlung (Diss. 2016)
Nr. 322	SMYRNAIOS, Marios:	Carrier-phase Multipath in Satellite-based Positioning (Diss. 2016)
Nr. 323	MENZE, Moritz:	Object Scene Flow (Diss. 2016)
Nr. 324	WU, Hu:	Gravity field recovery from GOCE observations (Diss. 2016)
Nr. 325	XU, Xiangyang:	Terrestrial Laser Scanning for the Generation and Calibration of Finite Element Models (Diss. 2016)
Nr. 326	SAYYAD, Muhammad Naeem Shahzad:	Joint use and mutual control of terrestrial laser scans and digital images for accurate 3D measurements (Diss. 2016)
Nr. 327	SCHACK, Lukas:	Object-based matching of Persistent Scatterers to Optical Oblique Images (Diss. 2016)
Nr. 328	REICH, Martin:	Global Image Orientation from Pairwise Relative Orientations (Diss. 2016)
Nr. 329	KLINGER, Tobias:	Probabilistic multi-person localisation and tracking (Diss. 2016)
Nr. 330	SCHMIDT, Alena:	Markierte Punktprozesse für die automatische Extraktion von Liniennetzen in Rasterdaten (Diss. 2016)
Nr. 331	HOFMANN, Franz:	Lunar Laser Ranging - verbesserte Modellierung der Monddynamik und Schätzung relativistischer Parameter (Diss. 2017)
Nr. 332	BRIEDEN, Phillip:	Validierung von GOCE-Gravitationsgradienten in Kreuzungspunkten und Zukunftsperspektiven der Satellitengradiometrie (Diss. 2017)
Nr. 333	VON GÖSSELN, Ilka:	Simulationsbasierte Effizienzoptimierung von Messprozessen am Beispiel der tachymetrischen Netzmessung (Diss. 2017)
Nr. 334	HOFMANN, Sabine:	Potential von LiDAR Mobile Mapping für hochgenaue Karten (Diss. 2017)
Nr. 335	ALBERT, Lena:	Simultane Klassifikation der Bodenbedeckung und Landnutzung unter Verwendung von Conditional Random Fields (Diss. 2017)
Nr. 336	NIEMEYER, Joachim:	Verwendung von Kontext zur Klassifikation luftgestützter Laserdaten urbaner Gebiete (Diss. 2017)
Nr. 337	EGGERT, Daniel:	Effiziente Verarbeitung und Visualisierung von Mobile Mapping Daten (Diss. 2017)
Nr. 338	FITZNER, Daniel:	Estimation of Spatio-Temporal Moving Fields at High Resolution (Diss. 2017)
Nr. 339	CZIOSKA, Paul:	Meeting point locations for shared rides (Diss. 2018)
Nr. 340	FEUERHAKE, Udo:	Erfassung von Trajektorien und Erkennung von Bewegungsmustern (Diss. 2018)
Nr. 341	HUANG, Hai:	Bayesian Models for Pattern Recognition in Spatial Data (Habil. 2018)
Nr. 342	BOCK, Urs Fabian:	Dynamic Parking Maps from Vehicular Crowdsensing (Diss. 2018)
Nr. 343	KRAWINKEL, Thomas:	Improved GNSS Navigation with Chip-scale Atomic Clocks (Diss. 2018)
Nr. 344	GOSWAMI, Sujata:	Understanding the sensor noise in the GRACE range-rate observations by analyzing their residuals (Diss. 2018)
Nr. 345	ZHANG, Yin:	Expected Utilities for Decision Making and Steering of Measurement Processes (Diss. 2018)
Nr. 346	SCHLICHTING, Alexander:	Fahrzeuglokalisierung durch Automotive Laserscanner unter Verwendung statischer Merkmale (Diss. 2018)
Nr. 347	RÖTH, Oliver	Extraktion von hochgenauer Fahrspurgeometrie und -topologie auf der Basis von Fahrzeugtrajektorien und Umgebungsinformationen (Diss. 2018)
Nr. 348	NEELMEIJER, Julia:	Observing Inter- and Intra-Annual Glacier Changes and Lake Loading Effects from Synthetic Aperture Radar Remote Sensing (Diss. 2018)

Die Arbeiten werden im Rahmen des wissenschaftlichen Schriftenaustausches verteilt und sind nicht im Buchhandel erhältlich. Der Erwerb ist zu einem Stückpreis von € 25,00 bei den herausgebenden Instituten möglich.

